Interactions and detection of R-hadrons

Aafke Christine Kraan

Department of Experimental High Energy Physics
The Niels Bohr Institute
Copenhagen University

Thesis for the Degree of Doctor of Philosophy

Thesis advisor: Peter Hansen

To be presented, with the permission of the Niels Bohr Institute for public criticism in Auditorium A of the Niels Bohr Institute on Monday the 29th of November 2004, 14.00

Abstract

In this thesis the interactions of new heavy hadron states are studied. Such states arise in several models for physics beyond the Standard Model. The focus here is on R-hadrons, which are stable hadronized gluinos, predicted by certain supersymmetric models. Three different studies are performed.

The first mainly concerns theoretical aspects of R-hadrons. Several scenarios, in which these particles could exist are investigated, and a new model is developed to describe the nuclear interactions of hadrons containing any new color triplet or octet parton, which is stable in the detector. This model is implemented in GEANT 3, which is then used to study experimental signatures.

The second part is a data analysis, using data recorded by the ALEPH detector at LEP2. A direct search is performed for scalar top pair production, with subsequent decays into an LSP gluino, $\mathrm{e^+e^-} \rightarrow \tilde{\mathrm{t}}\bar{\tilde{\mathrm{t}}} \rightarrow \mathrm{c}\tilde{\mathrm{g}}\bar{\mathrm{c}}\tilde{\mathrm{g}}$, at center-of-mass energies from 183 to 209 GeV. The scalar top quark would live long enough to hadronize, thereafter hadronizing into a stable gluino and a c-quark. The branching ratio of this decay is assumed to be 100%. If the gluino mass is larger than 30 GeV/$c^2$and the mass difference between stop and gluino is smaller than 3 GeV/c^2, scalar top quarks with masses below 80 GeV/c^2 are excluded at 95% confidence level. Combining this limit with other ALEPH data analyses including LEP1 data, scalar top quarks with masses below 80 GeV/c^2 are excluded at 95% confidence level, independent of the gluino mass, and below 63 GeV/c^2, irrespective of the nature of the LSP.

Third, signatures of R-hadrons in the ATLAS detector are studied. Specifically, signatures in the inner detector, calorimeters and muon chambers are investigated, and some issues concerning triggering on R-hadron events are addressed. The fast simulation framework ATLFAST has been extended to include parameterizations of R-hadronic interactions, hereby making use of fully simulated single R-hadrons. R-hadron events produced via the channel $\mathrm{pp} \rightarrow \tilde{\mathrm{g}}\tilde{\mathrm{g}}$ are studied in more detail, whereby the focus is on three points in parameter space. It is shown that R-hadrons will certainly be seen at the LHC, if they exist and have masses below the order of 600 GeV/c^2.

Contents

Preface

Particle physics is the branch of physics studying the smallest constituents of matter, and the interactions occurring among them. From the early notion of the Greek philosophers, that all matter was built up from the four constituents earth, water, fire and air, via the hypothesis of atoms and molecules as smallest constituents, it is currently accepted that matter is constructed from even smaller building blocks than protons and neutrons, namely the quarks and the leptons. Experiments over the past century have revealed three families of quarks and leptons, and have led to a deep understanding of the manner in which they interact.

Much of our progress in understanding the physics of elementary particles has been achieved through studying the symmetries they exhibit. Currently, the best framework describing their physics is the Standard Model, a theory based on the existence and breaking of symmetries. In a manner to be described in more detail below, this theory encompasses the electromagnetic, weak, and strong interactions of all known elementary particles. The only known interaction not described by the Standard Model is the gravitational one. Between individual particles, which have a mass of the order of $\sim 10^{-27}$ kg, this force is so tiny, that it has no measurable effect. In short, electromagnetic interactions are responsible for the repulsion or attraction of charged particles, the weak interactions are responsible for processes such as nuclear beta decay, and the strong interactions are responsible for keeping the particles inside nucleons, the quarks, together. Quarks cannot exist in isolation, but must combine with other quarks to form particles called hadrons, i.e. they 'hadronize'.

In the Standard Model, forces between elementary particles are mediated by force carrying particles called gauge bosons. Electromagnetic interactions are mediated by photons, weak interactions by the weak bosons, and strong interactions by gluons. Fig. 1 shows the Standard Model particles and the interactions between them. The gauge bosons, as well as the other elementary particles, are believed to be massless at very high energies. At such energies, the Lagrangian describing their interactions is invariant under certain symmetry group transformations. Below a given critical energy or temperature (ca 10^3 GeV or 10^{16} K), this symmetry breaks down, causing certain particles to acquire masses via the so-called Higgs mechanism. Experimental exploration has so far been restricted to the regions below this energy, and thus only the remnants of the broken symmetry are left to explore. Despite this complication, the Standard Model has experimentally been tested to very high precision during the past thirty years. One of the last pieces of the puzzle is the Higgs boson, which is an unavoidable consequence of the symmetry breaking. Due to the high level of confidence we have now in the essential aspects of the Standard Model, the discovery of the Higgs boson is by most particle physicists considered to be only a matter of time. Indeed, the verification of the Standard Model as the correct theory describing elementary particle interactions up to the weak scale can with justification be called one of the greatest scientific successes of the last thirty years.

In order to study the interactions of elementary particles, very high energetic particles are brought to collide with each other, from which derives the name 'high-energy physics' as a syn-

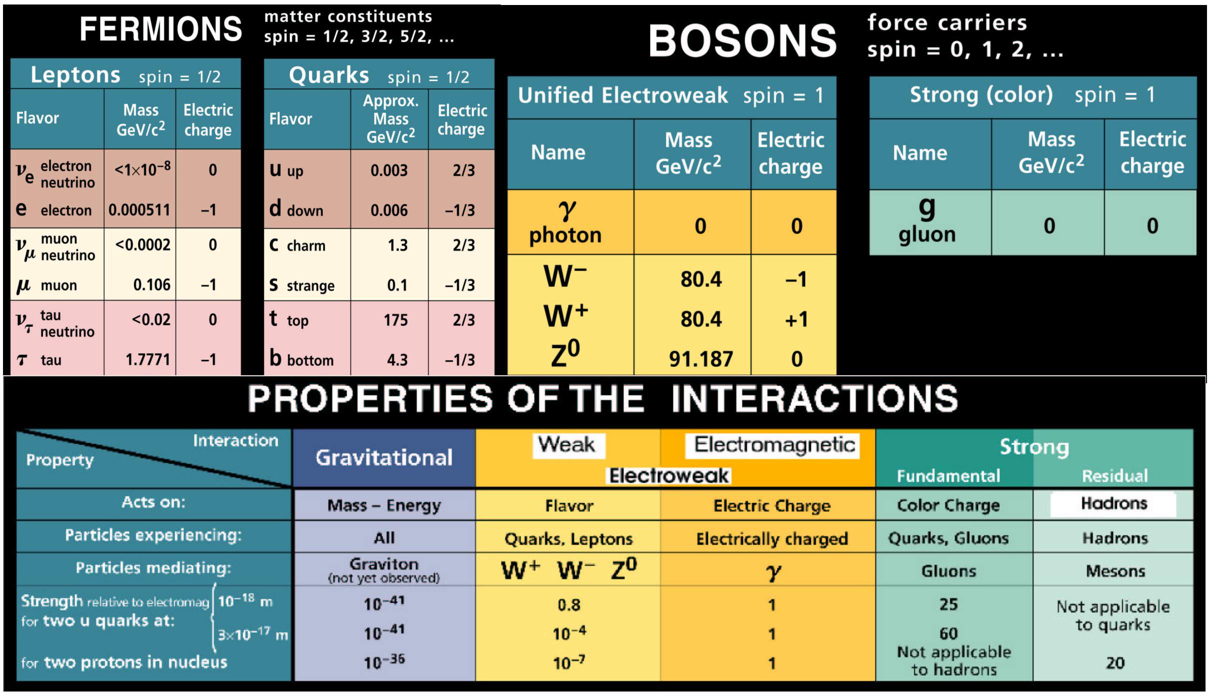

Figure 1: The Standard Model particles and the interactions between them.

onym of particle physics. To achieve this, powerful accelerators are required, in which particles can be accelerated to velocities close to the speed of light. The energies associated with collisions in these accelerators are several billion times higher than those in ordinary chemical reactions! It is under these extreme conditions, which are thought also to have existed in the early history of our universe, that new particles may be produced and measured by particle detectors. In Fig. 2, a collision of two particles is shown.

The largest laboratory in the world where high energy accelerators are built and operated is CERN (Centre Européenne pour la Recherche Nucléaire) in Geneva, Switzerland. From 1989 until 2000, electrons and positrons were accelerated and collided in a circular tunnel of 4 km radius, called LEP (Large Electron Positron collider). Its main achievement has been to measure with unprecedented accuracy some of the most important quantities in the Standard Model, like the masses and widths of the gauge bosons. Although it was operating very successfully, it was shut down in November 2000 to make space for the LHC (Large Hadron Collider), a proton proton collider, scheduled to start running in 2007. When the LHC starts operating, the collision energies can be roughly a factor of a hundred higher than at LEP, higher than ever has been reached before in a laboratory!

The main motivation for building LHC is that we believe that the Standard Model, despite its enormous successes, is not the ultimate theory of particle interactions. It gives an astoundingly accurate description of *almost all*, yet not *all*, of the current experimental data. Examples of limitations of the Standard Model are the fact that it does not account for neutrino masses, the lack of a description of gravity, and the problem that none of the Standard Model particles can account for the dark matter in the universe. In view of these imperfections, new, better theories, are being constructed, which must be capable both of agreeing with the existing experimental data, and of solving the problems associated with the Standard Model.

This thesis is dedicated to the search for particles which are associated with such a new theory,

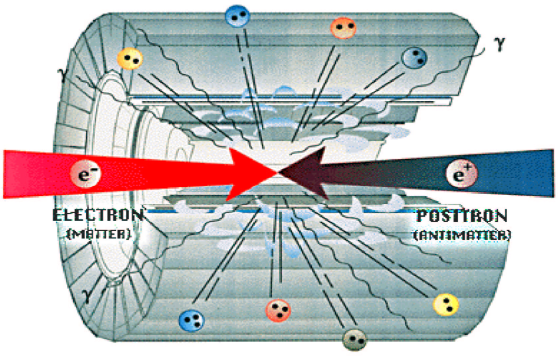

Figure 2: A collision of two elementary particles.

called supersymmetry. Supersymmetry proposes that the laws of nature are symmetric under the interchange of bosons and fermions. In short, bosons are particles that do not obey Pauli's exclusion principle because they have integer spin, while fermions are particles with half-integer spin that do obey this principle. The pion is an example of the first, while the electron is an example of the latter. Had the electron been a boson, our world would have looked fundamentally different, e.g. because no chemistry could then have existed. The theory of supersymmetry predicts that for every known elementary particle, a supersymmetric partner would exist with the same mass but with the spin differing by 1/2. No supersymmetric particles have been measured so far; for example, we have never found a particle behaving like an electron, but with integer spin. Thus, in order for the theory to be sensible, supersymmetry must be a broken symmetry, if it exists at all. In that way, the masses of the supersymmetric particles can be much higher than those of the Standard Model particles.

I have concentrated on one specific supersymmetric particle, called the gluino. This particle, the supersymmetric partner of the gluon, is purely hypothetical at this stage, having never been observed in experiments. Gluinos are electrically neutral particles, which experience only the strong force out of the three interactions in the Standard Model. In the specific models investigated here, gluinos are stable. Just like the quarks inside a proton or a neutron, a gluino cannot exist alone, but needs to combine with other particles like quarks to form a stable hadron: it hadronizes. Gluino hadrons are traditionally called R-hadrons, and they would be much heavier than protons or neutrons. R-hadrons would in some respects interact like normal hadrons in a detector, but being so much heavier, there are also many noteworthy differences. Similarly behaving particles are predicted by other theories besides supersymmetry. The concept of a very heavy stable particle, interacting like a hadron in a detector, is unexplored and fundamentally different from many standard supersymmetric scenarios, which often only include stable weakly interacting supersymmetric particles besides Standard Model particles. As such, many complications associated with hadronic interactions of heavy particles will be encountered and attacked along the course of this thesis.

In this work, the data taken by ALEPH, one of the LEP experiments, will be used to search for signals of R-hadrons. In Fig. 3, a typical R-hadron event in the ALEPH detector is shown. Also, it will be investigated whether we will be able to find these particles with the ATLAS detector, one of the future LHC detectors. A negative signal would imply that those theories, which predict R-hadrons, can be excluded. A positive signal however, would be a sign of new physics beyond the Standard Model, and would no doubt give headlines around the world!

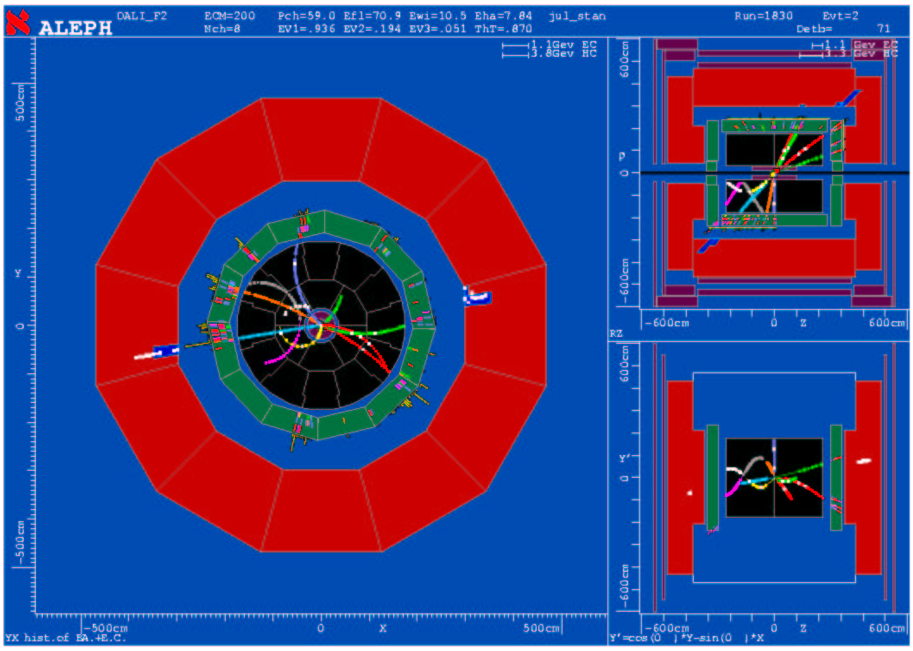

Figure 3: An example of a simulated event in ALEPH with two R-hadrons, a charged one at the left, and a neutral one at the right, the only particles in this case which reach the hadronic calorimeters (the outer region). Both R-hadrons are stopped in the hadronic calorimeter here.

Outline

This thesis is divided into three parts: a part covering general issues, a part devoted to ALEPH, and a part devoted to ATLAS.

In Part I, the general theoretical aspects of this work will be described, and an explanation of the simulation framework will be provided. Chapter 1 summarizes the Standard Model and the theory of supersymmetry, meant as a general introduction. Chapter 2 focuses then on R-hadrons. We present arguments why to perform a search for R-hadrons, the most relevant existing searches for R-hadrons are reviewed, and their production mechanisms at LEP and LHC will be discussed. Chapters 3, 4, and 5 are devoted to the understanding of the interactions of R-hadrons. In Chapter 3, the interactions of normal hadrons in matter are studied, which is meant as introduction to Chapter 4, which contains a theoretical platform for the description of the interactions of R-hadrons in matter. Chapter 5 is then dedicated to the implementation of this theory into a GEANT 3 computer simulation. In this chapter some important general signatures will be studied, and the simulations used in the ALEPH and in the ATLAS analyses will be reviewed, and compared.

Part II is dedicated to the search for R-hadrons using data taken by the ALEPH detector. It starts in Chapter 6 with a short description about LEP and the ALEPH detector. Chapter 7 is devoted to the Monte Carlo generation of R-hadron and background events in ALEPH, and Chapter 8 explains the search strategy and selections. In Chapter 9 and 10, we present the systematic error analysis and results.

Part III concentrates on ATLAS. A description of the ATLAS detector is given in Chapter 11. In Chapter 12 manifestations of R-hadrons in the ATLAS detector are discussed. Chapter 13 describes an analysis of R-hadron events for three points in parameter space.

Conclusions of the thesis will be presented in Chapter 14.

Acknowledgements

This thesis is the final result of three years of work in the Experimental High Energy Department at the Niels Bohr Institute in Copenhagen, Denmark. It is also the result of collaboration across borders, quite literally. Living in Sweden, working in Denmark, having many close friends and family in the Netherlands, and traveling often to different places in Europe, have made the past three years a challenging but worthwhile experience. From many different people from different countries, I have received help and guidance along the way, and this is my chance to thank them.

First, I thank my advisor Peter Hansen, and Jørn Dines Hansen and John Renner Hansen for having given me the opportunity to do a PhD at the Niels Bohr Institute in Copenhagen. I have very much enjoyed the nice and social atmosphere in the group, and the freedom to travel to any place necessary was without any doubt indispensable. Thanks for having made this possible! Thanks also to all my collaborators from the past three years; the HEP group in Copenhagen, and collaborators at CERN. I want to mention a few people in particular, starting at the very beginning.

During the first year, I have received most guidance and help mainly from Giacomo Sguazzoni, Mario Antonelli, Patrick Janot, and Torbjörn Sjöstrand. Giacomo, I am very grateful that you introduced me to many aspects of experimental high energy physics, from Paw and Fortran to various issues in doing an ALEPH analysis. Thanks a lot for all your support, both at CERN and in Copenhagen. I would like to thank Mario for always answering my questions, and for guidance during the project. And also, thanks for a very enjoyable stay in Frascati in October 2002! After the summer of 2002, Patrick Janot got involved in the work and contributed significantly. It was a very good and motivating experience to collaborate, and it was great that you knew a solution for all the problems we encountered during the analysis. Thanks for your indispensable help in getting a very nice publication out of the gluino search! Finally, thanks to Roberto Tenchini for keeping the last ALEPH members together. I deeply acknowledge the help I got from the ALEPH collaboration. It was a very encouraging experience to produce some real results.

I started working on ATLAS in May 2003, under the guidance of Peter Hansen. Peter, I appreciated highly that your door was always open for discussion and questions. You were willing to discuss any subject at any time of the day, and in that way I have gained a lot of knowledge on many experimental aspects. Thanks for having guided me to the end of my PhD!

Working in ATLAS, I got again in touch with different people helping me along. I am deeply grateful to Pavel Nevski, who was extremely effective in helping me to quickly obtain physics results with Atlsim. I have very much enjoyed our discussions and sessions at your computer, drawing the ATLAS detector from any angle, looking at R-hadron events, and trying to debug Atlsim, Age, and Gheisha routines. Thanks also for the efforts to understand timing issues with the triggers.

As the project evolved, and during repeated stays at CERN, Jørgen Bech Hansen got involved in the work. I want to give a very warm thanks to Jørgen for all the indispensable help during the last few months with the ATLFAST simulation. Thanks for providing me with some of the R-hadron C++ routines, for helping with generating background, for quickly getting physics out of it, and for answering so many questions by phone and mail. I also want to thank you for all the lively and very motivating discussions we had every time I was at CERN, also during my ALEPH work. It has been a great experience to collaborate, and I hope that we will write a nice ATLAS note together with Pavel.

During the ATLAS period I have had repeatedly very useful discussions with different people. I am grateful to Andrew D. Jackson, for very helpful discussions about nucleon scattering. From the ATLAS SUSY group, I acknowledge help from Frank Paige, and in particular Dan Tovey for answering all my questions. I also thank Aleandro Nisati for discussions about triggering of heavy hadrons in ATLAS, and Andrea Romanino for a useful discussion about split supersymmetry. In addition, I thank Anders and Jakob for often having supported me on the software part.

With respect to the writing of this manuscript, I thank Peter Hansen, Torbjörn Sjöstrand, Peter Skands, Esben Klinkby, Jørgen Bech Hansen, Niels Obers and my parents for careful proofreading.

During these three years I have during the first years shared the office with Else, and I want to thank her for the cozy office atmosphere at NBI. Sometimes when I was at CERN, I shared the office with Henrik Bertelsen, who I want to thank for making the long working evenings a lot better by bringing some music, wine or cappuccino. Thanks also to Trine, Thomas, Esben and Rasmus for the nice atmosphere in general.

At CERN I have often had very good times with some of the Swedes, in particular I thank Johan Karlsson, for always making me feel so welcome at CERN, for all the lunches, for making me leave the office sometimes, and for convincing me to start eating salmon! And also Agnes and Serge for all the nice lunches, dinners, and cinema.

Pendling from Sweden to Denmark every day was less ideal and than I initially had hoped, and I am very grateful to Paula Eerola and Oxana Smirnova for arranging a working place for me at Lund university, and to Raluca for having taken me so often by car to NBI. Thanks to Paula also for organizing the nordic LHC workshops, which have been very enjoyable experiences. From Lund university, I also thank Chafik for providing me with ATLAS pion testbeam data.

Now, I want to express my heartfelt gratitude to one of the people who has supported me most during these three years, Torbjörn Sjöstrand. From right at the start, you helped with everything concerning QCD and event generation, and were always eager to discuss my physics problems. From our many discussions, I have gained an enormous amount of knowledge about QCD, but also about physics in general. Also thanks for stimulating me to turn all the effort with the theory of interactions of R-hadrons into a real article, and for the support in September and October while I was working so hard at CERN. Then, apart from physics, thanks for having made me feel so much at home in Sweden. Moving from the Netherlands to Sweden meant for me leaving a big part of my life behind. However, the weekends in the summer cottage in the Swedish forests, together with Peter, Mona, Ingemar, Gunhild, Kaj, and Kerstin, made Sweden like my home, and those weekends have become unforgettable memories; thanks to you and your family for all this. Jag kommer till at sakna er alla i USA!

Jeg vil også give et rigtigt stort 'tak' til Conrad og Suzanne, Michael og Merete, og Pernille, for at have gjort mit liv her i Scandinavien så utroligt meget varmere og hyggeligere.

Then, I want to express my deepest gratitude to my family and friends in the Netherlands, who have so often visited me here and supported me by email and phone. I thank my sister Elise, and my friends Mariëlle, Vanessa, Reinout, Aline, Nadja, and Natascha, for all their support during these three years; I could never have done it without this. I also thank my parents for their continuous support these three years and for always believing in me. And Dr. Wicher Kraan, congratulations!

Finally, no words are enough to thank Peter, min allerallerkæreste. Thanks for always having been so enthusiastic to discuss interesting physics, and for the support in times when I was seriously in doubt whether there was any use in studying possibly non-existing particles ('just think about them as if you look for small animals in the detector...'), and most of everything, thanks for being there for me.

Now, it's time for a new adventure, going to Fermilab!

Part I

General framework

Chapter 1

Supersymmetry

Supersymmetry [1] is a theory which proposes that the laws of nature are symmetric under the interchange of bosons and fermions. The concept of such a symmetry was proposed in the early seventies, and has been developed over the past decades to what is nowadays thought to be one of the most attractive theories of physics beyond the Standard Model.

In this chapter the motivations for introducing supersymmetry are discussed. The reader is assumed to be familiar with the Standard Model of electromagnetic, weak and strong interactions. Otherwise, Ref. [2] and Ref. [3] provide good introductions. The outline of this Chapter is as follows. Basic aspects of the Standard Model will be refreshed in Section 1.1. The Standard Model Lagrangian will briefly be reviewed, this being convenient for the subsequent discussion of supersymmetry. The main problems associated with the Standard Model will be outlined, and possible theories which can solve these problems will be reviewed. After this, the focus will be on supersymmetry. Following a review of the most important motivations of supersymmetry in Section 1.2, some technical details will briefly be considered, such as the supersymmetry algebra in Section 1.3.1, supermultiplets in Section 1.3.2, the concept of R-parity in Section 1.3.3 and the most relevant parts of the supersymmetry Lagrangian in Section 1.4. In Sections 1.5 and 1.6, the breaking of supersymmetry and the electroweak symmetry will be outlined. Section 1.7 reviews the special role played by the lightest supersymmetric particle. Because the particles considered in this thesis are the strongly interacting ones, we end this Chapter by discussing the spectrum of the strongly interacting supersymmetric particle sector.

1.1 The Standard Model

1.1.1 Introduction

To a large extent our understanding of the physics of elementary particles is based on studying the symmetries they exhibit. The importance of symmetries in nature was already emphasized in 1918, when the mathematician Emmy Noether demonstrated that there is a symmetry associated with every conservation law. Later on, this principle was used when building new theories based on Lagrangian densities, which were invariant under certain transformation groups. The Standard Model of electromagnetic, weak, and strong interactions is one of the best examples of the importance of symmetries, and of the breaking of symmetries. It is based on three theories, each associated with a symmetry: the theory of quantum electrodynamics (QED), the theory of weak interactions (sometimes called quantum flavour dynamics, QFD), and the theory of quantum chromo dynamics (QCD), all of which have been developed during the past century. The theory of QED is one of the most fundamental and predictive theories of physics, and was formed by covariantly quantizing the theory of classical electrodynamics. In the fifties and sixties, the theory of weak interactions, originating from Fermi's four-fermion theory, was developed by introducing the idea that a weak interaction is mediated by massive intermediate bosons, rather than a point interaction between the participating fermions. A model unifying these two theories was built in the sixties by Glashow, Salam and Weinberg, employing the Higgs mechanism of spontaneous symmetry breaking, and gained credibility by the proof of Veltman and 't Hooft in 1972 that non-Abelian gauge theories are renormalizable. The most important prediction of this model was the existence of the massive gauge bosons Z, W^+ and W^-, which have been measured with great accuracy at LEP.

With deep inelastic lepton-nucleon scattering experiments in the sixties and seventies, revealing the structure of the proton, QCD was developed, describing the strong interaction of the quarks inside the hadrons. It is a non-Abelian gauge field theory, based on the local color symmetry of quarks. The three theories together form the Standard Model, describing electromagnetic, weak and strong interactions of the elementary particles.

The basic idea of the Standard Model is that interactions are mediated by gauge bosons, which a priori are massless. The corresponding Lagrangian for the theory also contains terms for massless leptons and quarks and is symmetric under the gauge group of the Standard Model, $SU(3) \times SU(2) \times U(1)$. A scalar Higgs field H is then introduced, which acquires a non-zero vacuum expectation value at a certain scale, causing a spontaneous breakdown of the electroweak $SU(2) \times U(1)$ gauge symmetry, but leaving the $SU(3)$ color symmetry intact. This gives masses to electrons, muons, taus, quarks, and also to the gauge bosons, but not to the photon, the gluons and the neutrinos. In the following section, only the most important ingredients of the Standard Model will be summarized. For a detailed overview, the reader is referred to Ref.[2] and Ref.[3].

1.1.2 The Standard Model Lagrangian

The Standard Model is based on the gauge symmetry $SU(3)_c \times SU(2)_L \times U(1)_Y$. The $SU(3)_c$ is generated by color, the $SU(2)_L$-symmetry is generated by weak isospin $\boldsymbol{I}$ and the $U(1)_Y$ part is generated by weak hypercharge Y. Unification of weak and electromagnetic interactions yields the Gell-Mann-Nishijima relation for the electromagnetic charge $Q = \frac{Y}{2} + I_3$, where I_3 is the third component of isospin. The particles, represented by chiral (left-and right-handed) fields, form three generations and are represented by 3-component vectors in generation space. The left- and right-handed fermion fields of the unbroken theory (i.e. before spontaneous symmetry breaking) transform under the gauge group as doublets and singlets respectively and are denoted by

$$\ell_{A_L} = \begin{pmatrix} \nu_A \\ l_A \end{pmatrix}_L, \qquad l_{A_R} \qquad\qquad \mathrm{q}_{A_L} = \begin{pmatrix} \mathrm{p}_A \\ \mathrm{n}_A \end{pmatrix}_L, \qquad \mathrm{p}_{A_R}, \qquad \mathrm{n}_{A_R} \tag{1.1}$$

where

$$\nu_A = (\nu_\mathrm{e}, \nu_\mu, \nu_\tau) \tag{1.2}$$
$$l_A = (l_\mathrm{e}, l_\mu, l_\tau) \tag{1.3}$$
$$\mathrm{p}_A = (\mathrm{u}, \mathrm{c}, \mathrm{t}) \tag{1.4}$$
$$\mathrm{n}_A = (\mathrm{d}, \mathrm{s}, \mathrm{t}) \tag{1.5}$$

so that A is the generation index ($= \mathrm{e}, \mu, \tau$) and ν_A and p_A are weak isospin up fields and l_A and n_A are weak isospin down fields. These fields are the gauge-eigenstates, i.e. the eigenstates with definite gauge properties before spontaneous symmetry breakdown occurs. Since the $SU(3)_c$ symmetry is not broken, we now concentrate only on the electroweak part of the theory, omitting color labels of quarks. In this minimal version of the Standard Model no right handed neutrinos are present.

The fundamental electroweak Lagrangian can be written as a sum of four parts:

$$\mathcal{L} = \mathcal{L}_F + \mathcal{L}_G + \mathcal{L}_{HG} + \mathcal{L}_Y, \tag{1.6}$$

with

$\mathcal{L}_F$:	the fermion part, describing kinetic energy of fermions and their interactions with the gauge fields,
$\mathcal{L}_G$:	the gauge part, describing gauge fields and their self interactions,
$\mathcal{L}_{HG}$:	describing the Higgs-gauge interactions and Higgs potential,
$\mathcal{L}_Y$:	describing the Higgs-fermion (Yukawa) interactions.

The first term, $\mathcal{L}_F$ is given by

$$\mathcal{L}_F = i\sum_A \left(\overline{\ell_{A_L}}\not{D}_L\ell_{A_L} + \overline{l_{A_R}}\not{D}_R l_{A_R} + \overline{\mathrm{q}_{A_L}}\not{D}_L\mathrm{q}_{A_L} + \overline{\mathrm{p}_{A_R}}\not{D}_R\mathrm{p}_{A_R} + \overline{\mathrm{n}_{A_R}}\not{D}_R\mathrm{n}_{A_R}\right), \tag{1.7}$$

where $\not{D}_{R,L} = D_{L,R_\mu}\gamma^\mu$, and D_{L_μ} and D_{R_μ} are the covariant derivatives for left and right handed field respectively, defined as

$$D_{L_\mu} = \partial_\mu - ig\boldsymbol{I}\cdot\boldsymbol{W}_\mu - ig'\frac{Y}{2}B_\mu \tag{1.8}$$

$$D_{R_\mu} = \partial_\mu - ig'\frac{Y}{2}B_\mu. \tag{1.9}$$

A weak isospin triplet $\boldsymbol{W}_\mu = (W^1_\mu, W^2_\mu, W^3_\mu)$ and a weak isospin singlet B_μ, are introduced here. Note that the weak hypercharge Y is not the same in Eq. (1.8) and in (1.9), because it has a different value for a right-handed fermion than for a left-handed fermion. Furthermore, g is the $SU(2)$ coupling constant and g' is the weak hypercharge coupling constant. They are related to the electromagnetic coupling constant e by the Weinberg angle θ_W as $g = e/\sin\theta_W$ and $g' = e/\cos\theta_W$.

The second term, $\mathcal{L}_G$, reads

$$\mathcal{L}_G = -\frac{1}{4}F^a_{\mu\nu}F^{\mu\nu}_a - \frac{1}{4}F_{\mu\nu}F^{\mu\nu}, \tag{1.10}$$

where

$$F^a_{\mu\nu} = \partial_\mu W^a_\nu - \partial_\nu W^a_\mu + g\epsilon^{abc}W^b_\mu W^c_\nu \qquad \text{(a=1,2,3))} \tag{1.11}$$

$$F_{\mu\nu} = \partial_\mu B_\nu - \partial_\nu B_\mu. \tag{1.12}$$

Here F is the Yang-Mills field strength tensor, with ϵ^{abc} in Eq (1.11) the Levi-Civita tensor.

The third term, $\mathcal{L}_{HG}$ has the form

$$\mathcal{L}_{HG} = (\mathcal{D}^\mu_L H)^\dagger(\mathcal{D}_{L_\mu}H) - V(H, H^\dagger), \tag{1.13}$$

where H is an $SU(2)_L$-doublet, the Higgs doublet, with a neutral and a charged component and with $Y = 1/2$. The potential $V(H)$ is given by

$$V(H) = -\mu^2 H^\dagger H + \lambda(H^\dagger H)^2 \qquad \lambda > 0. \tag{1.14}$$

This potential (which has the famous Mexican hat shape) is constructed so that it leads to a *non-zero* vacuum expectation value (VEV) of the Higgs doublet. To conserve electromagnetic charge, it must be the neutral component of the Higgs doublet which develops the VEV:

$$\langle H \rangle = \frac{1}{\sqrt{2}} \begin{pmatrix} 0 \\ v \end{pmatrix}, \tag{1.15}$$

with $v = \frac{\mu}{\sqrt{\lambda}}$. We can parameterize H now around its minimum as

$$H = \frac{1}{\sqrt{2}} \begin{pmatrix} i\chi_1 + \chi_2 \\ v + \phi - i\chi_3 \end{pmatrix}, \tag{1.16}$$

with $(i\chi_1 + \chi_2)/\sqrt{2} = i\chi^+$. It is the neutral field ϕ which is usually referred to as the Higgs particle or Higgs boson. The original $SU(3)_c \times SU(2)_L \times U(1)_Y$ symmetry of the Standard Model is in this way broken and the remaining symmetry is $SU(3)_c \times U(1)_{em}$. This mechanism, called the Higgs mechanism of spontaneous symmetry breaking, gives rise to masses for the gauge fields $W^\pm_\mu$ and Z_μ and leaves the photon field A_μ massless. These gauge fields are defined as

$$W^\pm_\mu = \frac{W^1_\mu \mp iW^2_\mu}{\sqrt{2}} \tag{1.17}$$

$$Z_\mu = \frac{gW^3_\mu - g'B_\mu}{\sqrt{g'^2 + g^2}} \tag{1.18}$$

$$A_\mu = \frac{g'W^3_\mu + gB_\mu}{\sqrt{g'^2 + g^2}}, \tag{1.19}$$

and acquire masses

$$M_W^2 = \frac{g^2 v^2}{4} \qquad M_Z^2 = \frac{M_W^2 (g^2 + g'^2)}{g^2} = \frac{M_W^2}{\cos^2 \theta_W}, \tag{1.20}$$

where θ_W is the Weinberg angle. The value for $\sin^2 \theta$, measured at the Z-mass, is 0.23 [4]. The masses for the W- and the Z boson are 80.4 and 91.2 GeV/c^2. The measured values for the masses and couplings then lead to $v = 246$ GeV. The mechanism of spontaneous symmetry breaking is also responsible for the generation of fermion masses. The starting point to explain this is $\mathcal{L}_Y$, which describes the interactions between fermions and the Higgs-doublet:

$$\mathcal{L}_Y = -\sum_{AB} \left(\lambda^{(l)}_{AB} \overline{\ell_{A_L}} H l_{B_R} + \lambda^{(\mathrm{n})}_{AB} \overline{\mathrm{q}_{A_L}} H \mathrm{n}_{B_R} + \lambda^{(\mathrm{p})}_{AB} \overline{\mathrm{q}_{A_L}} (i\tau_2 H^*) \mathrm{p}_{B_R} \right) + h.c. \tag{1.21}$$

Here τ_2 is the SU(2) matrix and $\lambda^{(l,n,p)}_{AB}$ are the Yukawa couplings. Since no right-handed neutrinos exist in this minimal version of the Standard Model, no term with $i\tau_2 H^*$ is present for leptons. A point to note, which will be important when we later extend the theory with supersymmetry, is that the mass generation of weak-isospin up type fermions differs slightly from the mass generation of weak-isospin down type fermions. For fermions of the former type the Higgs doublet itself is involved, for fermions of the latter type its conjugate is involved. To generate masses, one substitutes Eq. (1.15) for H. In this way we obtain in the gauge-eigenstate basis the following fermionic mass matrices:

$$M^{(i)}_{AB} = \frac{v}{\sqrt{2}} \lambda^{(i)}_{AB} \qquad i = l, p, n. \tag{1.22}$$

The Yukawa couplings are arbitrary values, determined by experimental data.

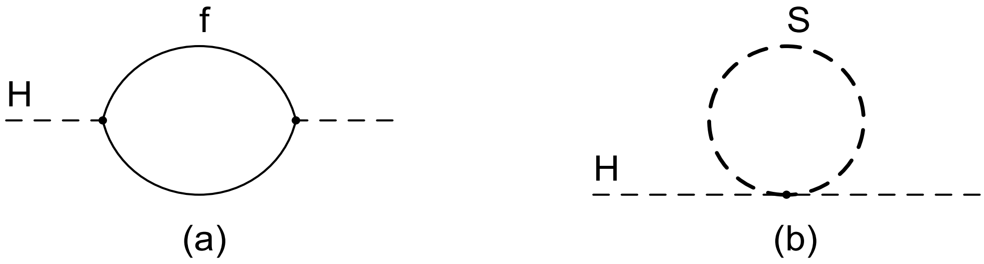

Figure 1.1: Diagrams contributing to the quantum corrections of the Higgs mass from (a) fermions and (b) scalars. These figures are obtained from Ref. [5].

1.1.3 Shortcomings of the Standard Model

Experimental data have so far been consistent with the correctness of the Standard Model up to an astonishing accuracy. Yet despite its successes, it is generally believed that the Standard Model cannot be the whole story, for the following reasons:

- The hierarchy problem, or fine-tuning problem. This is the difference between the experimental value of the Higgs mass, and its theoretically 'natural' value. The Standard Model Higgs potential was given in Eq. (1.14), where the parameter μ is the Higgs boson mass squared: $\mu = m_H^2$. If the Higgs scalar field indeed has a vacuum expectation value of the right size to give the observed Z and W boson masses, m_H^2, should be of the order of (100 GeV)^2. However, in the SM framework the Higgs mass receives large radiative corrections from vacuum polarization diagrams [5]. The largest corrections come from the Yukawa couplings to fermions, in particular to the top quark, as shown in Fig. 1.1 (a). The corrections associated with this diagram are of the form (in the momentum cut-off regularization) [5]

$$\Delta m_H^2 = \frac{|\lambda_f|^2}{16\pi^2}\Big[-2\Lambda_{UV}^2 + 6m_f^2 \ln(\Lambda_{UV}/m_f) + ...\Big], \tag{1.23}$$

  where λ_f is the Yukawa coupling introduced in Eq. (1.21), here for convenience omitting the mixing between different generations, and Λ_{UV} is an ultraviolet momentum cutoff used for regularization of the loop integral. It can be interpreted as the upper limit for which the Standard Model is valid, i.e. as the scale where some new physics comes in. Based on the evolution of the gauge couplings with energy, and in the lack of observation of any new physics, a natural assumption for this limit is the Grand Unification Theory (GUT) scale $M_{GUT} \sim 10^{15}$ GeV, where the gauge couplings are thought to unify, as will be shown in Section 1.2. The natural value of the Higgs boson mass squared is then of the order of $\Lambda_{UV}^2 \approx 10^{30}$ GeV, a factor 10^{26} higher then the value experimentally determined! The difference between these two scales is referred to as the hierarchy problem.

  There are several mechanisms suggested to solve this problem. The most obvious solution is to assume new physics to come in at a scale $\Lambda_{UV} \ll M_{GUT}$. Below Λ_{UV}, the Standard Model particles would then cause quantum corrections to the Higgs mass but, Λ_{UV} being small, these corrections would only be of relatively moderate sizes. No significant quantum corrections would arise from new physics fields below Λ_{UV}, given that particles associated with a new theory have masses M of order Λ_{UV}[1]. Above the scale Λ_{UV}, quantum corrections

[1] Particles only start contributing dynamically at energies above the masses of the fields, where the propagators in the loops of diagrams like those of Fig. 1.1 are approximately proportional to $1/s$, rather than to $1/M^2$ at lower energies.

to the Higgs mass come *both* from the Standard Model fields *and* the fields associated with the new physics! The only way to avoid unacceptably large quantum corrections at high scales is if there is a *cancellation* between them. This mechanism will be illustrated in Section 1.2. Another way to obtain a small value for Λ_{UV} is if the Planck scale M_P forms the ultimate limit up to which the Standard Model is valid. If this scale is much lower than 10^{18} GeV, gravitational interactions could start playing a role already at low energies. This could be the case if gravitational interactions are able to propagate in more than the normal four dimensions, so that the Standard Model particles experience only a small part of the total gravitational force. A larger fundamental gravitational coupling constant results in a much lower energy scale M_P, and thereby in much smaller quantum corrections to the Higgs mass.

- The flavor problem. Why are there exactly six flavors of leptons and quarks, and why are there three generations? The number of light neutrinos as determined from the Z line-shape rules out the existence of more than three generations. Within the framework of the Standard Model, there is no answer to this question.

- The size of the masses of the fermions is not understood. From the vacuum expectation value of the Higgs and the fermion masses, the sizes of the Yukawa couplings can be evaluated. However, these values are not specified by the model and hence arbitrary. One of the biggest mysteries in the Standard Model is for example how to explain the mass-hierarchy in the lepton and quark sectors.

- The unification problem. The gauge group of the Standard Model, $SU(3)_c \times SU(2)_L \times U(1)_Y$, is a product of three groups, with three different coupling constants. These coupling constants have been measured and appear to be changing ('running') as a function of the energy scale, and, when extrapolating data to large energy values, they approximately converge toward a common value. However, although they *almost* unify at around 10^{15} GeV, they do *not exactly* meet. This is referred to as the unification problem.

- Gravity is not included in the $SU(3)_c \times SU(2)_L \times U_Y(1)$-theory, although we know that this force exists. Thus, the Standard Model cannot be the 'ultimate theory' describing all four fundamental forces.

- Charge quantization is not understood. Why do all the known particles have discrete charge values? The only understanding of the charges of all particles concerns the sum of the charges of all left-handed fermions in one generation, required to be zero by anomaly cancellation [6]. It is a mystery why the charges are quantized.

- Neutrino masses. From observations, we know that neutrinos oscillate between different weak eigenstates. Although the Lagrangian of the Standard Model is easily extended to incorporate neutrino masses (see e.g. Ref. [7] for an overview), it does strictly speaking not include terms for neutrino masses.

- The dark matter problem. From astrophysical observations such as the cosmic microwave background and the structure and movements of galaxies, we know that there is a significant amount of dark matter in the universe. None of the Standard Model particles can account for dark matter.

1.1.4 Extensions of the Standard Model

There are several ways to extend the Standard Model, some of which can solve one or more of the above problems:

- Extending the field content of the Standard Model. Examples are theories including a 4th generation of fermions, a right handed neutrino, or a second Higgs doublet. Other examples are theories with leptoquarks, particles carrying quantum numbers associated with both leptons and quarks.
- To modify the existing Standard Model particles. One of the possibilities is to assume that they are not fundamental. Examples are technicolor, based on the viewpoint that the Higgs boson is a composite particle, or compositeness, where the Standard Model fermions are assumed to be composite particles.
- Imposing new symmetries on the existing particles. An example of this idea is supersymmetry, which assumes the existence of a symmetry between fermions and bosons. Other examples are grand unification theories, based on embedding the symmetry group $U(1)_Y \otimes SU(2)_L \otimes SU(3)_c$ into one larger symmetry group (e.g. $SO(10)$ or $SU(5)$).
- To modify the number of space-time dimensions by introducing extra dimensions, and assuming the four-dimensional world to be embedded in this higher dimensional space.
- Assuming interactions to be extended, rather than point like. String theory is an example of this idea. These theories often also require the existence of extra symmetries.

1.2 Why supersymmetry?

If supersymmetry was an exact symmetry, there would exist for every elementary particle a partner with the same mass and charge, but with its spin differing by 1/2. Such particles have so far not been detected, so how can supersymmetry be the most attractive Standard Model extension? The main motivation is that supersymmetry can provide a solution to the hierarchy problem. From our previous experience of the electroweak symmetry, we know that fundamental symmetries may be broken and hence can be hard to detect. If supersymmetry is broken, the supersymmetric partners of the Standard Model particles can have masses above the current experimental limits. How would this affect the hierarchy problem? If the supersymmetric particles have masses higher than the experimental limit, and if their masses are not significantly higher than the TeV scale, the way in which supersymmetry solves the hierarchy problem is as follows. Below the supersymmetric particle mass scale m_{SUSY}, the Standard Model particles cause quantum corrections to the Higgs mass but, m_{SUSY} being small, these corrections are of acceptable sizes. At energies above m_{SUSY}, the Standard Model particles *plus* their supersymmetric partners contribute to the quantum corrections to the Higgs mass. However, introducing a boson for each fermion, allows for a cancellation of the quantum corrections up to an arbitrarily large scale, because a counter-term to the Higgs mass is provided, with a diagram as given in Fig. 1.1(b) and a correction to the Higgs mass given by (in the momentum-cutoff regularization) [5]

$$\Delta m_H^2 = \frac{|\lambda_S|}{16\pi^2}\Big[\Lambda_{UV}^2 - 2m_S^2 \ln(\Lambda_{UV}/m_S) + ...\Big]. \tag{1.24}$$

Here λ_S is the coupling between Higgs boson and the scalar field and m_S is the mass of the scalar field. Given firstly that $\lambda_S = |\lambda_f|^2$ (as required by supersymmetry), secondly that two scalar fields

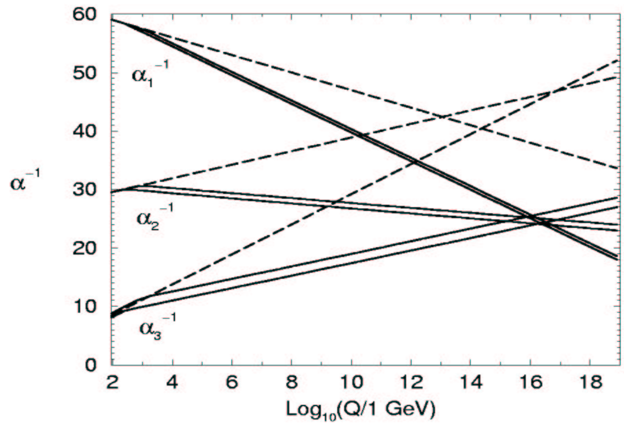

Figure 1.2: The evolution of the gauge couplings for purely the Standard Model (dashed lines) and for a minimal supersymmetric extension of the Standard Model (solid lines). The two solid lines for each coupling constant represent two different supersymmetric scenarios. This figure is obtained from Ref. [5].

would exist for every fermion field, and thirdly that fermions and bosons contribute to the loops with a different relative sign, a systematic cancellation in the quantum corrections to Δm_H^2 takes place! However, the higher the masses of the supersymmetric particles, the larger the quantum corrections from Standard Model particles, and the more fine-tuning is necessary to obtain the measured value of M_H^2. It must be noted that the cancellation is not exact, since a logarithmic divergence still exists, however this is a significantly smaller divergence! Although the above is a very striking consequence of supersymmetry, it must be recalled that the original reason for introducing supersymmetry was simply to extend the group of space-time-symmetries [8], rather than to solve the hierarchy problem.

Besides this astonishing feature, supersymmetry has another striking consequence: it can solve the gauge coupling unification problem. The one-loop renormalization group equations for the Standard Model gauge couplings g_1, g_2 and g_3 are [5]

$$\frac{\mathrm{d}g_a}{\mathrm{d}t} = \frac{1}{16\pi^2} b_a g_a^3 \qquad \text{a=1,2,3,} \tag{1.25}$$

where $t = \ln\ Q/Q_0$, with Q the renormalization scale. Using $\alpha_a = \frac{g_a^2}{4\pi}$, this leads to

$$\frac{\mathrm{d}\alpha_a^{-1}}{\mathrm{d}t} = -\frac{b_a}{2\pi} \qquad \text{a=1,2,3.} \tag{1.26}$$

It must be noted that $g_1 = \sqrt{5/3}g'$ and $g_2 = g$. In the Standard Model, the coefficients $b_a = (41/10, -19/6, -7)$, while in the MSSM they are $b_a = (33/5, 1, -7)$ due to the presence of the extra particles (note the sign difference of b_2!).

In the MSSM, the gauge couplings unify *precisely* (within errors), rather than *almost*, as illustrated in Fig. 1.2. This is one of the strongest motivations for introducing supersymmetry.

Furthermore, supersymmetry can accommodate a description of gravitational interactions in the form of supergravity models [5], and it can play an important role in cosmology by providing a dark matter candidate, as will be explained below.

Finally, supersymmetry has a rich phenomenology, which is testable in a laboratory.

To conclude, although supersymmetry does not solve all problems, it is a highly interesting and promising scenario of physics beyond the Standard Model.

1.3 Technicalities

In the following sections, some technicalities associated with supersymmetry will be summarized before the discussion of the Lagrangian. The discussion below is based on Refs. [5, 9], both providing excellent introductions to supersymmetry. The notation and conventions of Ref. [5] are used throughout this Chapter, apart from the fact that we denote the fermion fields and the superfields by regular letters such as u, d, Q, $\mathrm{H_d}$, etc, rather than italic letters such as u, d, q, Q, H_d, etc.

1.3.1 Supersymmetry algebra

The generators of supersymmetry transformations carry spin 1/2, and transform a state $|S\rangle$ into $|S \pm \frac{1}{2}\rangle$. The supersymmetry operators Q and $Q^\dagger$, are anti-commuting Majorana spinors, and are responsible for transformations between bosonic and fermionic states.

$$Q \mid \text{Boson}\rangle = \mid \text{Fermion}\rangle, \qquad Q \mid \text{Fermion}\rangle = \mid \text{Boson}\rangle. \tag{1.27}$$

They satisfy a highly constrained algebra of commutating and anti-commutating relations, which is are normally symbolically displayed without any indices as

$$\begin{aligned} \{Q, Q^\dagger\} &= P^\mu & (1.28)\\ \{Q, Q\} &= \{Q^\dagger, Q^\dagger\} = 0 & (1.29)\\ \{P^\mu, Q\} &= [P^\mu, Q^\dagger] \;= 0, & (1.30) \end{aligned}$$

where P^μ is the four-momentum operator. This algebra is an extension with fermionic operators of the Poincare-algebra, which describes bosonic space-time symmetries. The first relation can be understood by remembering that the operators $QQ^\dagger$ and $Q^\dagger Q$ both carry spin 1, and hence transforms as a spin-1 object under Lorentz transformations, as does the right hand side. The third relation implies that the operators of supersymmetry transformations conserve momentum. The operators Q and $Q^\dagger$ commute with the generators of the gauge transformations. Usually only one set of $\{Q, Q^\dagger\}$ is assumed to exist, which is referred to as an $N = 1$ supersymmetry.

Name	Supermultiplet	Spin-0	Spin-1/2	$SU(3)_c \times SU(2)_L \times U_Y(1)$
Quarks, squarks	Q	$\tilde{Q} = (\tilde{\mathrm{u}}_L, \tilde{\mathrm{d}}_L)$	$Q = (\mathrm{u}_L, \mathrm{d}_L)$	$(\mathbf{3}, \mathbf{2}, \frac{1}{6})$
(3 families)	$\bar{\mathrm{u}}$	$\tilde{\mathrm{u}}^*_R$	$\mathrm{u}^\dagger_R$	$(\bar{\mathbf{3}}, \mathbf{1}, -\frac{2}{3})$
	$\bar{\mathrm{d}}$	$\tilde{\mathrm{d}}^*_R$	$\mathrm{d}^\dagger_R$	$(\bar{\mathbf{3}}, \mathbf{1}, \frac{1}{3})$
sleptons,leptons	L	$\tilde{L} = (\tilde{\nu}, \tilde{\ell}_L)$	$L = (\nu, \ell)$	$(\mathbf{1}, \mathbf{2}, -\frac{1}{2})$
(3 families)	$\bar{\mathrm{e}}$	$\tilde{\mathrm{e}}^*_R$	$\mathrm{e}^\dagger_R$	$(\mathbf{1}, \mathbf{1}, 1)$
Higgs, Higgsinos	$\mathrm{H_u}$	$H_\mathrm{u} = (H^+_\mathrm{u}, H^0_\mathrm{u})$	$\tilde{H}_u = (\tilde{H}^+_\mathrm{u}, \tilde{H}^0_\mathrm{u})$	$(\mathbf{1}, \mathbf{2}, +\frac{1}{2})$
	$\mathrm{H_d}$	$H_\mathrm{d} = (H^0_\mathrm{d}, H^-_\mathrm{d})$	$\tilde{H}_d = \tilde{H}^0_\mathrm{d}, \tilde{H}^-_\mathrm{d})$	$(\mathbf{1}, \mathbf{2}, -\frac{1}{2})$

Table 1.1: Chiral supermultiplets present in a minimal supersymmetric extension of the Standard Model. Due to the convention that chiral supermultiplets are given in terms of left handed Weyl spinors, the conjugates of the right handed fields appear, denoted by $*$ for scalars and $\dagger$ for fermions.

Name	Symbol	Spin-1/2	Spin-1	$SU(3)_c \times SU(2)_L \times U_Y(1)$
Gluino, gluon	G	$\tilde{\mathrm{g}}$	g	$(\mathbf{8}, \mathbf{1}, 0)$
Winos, W-bosons	W	$\tilde{\mathrm{W}}^{\pm}\tilde{\mathrm{W}}^{0}$	$\mathrm{W}^{\pm}$ W^{0}	$(\mathbf{1}, \mathbf{3}, 0)$
Bino, B-boson	B	$\tilde{\mathrm{B}}^{0}$	B^{0}	$(\mathbf{1}, \mathbf{1}, 0)$

Table 1.2: Gauge supermultiplets present in a minimal supersymmetric extension of the Standard Model.

1.3.2 Particle content

The irreducible representations of the supersymmetry algebra in Eqs. (1.28), (1.29) and (1.30) are called supermultiplets. Each supermultiplet contains a fermion and a boson, which are *superpartners* of each other. It follows from the supersymmetry algebra relations that all particles which belong to the same multiplet must first of all have the same mass. Further, since the operators Q commute with the generators of the gauge transformations, the components of a supermultiplet have the same charges, isospin etc. Finally, a supermultiplet contains the same number of degrees of freedom for bosons, n_B, and fermions, n_F; $n_B = n_F$. In the most simple supersymmetric extension of the Standard Model, there are two kinds of supermultiplets:

- *Scalar/chiral multiplets*, which contain a two-component Weyl fermion and a complex scalar field (or two real scalar fields). Both have two degrees of freedom. The standard convention for chiral multiplets is that they are defined in terms of left-handed Weyl spinors.

- *Vector/gauge multiplets*, which contain a massless spin-one boson, with two degrees of freedom, and one real two-component Weyl spinor, also carrying two degrees of freedom.

In Table 1.1, the chiral supermultiplets as present in the minimal viable supersymmetric extension of the Standard Model are listed. Supermultiplets are denoted by Q, $\bar{\mathrm{u}}$, $\bar{\mathrm{d}}$, L, $\bar{\mathrm{e}}$, $\mathrm{H_d}$ and $\mathrm{H_u}$. Names, notations and quantum numbers under the SM gauge group are given. The bosonic supersymmetric partners of the Standard Model fermions are denoted with 's' in front of the SM fermion, while the supersymmetric fermionic partner of a SM boson ends with 'ino'. Due to the convention for chiral multiplets to be defined in terms of left-handed Weyl spinors, the conjugates of the right-handed fields appear in this table. In Table 1.2, the gauge supermultiplets G, W and B are listed. The collection of particles listed in Table 1.1 and 1.2 is referred to as the Minimal Supersymmetric Standard Model (MSSM).

There are two chiral multiplets containing a Higgs field. The reason for introducing a second Higgs multiplet is twofold. The first reason is the cancellation of triangle anomalies, associated with left handed fermions contained in the SU(2) doublets with non-zero quantum numbers under $U(1)$ transformation [6]. The Standard Model Higgs field carries $Y = 1/2$, but being a scalar, it does not contribute to triangle anomalies. The presence of its super-partner however, also carrying $Y = 1/2$ but being spin 1/2 and contained in an SU(2) left handed doublet, does result in a triangle anomaly! The existence of a second Higgs with opposite hypercharge eliminates this anomaly. The second reason has to do with the analyticity of the superpotential and will become clear later. Note that the particles listed in Tables 1.1 and 1.2 are eigenstates of the gauge-group, but they are not necessarily mass eigenstates, as will be discussed in Section 1.6.

1.3.3 R-parity

The promotion of the Standard Model particles to supermultiplets has an important consequence: the most general supersymmetric Lagrangian contains renormalizable lepton and baryon number violating couplings. Such couplings induce fast proton decay, while the experimental limit on the proton lifetime τ is $\tau > 10^{31}$ years [4]. Thus, in a realistic supersymmetric scenario, an additional symmetry is necessary, to prevent the proton from decaying. This symmetry is often chosen to be R-parity, defined as

$$R = (-1)^{3(B-L)+2s}, \tag{1.31}$$

where s is the spin of the particle, and B and L are baryon number and lepton number respectively. All baryons have $B = 1$, all anti-baryons have $B = -1$, and all other particles have $B = 0$. Similarly, leptons and sleptons have $L = 1$, their anti-particles $L = -1$, and all other particles have $L = 0$. The spin difference of $1/2$ then implies that all Standard Model particles carry $R = 1$, and all SUSY particles $R = -1$. The phenomenological consequences of R-parity conservation are essentially the following:

- Supersymmetric particles are only produced in even numbers.
- The lightest supersymmetric particle (LSP) must be stable.
- Each supersymmetric particle except the LSP decays eventually into an odd number of LSP's.

Since R-parity conservation is well-motivated from a phenomenological perspective, only R-parity conserving models will be discussed. A review on R-parity violating phenomenology can be found in Ref. [10].

1.4 A supersymmetric Lagrangian

Cancellation of the quadratically divergent terms as arising from the diagrams in Fig. 1.1 requires that $|\lambda_S| = |\lambda_f|^2$. The only way for supersymmetric particles to get different masses than their Standard Model partners, but at the same time have equal Yukawa couplings, is that new mass terms are present for the supersymmetric particles. These terms should then be unlike the Yukawa terms. In the lack of understanding what underlying mechanism could give rise to such terms, new mass terms for the supersymmetric particles are introduced explicitly, hereby leaving the Yukawa couplings of the Standard Model fermions intact: *soft-supersymmetry breaking.* The effective Lagrangian density of a supersymmetric model would then be a sum of two terms, a term preserving supersymmetry, $\mathcal{L}_{SUSY}$, and a term breaking supersymmetry softly at a scale m_S, $\mathcal{L}_{soft}$:

$$\mathcal{L} = \mathcal{L}_{SUSY} + \mathcal{L}_{soft}. \tag{1.32}$$

Below, a general form for an effective Lagrangian density for a simple supersymmetric theory will be discussed.

1.4.1 The supersymmetry-conserving Lagrangian

In trying to make a supersymmetric generalization of Eq. (1.6), it is useful to divide the MSSM Lagrangian density into two parts: a part describing interactions of the chiral multiplets, $\mathcal{L}_{chiral}$, and a part describing interactions of the gauge supermultiplets, $\mathcal{L}_{gauge}$. The total supersymmetry conserving Lagrangian is a sum of the two:

$$\mathcal{L}_{SUSY} = \mathcal{L}_{chiral} + \mathcal{L}_{gauge}. \tag{1.33}$$

Without going into much detail, we will briefly describe these two terms. For a complete derivation of the Lagrangian density, the reader is referred to Refs. [5, 9].

Interactions of chiral supermultiplets

The Lagrangian density describing interactions of the chiral multiplet members is given by

$$\begin{aligned}\mathcal{L}_{chiral} &= -\partial^\mu\phi^{i*}\partial_\mu\phi_i - \psi^{\dagger i}\bar{\sigma}^\mu\partial_\mu\psi_i \\ &\quad -\frac{1}{2}(W^{ij}\psi_i\psi_j + W^{*ij}\psi^{\dagger i}\psi^{\dagger j}) \\ &\quad -W^i W_i^*. \end{aligned} \tag{1.34}$$

Here the summation over i runs over all gauge and flavour degrees of freedom, ϕ_i are the scalar fields, ψ_i are the fermion fields, and W^{ij} and W^i are derived from an object called the *superpotential*, denoted by W, as

$$W^i = \frac{\partial W}{\partial \phi_i} \qquad W^{ij} = \frac{\partial^2}{\partial\phi_i\partial\phi_j}W. \tag{1.35}$$

The derivatives in the first line of Eq.(1.34) must be replaced by covariant derivatives D_L and D_R to obtain a gauge invariant theory. The first two terms in Eq. (1.34) are the supersymmetric generalization of the SM Lagrangian $\mathcal{L}_F$ in Eq. (1.7), and of the term $(\mathcal{D}_L^\mu H)^\dagger(\mathcal{D}_{L_\mu}H)$ in Eq. (1.13), thus being kinetic energy terms for the fermions (SM fermions and Higgsinos) and scalars (sfermions and Higgses), as well as their gauge interactions. The remaining four terms in Eq. (1.34) involve the superpotential W, which is an analytic function of the scalar fields ϕ of the theory, i.e. the sfermions and the Higgs scalars. Since the Lagrangian must be gauge invariant, and since gauge quantum numbers of the chiral superfields as a whole are the same as those of their scalar components, it can as well be written in terms of chiral superfield (gauge supermultiplets do not contain scalars) notation Φ_i as

$$W = \frac{1}{2}M^{ij}\Phi_i\Phi_j + \frac{1}{6}y_{ijk}\Phi_i\Phi_j\Phi_k, \tag{1.36}$$

where possibilities for Φ_i are given in Table 1.1. This expression is the most general expression which is still renormalizable. Using the definitions in Eq. (1.35), it becomes apparent that the middle two terms in Eq. (1.34) describe Yukawa interactions of the fermions. It can be seen as a supersymmetric generalization of $\mathcal{L}_Y$ in Eq. (1.6). The last term of $\mathcal{L}_{chiral}$ is a supersymmetry respecting generalization of $V(H, H^\dagger)$ in Eq. (1.13), however note that $-W^iW_i^*$ is not only the Higgs scalar potential now, but a more general expression for any scalar field!

Interactions of gauge supermultiplets

Interactions of gauge supermultiplets involve both the usual gauge bosons W_μ^a and their supersymmetric spin 1/2 partners λ^a, where $a = 1, 2, 3$ for the SU(2) gauge group and $a = 1, 8$ for the SU(3) gauge group. The supersymmetric generalization of $\mathcal{L}_G$ in Eq. (1.6) is

$$\mathcal{L}_{gauge} = -\frac{1}{4}F_{\mu\nu}^a F^{\mu\nu a} - i\lambda^{\dagger a}\bar{\sigma}^\mu D_{L_\mu}\lambda^a + \frac{1}{2}D^aD^a. \tag{1.37}$$

Here $F_{\mu\nu}^a$ is the Yang-Mills field strength defined in Eq. (1.11), D_{L_μ} is given in Eq. (1.8), and D^a is a bosonic auxiliary field with dimension mass^2, introduced only for having a consistent supersymmetry algebra. The first term is simply the kinetic energy of the Yang-Mills gauge fields, corresponding directly to $\mathcal{L}_g$ given in Eq. (1.11), thus with only SM gauge bosons involved. The middle term describes kinetic energy and gauge interactions of the gauginos, and the right most term describes the self-interactions of the auxiliary field. For the auxiliary field, only mass terms are present, no kinetic ones.

1.4.2 The supersymmetry breaking Lagrangian

As previously explained, soft supersymmetry breaking terms should give explicit masses to supersymmetric particles, while preserving the relation $|\lambda_S| = |\lambda_f|^2$. A possible gauge invariant term giving explicit masses to sfermions could be e.g. $M^2\phi^i\phi^i$, while for gauginos it could be $M\lambda_a\lambda_a$. A general expression for a Lagrangian breaking supersymmetry softly can also contain trilinear gauge invariant interactions, and is given by:

$$\begin{aligned}\mathcal{L}_{soft}^{breaking} &= -\frac{1}{2}(M_\lambda\lambda^a\lambda^a + c.c.) - (m^2)^i_j\phi^*_j\phi_i \\ &\quad -(\frac{1}{2}b^{ij}\phi_i\phi_j + \frac{1}{6}a^{ijk}\phi_i\phi_j\phi_k + c.c.),\end{aligned} \tag{1.38}$$

where λ^a are the gauginos with mass parameter M_λ, the fields ϕ_i are the scalar (sfermion) fields, with the quadratic mass terms $(m^2)^i_j$ and b^{ij} and the trilinear couplings a^{ijk}. Many gauge invariant and gauge breaking combinations are possible, however only gauge invariant terms can occur in a final realistic supersymmetric theory.

1.4.3 The MSSM Lagrangian

Now that the general framework is clear, it can be applied to the MSSM. The supersymmetry conserving Lagrangian $\mathcal{L}_{SUSY}$ is derived from the MSSM superpotential, which is given by

$$W_{MSSM} = \bar{\mathrm{u}}\mathbf{y_u}\mathrm{Q}\mathrm{H_u} - \bar{\mathrm{d}}\mathbf{y_d}\mathrm{Q}\mathrm{H_d} - \bar{\mathrm{e}}\mathbf{y_e}\mathrm{L}\mathrm{H_d} + \mu\mathrm{H_u}\mathrm{H_d}, \tag{1.39}$$

where H_u, H_d, Q, L, $\bar{\mathrm{u}}$, $\bar{\mathrm{d}}$ and $\bar{\mathrm{e}}$ are chiral superfields as defined in Table 1.1, and $\mathbf{y_u}$, $\mathbf{y_d}$ and $\mathbf{y_e}$ are dimensionless 3×3 matrices in generation space, with subscript corresponding to the three generations up type quarks, down type quarks, and down type leptons. In this expression, all indices are suppressed. For example, $\mathrm{U}\mathbf{y_u}\mathrm{Q}\mathrm{H_u}$ means $\mathrm{U}^i_a\mathbf{y_u}{}^j_i\mathrm{Q}^a_{j\alpha}(\mathrm{H_u})_\beta\epsilon^{\alpha\beta}$, implying summation over the family indices $i = 1,2,3$, over the color index $a = 1,2,3$ and over weak isospin indices $\alpha,\beta = 1,2$. This form follows by requiring a Lagrangian which is renormalizable, invariant under supersymmetry, analytic, R-parity conserving, and Lorentz and gauge invariant, while containing only the fields of the MSSM. One Higgs field, $\mathrm{H_u}$, gives masses to the up-type fermions (u, c, t quarks) and their supersymmetric partners, while another, H_d, give masses to the down-type fermions (e, μ, τ, d, s and b). Now the reason for requiring two Higgs fields in the theory becomes clear: a term in the superpotential involving the complex conjugate of a Higgs field is not differentiable with respect to that Higgs field itself (not analytic), and thus the Lagrangian could never be built from Eq.(1.34)! The last term in Eq. (1.39) is usually referred to as the 'μ-term', not having an analogue in the Standard Model, but not breaking any symmetries either. From the superpotential, the complete supersymmetry respecting part of the total MSSM Lagrangian can be derived. The entire soft supersymmetry breaking Lagrangian is found from the general expression in Eq. (1.38), imposing gauge invariance and is given by

$$\begin{aligned}\mathcal{L}_{MSSM}^{soft} \;=\; & -\frac{1}{2}(M_3\tilde{\mathrm{g}}\tilde{\mathrm{g}} + M_2\tilde{\mathrm{W}}\tilde{\mathrm{W}} + M_1\tilde{\mathrm{B}}\tilde{\mathrm{B}}) + c.c. \\ & -(\tilde{\bar{\mathrm{u}}}\mathbf{a}_u\tilde{Q}H_\mathrm{u} - \tilde{\bar{\mathrm{d}}}\mathbf{a}_d\tilde{Q}H_\mathrm{d} - \tilde{\bar{e}}\mathbf{a}_e\tilde{L}H_\mathrm{d}) + c.c. \\ & -\tilde{Q}^\dagger\mathbf{m_Q}{}^2\tilde{Q} - \tilde{L}^\dagger\mathbf{m_L}{}^2\tilde{L} - \tilde{\bar{\mathrm{u}}}^\dagger\mathbf{m_u}{}^2\tilde{\bar{\mathrm{u}}}^\dagger - \tilde{\bar{\mathrm{d}}}^\dagger\mathbf{m_d}{}^2\tilde{\bar{\mathrm{d}}}^\dagger - \tilde{\bar{e}}^\dagger\mathbf{m_e}{}^2\tilde{\bar{e}}^\dagger \\ & -m^2_{H_\mathrm{u}}H^*_\mathrm{u}H_\mathrm{u} - m^2_{H_\mathrm{d}}H^*_\mathrm{d}H_\mathrm{d} - (bH_\mathrm{u}H_\mathrm{d} + c.c.).\end{aligned} \tag{1.40}$$

The first line generates masses M_3, M_2 and M_1 for the gluino, winos and bino. The second line generates the mass matrices for the three generations of scalar fermions, in analogy to the

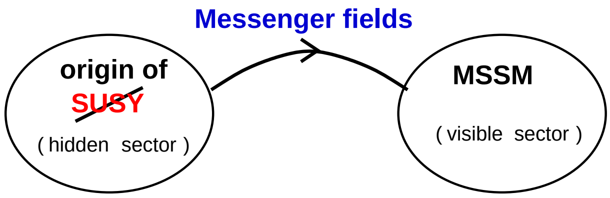

Figure 1.3: Presumed way of supersymmetry breaking.

Yukawa terms in the superpotential. The (scalar)^3 couplings a^{ijk} introduced in Eq. (1.38) can be recognized. The third line generates explicit masses for all the sfermions. Finally the fourth line generates masses for the two Higgs fields. It must be noted that the matrices $\mathbf{a_u}$, $\mathbf{a_d}$, $\mathbf{a_e}$, $\mathbf{m_Q}$, $\mathbf{m_L}$, $\mathbf{m_u}$, $\mathbf{m_d}$, $\mathbf{m_e}$ are 3×3 matrices in generation space. Obviously, soft-supersymmetry breaking introduces an enormous number of arbitrary new parameters. However, the amount of parameters can strongly be reduced by applying experimental constraints like flavor mixing and CP violation, or by modeling the origin of supersymmetry breaking.

1.5 Supersymmetry breaking

In the discussion of the MSSM, only the effective Lagrangian for the theory has been discussed. Supersymmetry breaking was introduced by explicitly adding terms in the Lagrangian. However, this effective Lagrangian should result from a fundamental theory, incorporating some kind of spontaneous supersymmetry breaking. Since there is no well established consensus on what this theory might be, it goes beyond the scope of this work to describe all the possible origins of supersymmetry breaking. The reader is referred to Ref. [5] for an overview. Only a few remarks should be made.

Firstly, none of the MSSM scalar fields would be appropriate for acquiring a vacuum expectation value to break supersymmetry: giving squarks and charged sleptons a VEV would violate gauge charges, giving sneutrinos a VEV would break lepton number, and the Higgs scalar field is already used for electroweak symmetry breaking. Thus, the MSSM must be extended with new fields which can acquire a VEV to break supersymmetry spontaneously. Tree level couplings of the MSSM particles with such a field are not probable, keeping in mind that no such couplings have been observed, and thus the soft supersymmetry breaking terms are expected to arise indirectly, at loop level, from such fields. Generally, supersymmetry is believed to be broken somewhere in a 'hidden' sector of particles, where 'hidden' means that the particles have no, or negligible direct interactions with the normal MSSM particles. Supersymmetry breaking is then communicated to the MSSM sector, or 'visible' sector, through certain messenger fields, as is displayed in Fig. 1.3. There are several possibilities for the nature of the messenger fields:

- The messenger field can be gravitational fields. Such scenarios are collected under the name of *gravity mediated supersymmetry breaking* scenarios.

- The messenger fields are fields, which have $SU(3)_c \times SU(2)_L \times U(1)_Y$ interactions. These scenarios go under the name of *gauge mediated supersymmetry breaking* models.

- Anomaly mediated supersymmetry models, where supersymmetry is broken by so-called anomalous interactions.

Based on the experimentally measured evolution of the gauge couplings, most scenarios have as starting point the unification of the gauge couplings $\alpha_1^{-1}, \alpha_2^{-1}$ and α_3^{-1} at the GUT scale, as was illustrated in Fig. 1.2. The same one-loop renormalization groups equations as shown in Eq. (1.25) are responsible for the running of the gaugino masses [5]:

$$\frac{\mathrm{d}M_a}{\mathrm{d}t} = \frac{1}{8\pi^2} b_a g_a^2 M_a \qquad \text{a=1,2,3} \qquad b_a = (33/5, 1, -7). \tag{1.41}$$

Combining Eq.(1.25) and (1.41), it is easily shown that

$$\frac{M_a(Q)}{g_a^2(Q)} = c_a, \tag{1.42}$$

where c_a is constant. Thus, this quantity is independent of the scale for all the three gauge groups! A widely spread, but certainly not inviolate, assumption is then assuming unification of the gaugino masses M_1, M_2 and M_3 at the GUT scale:

$$M_1 = M_2 = M_3 = m_{1/2}, \tag{1.43}$$

corresponding to assuming that $c_1 = c_2 = c_3$, i.e.

$$\frac{M_1}{g_1^2} = \frac{M_2}{g_2^2} = \frac{M_3}{g_3^2}. \tag{1.44}$$

It can easily been seen that in the latter case, the gluino is always the heaviest gaugino, while the lightest neutralino, a state arising after electroweak symmetry breaking from the bino and higgsinos, is always the lightest gaugino. Within gravity and gauge mediated supersymmetry breaking scenarios, models based on Eq. (1.44) are called minimal gravity mediated supersymmetry breaking (*mSUGRA*) and minimal gauge mediated supersymmetry breaking models (*mGMSB*), respectively. These models are by far the most (over-)investigated. Particularly since the gauge unification involves only the gauge *couplings*, the assumption of *mass* unification can be considered as rather arbitrary. No underlying principle exists that would *forbid* the gluino to be the lightest gaugino.

1.6 Electroweak breaking

As soon as supersymmetry is broken, the supersymmetric particles listed in Tables 1.1 and 1.2 have obtained masses. The Standard Model particles acquire mass only after electroweak symmetry breaking. Since supersymmetry involves two Higgs fields, the manner in which the electroweak symmetry gets broken, is slightly changed. The scalar fields H_u and H_d both acquire a VEV:

$$\langle H_\mathrm{u} \rangle = \frac{1}{\sqrt{2}} \begin{pmatrix} 0 \\ v_\mathrm{u} \end{pmatrix} \qquad \langle H_\mathrm{d} \rangle = \frac{1}{\sqrt{2}} \begin{pmatrix} 0 \\ v_\mathrm{d} \end{pmatrix}. \tag{1.45}$$

These VEV's are related to the known mass of the Z-boson:

$$v^2 = v_\mathrm{u}^2 + v_\mathrm{d}^2 = \frac{4m_Z^2}{g^2 + g'^2} \approx (246 \text{ GeV})^2. \tag{1.46}$$

Traditionally the ratio of the two VEV's is written as

$$\tan\beta = \frac{v_\mathrm{u}}{v_\mathrm{d}}. \tag{1.47}$$

After electroweak symmetry breaking, the Higgsinos and the the electroweak gauginos mix. For example, the neutral Higgsinos ($\tilde{H}_{\mathrm{u}}^0$ and $\tilde{H}_{\mathrm{d}}^0$) and the neutral gauginos ($\tilde{B}$ and $\tilde{W}^0$) mix with each other and form four neutral mass eigenstates called *neutralinos*. Furthermore, the charged Higgsinos ($\tilde{H}_{\mathrm{u}}^+$ and $\tilde{H}_{\mathrm{d}}^-$) and the charged gauginos ($\tilde{\mathrm{W}}^+$ and $\tilde{\mathrm{W}}^-$) mix with each other and form states with charge ± 1 called the *charginos*.

1.7 The LSP

The phenomenology of any supersymmetric theory depends strongly on the nature of the lightest supersymmetric particle (LSP). In most scenarios, the LSP is the lightest neutralino or the sneutrino. Since these particles travel through the detector without interacting, manifestations of their existence are typically missing energy. If instead the LSP is a particle carrying color-charge, like the gluino or a squark, it will hadronize and interact hadronically in the detector. If the LSP is a slepton, carrying electromagnetic charge, only electromagnetic interactions will occur. For detector experiments, the important issue is whether a particle is stable inside the detector, and behaves like the LSP, but it does not have to be strictly stable. For cosmology however, the existence of an absolutely stable LSP can have important consequences, in particular in the context of dark matter.

1.8 Squarks

Squarks in the MSSM acquire mass through the soft-supersymmetry breaking terms in the Lagrangian given in Eq. (1.40), as well as via the Yukawa interactions in the supersymmetry conserving Lagrangian, derived from the superpotential in Eq. (1.39). The terms in the Lagrangian responsible for squark masses can be selected from the total Lagrangian, and are collectively given by [11]:

$$-\mathcal{L}_{mass} = \begin{pmatrix} \tilde{\bar{\mathrm{q}}}_L & \tilde{\bar{\mathrm{q}}}_R \end{pmatrix} \mathcal{M}_{\tilde{\mathrm{q}}}^2 \begin{pmatrix} \tilde{\mathrm{q}}_L \\ \tilde{\mathrm{q}}_R \end{pmatrix} = \begin{pmatrix} \tilde{\bar{\mathrm{q}}}_L & \tilde{\bar{\mathrm{q}}}_R \end{pmatrix} \begin{pmatrix} m_{\tilde{\mathrm{q}}_L}^2 & b \\ b & m_{\tilde{\mathrm{q}}_R}^2 \end{pmatrix} \begin{pmatrix} \tilde{\mathrm{q}}_L \\ \tilde{\mathrm{q}}_R \end{pmatrix}, \tag{1.48}$$

where for an up-type scalar quark, it can be derived that

$$\begin{aligned} m_{\tilde{\mathrm{q}}_L^2} &= \mathbf{m_Q}^2 + m_Z^2 \cos 2\beta(\frac{1}{2} - \frac{2}{3}\sin^2\theta_W) + \mathbf{m_q}^2, & (1.49)\\ m_{\tilde{\mathrm{q}}_R^2} &= \mathbf{m_u}^2 + m_Z^2 \cos 2\beta(\frac{2}{3}\sin^2\theta_W) + \mathbf{m_q}^2, & (1.50)\\ b &= v(\mathbf{a_u}\sin\beta - \mu \mathbf{y_u}\cos\beta), & (1.51) \end{aligned}$$

while for down-type squarks we have

$$\begin{aligned} m_{\tilde{\mathrm{q}}_L^2} &= \mathbf{m_Q}^2 - m_Z^2 \cos 2\beta(\frac{1}{2} - \frac{1}{3}\sin^2\theta_W) + \mathbf{m_q}^2, & (1.52)\\ m_{\tilde{\mathrm{q}}_R^2} &= \mathbf{m_d}^2 + m_Z^2 \cos 2\beta(\frac{1}{3}\sin^2\theta_W) + \mathbf{m_q}^2, & (1.53)\\ b &= v(\mathbf{a_d}\cos\beta - \mu \mathbf{y_d}\sin\beta). & (1.54) \end{aligned}$$

The diagonal terms in the matrix in Eq. (1.48), $m_{\tilde{\mathrm{q}}_L^2}$ and $m_{\tilde{\mathrm{q}}_R^2}$, result partly from the soft breaking terms, the terms with $\mathbf{m_Q}^2$ and $\mathbf{m_d}^2$ in the third line in Eq. (1.40), and partly from the electroweak symmetry breaking. The off-diagonal terms in the matrix, b, result partly from the soft breaking terms proportional to the Yukawa interactions, second line in Eq. (1.40) and partly from the Yukawa couplings in the superpotential in Eq. (1.39), giving quarks their masses. It must be remembered that all masses here are actually 3×3 matrices in generation space. As can be seen from Eqs. (1.48), (1.49), (1.50), (1.52) and (1.53), the off-diagonal terms are very small for the light first and second generations. However, for the third generation quarks, they get substantial. Thus, let's study what happens for scalar top (stop) quarks. The actual scalar top mass eigenstates can be found by diagonalizing Eq. (1.48). For this purpose we introduce an orthogonal matrix U which diagonalizes the matrix $\mathcal{M}_{\tilde{t}}$ for a scalar top:

$$U \begin{pmatrix} m^2_{\tilde{t}_L} & b \\ b & m^2_{\tilde{t}_R} \end{pmatrix} U^T = \begin{pmatrix} m_{\tilde{t}_1^2} & 0 \\ 0 & m_{\tilde{t}_2^2} \end{pmatrix}, \tag{1.55}$$

where U is

$$U = \begin{pmatrix} \cos\theta_{\tilde{t}} & -\sin\theta_{\tilde{t}} \\ \sin\theta_{\tilde{t}} & \cos\theta_{\tilde{t}} \end{pmatrix} \qquad \tan\theta_{\tilde{t}} = \frac{2b}{m^2_{\tilde{t}_R} - m^2_{\tilde{t}_L}}. \tag{1.56}$$

The mass eigenstates $\tilde{t}_1$ and $\tilde{t}_2$ have eigenvalues m_1 and m_2, given by

$$\tilde{t}_1 = \cos\theta_{\tilde{t}}\tilde{t}_L - \sin\theta_{\tilde{t}}\tilde{t}_R \qquad m^2_{\tilde{t}_1} = \frac{m^2_{\tilde{t}_L} + m_{\tilde{t}_R^2}}{2} - \sqrt{\left(\frac{m^2_{\tilde{t}_L} - m_{\tilde{t}_R^2}}{2}\right)^2 + b^2} \tag{1.57}$$

$$\tilde{t}_2 = \cos\theta_{\tilde{t}}\tilde{t}_L + \sin\theta_{\tilde{t}}\tilde{t}_R \qquad m^2_{\tilde{t}_2} = \frac{m^2_{\tilde{t}_L} + m_{\tilde{t}_R^2}}{2} + \sqrt{\left(\frac{m^2_{\tilde{t}_L} - m_{\tilde{t}_R^2}}{2}\right)^2 + b^2}, \tag{1.58}$$

so that $m_{\tilde{t}_1} < m_{\tilde{t}_2}$. Thus, due to the large value of the top quark mass, an enormous mixing results and the two mass eigenstates of the scalar top quark are very much non-degenerate. This situation is unique for the scalar top. For sbottoms the effect is smaller, but still significant, while for the other generations it is negligible. Thus, the third generation squarks are probably the lightest ones.

1.9 Gluinos

The gluino is the only color-octet fermion in the MSSM and cannot mix with any other particles. Since the gluon is massless, the gluino mass arises entirely by the soft supersymmetry breaking terms in Eq. (1.40). It must be remembered that the parameter M_3 is running. Since the strong coupling constant is large, the mass M_3 is running quickly with the energy scale, and the gluino pole mass can be considerably different from M_3. Whether the gluino is heavy or light at electroweak energy scales depends entirely on its mass value at the GUT scale and on the masses of the squarks, which enter in the renormalization.

Chapter 2

Exotic heavy hadrons

We have seen in the previous chapter that supersymmetry is an attractive extension of physics beyond the Standard Model. The chapter was concluded by a discussion of the colored supersymmetric particles, the squarks and gluinos. In this chapter, we continue this discussion, and investigate the consequences of the existence of colored, *stable*, particles, with masses far above the Standard Model particle masses. Such colored stable heavy states would hadronize into heavy hadrons due to color confinement. These particles and their interactions constitute the main topic of this thesis.

This chapter begins with giving motivations in Section 2.1 for searching for exotic heavy hadrons. This is followed by an overview in Section 2.2 of some of the physics models, in which exotic heavy hadrons could exist. The emphasis will be on supersymmetric models, which predict the existence of heavy hadrons called R-hadrons. Section 2.3 summarizes the most relevant existing searches for heavy hadrons, followed by a very brief discussion of cosmological aspects in Section 2.4, which is meant only to answer the most immediate questions of curious readers about cosmology, rather than to provide an extensive review. In Sections 2.5 and 2.6, attention will be paid to the production of R-hadrons at LEP and at LHC, respectively. Relevant Feynman diagrams and production cross sections will be given. In this chapter, and in the rest of the thesis, the focus is on gluino R-hadrons.

2.1 Motivations

There are several reasons to search for heavy hadrons in collider experiments like LEP and LHC:

- The possibility of the existence of stable heavy hadrons has received very little attention up till May 2004, when Ref. [12] was published. As will be stressed in Section 2.2, heavy hadrons are predicted in several appealing models of physics beyond the Standard Model which were available long before. These models have however never received much attention. A vast amount of studies at LEP and LHC has been dedicated to searches in the framework of *mSUGRA*. Although such models are indeed the most straightforward and easiest to look for, it is important to be prepared for any new physics signal, rather than to focus on signals of one particular class of models. The recent theoretical work [12, 13], which will be discussed Section 2.2, and as a consequence the explosion of interest in stable gluinos, has clearly made a search for heavy gluino hadrons even more relevant.

- A search for stable gluinos at LEP is highly relevant, because the sensitivity of LEP to stable gluinos is in the range of the so-called 'gluino mass window'. More details on this will be discussed in Section 2.3.1.

- Stable strongly interacting hadrons have been proposed to explain certain cosmological observations. For example, these particles can explain the detection of a handful of ultra high energy events in the cosmic ray spectrum [14], because the effective path-length of a heavy particle is larger than that of an ordinary nucleon with comparable energy, following from kinematics. Such particles could then reach the earth, and would produce showers [15] in the atmosphere. Furthermore, stable neutral gluino baryons have been proposed as candidates for so-called self-interacting dark-matter [16, 17], and as constituents of neutron stars [18].

- It is fun to study stable particles, which interact hadronically in a detector, rather than punch through without interaction, like weakly interacting stable particles. The understanding of these interactions brings us a step closer to recognizing the actual signal in a collider experiment in case heavy stable hadrons would be produced.

2.2 Models incorporating heavy hadrons

2.2.1 Supersymmetry models and R-hadrons

First of all, it must be emphasized that particles are regarded as *stable* if they do not decay while traversing a typical detector. Models predicting heavy hadrons are those with LSP or just long-lived gluinos and squarks. As explained in Section 1.5, conventional SUSY models, based on the relation in Eq. (1.44), always predict a neutral and colorless LSP and a heavy gluino. However a broad range of other models exist. Scenarios with a gluino LSP are reviewed in Ref. [19], and include GMSB models, and string models based on supergravity. Within the first class, the masses of the messengers transferring supersymmetry breaking from the hidden sector to the visible sector are of the order of the GUT scale. Mixing of these messengers with the Higgs field causes gluinos to be the lightest gauginos, and often to be LSP [20]. Light gluinos also arise naturally in a number of string models, e.g. the O-II string models [21, 22].

Very recently, long-lived gluinos have been predicted in the context of *split supersymmetry* models [12, 13]. These models suggest that the same fine-tuning mechanism, which tunes the cosmological constant to such a value that galaxies, stars, planets and biology can form, may be responsible for the fine-tuning of the Higgs mass. The amount of fine tuning of the Higgs mass however is insignificant in comparison with that of the cosmological constant. Refs. [12, 13] therefore abandon a solution to the hierarchy problem with low energy supersymmetry, i.e. supersymmetry with supersymmetric particle masses of the order of 1 TeV. Supersymmetry is still necessary to unify the gauge couplings, but it can now be broken at a very high scale $m_S \sim 10^{10}\text{GeV}/c^2$. Since there are no big contributions of the squarks and sleptons to the gauge unification issue [12], all scalar masses, except for one Higgs scalar, are or the order of m_S. This is an attractive feature: it removes several difficulties associated with the Standard Model, such as the absence of a light Higgs. The gauginos, being fermions, are protected by chiral symmetries and can as such not be very heavy, i.e. they should not be heavier than a few TeV. A strikingly long-lived gluino is predicted, not necessarily because it is the LSP, but because its decay, always mediated by a squark, is highly suppressed due the large squark mass. Gluino lifetimes are predicted in between 10^{-6} s and the age of the universe. The phenomenology of these models has recently been studied in Refs. [23, 24].

Concerning stable squarks, these are cosmologically disfavoured because of their nonzero electric charge [25], but could be sufficiently long-lived to behave like an effectively stable LSP in a detector experiment.

A gluino or squark, carrying color charge, would hadronize into heavy (charged and neutral) bound states. These bound states (for example $\tilde{g}g$, $\tilde{g}q\bar{q}$, $\tilde{g}qqq$, $\tilde{q}\bar{q}$, $\tilde{q}qq$) are generically called **R–hadrons**, where the "R" refers to the fact that they carry one unit of R–parity [26]. States like $\tilde{g}g$ are usually referred to as gluino-balls, $\tilde{g}q\bar{q}$ or $\tilde{q}\bar{q}$-states as R-mesons and $\tilde{g}qqq$ or $\tilde{q}qq$ as R-baryons. In this thesis we focus on R-hadrons containing a gluino.

2.2.2 Alternative models

In addition to supersymmetry, other extensions of the Standard Model exist, which predict the existence of heavy hadrons, either due to a new conserved quantum number, or because the decays are suppressed by kinematics or couplings. For example, theories with leptoquarks predict the existence of stable hadronized states, if the Yukawa coupling between the leptoquark and its decay products is so small, that the leptoquark lives long enough to hadronize [27], as is displayed in Fig. 2.1. Another example is theories with universal extra dimensions, *universal* referring to the fact that the extra dimensions are accessible to Standard Model fields, rather than that the Standard Model fields are confined to a flat 4-D brane. The extra dimensions lead to heavy Kaluza-Klein excitation modes, resulting from the compactification of the extra dimensions. In models requiring momentum conservation in all universal dimensions, stable Kaluza-Klein excitations of quarks and gluons may arise, which would form stable hadronized states [28]. For the curious reader, other examples of models suggesting heavy hadrons are models with new Standard Model fermions [29, 30, 31] and certain unification models [32].

2.3 Existing searches for heavy hadrons

Several searches for signals of R-hadrons and heavy stable particles in general have been performed. These include accelerator searches, cosmic ray studies, and searches in ordinary matter. A good review of limits on stable, massive particles can be found in Refs. [4, 33]. For completeness, the most important limits are summarized below, hereby motivating an additional search with ALEPH data.

2.3.1 Accelerator searches

The most direct way of searching for the existence of any new particle is by using accelerators. Existing limits on R-hadrons are partly those obtained with stable gluino searches, and partly those obtained by searching for charged massive particles in general:

- Searches for a stable gluino. A complete list of stable gluino searches is given in Ref. [4]. The following searches are most relevant:

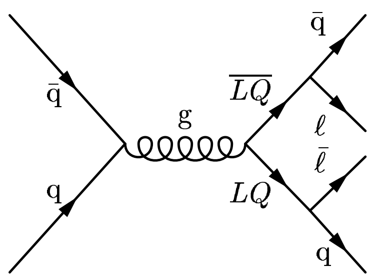

Figure 2.1: The possible production and decay of a leptoquark state.

  - Searches for light gluinos based on QCD color factors and the running of α_S, see Ref. [4].
  - Recently, a search for signals of stable gluinos was performed by setting a limit on the partial width of any purely hadronic exotic contribution to Z-decays [34]. This search excluded gluinos below 6.3 GeV/c^2 at 95% confidence level. This limit was model independent and based on the so-called ϵ-formalism, a method to constrain Standard Model deviations arising from new physics.
  - A direct search for stable gluino hadrons was done in the channels mentioned in Section 2.5.2 with data taken by the DELPHI detector [35]. The analysis was based on missing energy and heavily ionizing tracks. Charged R-hadrons were treated as heavy muons in the detector, and neutral R-hadrons as neutral kaons but with a different energy deposit. A limit on the squark mass, depending on the fraction of charged gluino hadrons, was obtained. Scalar top quarks with masses below 87 GeV/c^2 and scalar bottom quarks with masses below 82 GeV/c^2 were excluded at 95% confidence level, independent of the squark mixing angle.
  - A limit on stable gluinos using CDF data is described in Refs. [19, 36]. In Ref. [36], a model for R-hadron nucleon scattering was developed to predict energy losses, but no full detector simulation is used. The search topology was based on missing transverse energy plus jets. The derived limit depends on the amount of charged gluino-hadrons present; if more than half of the hadrons are charged, the only values allowed for an LSP gluino are between 25 and 35 GeV/c^2, the 'heavy gluino window' (in contrast to the 'light gluino window' for gluino masses below approximately 5 GeV/c^2, recently excluded [34])). This result was obtained in combination with Ref. [19], where stable gluino-hadrons were searched for in OPAL and CDF data by looking at transverse missing energy and jets, in combination with signatures for heavily ionizing particles.
  - Several searches have been done for squarks. For example, searches for squarks have already been performed by ALEPH [37, 38] in the framework of the MSSM, with R-parity conservation and the assumption that the lightest supersymmetric particle (LSP) is the lightest neutralino or the sneutrino. These searches yielded an absolute lower limit on the stop mass of 63 GeV/c^2 at the 95% confidence level. However, this absolute lower limit does not apply if the LSP is either the gluino or the squark itself.

- Apart from searches for gluinos, a vast amount of searches for weakly interacting heavy stable particles has been done, in particular for charged particles, see for example Ref. [39]. These analyses are all based on searching for heavy ionizing tracks. Limits are in all cases dependent on the particular supersymmetry model, and all searches are focused on specific topologies. No general results can be derived.

In conclusion, the 'gluino window' makes it is highly relevant to search for gluinos at moderately high masses. In particular, it would be challenging to set mass limits which are independent of the R-hadron's charge. A search for R-hadrons at LEP is in particular interesting, because it may cover the light (not excluded at the time this work was started) and heavy gluino mass windows. At LHC, larger center-of-mass energies are available, enabling to search for hadrons with very high masses.

2.3.2 Searches in ordinary matter

If heavy exotic hadrons exist, they should have been produced during the early periods of the universe, and, in case they would be strictly stable, still be present now. The abundance of a particle at present is inversely proportional to the annihilation cross section in early times [40], and therefore limits on the mass of strictly stable gluinos can be set by searching for R-hadrons at present. Since R-hadrons would probably condense in ordinary baryonic matter [33], searches in ordinary matter on Earth have been performed, including the following:

- Searches in water. Any positively charged heavy hadron could be bound in water by forming heavy hydrogen-like atoms in water, e.g. HRO if the heavy hadron is a charged R-hadron. Searches in terrestrial water for super heavy hydrogen atoms exclude charged massive particles with masses below 10 TeV, see e.g. Ref. [41].
- Searches in isotopes. A negatively charged heavy state would bind to nucleons and form super heavy nuclei. Searches in low and high Z nuclei have resulted in the exclusion of any stable isotopes with masses up to about 10 TeV [42, 43]. In addition, constraints from nucleosynthesis have been set by studying the abundance of the light elements such as H, He and Be present in the universe today [44].
- Searches for heavy hadrons in iron meteorites have been performed for heavy hadrons with masses below 650 GeV with negative results [43].

In conclusion, very strong limits have been set by searching for heavy nuclei in ordinary matter. Thus, if R-hadrons really existed in the early universe, some mechanism should exist which would cause these particles to avoid all these limits limits.

2.3.3 Searches in cosmic rays

If for some reason or another those states did not get trapped in matter, like perhaps the neutral heavy states, these would currently be present in the halo of galaxies. If these particles would be their own anti-particles, they could annihilate and cause gamma ray burst events (see Section 2.1), possibly detectable by cosmic ray experiments. Heavy stable hadrons have also been proposed as galactic dark matter candidates. Experiments such as balloon flights, satellites and underground experiments, mostly intended for dark matter searches or research of the cosmic microwave background (CMB), have derived strong limits on the fluxes and masses of neutral as well as charged particles [45, 46].

2.4 Small relic density?

From the above it is clear that searches for heavy hadrons have so far been negative. One of the reasons why heavy hadrons might have escaped all observation is that their relic density is small. The standard approach in computing a relic density is to compare the annihilation rate of a particle species to the expansion rate of the universe [40], and calculate when the annihilation rate falls below the expansion rate. With the Boltzmann equation, the density of the particle species at the moment of freeze-out is calculated, and taking into account the expansion of the universe, the density today is calculated. Applying this recipe to gluino R-hadrons, it is concluded that R-hadrons cannot have escaped detection [19], and that thus very strict limits on stable gluinos can be set from cosmology. However, Ref. [19] discusses several reasons why the density of heavy hadrons, in particular R-hadrons, could be much lower than expected:

- Multiple gluon exchange between the annihilating gluinos (Sommerfeld enhancement) would enhance the annihilation cross section $\sigma(\tilde{g}\tilde{g} \to gg)$ at threshold. Close to threshold, where the velocities of the gluinos become tiny, multiple gluon exchange between the slowly moving gluinos, a loop effect, becomes important, so that the cross section does not vanish, like e.g. the neutralino annihilation cross section does. A larger annihilation cross section would result in a lower relic density today.

- The inflation model. Contrary to conventional inflation models, where reheating of the universe, and later freeze-out of the particle species takes place after inflation, unconventional inflation scenarios exist, where the abundance would decrease significantly if the temperature of reheating of the universe was lower [47], because the production cross section for heavy particles is smaller at lower temperature. Another class of non-conventional inflation models employs the idea that inflation takes place at temperatures below the electroweak scale, rather than above [48], diluting the mass density of heavy particles.

Of course, all problems with cosmology are avoidable in case slow decay of R-hadrons would occur, either by R-parity violating couplings or decay into another SUSY particle. As long as the R-hadron has a lifetime larger than $\sim 10^{-7}$ seconds, it would be stable for detector experiments. In conclusion, no model-independent bounds can be set on stable gluinos from cosmology.

2.5 R-hadron production at LEP

Below, the production of squarks and gluinos will be discussed, and the search channel will be proposed which will be investigated later in this thesis. The subsequent hadronization will be discussed in Chapter 7.

2.5.1 Squark production

Squarks would be be produced through s-channel exchange of a virtual Z or γ:

$$\mathrm{e}^+ + \mathrm{e}^- \quad \rightarrow \quad \tilde{\mathrm{q}} + \bar{\tilde{\mathrm{q}}}. \tag{2.1}$$

The relevant Feynman diagram is displayed in Fig. 2.2. The cross section for $\mathrm{e}^+ + \mathrm{e}^- \rightarrow \tilde{\mathrm{q}}_\mathrm{i} + \bar{\tilde{\mathrm{q}}}_\mathrm{j}$

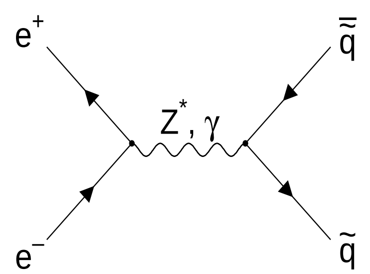

Figure 2.2: Squark production at LEP.

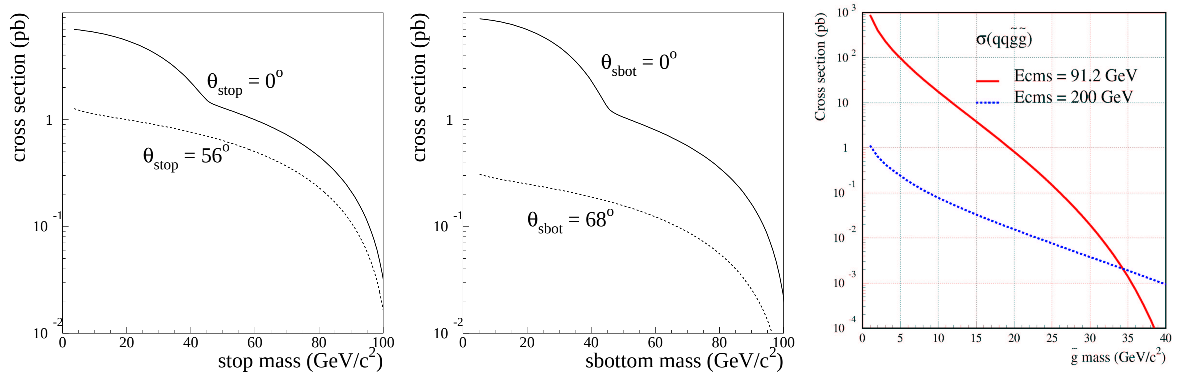

(a) (b) (c)

Figure 2.3: Cross section for stop production (a) and sbottom (b) production at $\sqrt{s}$ = 200 GeV. The dashed and solid curves are the cross sections for maximal and minimal coupling to the Z-boson, respectively. (c) Cross section for the process $e^+e^- \to q\bar{q}\tilde{g}\tilde{g}$ at $\sqrt{s}$ = 92.1 GeV and $\sqrt{s}$ = 200 GeV. Fig. (c) is obtained from Ref. [35].

(i,j=1,2, the squark mass eigenstates) at tree level is given by [11, 49]

$$
\begin{aligned}
\sigma^0_{e^+ + e^- \to \tilde{\mathrm{q}}_\mathrm{i} + \bar{\tilde{\mathrm{q}}}_\mathrm{j}} &= \frac{\pi\alpha^2}{s}\lambda_{\mathrm{ij}}^{3/2} \times \\
\gamma - \text{exchange} \quad & \Big[Q^2_{\tilde{\mathrm{q}}}\delta_{\mathrm{ij}} \\
\mathrm{Z} - \gamma - \text{interference} \quad & -\frac{Q_{\tilde{\mathrm{q}}}\delta_{\mathrm{ij}} a_{\mathrm{ij}} v_e}{8\sin^2\theta_W \cos^2\theta_W} \frac{s(s-m^2_{\mathrm{Z}})}{(s-m^2_{\mathrm{Z}})^2 + m^2_{\mathrm{Z}}\Gamma^2_{\mathrm{Z}}} \\
\mathrm{Z} - \text{exchange} \quad & +\frac{a^2_{\mathrm{ij}}(v^2_e + a^2_e)}{256\sin^4\theta_W \cos^4\theta_W} \frac{s^2}{(s-m^2_{\mathrm{Z}})^2 + m^2_{\mathrm{Z}}\Gamma^2_{\mathrm{Z}}} \Big],
\end{aligned}
\tag{2.2}
$$

where s is the center-of-mass energy, $\lambda_{\mathrm{ij}} = (1 - m^2_{\tilde{\mathrm{q}}_\mathrm{i}}/s - m^2_{\tilde{\mathrm{q}}_\mathrm{j}}/s)^2 - (4m^2_{\tilde{\mathrm{q}}_\mathrm{i}} m^2_{\tilde{\mathrm{q}}_\mathrm{j}})/s^2$, $Q_{\tilde{\mathrm{q}}}$ is the charge of the squarks in units of $e = \sqrt{4\pi\alpha}$, Γ_Z is the Z-width, and a_{ij} are the $\tilde{\mathrm{q}}\tilde{\mathrm{q}}Z$-couplings

$$a_{11} = 4(I^{3L}_\mathrm{q}\cos^2\theta_{\tilde{\mathrm{q}}} - \sin^2\theta_W Q_{\tilde{\mathrm{q}}}) \tag{2.3}$$

$$a_{22} = 4(I^{3L}_\mathrm{q}\sin^2\theta_{\tilde{\mathrm{q}}} - \sin^2\theta_W Q_{\tilde{\mathrm{q}}}) \tag{2.4}$$

$$a_{12} = a_{21} = -2I^{3L}_\mathrm{q}\sin^2\theta_{\tilde{\mathrm{q}}}. \tag{2.5}$$

Here I^{3L}_q is the third component of isospin of quark q, see Section 1.1.2. Furthermore, v_e and a_e are the vector and axial vector couplings of the eeZ-vertex:

$$v_\mathrm{e} = -1 + 4\sin^2\theta_W \qquad\qquad a_\mathrm{e} = -1. \tag{2.6}$$

In the case where i=j, then $\lambda_{\mathrm{ij}} = \beta^2_{\tilde{\mathrm{q}}_\mathrm{i}}$, with $\beta_{\tilde{\mathrm{q}}_\mathrm{i}}$ being the velocity of the outgoing squark.

The expression in Eq. (2.2) is valid at tree level and must be corrected for strong and electroweak corrections [11, 49]. For stop and sbottom quarks, the cross section is minimal if the mixing angles $\theta_{\tilde{\mathrm{t}}}$ and $\theta_{\tilde{\mathrm{b}}}$ are 56^0 and 68^0, respectively. In that case there is basically no coupling to the Z, and only γ-exchange can contribute to the cross section. A zero mixing angle corresponds for both up and down type squarks to maximal coupling to the Z-boson and thus a maximum cross section. In Fig. 2.3, the cross section for the production of stop and sbottom quarks are

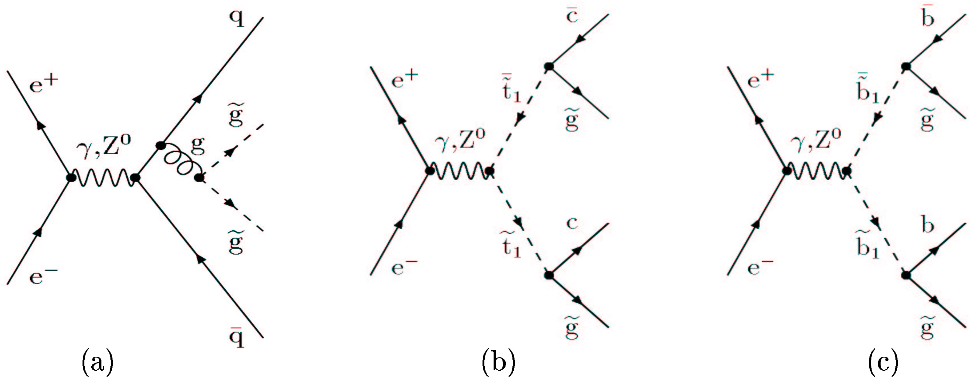

Figure 2.4: (a) Gluino production via gluon splitting into a pair of gluinos. (b) Gluino production via stop decay, and (c) via sbottom decay.

shown, with initial state radiation included. The behaviour of the cross section around $m_{\tilde{\mathrm{q}}} \approx 45$ GeV, for the case of maximal coupling to the Z-boson, is due to the decay width $\mathrm{Z} \to \tilde{\mathrm{q}}\bar{\tilde{\mathrm{q}}}$ having a minimum. As such, the mixing angle influences directly the amount of initial state radiation (ISR) emitted by the electrons.

2.5.2 Gluino production

Possible gluino production channels at $\mathrm{e}^+\mathrm{e}^-$-colliders would be

$$\mathrm{e}^+ + \mathrm{e}^- \to \quad \mathrm{q} + \bar{\mathrm{q}} + \mathrm{g} \quad \to \mathrm{q} + \bar{\mathrm{q}} + \tilde{\mathrm{g}} + \tilde{\mathrm{g}} \tag{2.7}$$

$$\mathrm{e}^+ + \mathrm{e}^- \to \quad \tilde{\mathrm{t}}_1 + \bar{\tilde{\mathrm{t}}}_1 \quad \to \mathrm{c} + \tilde{\mathrm{g}} + \bar{\mathrm{c}} + \tilde{\mathrm{g}} \tag{2.8}$$

$$\mathrm{e}^+ + \mathrm{e}^- \to \quad \tilde{\mathrm{b}}_1 + \bar{\tilde{\mathrm{b}}}_1 \quad \to \mathrm{b} + \tilde{\mathrm{g}} + \bar{\mathrm{b}} + \tilde{\mathrm{g}}, \tag{2.9}$$

where $\tilde{\mathrm{t}}_1$ and $\tilde{\mathrm{b}}_1$ denote the lightest mass eigenstates of the scalar top and scalar bottom quarks respectively. The first channel, where gluinos are produced via gluon splitting, dominates at LEP1 energies. Fig. 2.4(a) shows the Feynman diagram of this process and the corresponding cross sections are given in Fig. 2.3(c) at LEP1 and LEP2 center-of-mass energies. Evolving to higher energies, the cross section for this process decreases, and gluino production dominantly takes place via stop or sbottom decay. Since the stop is probably the lightest squark, as was clarified with Eq. (1.57), and hence has the largest probability to be in the reach of LEP2, this thesis focuses on a search for LSP gluinos produced via $\mathrm{e}^+\mathrm{e}^- \to \tilde{\mathrm{t}}\bar{\tilde{\mathrm{t}}} \to \mathrm{c}\tilde{\mathrm{g}}\bar{\mathrm{c}}\tilde{\mathrm{g}}$. Stop quarks are produced as displayed in Fig. 2.2. The stop quarks decay subsequently into a charm and a gluino, a one-loop process [50], mediated by W-bosons, charginos, higgsinos, bottoms and sbottoms, and gauge-related fields. The lifetime of a stop decaying into a charm and a gluino is [50]

$$\Gamma(\tilde{\mathrm{t}}_1 \to c\tilde{\mathrm{g}}) = \frac{2}{3}\alpha_s|\epsilon|^2 m_{\tilde{\mathrm{t}}_1}\left[1 - \frac{m^2_{\tilde{\mathrm{g}}}}{m_{\tilde{\mathrm{t}}^2_1}}\right]^2, \tag{2.10}$$

where α_s is the strong coupling constant and ϵ is a constant which includes the couplings of the involved vertices. The value for ϵ is $\sim (1-4)\times 10^{-4}$, the uncertainty coming from the uncertainties in the relevant matrix elements of the CKM matrix. The lifetime is of the order of 10^{-18} s, which is much larger than the typical hadronization time of $\sim 10^{-23}$ s. Consequently, the stop would hadronize before it decays. Assuming that the branching ratio of stops into gluinos is unity, the cross section for gluino production is given by the cross section for stop production as displayed in Fig 2.3. Some relevant distributions at event generator level are given in Appendix C. A discussion of the topology of the events will be postponed until Chapter 7.

2.6 R-hadron production at LHC

2.6.1 Squark production at LHC

At LHC, squarks would be produced in pairs. The leading production channels would be [51]

$$\begin{aligned} \tilde{q}\bar{\tilde{q}}\text{ production}: \quad & q_i + \bar{q}_j && \rightarrow \tilde{q}_k + \bar{\tilde{q}}_l && (2.11)\\ & g + g && \rightarrow \tilde{q}_i + \bar{\tilde{q}}_i && (2.12)\\ \tilde{q}\tilde{q}\text{ production}: \quad & q_i + q_j && \rightarrow \tilde{q}_i + \tilde{q}_j \text{ and } c.c. && (2.13)\\ \tilde{q}\tilde{g}\text{ production}: \quad & q_i + g && \rightarrow \tilde{q}_i + \tilde{g} \text{ and } c.c.. && (2.14) \end{aligned}$$

The relevant Feynman diagrams are displayed in Fig. 2.5(a), (b), (c) and (d). Depending on the quark masses, production may be possible via decay of other sparticles, such as the gluino. The process is purely strong, and therefore depends only on the squark and gluino masses, and on the strong coupling constant. The fact that we do not collide elementary particles like gluons or quarks, but protons, having a certain internal structure, complicates the calculation of the cross section. In contrast to $e^+ - e^-$ annihilations, where the whole center-of-mass energy $\sqrt{s}$ is used in the production of new particles, only a part $\sqrt{\hat{s}}$ of the total center-of-mass energy is available in the collision of two protons. In terms of the fractions x_1 and x_2 of the momenta of the two incoming protons, we have $\hat{s} = x_1 x_2 s$. Cross sections generally depend on the masses of the supersymmetric particles being produced. The production of large masses implies that the colliding partons need to take a large fraction of the incoming hadron momenta. In this region of large x-values, the parton density inside the proton is dominated by the valence quark content, and the production channel from quarks probably dominates. On the contrary, when producing lighter particles, the gluon density in the proton dominates, and the production channel via gluon fusion is dominant. At such x-values, the sea-quark density also starts playing a role, so that the channel via quark-antiquark annihilation can contribute as well. Whether the production channels via quarks, via quark-antiquark annihilation, or via gluon fusion dominates, depends thus mainly on the $\hat{s}$. Cross sections for squark production at hadron colliders are given in Ref. [51].

2.6.2 Gluino production at LHC

At hadron colliders, the leading production channels for gluinos would be

$$\begin{aligned} \tilde{g}\tilde{g}\text{ production}: \quad & q_i + \bar{q}_i && \rightarrow \tilde{g} + \tilde{g} && (2.15)\\ & g + g && \rightarrow \tilde{g} + \tilde{g} && (2.16)\\ \tilde{q}\tilde{g}\text{ production}: \quad & q_i + g && \rightarrow \tilde{q}_i + \tilde{g} \text{ and } c.c. && (2.17) \end{aligned}$$

Relevant Feynman diagrams are given in Fig. 2.5. In view of the analysis which will be discussed in Chapter 13, it is appropriate to divide the events into different classes.

$$\begin{aligned} pp &\rightarrow \tilde{g}\tilde{g} && && \text{class I} && (2.18)\\ pp &\rightarrow \tilde{q}\tilde{g} && \rightarrow \tilde{g}\tilde{g}\tilde{q} && \text{class II} && (2.19)\\ pp &\rightarrow \tilde{q}\tilde{q} && \rightarrow \tilde{g}\tilde{g}qq && \text{class III} && (2.20) \end{aligned}$$

These processes are purely strong and, given the incoming beams and energies, depends again only on squark and gluino masses and the strong coupling constant. Of course, this is under the

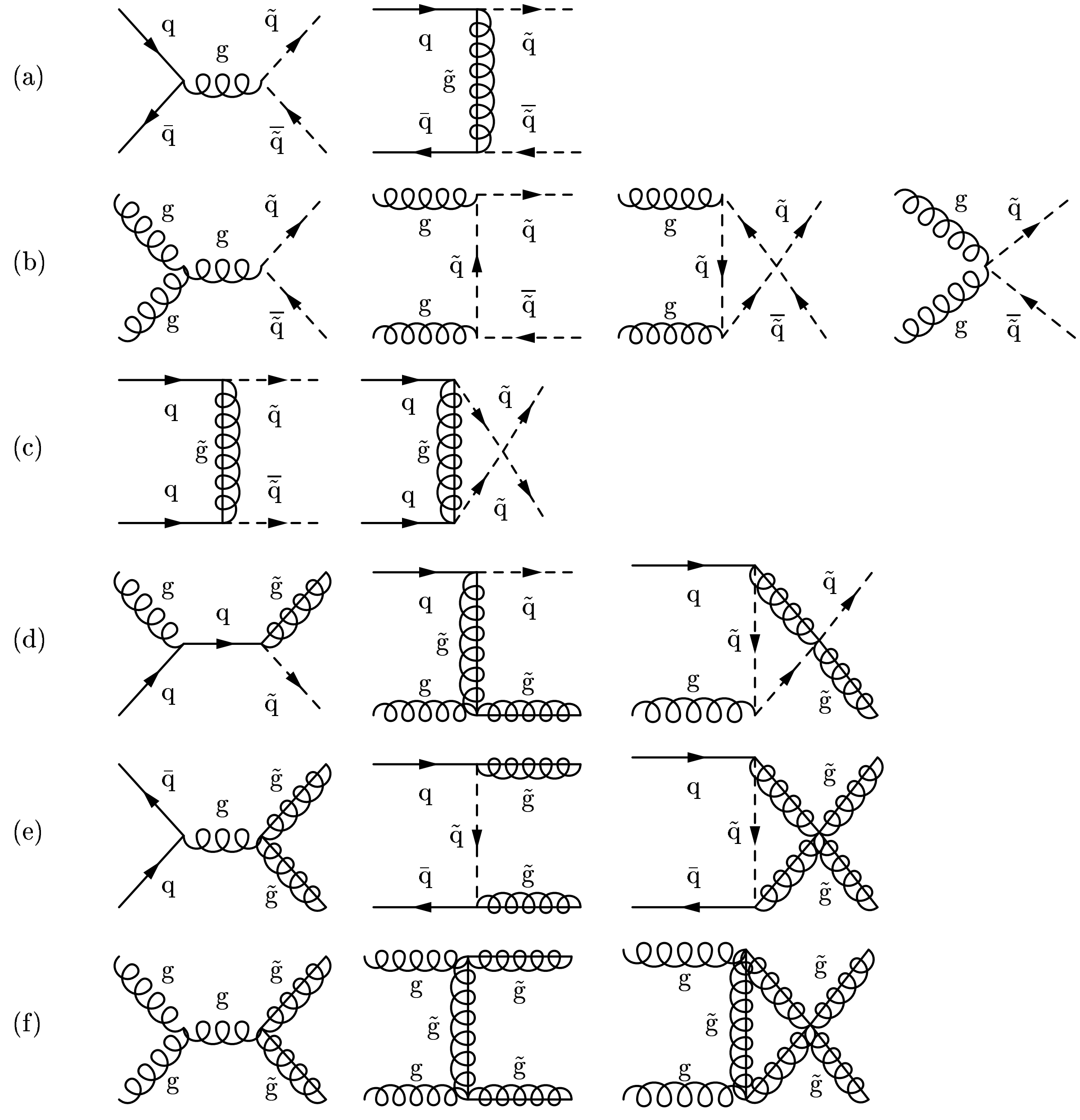

Figure 2.5: Squark and gluino production at LHC. Squark production is displayed in the diagrams (a), (b), (c) and (d), while gluino production is displayed in (d), (e) and (f).

assumption that the branching ratio for squarks into gluinos is 100%. For the evaluation of the cross sections of class II and II events, the branching ratio of squarks decaying into gluinos is relevant. These can e.g. be verified with the program ISASUSY [116]. For class I events, the branching ratio is not relevant. Fig. 2.6 shows cross sections for class I and class II events.

In Appendix C2 some relevant distributions at generator (PYTHIA) level are given for the channels $\mathrm{pp} \to \tilde{\mathrm{g}}\tilde{\mathrm{g}}$, $\mathrm{pp} \to \tilde{\mathrm{q}}\tilde{\mathrm{g}} \to \tilde{\mathrm{g}}\tilde{\mathrm{g}}\mathrm{q}$ and $\mathrm{pp} \to \tilde{\mathrm{q}}\tilde{\mathrm{q}} \to \tilde{\mathrm{g}}\tilde{\mathrm{g}}\mathrm{qq}$. A few things are noteworthy. First of all, looking at the distribution of the R-hadron velocity, it is seen that indeed the R-hadrons have an average velocity significantly smaller than one. Second, R-hadrons produced in class II and III

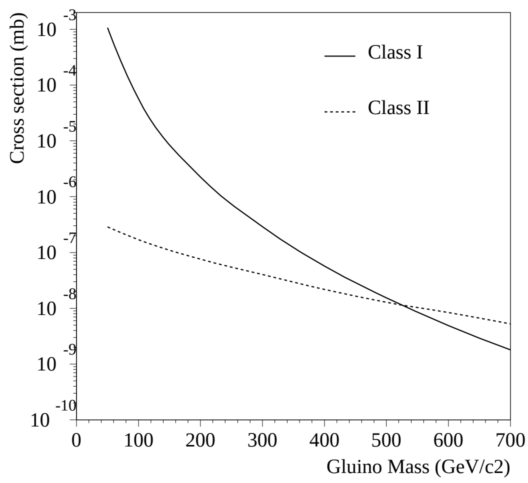

Figure 2.6: A typical example if the total cross section for gluino production at the LHC, as obtained from the PYTHIA event generator [52]. All supersymmetric particles, except for the gluino, are assumed to have masses of 800 GeV, as suggested by Ref. [53]. The branching ratio for squark to gluino is evaluated to be very close to 100% for the class II events.

have a larger average velocity. This is because gluinos produced via a (heavy) squarks receive a 'kick'. Third, in the case of class I events, two R-hadrons are seen to be produced approximately back-to-back, while they are more acoplanar in the case where they are produced via a squark. The topology of these events will be discussed in Chapter 13.

Chapter 3

Interactions of light hadrons in matter

The main goal of this chapter is to describe the interactions of neutral and charged ordinary hadrons. It is meant to provide preface to the next chapter, where interactions of heavy hadrons will be discussed. In Section 3.1, a quick summary will be given concerning electromagnetic energy losses of charged particles in matter. After that, attention is paid to nuclear interactions in Section 3.2. A few introductory remarks will be given first in Section 3.2.1. Then, the energy dependence of cross sections will be considered in Sections 3.2.2, 3.2.3 and 3.2.4. Section 3.2.5 briefly discusses energy losses, and the concept of nuclear cascades will be emphasized in 3.2.6. Finally, in Section 3.3, these topics will be clarified by going through a typical example of a relatively well understood process, which exhibits a variety of interesting features: pion-nucleon scattering.

3.1 Electromagnetic interactions

Charged particles other than electrons lose their energy mainly by ionization or excitation of atomic electrons when they traverse a certain material. The mean rate of ionization loss of a charged particle is given by the Bethe-Bloch formula [4]. This formula depends only on the charge and velocity of the particle, and on the medium. In Fig. 3.1 the ionization loss is shown for muons, pions and protons in different materials. In addition to energy losses through ionization, a charged particle traversing a medium suffers repeated elastic Coulomb scatterings from nuclei. The resulting scattering angle follows a Gaussian distribution with a width given by [4]

$$\theta_0 = \frac{13.6\ \mathrm{MeV}}{\beta c p} z \sqrt{x/X_0}[1 + 0.038\ln(x/X_0)], \tag{3.1}$$

where p, βc and z are momentum, velocity and charge number of the incident particle, respectively, and where x and X_0 are the traversed length and the radiation length, respectively.

3.2 Nuclear scattering

The dominating energy loss mechanism for neutral particles (disregarding photons) with energies above a few MeV is through scattering on nuclei [4]. The amount of energy lost through nuclear scattering depends on two quantities:

- The interaction length or nuclear scattering cross section.

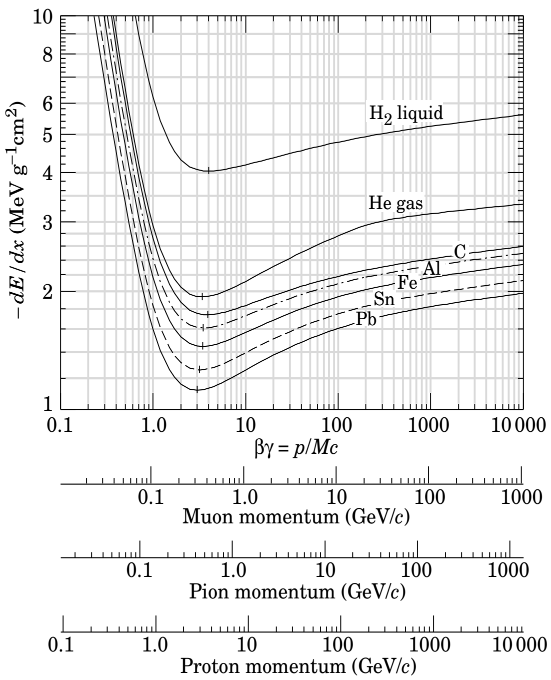

Figure 3.1: Energy loss rate as a function of $\beta\gamma$ in different materials. This figure is obtained from Ref. [4].

- The amount of energy lost per interaction.

Below, the most important issues determining these quantities will be outlined, starting with a few basic definitions.

3.2.1 Introductory remarks

The nuclear interaction length λ_I of a particle traveling through matter is determined by the total nuclear scattering cross section σ_{total}, as [54]

$$\lambda_I = \frac{A}{N_A \rho \sigma_{total}}, \tag{3.2}$$

where A, N_A and ρ are the atomic number of the material, the number of Avogadro, and the density of the material. The interaction length defines the probability $P(x)$ for a particle to not have undergone a nuclear interaction after traveling a distance x:

$$P(x) = e^{-\frac{x}{\lambda_I}} = e^{-N}. \tag{3.3}$$

Thus, the parameter N represents the number of interaction lengths which the particle travels before interacting at distance x. The total cross section σ_{tot} for hadron nucleon scattering is a sum of two contributions:

$$\sigma_{\text{tot}} = \sigma_{\text{elas}} + \sigma_{\text{inelas}}, \tag{3.4}$$

where σ_{elas} is the cross section due to elastic processes and σ_{inelas} is the cross section due to inelastic processes. An elastic interaction is an interaction in which the initial and final states consists of the same two particles:

$$a + b \to a + b. \tag{3.5}$$

An inelastic interaction is any process in which this is not the case:

$$a + b \rightarrow c + d + ... \tag{3.6}$$

Whether elastic or inelastic processes take place depends on:

- The identity of initial and final state particles. This will extensively be discussed in the current chapter, as well as in Chapter 4.
- The available phase space. We return to this issue in detail in Chapter 4, particularly in Section 4.3.7.
- The center-of-mass energy of the scattering. In the following Section, the dependence on the center-of-mass energy, or equivalently the dependence on the momenta of the initial particles will be outlined.

3.2.2 Energy dependence in nuclear scattering

Nuclear scattering can be described with partial wave analysis [55]. An initial particle with momentum k traveling in the z-direction is described by the plane-wave solution of the Schrödinger equation

$$\psi = e^{ikz}. \tag{3.7}$$

After scattering, the wave associated to this particle is a sum of the original wave and the scattered wave:

$$\psi = \psi_{original} + \psi_{scat} = e^{ikz} + e^{ikr}\frac{f(\theta)}{r}, \tag{3.8}$$

where r is the new propagation direction, θ is the scattering angle and the function $f(\theta)$ is the scattering amplitude. The incoming plane wave e^{ikz} can be decomposed into eigenfunctions of the orbital angular momentum number l of a particle with angular momentum $\hbar l$ [55]:

$$e^{ikz} = \sum_{l=0}^{\infty}(i^l)(2l+1)P_l(\cos\theta)j_l(kr), \tag{3.9}$$

where P_l is the lth Legendre polynomial and j_l is the solution to the radial wave equation. At low momenta, the functions j_l are only of significant magnitude at low l-values, while at higher momenta the higher angular momenta start being important. That only small l values can contribute at low energy can also be understood by considering a classical example of a particle with momentum p, scattering on a black disk of radius a, with impact parameter (classical distance of closest approach) b. The angular momentum is then given by

$$|\mathbf{r} \times \mathbf{p}| = bp \simeq l\hbar \qquad \Rightarrow \qquad l \simeq b(p/\hbar) = b2\pi/\lambda, \tag{3.10}$$

where λ is the wavelength associated to the particle. An interaction can take place if the radius a of the black disk, representing the range of the forces exchanged between the stationary and incoming particle, exceeds the impact parameter b, i.e. if

$$l \lesssim a2\pi/\lambda. \tag{3.11}$$

Therefore, for low momenta, corresponding to large values of λ, only $l = 0$ waves can contribute: s-wave scattering. At slightly higher momenta, $l = 1$ waves may dominate: p-wave scattering, and so on.

3.2.3 Low energy scattering

Low energy scattering is characterized by several features [55]. As just mentioned, only partial waves with small values of angular momentum l contribute. Scattering processes at low energy are mainly t and s channel $2 \to 2$ processes. Low energy scattering processes in the t-channel are mediated by the exchange of a quark-anti-quark pair, called a Reggeon. The energy dependence of the Reggeon region is approximately $\sigma \propto 1/\sqrt{s}$ [56]. The s-channel processes are characterized by the formation of nuclear resonances, manifesting themselves as peaks in the cross section. Resonances are short-lived intermediate states. In case scattering takes place only via resonances, the scattering cross section σ near the resonance energy E_0 is well described by the Breit-Wigner shape:

$$\sigma \propto \frac{1}{(E - E_o)^2 + \Gamma^2/4}, \tag{3.12}$$

where Γ is the decay rate of the resonance. In general, the low energy behaviour of scattering processes is very irregular and poorly understood, with many resonances overlapping and interfering.

3.2.4 High energy scattering

The high energy cross section behaviour is totally different from that at low energy. Concerning partial waves of the scattered particle, many values of the angular momentum l can contribute. Scattering processes at high energy are $2 \to N$ processes, in which $N \geq 2$. The magnitude of the total cross section at high energies shows little variety: it is relatively stable, rising slowly for higher momenta. The main contribution (80-90%) to the total cross section comes from a number of inelastic processes with multiparticle production. Most of these particles are pions (70-90%), and to a smaller extent protons, neutrons and strange particles. Elastic scattering plays a less prominent role, and is dominated at high momenta by small t-exchange, $|t| \lesssim 0.5$ GeV. It is believed that high energy hadron-nucleon scattering processes are mediated by colorless two-gluon states called Pomerons. The energy dependence of the total cross section at high energy is approximately given by $\sigma \propto s^{0.08}$ [56].

3.2.5 The energy loss per interaction

The energy lost by a particle scattering off a nucleon at rest depends on several factors. Firstly, energy is lost to produce the kinetic energy of the kicked-out nucleon. This amount depends on the energy and masses of the initial and final particles, and is determined by kinematics. Secondly, energy is lost in the production of extra final state particles. An estimate about this number can be made by calculating the energy Q available for kinetic energy, or potentially the production of extra particles. In the case of a $2 \to N$ scattering, where an incoming particle with mass m_1 scatters on a particle at rest with mass m_2, we define the Q-value by

$$Q = \sqrt{s} - m_3 - m_4 - ... - m_{N+2}, \tag{3.13}$$

where m_i is the mass of final–state particle i. If the Q-value does not exceed the mass of a pion, no extra particle can be produced, while if the Q-value is large, a large number of extra final state particles can be produced. Third, energy is dissipated to internal degrees of freedom in the remnant nucleus containing the nucleon.

3.2.6 The nuclear cascade

The incoming particle interacts with a nucleon inside a nucleus. Thus, effects like the Fermi motion of the nucleons inside the nucleus, binding energy of the nucleus, evaporation energy of a nucleus, and instability of the nucleus after the interaction play an important role [57]. Whether the interaction is mainly with a free nucleon or with the nucleus as whole, depends on the energy of the incident hadron [57]. To estimate this, the wavelength associated with the incident hadron can be compared with the size of the nucleus. For a particle of energy E, the associated wavelength λ is given by the well-known formula

$$\lambda = \frac{hc}{E}. \tag{3.14}$$

For example, a pion of momentum 300 MeV has a wavelength associated with it of ca 4 fm, which is of the order of the size of a nucleus, while a pion of 100 GeV has a wavelength of ca 0.01 fm, much smaller than the size of a nucleus.

The development of a nuclear cascade is as follows. First, the particles arising from the primary scattering process, i.e. scattering on a single nucleon, are produced. These then interact with a nucleon inside the nucleus, hereby producing several new hadrons, each of which will interact with a downstream nucleon inside the nucleus, etc. The extra particles produced during this cascade process are called *grey track* particles. A cascade develops in a timescale of the order of the strong interaction scale 1×10^{-24} s. A very high energetic particle will therefore already have left the nucleus before a real cascade can develop, and the resulting number of grey track particles is small. A slow particle however, with a wavelength comparable with that of the size of the nucleus, may result in large number of grey track particles, i.e. a violent cascade. After the interaction, the nucleus remains in a highly excited state. Depending on the character of the cascade, the nucleus may totally fragment into protons, neutrons and small nuclei: nuclear evaporation. The fragments arising in the latter process are usually referred to as *black track particles*. The kinetic energies of such fragments are very low ($\leq$ 20 MeV) and their angular distributions are isotropic in the laboratory system[1]. The number of black track particles is found to be proportional to the number of grey track particles [57]. Thus, a particle with wavelength of the order of magnitude of the size of the nucleus often causes nuclear evaporation, while a highly energetic particle often leaves the nucleus nearly intact.

3.3 Pion-nucleon scattering

3.3.1 Low momentum behaviour

In Fig. 3.2 cross section data for pion-nucleon scattering are shown as a function of the laboratory momentum of the incoming pion, scattering on a nucleon at rest. At low pion momenta ($p < 1$ GeV/c), the pion-nucleon cross section shows a very irregular behaviour. Three observations should be made:

- The presence of nuclear resonances. In π^+p$-$scattering, the peak of the highest resonance is seen to be located at approximately 1.2 GeV, corresponding to the Δ^{++} state. The way in which this resonance arises is displayed in Fig. 3.3(c). In π^-p$-$scattering, the resonances which are clearly visible are the Δ^0-resonance with a mass of 1.2 GeV/c^2, and the N-resonances with masses of 1.5 and 1.7 GeV/c^2.

[1]The terms *grey* and *black* derive from emulsion experiments: black track particles are very slow and heavily ionizing, leaving a clear black track, while grey track particles are faster and thus less ionizing.

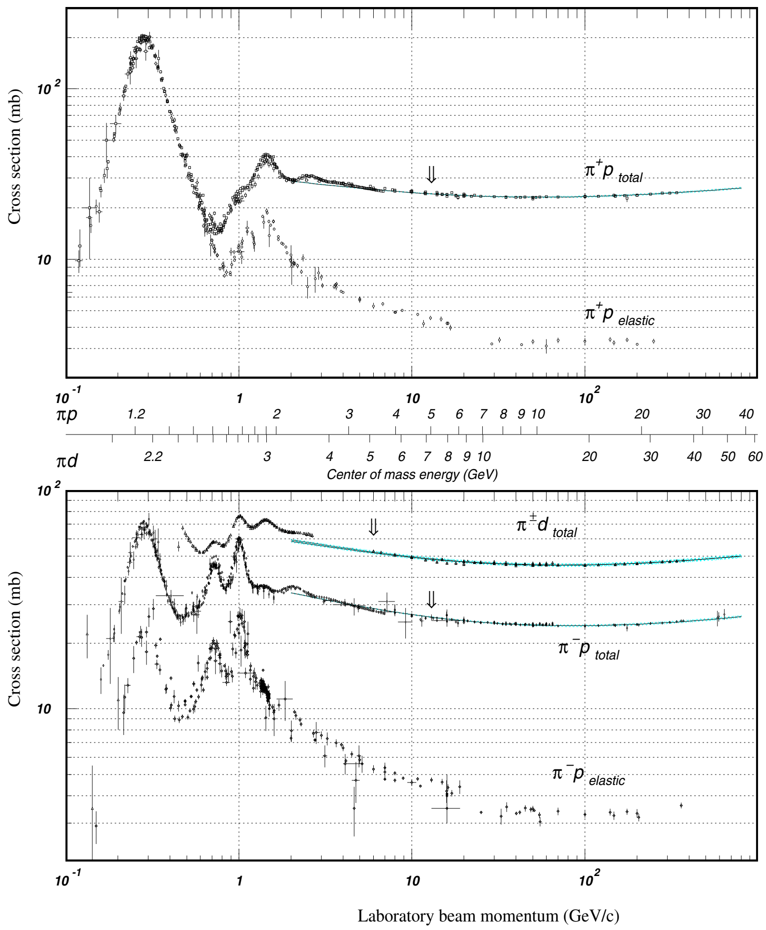

Figure 3.2: Total and elastic cross section for $\pi^{\pm}$p (top) and $\pi^{\pm}$n (bottom) scattering as a function of the laboratory momentum and total center-of-mass energy. The arrows represent the lower limits on p_{lab} and $\sqrt{s}$ used in the fit (solid line) of high energy cross section data. This figure is obtained from Ref. [4].

- The relative occurrence of elastic and inelastic processes. Elastic processes are dominating at low energy. An example of a Reggeon mediated elastic process is shown in Fig. 3.3(b). It must be noted that in π^+p−scattering the inelastic processes are absent at low energies, while in π^-p−scattering the cross section is significant. This can simply be explained by the fact that no charge exchange processes are possible in the former case, while in the latter case they are. It is interesting to note that the observed lower limit for the production of an extra pion occurs at $\sqrt{s}$ ≈1.5 GeV, corresponding to a Q-value of 1.5-0.93-0.13=0.4 GeV, much larger than the mass of a pion!

- The vanishing behaviour of the cross section at very small $\sqrt{s}$. In principle, the cross section for every scattering vanishes at $\sqrt{s} \to 0$ due to the fact that phase space decreases. However, in the case of pion-nucleon scattering, the cross section becomes zero faster than phase space vanishes. As explained in Section 3.2.3, the only partial waves which can contribute to the scattering process are here $l = 0$ waves. Thus, the intermediate Reggeon must be a scalar particle, like a π (pseudoscalar) or an other scalar field. A $\pi\pi\pi$ vertex is forbidden by G-parity [55, 58]. A $\pi\pi\rho$ vertex is allowed but ρ being a spin-1 particle, the coupling is proportional to the momentum $\mathbf{p}$ and thus vanishing in the limit $\mathbf{p} \to 0$. The only possibility for a coupling not vanishing in the limit $\mathbf{p} \to 0$ is a $\pi\pi$-scalar vertex, however, such a vertex is forbidden by chiral symmetries [59]. The vanishing of the cross section at low momentum is not a generic property of low energy nuclear scattering processes. On the contrary, it is unique for pion-proton scattering.

3.3.2 High momentum behaviour

At high momentum ($p > 1$ GeV/c), the behaviour of the cross section is relatively stable, rising slowly for higher momenta, as can be seen from Fig. 3.2. At high momentum, the cross section for elastic scattering is ca 15% of the total cross section, while the inelastic processes contribute ca 85%. Fig. 3.3(a) shows a Pomeron mediated pion-proton scattering. In this example, the Pomeron has six different exchange possibilities between the different partons. For proton-proton scattering, there would be nine possibilities, explaining the fact that the proton-proton scattering cross section at high momenta is approximately one and a half times larger than the pion-proton cross section [56, 60]. This rule is called the additive quark rule.

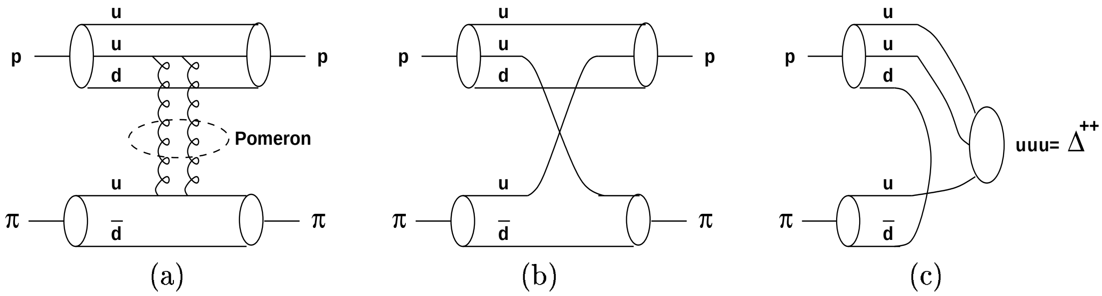

Figure 3.3: Proton scattering for pions and R-hadrons. (a) Pomeron mediated elastic pion-proton scattering(a), (b) Reggeon mediated elastic scattering, (c) the arise of a nuclear resonance.

Chapter 4

Interactions of heavy hadrons in matter

In the previous chapter, electromagnetic and nuclear interactions of ordinary hadrons have been discussed. This chapter focuses on interactions of heavy hadrons. First, the main differences compared to light hadrons will be stressed in Section 4.1. Electromagnetic interactions of charged heavy hadrons will be discussed in Section 4.2. In Section 4.3, the experience with nuclear interactions of light hadrons, obtained in the previous chapter, will be used to propose a model for nuclear interactions of hadrons containing any new color triplet or octet stable parton. While being completely independent of the model in which the heavy hadron arises, we will consider the role of the heavy object, hadron mass spectra and nuclear scattering cross sections. In Section 4.3.8 specific interaction processes will be discussed. The chapter finishes with a summary of the model. This model has been published in Ref. [62].

4.1 Differences with light hadrons

The main difference between light and heavy hadrons is their production velocities. In e^+e^- annihilations, where the full center-of-mass energy is available in particle production, the momentum of a heavy colored state like a squark is limited mainly by the center-of-mass energy. In the process $e^+e^- \rightarrow \tilde{q}\bar{\tilde{q}}$, the sum of the energy of the squarks equals the center-of-mass energy, neglecting ISR and FSR. Thus, whether the hadron is relativistic or not depends for this process only on its own mass. At a hadron collider like the LHC, only a small fraction of the total center-of-mass energy is used for the production of new particles. In a process like $pp \rightarrow \tilde{q}\bar{\tilde{q}}$, the energies of heavy hadrons are typically about two to three times their own mass. The reason why the momenta are not higher is that the probability to find a parton with certain momentum in the proton (the structure functions) is falling rapidly with the parton momentum. In general, this means that the hadrons which will be investigated in this thesis may be relativistic, but not ultra-relativistic, and that their mass is far from negligible. Typical distributions for production momenta and velocities at generator level are given in Appendix C.

4.2 Electromagnetic interactions of heavy charged hadrons

A charged heavy particle suffers continuous ionization losses and repeated Coulomb scatterings [4]. Continuous ionization losses are proportional to $1/\beta^2$, since the ultra-relativistic rise is not relevant here, as can be seen from Fig. 3.1. For Coulomb scatterings, the deflection angle, given in

Eq. (3.1), is small, the small velocity being compensated for by the relatively large momentum.

4.3 Nuclear interactions of heavy hadrons

Both charged and neutral heavy hadrons lose energy through scattering off nuclei. In the following, a simple and general framework is presented for simulating nuclear interactions of heavy hadrons, independent of the new physics model in which the hadron arises. Exotic color triplet states will be denoted by C_3, color antitriplet states by $C_{\bar{3}}$ and color octet states by C_8. When referring to the mass of a parton, we always mean the constituent mass. For simplicity, we take into account only states containing u and d quarks, with constituent masses assumed to be $m_{\mathrm{q}} = 0.3$ GeV.

4.3.1 The role of the heavy object

Any stable heavy colored exotic particle hadronizes and forms a color singlet, for example $C_3\bar{q}$, C_3qq, $C_{\bar{3}}q$, $C_8q\bar{q}$, C_8qqq, C_8g. In Appendix A.2 is shown why precisely these combinations are possible, and no combinations like e.g. $C_3\bar{q}q$, C_8q, etc. The probability that the parton C_i of color state i will interact perturbatively with the quarks in the target nucleon is small, since such interactions are suppressed by the squared inverse mass of the parton. As a consequence, the heavy hadron can be seen as consisting of an essentially non-interacting heavy state C_i, accompanied by a colored hadronic cloud of light constituents, responsible for the interaction. The effective interaction energy of the hadron is therefore small, as can be seen by considering a $C_8q\bar{q}$ state, e.g. with a total energy E=450 GeV and a mass m of the C_8 parton of 300 GeV, i.e. with a Lorentz factor of γ=1.5. Although the kinetic energy of the hadron is 150 GeV, the kinetic energy of the interacting $q\bar{q}$ system is only $(\gamma - 1)m_{q\bar{q}} \approx 0.3$ GeV, (if the quark system consists of up and down quarks). Thus, the energy scales relevant for heavy hadron scattering processes off nucleons are low! It is therefore most likely that interaction processes are mediated by Reggeons (Fig. 4.1a) and not by Pomerons (Fig. 4.1b). In conclusion, it becomes apparent that the presence of the heavy parton C_i has two basic consequences:

- It acts as a reservoir of kinetic energy. After an interaction, where the light interacting system loses kinetic energy, new kinetic energy is transferred to it from the co-moving C_i-parton.
- The parton C_i forces the quark system to be in a certain color-state, in order for the system as a whole to form a color-singlet state. This influences the mass spectrum of the hadrons, as will be explored in detail in Section 4.3.2.

The following issues are not influenced by the presence of the heavy parton:

- The interactions of the light constituents are of the same character as for an ordinary hadron. As stressed in the beginning of this section, the heavy state C_i acts merely as a spectator in an interaction.
- The overall size of the hadron as a whole is probably not strongly influenced. This can be understood by recalling that the wave-function associated with a particle with mass M roughly scales as $1/M^2$. The influence of the heavy object C_i on the size of the total hadron is therefore minimal, and the light quarks dominate completely.

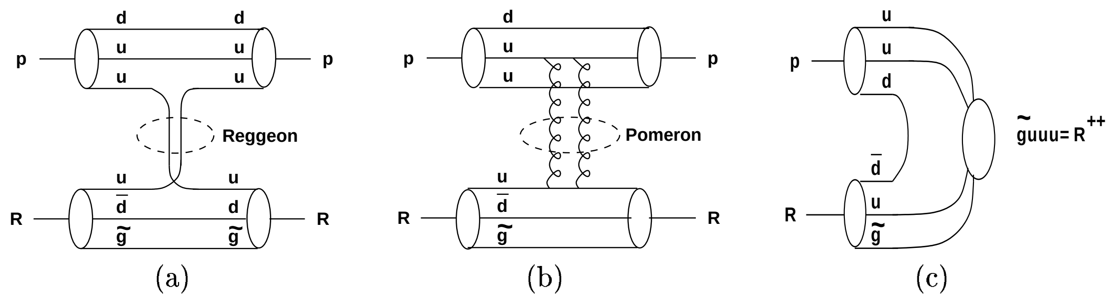

Figure 4.1: R–hadron scattering of a proton. (a) Reggeon mediated elastic scattering, (b) Pomeron mediated elastic scattering, (c) the formation of a nuclear resonance

4.3.2 Hadron mass spectrum

In order to establish the signatures of heavy hadrons in a detector, it is important to know the lowest lying mass states. For example, if the C_8uuu state were the lightest baryonic state, then decays into it would be kinematically favorable. This would be important, since the electromagnetic energy losses would then be increased significantly (if the C_8 parton does not carry negative charge). A completely different signature would result if a neutral C_8udd state would be the lightest.

The mass of the lowest-lying hadronic states, with no radial excitation or orbital angular momentum, can be approximated by [61, 63]

$$m_{\text{hadron}} = \sum_i m_i - k \sum_{i \neq j} \frac{(\mathbf{F_i} \cdot \mathbf{F_j})(\mathbf{S_i} \cdot \mathbf{S_j})}{m_i m_j}, \tag{4.1}$$

in which the summation is over all partons i contained in the hadron, m_i is the parton constituent mass, $\mathbf{F}_i$ is the $SU(3)$ color matrix for parton i, $\mathbf{S}_i$ is the $SU(2)$ spin matrix for parton i, and k is a constant with dimension $(\text{mass})^3$. The second term, responsible for the mass splitting, depends on the color-state and spin-state of the hadron. In this equation, we have implicitly assumed operation on eigenstates with definite $SU(3)$ of color and $SU(2)$ of spin properties. In the derivation of the hadron mass spectrum of heavy hadrons, terms involving the heavy parton in the denominator can be neglected. Expressions for $(\mathbf{F}_1 \cdot \mathbf{F}_2)$ and for $(\mathbf{S}_1 \cdot \mathbf{S}_2)$ can easily be derived for a qq and q$\bar{\text{q}}$ state, see Appendix A.1 and A.2. A qq state can either form a color antitriplet or a sextet configuration ($\mathbf{3} \otimes \mathbf{3} = \bar{\mathbf{3}} \oplus \mathbf{6}$), while a q$\bar{\text{q}}$ state can form a color singlet or an octet state ($\mathbf{3} \otimes \bar{\mathbf{3}} = \mathbf{1} \oplus \mathbf{8}$). With the help of Appendix A.2, the eigenvalues of the operator $(\mathbf{F}_1 \cdot \mathbf{F}_2)$ can be evaluated to be $-4/3$, $-2/3$, $1/3$ and $1/6$ when the quark-pair is in a color singlet, antitriplet, sextet and octet configuration, respectively. The eigenvalues of $(\mathbf{S}_1 \cdot \mathbf{S}_2)$ are $-3/4$ and $+1/4$ for a qq or q$\bar{\text{q}}$ state with total spin zero and spin one, respectively, see Appendix A.1. Eq. (4.1) leads to the familiar mass patterns of the known hadrons. For example, the $\pi - \rho$, $K - K^*$, $D - D^*$ and $B - B^*$ systems follow Eq. (4.1) reasonably well, with $k \approx 0.043$ GeV^3. The mass spectra of heavy meson and baryon states are discussed below, using Eq. (4.1). Only systems with u and d quarks are considered, and a universal constituent mass of 0.3 GeV/c^2 is assumed. With more refined methods, it would be possible to calculate the spectrum of all possible heavy mesons and baryons precisely. Here, we are mainly interested in the order of magnitude of the mass splittings and not in fine details.

Meson mass spectrum Possible heavy mesons are $C_{\bar{3}}$q, $C_3\bar{\text{q}}$ and C_8q$\bar{\text{q}}$ states. For $C_{\bar{3}}$q and $C_3\bar{\text{q}}$ states, no significant mass splitting is expected to occur, since the second term of Eq. (4.1) is negligible (certainly significantly smaller than that of the $B - B^*$ system, which is only 46 MeV).

For a $C_8 q\bar{q}$ state, the mass spectrum, in units of GeV/c^2, is given by:

$$\begin{aligned}
M_{C_8 q\bar{q}} &\approx M_{C_8} + 0.3 + 0.3 - 0.043 \times \frac{(\frac{1}{6} \times -\frac{3}{4})}{0.3 \times 0.3} && s_{q\bar{q}}=0 \\
&\approx M_{C_8} + 0.66 \\
M_{C_8 q\bar{q}} &\approx M_{C_8} + 0.3 + 0.3 - 0.043 \times \frac{(\frac{1}{6} \times +\frac{1}{4})}{0.3 \times 0.3} && s_{q\bar{q}}=1 \\
&\approx M_{C_8} + 0.58
\end{aligned}$$

There are two noticeable aspects. First, the mass hierarchy is reversed, as compared to that of the $\pi - \rho$ mass splitting: the spin-0 state is the heaviest. Second, the mass splitting between different spin states is much smaller than the $\pi - \rho$ splitting. Consequently, mass splittings for heavy mesons may safely be neglected.

Baryon mass spectrum Possible heavy baryons are C_3qq and $C_{\bar{3}}\bar{q}\bar{q}$, C_8qqq and $C_8\bar{q}\bar{q}\bar{q}$ states. The mass spectra are obtained by a similar calculation as for the mesonic case, with $k \approx 0.026$ GeV^3, as derived from the ordinary baryon sector. For C_3qq states (and, by symmetry for the $C_{\bar{3}}\bar{q}\bar{q}$ baryons) we obtain the mass spectrum

$$\begin{aligned}
M_{C_3 qq} &\approx M_{C_3} + 0.3 + 0.3 - 0.026 \times \frac{(-\frac{2}{3} \times -\frac{3}{4})}{0.3 \times 0.3} && s_{qq}=0 \\
&\approx M_{C_3} + 0.46 \\
M_{C_3 qq} &\approx M_{C_3} + 0.3 + 0.3 - 0.026 \times \frac{(-\frac{2}{3} \times +\frac{1}{4})}{0.3 \times 0.3} && s_{qq}=1 \\
&\approx M_{C_3} + 0.65
\end{aligned}$$

At this stage we must recall that the total wavefunction associated with a quark system can be decomposed in $flavor \times spin \times color$ [61]. For the case where the two quarks in the C_3qq state are identical, it is certain that they must have a total anti-symmetric wavefunction (fermions). Taking into account that the color wavefunction, associated with the two quarks, is antisymmetric (they are in an antitriplet configuration), it is seen that the two quarks in a C_3uu or C_3dd state can only be in a symmetric spin-configuration, i.e. $s_{qq} = 1$, the heavier state. Two non-identical quarks would have possibilities to be in both mass states. This implies that it will kinematically be favourable for the other baryons to decay into the lighter C_3ud state with $s_{qq} = 0$ rather than in the heavier C_3uu, C_3ud or C_3dd states with $s_{qq} = 1$.

Deriving the mass spectrum of C_8qqq is considerably more complicated. At this point, the reader is encouraged to read Appendix A.3, in order to understand the following line of arguments why the mass splitting is expected to be small.

Recall that the total wavefunction associated with the three quarks in a C_8qqq state must be anti-symmetric. For the C_8uuu or C_8ddd states, the three quarks are in a symmetric flavor configuration, and thus the $spin \times color$ wavefunction should be anti-symmetric. The three quarks being in a color octet configuration implies that s_{qqq}=1/2, as is easily seen by using Table A.2 in Appendix A.3. Thus, the qq states involved in Eq. (4.1) have spin $s_{qq} = 1$ or $s_{qq} = 0$ and the associated wavefunctions are mixed symmetric and anti-symmetric. The color configuration of the qq states is also mixed: either color antitriplet or sextet, see Appendix A.2.

For the C_8uud and C_8udd states, the situation is slightly different. The wavefunction associated with flavor can either be totally symmetric, or mixed symmetric and anti-symmetric. In the former case, the situation is exactly the same as for the C_8uuu and C_8ddd states. In the latter case, the *spin* × *color* wavefunction associated to the three quarks must also be mixed, the three quarks being in a color-octet configuration. Using Table A.2 in Appendix A.3, and recalling that the three quarks are in a color-octet configuration, it is seen that such mixed states can be obtained with $s_{\rm qqq}$=1/2 or $s_{\rm qqq} = 3/2$. The spin doublet case, $s_{\rm qqq}$=1/2, implies a mixed color configuration and a mixed spin configuration for the three quarks together. For the quark pairs involved in Eq. (4.1), this means that they have a mixed $s_{\rm qq} = 1$ or $s_{\rm qq} = 0$ configuration, and a mixed color antitriplet and sextet configuration. On the other hand, the spin quartet case, $s_{\rm qqq} = 3/2$, implies a mixed color configuration and a symmetric spin configuration for the three quarks. For the quark pairs involved in Eq. (4.1), this means that they have a symmetric $s_{\rm qq} = 1$ spin configuration, and again their color configuration is a mixture of color antitriplet and sextet.

Summarizing, C_8uuu or C_8ddd states only arise if $s_{\rm qqq}$=1/2, while C_8uud and C_8udd states arise if $s_{\rm qqq}$=1/2 or 3/2. (Note that this is the opposite for ordinary baryons!) We saw above that both in the $s_{\rm qqq} = 1/2$ case and in the $s_{\rm qqq} = 3/2$ case, the wavefunctions of the qq combinations involved in Eq. (4.1) are always strongly mixed: the color wavefunction is mixed, and either the spin, or the flavor wavefunctions, or both, are mixed for the qq combinations. The color antitriplet and sextet contributions enter with opposite sign, as do the $s_{\rm qq} = 1$ and $s_{\rm qq} = 0$ terms. Without having done the exact calculation, it is therefore certain that this feature will result in a partial cancellation of the mass splitting expression. Thus, the splitting is not expected to be more than the order of a hundred MeV. Exactly the same applies for $C_8\bar{\rm q}\bar{\rm q}\bar{\rm q}$ states. In conclusion, the mass splittings between the different C_8qqq and $C_8\bar{\rm q}\bar{\rm q}\bar{\rm q}$ spin states are not expected to be large and may therefore be neglected to first approximation. The mass of the C_8qqq states is thus approximately

$$M_{\rm C_8qqq} = M_{\rm C_8} + 0.9. \tag{4.2}$$

Gluon-hadron spectrum Using Eq. (4.1), the mass of a C_8g state is easily seen to be

$$M_{\rm C_8g} \approx M_{\rm C_8} + m_{\rm g}. \tag{4.3}$$

The constituent mass of a gluon is approximately 700 MeV [64]. Thus, C_8g states are expected to have a slightly higher mass than $C_8{\rm q}\bar{\rm q}$ states.

Side remark After the completion and publication of the above calculations [62], the explosion of interest in long-lived gluinos as a result of Refs. [12, 13] have made some old mass calculations resurface [65, 66, 67]. Ref. [65] calculates mass spectra of $\bar{\rm q}{\rm q}\tilde{\rm g}$, $\tilde{\rm g}$g and $\tilde{\rm g}\tilde{\rm g}$ states in the so-called bag-model [68], approximating quarks to move in a 'bag', corresponding to the hadron. Ref. [65] calculates gluino meson bound state spectra for gluino masses below 20 GeV. Although the results differ slightly quantitatively, they are qualitatively the same as those obtained above, i.e. the mass of the $\tilde{\rm g}{\rm q}\bar{\rm q}$ -state with the ${\rm q}\bar{\rm q}$ in a spin-1 configuration is lighter than that of the spin-0 state, and the mass of the $\tilde{\rm g}$g -state is slightly larger than that of the lightest $\tilde{\rm g}{\rm q}\bar{\rm q}$ -state. In Ref. [66], R-baryon masses have been calculated again in the framework of the bag-model. The mass splitting of the baryons is found to be slightly larger than 100 MeV, but no definite prediction is made about whether a neutral or charged baryon is the lightest. Besides, the masses of the baryons are such that a process with baryon exchange is kinematically favoured, as was also concluded above. Ref. [67] calculates R-meson mass spectra with lattice calculations. Again, results are similar to the above: a lighter $\tilde{\rm g}{\rm q}\bar{\rm q}$ -state when the ${\rm q}\bar{\rm q}$ is in a spin-1 configuration than when it is in a spin-0 configuration. The mass of the $\tilde{\rm g}$g -state comes out to be very close to that of the R-mesons. In conclusion, the above results support earlier calculations.

4.3.3 Resonances

The formation of resonances is closely connected with the discussion above. In the presence of a color state C_i, new resonances may arise, as illustrated in Fig. 4.1c where $C_i = C_8$ is a gluino. There is no guidance from theory about the detailed mechanism of resonance formation in heavy hadrons, but a few remarks can be made. Concentrating on C_8 hadrons, if indeed mass splittings between the different hadrons are not larger than the order of a hundred MeV, resonances will not play a significant role. The minimum center-of-mass energy for a scattering of for example a $C_8q\bar{q}$ state with a nucleon with mass m_n is $m_{C_8q\bar{q}} + m_n \approx m_{C_8} + 5m_d \approx m_{C_8} + 1.5$ GeV, an energy which is above the masses of the most significant resonances. Thus, even if resonances exist, they are not likely to play an important role, but they would be smoothly merged with the continuum, as for $\pi - p$ scattering above the Δ resonance region. Because of this, and lacking a detailed description of these resonances, we will not take them into account explicitly.

4.3.4 Black disk approximation

Predicting the total cross section of a heavy hadron scattering off a nucleon is non-trivial, having no definite theory guidance. Here, a series of arguments will be presented, that will be used as guidelines in constructing an effective model. At high center-of-mass energies, cross sections may be approximated by the geometrical cross section. At low energy, the cross section is hard to estimate; in fact, even for normal hadrons, low energy scattering cross sections are poorly understood. A vanishing cross section at low energy, as exhibited by pion-nucleon scattering, is not probable. The reason why this cross section vanishes is that s-wave scattering is forbidden, a unique feature for pion-nucleon scattering [59]. In a $C_8q\bar{q}$ hadron, even though containing u and d quarks, the quark system is in a color-octet state, and is thus no ordinary pion. In particular, a color octet pion is not light, as shown in the previous section, and can consequently not be treated as a Goldstone boson; hence s-wave scattering by (pseudo) scalar exchange should be possible. On the other hand, a rise in the cross section in for example the nuclear scattering of a C_8qqq state at low energies, as is the case for proton-neutron scattering, is likewise also improbable. The reason why this cross section is so large is again unique and is connected with the existence of the deuteron [59]. Expecting neither a rise, nor a vanishing behaviour, the pragmatic solution is to treat a heavy hadron simply as a 'black disk', and to use a fully absorbing geometrical cross section at all scattering center-of-mass energies.

4.3.5 The size of the total cross sections

The size of the heavy hadron being roughly the same as the size of the accompanying hadron system, the total cross section for nucleon scattering can be approximated by the asymptotic values for the cross sections for normal hadrons scattering off nucleons. For example, in the case of a $C_8q\bar{q}$ state, in which the $q\bar{q}$ system contains only u and d quarks, one can use the asymptotic value of the total cross section for pion-nucleon scattering, while in case one s quark is present, one can use asymptotic values for kaon-nucleon scattering, etc. A simple rule would be 12 mbarn for every u or d quark, and 6 mbarn for every s quark scattering off a nucleus. Cross sections for any C_i–hadron can then be calculated. The present study takes into account only u and d quarks. Although it is known that a significant amount of s quarks should in principle be present in the gluino R–hadrons (ca 15%), only a small error on the cross section is made, the difference only being 6 mbarn. The amount of hadrons with two s quarks or heavier is negligible.

Restricting the discussion to a gluino R–meson and R–baryon, the total cross sections are 24 mbarn and $3/2 \times 24$=36 mbarn, respectively. A gluino-gluon state can be assumed to have

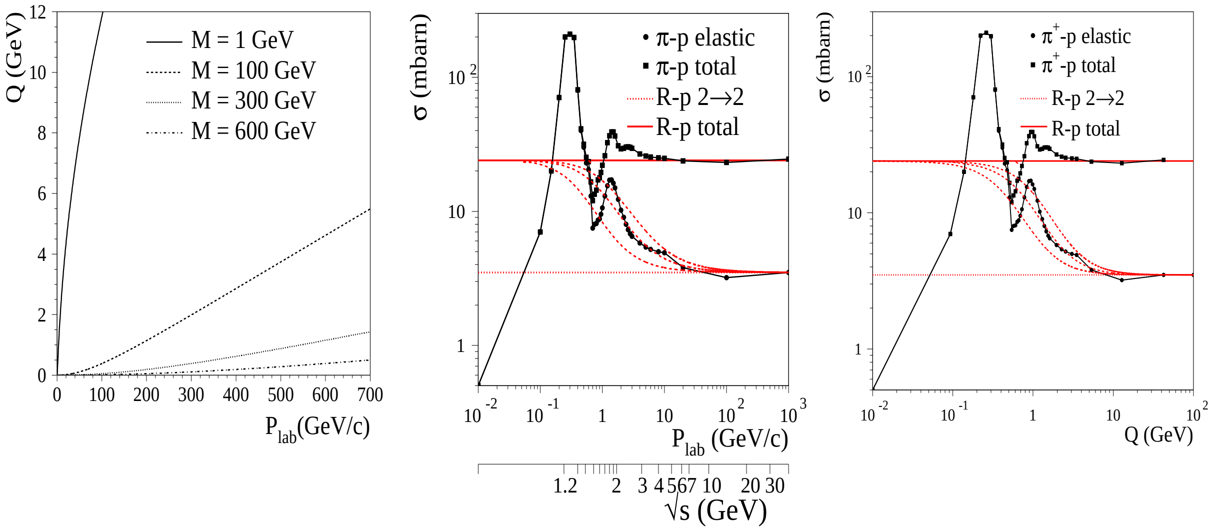

(a) (b) (c)

Figure 4.2: (a) The value of $Q = \sqrt{s} - m_{\mathrm{n}} - m_{\mathrm{R}}$, for hadrons with mass M scattering with laboratory momentum P_{lab} on a nucleon at rest. (b) The value of the cross section for gluino R–meson-proton scattering (horizontal lines) in comparison with π^+-proton scattering, as well as the determination of Q_0 and its uncertainty (curved dashed lines connecting the horizontal lines). (c) The same, but as a function of Q.

the same cross section as a gluino R–meson, since the geometrical cross section is approximated by the high energy hadron cross section, where gluon exchange would dominate. The gluon-gluon coupling is a factor 9/4 larger than the quark-gluon coupling, but a meson has two quarks, resulting in a cross section of a gluino-gluon state which is (9/4)/(1+1)≈1 times the cross section for a gluino R–meson.

4.3.6 The size of the partial cross sections

Besides the total cross section, which determines the interaction length, the partial cross sections for $2 \to 2$ and $2 \to 3$ processes must be known in order to estimate the energy loss per nuclear interaction. An estimate of the number of final–state particles can be made by studying the energy Q available for the production of kinetic energy and potentially extra particles, for which the expression was given in Eq. (3.13). The value of s is $m_1^2 + m_2^2 + 2E_1^{lab} m_2$, where E_1^{lab} is the energy of the incoming particle. If the Q-value exceeds the mass of a pion, then an extra pion may be produced. To determine the relevant order of magnitude of Q in the scattering of heavy objects, consider an elastic scattering of a heavy particle with mass m_1, moving with a Lorentz factor γ, off a light particle at rest with mass m_2. It is easily seen, e.g. by considering the system in the m_1 rest frame, that $\sqrt{s} \approx m_1 + \gamma m_2$ and $Q \approx (\gamma - 1)m_2$, the latter being obviously small if the incoming heavy particle has a small value of γ. Fig. 4.2(a) displays the Q-value of a process $\mathrm{R} + \mathrm{n} \to \mathrm{R} + \mathrm{n}$, in which a heavy gluino hadron R with mass M scatters off a nucleon n with mass m_{n} at rest. This shows that for heavy hadrons, the Q-value is much smaller in comparison with light hadrons of the same momentum, implying that the number of final–state particles is also much smaller. For the range of momenta of particles produced at a collider like LHC, the Q values are so small that the final–state multiplicity is rarely expected to

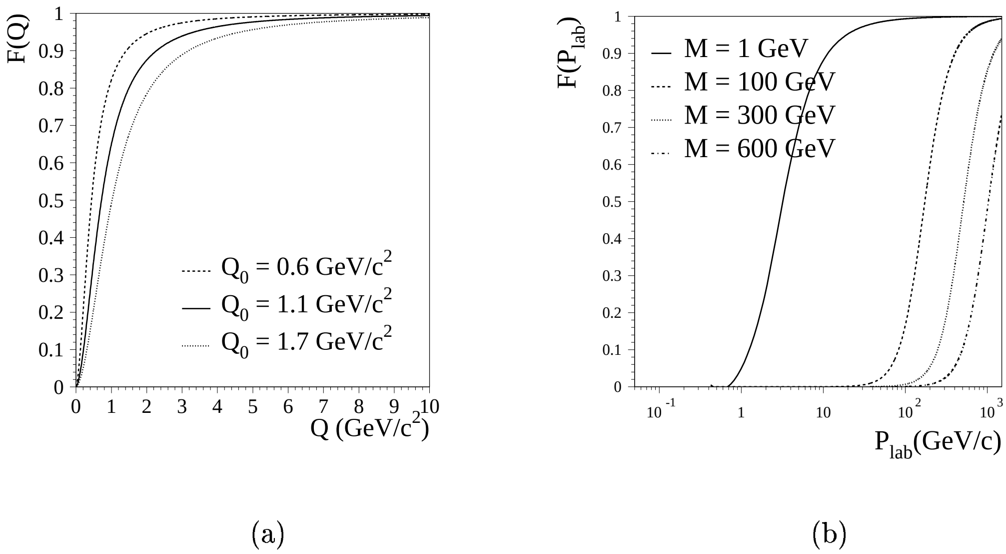

Figure 4.3: (a) The phase space function $F(Q)$ drawn for a few values of Q_0 and (b) as a function of the laboratory momentum P_{lab} of a heavy hadron with mass M scattering off a nucleon at rest, and with $Q_0 = 1.1$ GeV.

exceed three. Even though the Q-values may exceed the pion mass, observation of for example pion–proton scattering shows that three final–state particles are produced only above $\sqrt{s} \approx 1.5$ GeV, where $Q \approx 0.4$ GeV $\gg m_\pi$. Hence, R-hadron scattering is here restricted to $2 \to 2$ and $2 \to 3$ processes and the relative cross section of the $2 \to 3$ processes is taken to be 85%, as derived from high energy pion–proton scattering, see Fig. 4.2(b). At low momenta, the amount of $2 \to 3$ processes is then obviously overestimated, and sometimes $2 \to 3$ processes are even kinematically impossible. Thus, a phase space function describing the relative amounts of $2 \to 2$ and $2 \to 3$ processes is introduced, as follows.

4.3.7 Phase space considerations

Assuming a constant matrix element for both $2 \to 2$ and $2 \to 3$ processes, the relative yield of the three-body final states is solely determined by a phase space factor. A function describing the available phase space is expected to be a function of Q, defined in Eq. (3.13), and a reasonable ansatz is given by

$$F(Q) = \frac{\frac{d\Phi_3(Q)}{d\Phi_3(Q_0)}}{\frac{d\Phi_2(Q)}{d\Phi_2(Q_0)} + \frac{d\Phi_3(Q)}{d\Phi_3(Q_0)}}, \tag{4.4}$$

where $d\Phi_n$ is the available n-body phase space. The fact that the two- and three-body phase spaces do not have the same dimension (compensated for by the here neglected matrix elements) forces us to normalize phase space to that available at a certain value Q_0. For $Q < m_\pi$, the phase space for three-body scattering is vanishing, while for $Q \to \infty$, it is entirely open. Simplified phase space expressions [4] for $d\Phi_2$ and $d\Phi_3$ can be derived under the assumption that the mass of the heavy hadron is much larger than the nucleon mass. In Appendix B, explanations for the derivations are given, hereby covering different possible simplifications for the final–state particles. If one of the final–state particles in the three-body processes is a pion, a general expression describing the relative amount of three-body phase space as a function of Q, if $Q > m_\pi$, may be derived:

$$F(Q) = \frac{\sqrt{(1+\frac{Q}{2m_\pi})(\frac{Q}{Q_o})^{3/2}}}{1+\sqrt{(1+\frac{Q}{2m_\pi})(\frac{Q}{Q_o})^{3/2}}}. \tag{4.5}$$

From the optical theory for light hadrons, it is known that elastic scattering accounts for roughly 15% of the total cross section at high momenta. Taking this into account, a function $f(Q)$ representing the relative probability for $2 \to 3$ scattering is

$$f(Q) = 0.85F(Q). \tag{4.6}$$

An appropriate value for Q_0 can be determined from a fit to the non-resonant part of the elastic cross section, e.g. by finding the value where $F(Q) = 1/2$, thus where $f(Q) = 0.425$. Fig. 4.2(b) illustrates the way in which we determine empirically the value for Q_0 and its uncertainty. The phase space function as function of Q and its uncertainties is displayed in Fig. 4.2(c). The middle dashed curve represents the best fit and corresponds to $Q_0 = 1.1$ GeV, while the two other curves represent the uncertainty $\Delta Q_0 = 0.6$ GeV. Roughly the same value is obtained using p-p and p-K^+-scattering data. The range of possible phase space functions is displayed in Fig. 4.3(a) as function of Q, and in Fig. 4.3(b), the function with $Q_0 = 1.1$ GeV$/c^2$ is shown as function of the laboratory momentum of the incoming hadron for various hadron masses.

4.3.8 Nuclear scattering processes

As discussed in Section 4.3.1, the presence of the gluino changes the color-state of the hadron cloud, but not the character of the interactions of this cloud. Since scattering processes are low–energetic, all scattering processes for mesons and baryons can simply be discussed in the constituent interchange picture [61]. Below, interactions of hadronized color octet and color triplet states will be discussed.

Interactions of $\mathrm{C_8 q\bar{q}}$ Interactions of $\mathrm{C_8 q\bar{q}}$ states include the following processes. The $2 \to 2$ processes are purely elastic scattering (e.g. $\mathrm{C_8 d\bar{d} + uud \to C_8 d\bar{d} + uud}$), charge exchange (e.g. $\mathrm{C_8 d\bar{d} + uud \to C_8 u\bar{d} + udd}$) and baryon exchange (e.g. $\mathrm{C_8 d\bar{d} + uud \to C_8 udd + u\bar{d}}$) while the $2 \to 3$ processes include normal inelastic scattering (e.g. $\mathrm{C_8 d\bar{d} + uud \to C_8 u\bar{d} + udd + d\bar{d}}$) and inelastic scattering with baryon exchange (e.g. $\mathrm{C_8 d\bar{d} + uud \to C_8 uud + u\bar{d} + d\bar{u}}$).

It should be noted that the processes with baryon exchange are kinematically favoured due to the fact that a final-state pion is so light. In such processes, typically an extra $2m_\mathrm{d} - m_\pi \approx 500$ MeV of kinetic energy would be liberated. However, these processes could be dynamically suppressed because two quarks must be exchanged.

Interactions of $\mathrm{C_8 qqq}$ states. Interaction processes include $2 \to 2$ processes like purely elastic scattering (e.g. $\mathrm{C_8 uud + uud \to C_8 uud + uud}$) and charge exchange (e.g. $\mathrm{C_8 uud + udd \to C_8 udd + uud}$) and $2 \to 3$ processes like $\mathrm{C_8 uud + udd \to C_8 udd + uud + d\bar{d}}$. No baryon exchange is possible, since the probability that the $\mathrm{C_8 qqq}$ state interacts with a pion in the nucleus is negligible, and besides this process would kinematically be strongly disfavoured. Thus, mesons get converted into baryons during repeated interactions, but not vice versa!

Interactions of $\mathrm{C_8 \bar{q}\bar{q}\bar{q}}$ states. Only a very small amount of $\mathrm{C_8 \bar{q}\bar{q}\bar{q}}$ states will arise in the hadronization process. Interactions differ from those of $\mathrm{C_8 qqq}$ states, since scattering takes place on protons or neutrons, containing quarks rather than antiquarks. A $\mathrm{C_8 \bar{q}\bar{q}\bar{q}}$ state would thus interact dominantly by baryon annihilation, for example $C_8\bar{u}\bar{u}\bar{d}+uud \to C_8u\bar{d}+u\bar{d}$. This process would kinematically be favourable.

Interactions of C_8g states A gluon is able to convert into a $u\bar{u}$ or $d\bar{d}$ state, and as such, a C_8g state probably interacts like (and mixes with) $C_8u\bar{u}$ or $C_8d\bar{d}$ states. The mass of the active system, the gluon, is usually taken to be 0.7 GeV [64], approximately the same as the constituent mass of two first generation quarks. Thus, the possible interaction processes are expected to be similar to those for $C_8u\bar{u}$ or $C_8d\bar{d}$ states. Besides the fact that the interaction processes are similar, the cross section is expected to be roughly the same, as has already been explained in Section 4.3.5, allowing us to treat a C_8g state like a neutral $C_8q\bar{q}$ state. As for $C_8q\bar{q}$ states, the C_8g states will eventually convert into baryons.

Interactions of $C_3\bar{q}$ and $C_{\bar{3}}q$ states Interactions of a $C_3\bar{q}$ state include processes with quark–antiquark annihilation. Thus, there are $2 \to 2$ processes such as elastic scattering (e.g. $C_3\bar{u} + uud \to C_3\bar{u} + uud$), charge exchange (e.g $C_3\bar{d} + udd \to C_3\bar{u} + uud$), or baryon exchange ($C_3\bar{u} + udd \to C_3ud + \bar{u}d$). For $2 \to 3$ processes, these include normal inelastic processes, like $C_3\bar{u} + udd \to C_3\bar{d} + udd + \bar{u}d$, as well as processes with baryon exchange, like $C_3\bar{u} + udd \to C_3ud+\bar{u}d+u\bar{u}$. As above, baryon exchange is kinematically favoured by the possibility of having a light pion in the final state.

Interactions of a $C_{\bar{3}}q$ state include similar processes but without quark–antiquark annihilation and without baryon exchange. Possible processes in that case are $2 \to 2$ processes like elastic scattering (e.g. $C_{\bar{3}}u + uud \to C_{\bar{3}}u + uud$), charge exchange (e.g. $C_{\bar{3}}d + udd \to C_{\bar{3}}u + uud$), and $2 \to 3$ processes like $C_{\bar{3}}u + udd \to C_{\bar{3}}d + uud + \bar{d}d$.

Interactions of C_3qq and $C_{\bar{3}}\bar{q}\bar{q}$ states Interactions of C_3qq states are processes without quark annihilation and include $2 \to 2$ processes with purely elastic scattering (e.g. $C_3uu+uud \to C_3uu + uud$) and charge exchange (e.g. $C_3uu + udd \to C_3ud + uud$), and $2 \to 3$ processes like e.g. $C_3uu + udd \to C_3ud + udd + u\bar{d}$.

On the other hand, $C_{\bar{3}}\bar{q}\bar{q}$ states may interact by quark annihilation and thereby baryon annihilation. Processes include $2 \to 2$ processes like purely elastic scattering (e.g. $C_{\bar{3}}\bar{u}\bar{u} + uud \to C_{\bar{3}}\bar{u}\bar{u} + uud$), charge exchange (e.g. $C_{\bar{3}}\bar{u}\bar{u} + uud \to C_{\bar{3}}\bar{u}\bar{d} + udd$), and baryon annihilation (e.g. $C_{\bar{3}}\bar{u}\bar{u} + uud \to C_{\bar{3}}u + \bar{u}d$) and $2 \to 3$ processes like e.g. $C_{\bar{3}}\bar{u}\bar{u} + udd \to C_{\bar{3}}\bar{u}\bar{d} + udd + \bar{u}d$. Baryon annihilation would kinematically be favoured.

4.3.9 Relative probabilities of scattering processes

As is clear from the above, an enormous number of scattering processes is generally possible. Focusing on R-hadrons arising from a heavy color octet particle, over 140 processes should thus be considered. A summary of all possible processes for such hadrons is given in Table 4.1. To determine the relative frequency for each process, the relative couplings of all processes must be known, requiring the calculation of the Clebsch-Gordan coefficients of isospin-related processes, plus an evaluation of all additional dynamical effects for all processes. No attempt has been made to do this. Since the masses of the different lowest-lying C_8 mesons and baryons are degenerate, as discussed in Section 4.3.2, the phenomenology is not expected to be affected by the exact details. Therefore, after the target and the class of interaction processes, i.e. $2 \to 2$ or $2 \to 3$ processes, is determined, equal relative couplings for all processes inside this class are assumed.

4.3.10 The nuclear cascade

The incoming hadron interacts with a nucleon inside a nucleus. As explained in Section 3.2.6, the energy of the incident hadron determines whether the interaction causes a large nuclear cascade or not. Since the interacting system of a heavy hadron is low–energetic and corresponds to that of e.g. slow pions, the associated wavelengths are of the order of the size of the nucleus, and the development of a nuclear cascade is probable.

4.3.11 Nuclear energy losses

As argued in Section 4.3.6 the total energy loss in a collision of the heavy hadron is small. This small energy transfer is shared between the kinetic energy of the kicked-out nucleon or pion, its binding energy in the nucleus, the production of extra final–state particles, and nuclear degrees of freedom inside the remnant.

4.4 Summary

In this section, interactions of heavy hadrons, arising from any color triplet or octet state, have been described. The model presented here should not be viewed as a final description, but provides a convenient platform on which to build in the future. The approximations made in the model are the following:

- Since no description of heavy resonances can possibly be given, the cross sections for nuclear scattering are assumed to be purely geometrical and constant with respect to the center-of-mass energy.
- In the cross section estimates, only hadrons made of u and d quarks have been considered.
- Due to the small amount of energy available for the production of new particles, only $2 \to 2$ and $2 \to 3$ processes are assumed to take place.
- Instead of calculating all Clebsch-Gordon coefficients for ca 140 processes, the processes are assumed to have equal relative couplings.
- In the calculation of the relative probabilities for $2 \to 2$ and $2 \to 3$ processes, matrix elements are neglected, and only phase space factors are taken into account.

	R^+	R^0	R^-
proton scattering: 2→2 processes	$R^+p \to R^+p$ $R^+p \to S^{++}\pi^0$ $R^+p \to S^+\pi^+$	$R^0p \to R^0p$ $R^0p \to R^+n$ $R^0p \to S^{++}\pi^-$ $R^0p \to S^+\pi^0$ $R^0p \to S^0\pi^+$	$R^-p \to R^-p$ $R^-p \to R^0n$ $R^-p \to S^+\pi^-$ $R^-p \to S^0\pi^0$
neutron scattering: 2→2 processes	$R^+n \to R^+n$ $R^+n \to R^0 + p$ $R^+n \to S^{++}\pi^-$ $R^+n \to S^+\pi^0$ $R^+n \to S^0\pi^+$	$R^0n \to R^0n$ $R^0n \to R^-p$ $R^0n \to S^+\pi^-$ $R^0n \to S^0\pi^0$ $R^0n \to S^-\pi^+$	$R^-n \to R^-n$ $R^-n \to R^0\pi^-$ $R^-n \to S^0\pi^-$ $R^0n \to S^-\pi^0$
proton scattering: 2→3 processes	$R^+p \to R^+p\pi^0$ $R^0p \to R^+n\pi^+$ $R^+p \to R^0p\pi^+$ $R^+p \to S^{++}\pi^0\pi^0$ $R^+p \to S^{++}\pi^+\pi^-$ $R^+p \to S^+\pi^+\pi^0$ $R^+p \to S^0\pi^+\pi^+$	$R^0p \to R^0p\pi^0$ $R^0p \to R^0n\pi^+$ $R^0p \to R^+p\pi^-$ $R^0p \to R^+n\pi^0$ $R^0p \to R^-p\pi^+$ $R^0p \to S^{++}\pi^0\pi^-$ $R^0p \to S^+\pi^0\pi^0$ $R^0p \to S^+\pi^+\pi^-$ $R^0p \to S^0\pi^+\pi^0$ $R^0p \to S^-\pi^+\pi^+$	$R^-p \to R^-p\pi^0$ $R^-p \to R^-n\pi^+$ $R^-p \to R^+n\pi^-$ $R^-p \to R^0p\pi^-$ $R^-p \to R^0n\pi^0$ $R^-p \to S^{++}\pi^-\pi^-$ $R^-p \to S^+\pi^0\pi^-$ $R^-p \to S^0\pi^0\pi^0$ $R^-p \to S^0\pi^+\pi^-$ $R^-p \to S^-\pi^+\pi^0$
neutron scattering: 2→3 processes	$R^+n \to R^+n\pi^0$ $R^+n \to R^+p\pi^-$ $R^+n \to R^0p\pi^0$ $R^+n \to R^0n\pi^+$ $R^+n \to R^-p\pi^+$ $R^+n \to S^{++}\pi^0\pi^-$ $R^+n \to S^+\pi^0\pi^0$ $R^+n \to S^+\pi^+\pi^-$ $R^+n \to S^0\pi^+\pi^0$ $R^+n \to S^-\pi^+\pi^+$	$R^0n \to R^0n\pi^0$ $R^0n \to R^0p\pi^-$ $R^0n \to R^+n\pi^-$ $R^0n \to R^-p\pi^0$ $R^0n \to R^-n\pi^+$ $R^0n \to S^{++}\pi^-\pi^-$ $R^0n \to S^+\pi^-\pi^0$ $R^0n \to S^0\pi^0\pi^0$ $R^0n \to S^0\pi^+\pi^-$ $R^0n \to S^-\pi^+\pi^0$	$R^-n \to R^-n\pi^0$ $R^-n \to R^-p\pi^-$ $R^-n \to R^0n\pi^-$ $R^-n \to S^+\pi^-\pi^-$ $R^-n \to S^0\pi^-\pi^0$ $R^-n \to S^-\pi^0\pi^0$ $R^-n \to S^-\pi^+\pi^-$

	S^{++}	S^+	S^0	S^-
proton scattering: 2→2 processes	$S^{++}p \to S^{++}p$	$S^+p \to S^{++}p$ $S^+p \to S^{++}n$	$S^0p \to S^0p$ $S^0p \to S^+n$	$S^-p \to S^-p$ $S^-p \to S^0n$
neutron scattering: 2→ 2 processes	$S^{++}n \to S^{++}n$ $S^{++}n \to S^+p$	$S^+n \to S^+n$ $S^+n \to S^0p$	$S^0n \to S^0n$ $S^0n \to S^-p$	$S^-n \to S^-n$
proton scattering: 2→3 processes	$S^{++}p \to S^{++}p\pi^0$ $S^{++}p \to S^{++}n\pi^+$ $S^{++}p \to S^+p\pi^+$	$S^+p \to S^+p\pi^0$ $S^+p \to S^+n\pi^+$ $S^+p \to S^{++}n\pi^0$ $S^+p \to S^{++}p\pi^-$ $S^+p \to S^0p\pi^+$	$S^0p \to S^0p\pi^0$ $S^0p \to S^0n\pi^+$ $S^0p \to S^+n\pi^0$ $S^0p \to S^+p\pi^-$ $S^0p \to S^-p\pi^+$	$S^-p \to S^-p\pi^0$ $S^-p \to S^-n\pi^+$ $S^-p \to S^+p\pi^+$ $S^-p \to S^0p\pi^-$ $S^-p \to S^0n\pi^0$
neutron scattering: 2→ 3 processes	$S^{++}n \to S^{++}n\pi^0$ $S^{++}n \to S^{++}p\pi^-$ $S^{++}n \to S^+p\pi^0$ $S^{++}n \to S^+n\pi^+$ $S^{++}n \to S^0p\pi^+$	$S^+n \to S^+n\pi^0$ $S^+n \to S^+p\pi^-$ $S^+n \to S^{++}n\pi^-$ $S^+n \to S^0p\pi^0$ $S^+n \to S^0n\pi^+$ $S^+n \to S^-p\pi^+$	$S^0n \to S^0n\pi^0$ $S^0n \to S^0p\pi^-$ $S^0n \to S^+n\pi^-$ $S^0n \to S^-n\pi^+$	$S^-n \to S^-n\pi^0$ $S^-n \to S^-p\pi^-$ $S^-n \to S^0n\pi^-$

Table 4.1: All possible processes for R-mesons and R-baryons. To distinguish in this table between R-mesons and R-baryons, the former are denoted by R, and the latter by S. Thus, $C_8u\bar{d}$ states are denoted by R^+, $C_8u\bar{u}$, $C_8d\bar{d}$ and C_8g states by R^0 and $C_8\bar{u}d$ states by R^-. For baryons, C_8uuu states are denoted by S^{++}, C_8uud states by S^+, C_8udd states by S^0 and C_8ddd states by S^-. Because of the small amount of $C_8\bar{q}\bar{q}\bar{q}$ states, and because of their quick annihilation into R-mesons, these states have not been taken into account. Thus, no special columns devoted to $C_8\bar{u}\bar{u}\bar{u}$ (S^{--}) states are displayed. It must be noted that the notation for baryons by S is no generic notation and is only used in this table.

Chapter 5

Simulating heavy hadrons in GEANT

This chapter describes the technical aspects of the simulation of R-hadrons. After a short walk-through of the GEANT 3 framework in Section 5.1, an introduction to the GHEISHA package is provided in Section 5.2, in which the most important issues in the simulation of hadronic showers are treated. In Section 5.3, the simulation used in ALEPH is briefly discussed. It must be stressed that this simulation is *not* based on the *new* model for interactions of heavy hadrons, presented in the previous chapter, because the inspiration to develop this model came only during and after the completion of the ALEPH analysis. Section 5.4 provides an extensive discussion of the simulation in ATLAS, where the ideas of the previous chapter have been applied. In Section 5.5, results of this new simulation will be presented, together with studies of typical detector signals. Although the simulation is made inside the ATLAS software framework, the results presented in Section 5.5 are generally applicable to any detector, rather than merely to the ATLAS detector. The chapter ends by a simple comparison in Section 5.6 of the two models in the R-hadron mass region relevant for ALEPH.

5.1 The GEANT3 framework

The simulation of processes which accompany the propagation of an R-hadron through the detector material is performed within the framework of GEANT3 [69]. This was a natural choice in ALEPH, because all analyses have been performed with GEANT3. Although the c++ based GEANT4 framework finally will be the official simulation package in ATLAS, it was not ready for real physics studies at the time this work was commenced. In GEANT3, interactions are performed according to the following steps. First, the step distance Δx to the next interaction point is evaluated by the tracking routines `gtneut.F` (if the hadron is neutral) or `gthadr.F` (if the hadron is charged). The distance x_i which a particle travels on average before interacting via process i is

$$x_i = N_i \lambda_i, \tag{5.1}$$

where N_i is the number of interaction lengths that the particle will travel before interaction of kind i, and λ_i is the interaction length for process i, see Eq. (3.3). Since $P(x)$ in Eq. (3.3) is a number between 0 and 1, N_i is initially sampled by

$$N_i = -\log \eta, \tag{5.2}$$

where η is a random number between 0 and 1. The actual transportation step Δx is calculated by taking into account all processes and evaluating for which process i the interaction distance x_i is smallest: Δx =min(x_i). The particle is then transported over the distance Δx in a trajectory

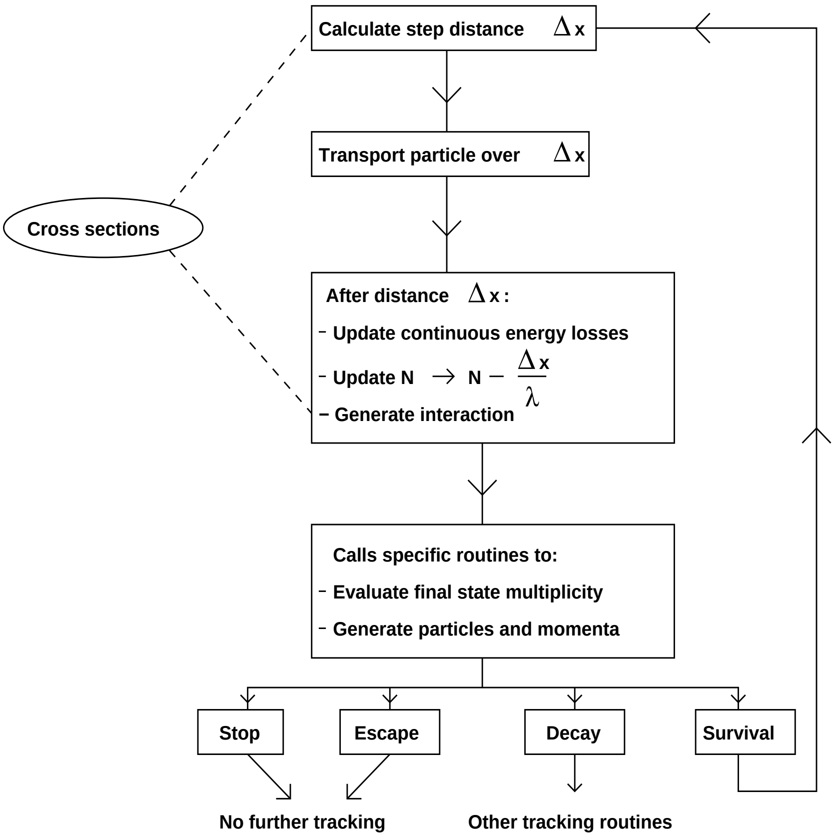

Figure 5.1: The tracking steps in GEANT 3.

depending on the magnet configuration. At distance Δx, the medium is verified, the particle energy is updated to account for continuous energy losses like e.g. ionization losses, and the relevant processes are generated. For all processes not having taken place, the value for N_i is then updated following

$$N_i \rightarrow N_i - x_i. \tag{5.3}$$

After the interaction, the particle can either survive, in which case the steps are repeated, or decay, in which case other tracking routines take over, or stop or escape, in which case no further tracking takes place. In Fig. 5.1 a flow-diagram is given showing a schematic representation of tracking in GEANT3. Details of hadronic tracking will be discussed in the following section.

5.2 The GHEISHA package

For the specific issue of describing hadronic interactions in matter, two packages are available in GEANT 3: the FLUKA package and the GHEISHA package. For our purpose, the GHEISHA package is used. In order to understand the R-hadronic code, some general information about GHEISHA is given below. Detailed information is provided in Ref. [57]. A flow diagram of some of the most important routines is given in Fig. 5.4. Three main issues characterize the generation of hadronic interactions in GHEISHA.

1. The evaluation of the cross sections, needed to calculate the mean free path. For ordinary hadrons, parameterizations of the nuclear scattering cross sections in terms of the

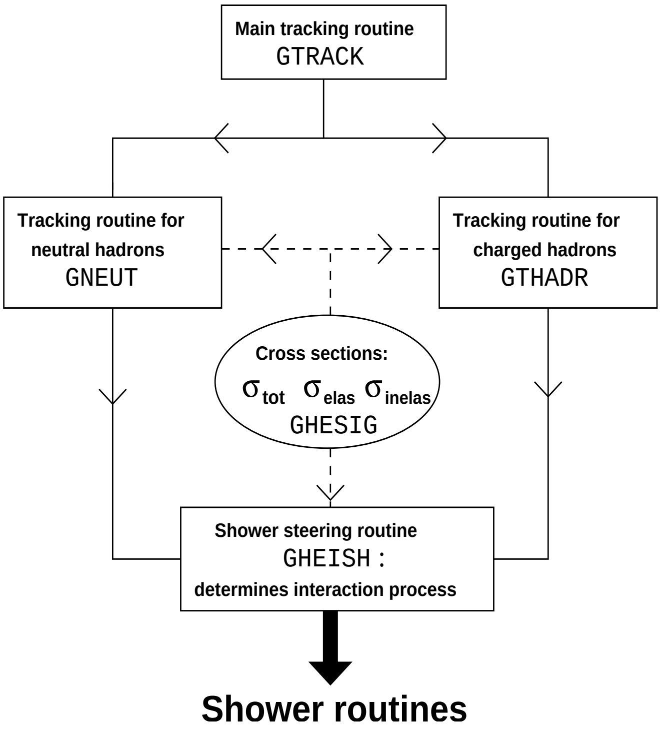

Figure 5.2: The most important GHEISHA routines.

atomic number A are used according to experimental data. The mean free path for nuclear scattering is calculated via Eq. (3.2), where σ is the total cross section, i.e. the sum of the inelastic and elastic cross section. The routine responsible for the evaluation of cross sections is `ghesig.F`.

2. The selection of the interaction and subsequent sampling of the final state multiplicities. This is done in the specific cascade routines, called from the main steering routine `gheish.F`. For example, for positive and negative pions, these are `caspip.F` and `caspim.F`, respectively. The cascade routines evaluate whether the target is proton or neutron, and whether $2 \to 2$ or $2 \to 3$ scattering is selected, with probabilities proportional to their cross sections. The selection of elastic scattering always implies a final state multiplicity of two primary final state particles. For normal hadrons undergoing inelastic scattering, the number of primary final state particles follows the Koba-Nielsen-Olesen-formula (KNO) [70], which can be written as [57]:

$$N = 3.62567 + 0.665843 \log Q + 0.336514 (\log Q)^2 + \quad (5.4)$$
$$0.117712 (\log Q)^3 + 0.0136912 (\log Q)^4, \quad (5.5)$$

where Q is the energy available for the generation of new particles, given in Eq. (3.13). The selection of the interaction processes for ordinary hadrons is based on parameterization of hadron scattering data.

3. The generation of the final state particles and their kinematics. The fact that the incoming particle scatters on a nucleon inside a nucleus complicates matters. In GHEISHA, the generation of final state particles and their momenta includes the following issues:

- The evaporation energy and binding energy of a nucleus is taken into account by changing the initial kinetic energy of the incoming hadron with a certain amount according to a Gaussian distribution.
- The Fermi motion of the nucleons inside the nucleus is taken into account by smearing the initial kinetic energy of the incoming hadron according to a Gaussian distribution.
- The primary interaction process is generated. The responsible routines are `twob.F` (if two-body scattering) or one of the routines `genxpt.F`, `higxpt.F` or `higclu.F` (if N-body scattering), which generate p_T-values and ϕ-values (azimuth angle) for the final state particles. Routine `genxpt.F` decides whether to use a two-cluster model (routine `higclu.F`) or an iterative cascade model (routines `genxpt.F` and `higxpt.F`) to generate final state kinematics (see Ref. [57] for details). In the center-of-mass energy of the scattering, the t-distributions are generated according to

$$\frac{\mathrm{d}\sigma}{\mathrm{d}t} \propto e^{-b|t|}, \tag{5.6}$$

  where b is again tabulated from experimental data. For elastic scattering for pions, the value of b is $4.225+1.795 \ln p$, where p is the momentum of the interacting particle. Given a value for t, the scattering angle can be determined, as has been explained in Appendix B.1. The longitudinal momenta are evaluated in such a manner that overall momentum and energy is conserved.
- The nuclear cascade is accounted for by generating a certain amount of grey track particles. This amount is derived from experimental scattering data and has a proportionality to the amount of particles produced in the primary interaction process and to the atomic mass of the target. The momenta of all final state particles are again smeared due to the Fermi motion of the nucleus. Furthermore, the momenta of all final state particles are decreased with a certain amount to account for the binding energy of the particles to the nucleus, according to the nuclear potential of the material.
- Depending on the stability of the nucleus and on the kinetic energy of the interacting hadron, black track particles arising from nuclear evaporation of the nucleus, are generated in the two-body and three-body scattering routines `twob.F`, `genxpt.F`, `higxpt.F`, `higclu.F`.

It must be emphasized that the way, in which GHEISHA simulates hadronic interactions is almost entirely based on parameterizations of existing data. This complicates the task to implement R-hadronic nuclear interactions considerably. For a detailed review of the GHEISHA package and all parameterizations therein, the reader is referred to Ref. [57].

5.3 R-hadron simulation in ALEPH

5.3.1 Technical details

The R-hadron simulation in the ALEPH detector is based on the existing code for interactions of stop hadrons very briefly described in Refs. [38, 71]. Ionization losses for R-hadrons are simulated using the available GEANT 3 code, based on the Bethe-Bloch formula and necessary corrections. Also multiple scattering is accounted for. The simulation of R-hadronic nuclear scattering is not available by default, and the existing GHEISHA routines for pion cascades have been used as a starting point. The three elements in GHEISHA are simulated as follows.

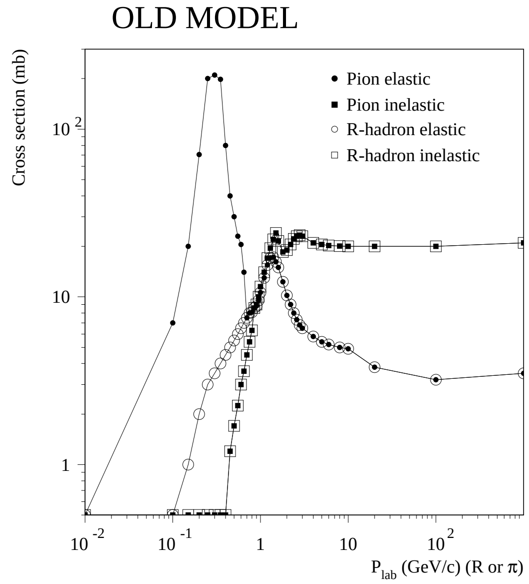

Figure 5.3: The cross section for π and R-hadron proton scattering as function of the laboratory momenta in ALEPH.

1. The cross section for nuclear scattering above R-hadron momenta of 1 GeV are taken to be equal to the cross sections for pion-proton scattering:

$$\sigma_{\mathrm{R-n}}(p_R) = \sigma_{\pi-\mathrm{p}}(p_\pi). \tag{5.7}$$

   Below 1 GeV, the cross sections decrease gradually and vanish below laboratory momenta of 0.1 GeV. The cross sections for pions and R-hadrons scattering on protons is shown in Fig. 5.3.

2. The selection of interaction processes and the evaluation of final state multiplicity is done in one of the three specific cascade routines for R-hadrons: CASQUZUP for negative R-hadrons, CASQUZDOWN for positive R-hadrons, and CASQUZERO for neutral R-hadrons, called in GHEISH. After the target has been selected, the different interaction processes are selected. The probability for charge exchange is implemented analogue to pions, depending on the laboratory momentum of the incoming hadron. No baryon exchange is included. In the case of inelastic scattering, final state multiplicities were obtained from Eq. (5.4).

3. The kinematics of the final state particles is done in the standard way with the routines TWOB and GENXPT. For the generation of the p_T values, the parameterizations for pions are used. Matters such as the calculation of the nuclear evaporation energy are handled exactly as for pions with the corresponding energy.

5.3.2 Drawbacks

There are a few drawbacks to the ALEPH simulation:

- Cross sections scale with the velocity of the particle rather than with the momentum. The interacting 'pion'-system is slow, and a rescaling of the pion cross section with the proper 'pion' (active system) velocities should have been made:

$$p \to \sqrt{(\frac{E_{\mathrm{R}}^2}{M_{\mathrm{R}}^2} - 1)} m_{\text{active cloud}}, \tag{5.8}$$

where the mass of the active cloud is 600 MeV if the active system consists two quarks or a gluon, and 900 MeV if the active system consists of three quarks.

- Second, assuming a vanishing cross section below laboratory momenta of 1 GeV is rather arbitrary, because there are no explicit reasons for the cross section to vanish. Probably, it does not influence the overall picture, since the R-hadron has lost most of its energy before reaching such low momenta and the remaining momentum is below the resolution of the ALEPH calorimeters. However, it must be noted that if the R-hadron has a momentum in the region where the nuclear interaction cross section is zero, it continues through the detector without suffering any nuclear interactions. A charged R-hadron will quickly lose it's remaining energy to ionization, but a neutral R-hadron would simply traverse through the detector without interacting, and escape.
- The simulation does not distinguish R-mesons and R-baryons, although in principle needed for the original purpose of simulating stop-hadrons [38]. Since R-baryons have a cross section 3/2 times larger than R-mesons, and since a considerable amount of R-baryons could be produced, the amount of interactions taking place in the detector is underestimated.
- No rescaling is applied anywhere in quantities as evaporation energy of the nucleus, etc. A 100 GeV R-hadron interacts with the nucleus as if it is a 100 GeV pion, while a rescaling as in Eq. (5.8) should have been made. One of the consequences is that the energy to spend on nuclear evaporation is underestimated.

All these issues will be covered by a thorough systematic error analysis presented in Chapter 9.

5.4 An improved R-hadron simulation in ATLAS

5.4.1 Technical details

For the simulation of R–hadronic interactions in ATLAS, again the GHEISHA package is used [57]. For the simulation of ionization losses and multiple scattering, as well as for the tracking of the particles, standard GEANT 3 code is used. This requires the introduction of seven new GEANT particles for R^+-mesons, R^0-mesons (also for gluino-balls), R^--mesons, R^{++}-baryons, R^+-baryons, R^0-baryons and R^--mesons, where it was necessary to enlarge several basic GEANT arrays. For the specific issue of describing R-hadronic interactions in matter, a special package based on GHEISHA devoted to R-hadronic is developed, called RGHEISHA [72]. Tracking of R-hadrons through the detector volume is done without modification. For the generation of R-hadronic nuclear interactions, the existing pion routines of the GHEISHA package are used as a starting point, like in ALEPH. In Fig. 5.4, the new routines are displayed. Fig. 5.5 shows the selection steps executed in a shower routine. The three issues characterizing hadronic interactions in GHEISHA are simulated as follows:

1. The evaluation of the cross sections, needed to calculate the mean free path, is performed by the routine `rghesig.F`, derived from the original routine `ghesig.F`. Cross sections are calculated according to the arguments in Section 4.3.5. Their parameterizations are contained in `s_csdat35.inc`.

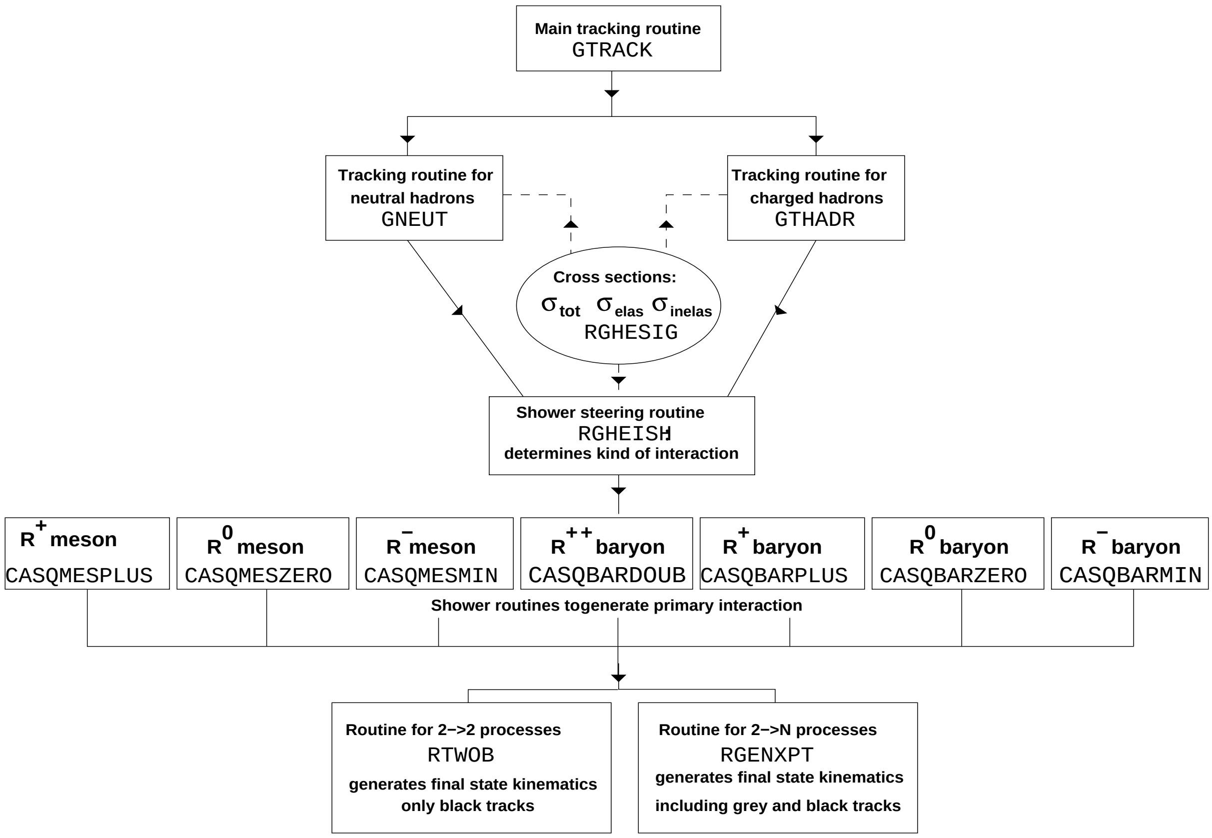

Figure 5.4: The tracking steps in GHEISHA. The routines are explained in detail in the text.

2. The selection of the interaction and subsequent sampling of the final state multiplicities. The main steering routine is `aguhadr.F`, derived from `gheish.F`. The evaluation of the final state particles is done with the help of seven new shower routines called from `aguhadr.F`:
   - `casqmesplus.F` for R^+-mesons
   - `casqmeszero.F` for R^o-mesons and R^o gluino-balls
   - `casqmesmin.F` for R^--mesons
   - `casqbardoub.F` for R^{++}-baryons
   - `casqbarplus.F` for R^+-baryons
   - `casqbarzero.F` for R^0-baryons
   - `casqbarmin.F` for R^-baryons.

   In these routines, the relative amount of $2 \to 2$ and $2 \to 3$ processes is chosen according to the explanations in Section 4.3.7, taking into account phase space. Thus, no Koba-Nielsen-Olesen- multiplicity distributions are used, as in the case of ordinary hadrons. The processes are selected, after the target and interaction class ($2 \to 2$ or $2 \to 3$) is fixed, with equal probabilities. In Table 4.1, all different processes are shown. All routines include the file `r_input.inc`, containing a common block related to R-hadron parameters.

3. The generation of the final state particles and their kinematics. This is done either with the routine `rtwob.F` (if two-body scattering), the analogue of `twob.F`, or one of the routines

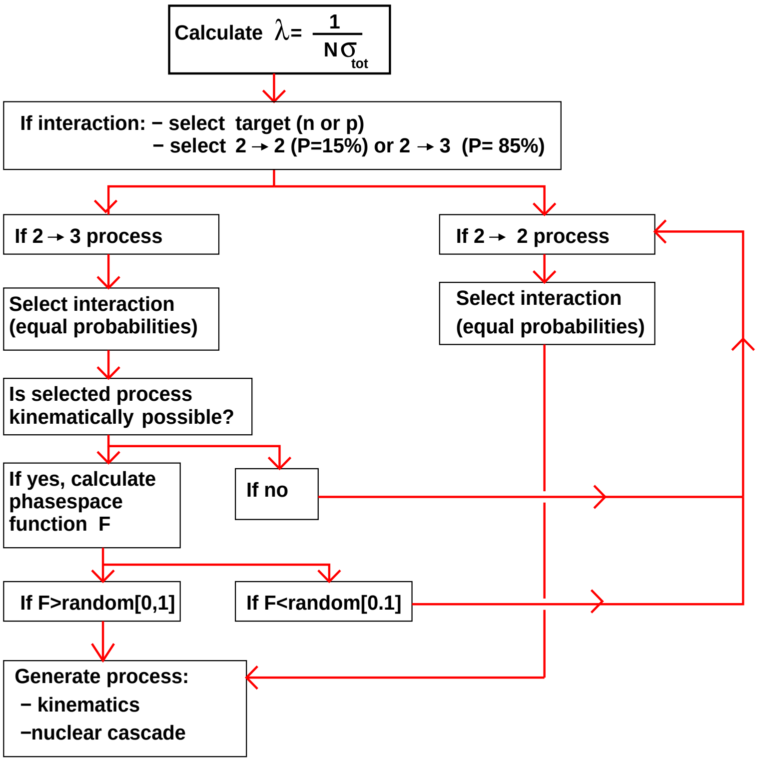

Figure 5.5: Overview of process selection in a shower routine.

rgenxpt.F, rhigxpt.F or rhigclu.F (if three-body scattering), the analogues of higxpt.F, genxpt.F and higclu.F, respectively. Here, routine rhigclu.F is most relevant. This routine contains two modifications. First, a modification is made to protect the unphysical situation that the scattered hadron, has a larger momentum after the scattering than before, even if no baryon number is exchanged. This piece of code is default for scattering of low energetic pions (routine genxpt.F), and is thus necessary in this case also. The second modification is in the generation of the p_T-values for the final state particles, which are tabulated from experimental data. For R-hadrons, the parameterization of t values for pions is used both in rtwob.F and in rhigclu.F, see the previous section. For R-hadrons, a rescaling of momenta to the momenta of the active quark (or gluon) system is applied as given in Eq. 5.8.

5.4.2 Incorporation in ATLSIM

The routines mentioned above are pure GEANT/GHEISHA routines and can be used for any purpose, provided that the user has defined the seven new R-hadrons (i.e. charges, tracking types, lifetime). All routines can be found in Ref. [72]. If one does not wish to use the ATLAS framework, ATLAS related routines, i.e. the .age routines, should be removed and substituted by other routines. In ATLAS, R-hadron events can be simulated with ATLSIM [73], a generic PAW-based framework to run ATLAS detector simulations using GEANT3. Interested readers can find the necessary information to fully simulate R-hadrons in Ref. [72]. Extracting specific information about the particles traversing a detector volume, like the ATLAS detector, or a self-defined volume like a block of material, can be done in various ways:

- By writing analysis routines in Age, a language mixing between Fortran and C++ syntax [74, 75], allowing direct access to information about GEANT 3 particles to be obtained. Quantities such as position, secondary particles, energy deposition in a cell, etc, can be accessed. For reconstructing tracks, existing FORTRAN track-reconstruction programs are normally used. The Age-language also allows one to define an arbitrary detector [76], like a block of a certain material, enabling fast studies about e.g. energy losses. This method has been applied to obtain the results presented in Section 5.5 below.

- By using the Athena framework, a C++ based operating system for the ATLAS software. The advantage of Athena is the fact that it provides a standard software to produce ntuples with information about reconstructed events. One disadvantage is that the output is limited to standard output, and any non-standard modifications in the code causes regular crashes. Besides, Athena reconstruction requires ZEBRA files as input files, resulting from ATLSIM, the size of which causes storing problems. Most results in Chapter 12 are based on this method.

5.5 Results

5.5.1 Meson-baryon conversion

As explained in Section 4.3.8, an R–meson is able to convert into an R–baryon by scattering off a nucleon, but not vice-versa. The amount of converted mesons as a function of the traveling length in a piece of iron is shown in Fig. 5.6. Note that an R–baryon has a larger cross section for nuclear interactions than an R–meson. The conversion therefore increases the subsequent energy losses in a calorimeter.

5.5.2 Kinematics

We cross-check the values for the scattering angle in the center of mass system, $\cos\theta^*$, and for the transverse momentum p_T of the scattered R–hadron. Results are shown in Fig. 5.7. At small momenta, the $2 \to 2$ scattering processes are isotropic, while at large momentum, a clear forward

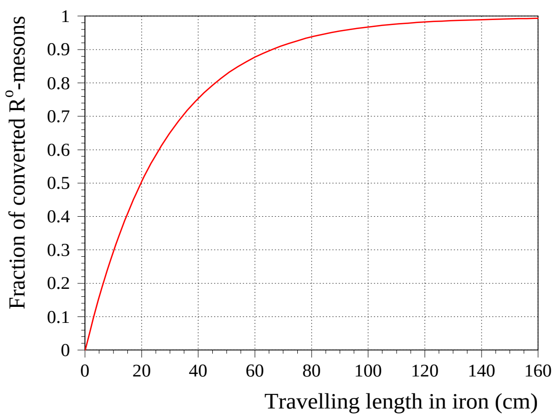

Figure 5.6: The fraction of R–mesons converted into R–baryons as function of the traveling length, starting with a neutral R–meson.

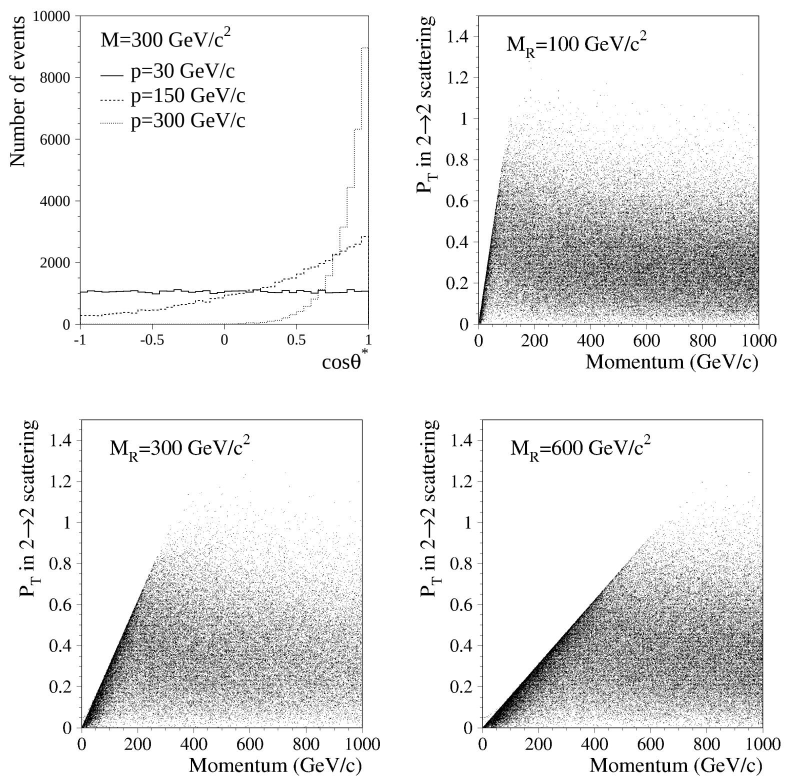

Figure 5.7: At the left, distributions for $\cos\theta^*$ in $2 \to 2$ scattering for different values of the R–hadron initial momentum (left). At the right, scattering plots for the generated p_T value of the R–hadron in $2 \to 2$ scattering for three different values of the R–hadron mass: 100, 300 and 600 GeV$/c^2$.

peak is seen, explained by the fact that the p_T in nuclear scatterings is limited to the order of 1 GeV.

5.5.3 Losses per collision

To check whether non-trivial nuclear effects are simulated correctly, the losses per nuclear collision have been evaluated in iron, carbon and liquid hydrogen. In Fig. 5.8, the losses per collision are displayed for $2 \to 2$ and $2 \to 3$ scatterings in the three materials for different values of the R–hadron mass. From the three figures obtained for e.g. iron, it can be seen that the loss per collision decreases with increasing R–hadron mass for fixed kinetic energy. This is logically explained by the fact that the energy available for the production of new particles in a scattering becomes smaller. From these plots, we also note that the energy loss per collision is generally much larger for a $2 \to 3$ process than for $2 \to 2$ processes, which follows from kinematics. If we compare different target materials, the loss per collision increases for heavy elements. This can be explained by the fact that the R–hadron is slow, and can scatter several times with the different nucleons inside one nucleus. For hydrogen, it should be noted that the energy loss for $2 \to 3$ processes vanishes at small momenta, a feature which is not seen for heavier elements, where this effect is washed out by the nuclear cascade. This is the result of the modification which was already mentioned in item 3 in Section 5.4.1. Repairing this 'bug', and making the package optimal for heavy hadrons rather than using the existing parameterizationa for pions,

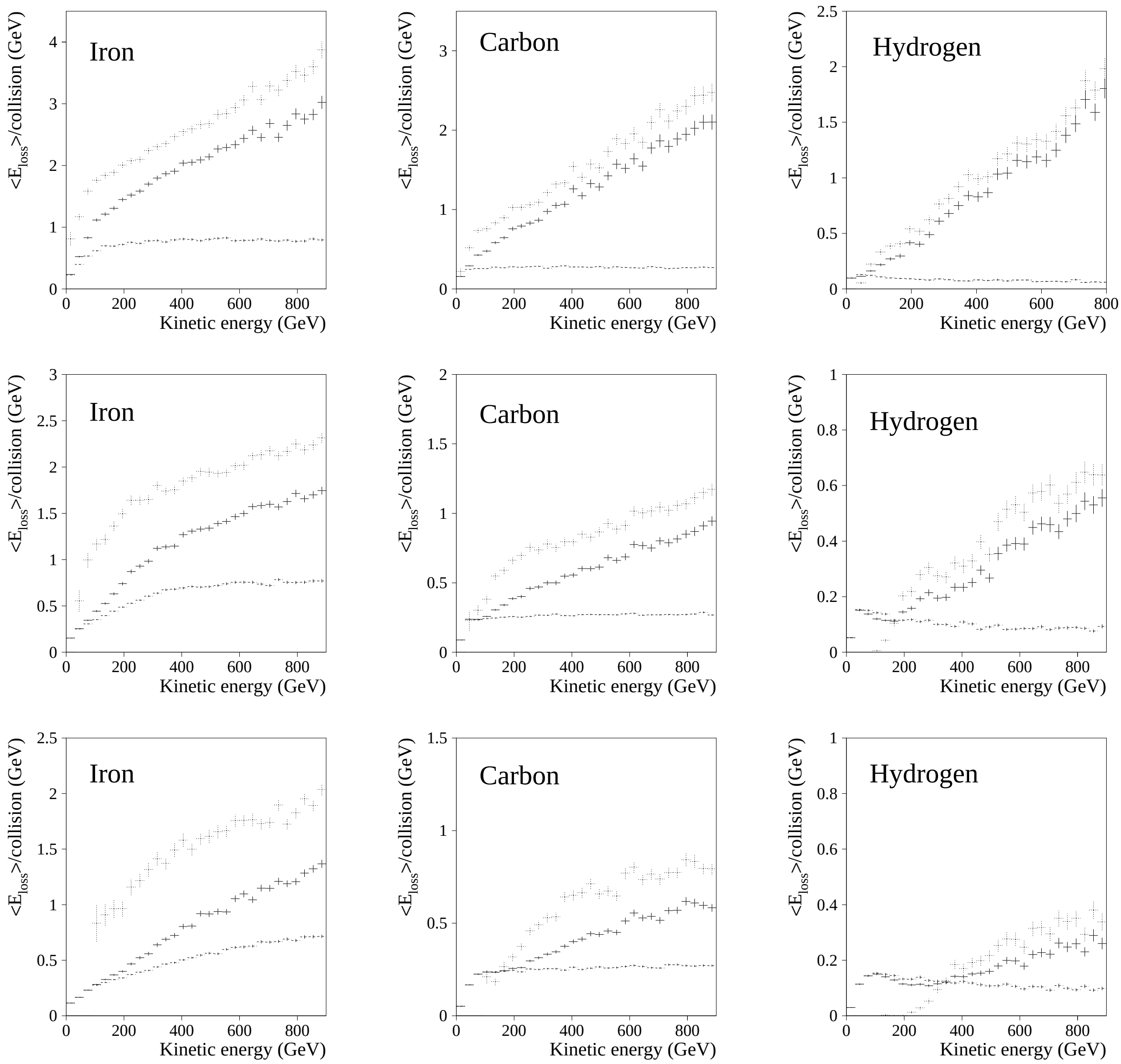

Figure 5.8: Profile plots representing the mean value of the energy loss per collision of an R–baryon for three different values of the R–hadron mass: 100 (three upper figures), 300 (three middle figures) and 600 GeV/c^2 (three lower figures). The lines represent the mean value and its error. The lower and upper profiles in each plot correspond to the energy loss in a $2 \to 2$ scattering and a $2 \to 3$ scattering, respectively, while the middle profiles represent the average loss per collision.

would require a considerable rewrite of the code. This is beyond the scope of this work and, besides, $2 \to 2$ scattering processes dominate completely at low energies. Energy losses for an R–hadron which converts from meson into baryon result in a larger total energy deposited in the detector due to the larger kinetic energy released in the process.

5.5.4 Nuclear energy losses in different materials

We compare the energy loss to purely nuclear interactions (i.e. no ionization losses) of an R–hadron in different materials, when the total amount of nucleons traversed is the same. Total

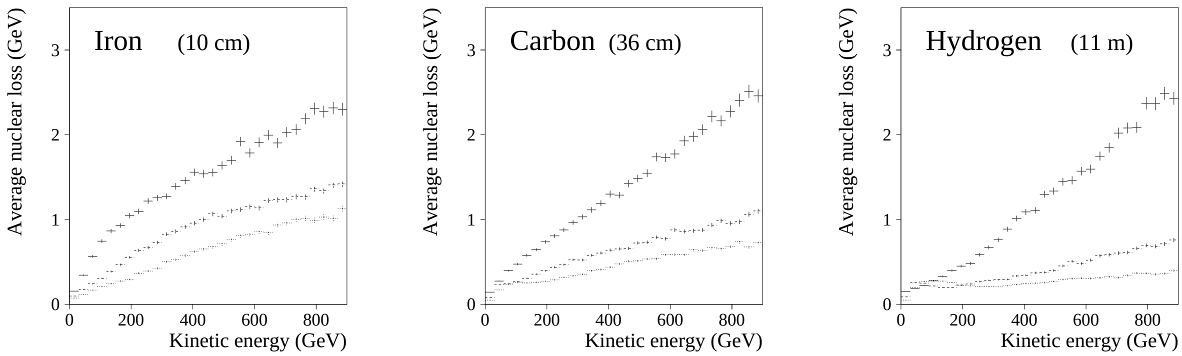

Figure 5.9: Comparison of the total nuclear energy losses in 10 cm iron, in 36 cm carbon and in 11 m liquid hydrogen, corresponding to the same amount of nucleons, for an R–hadron mass of 100 GeV/c^2 (upper curves), 300 GeV/c^2 (middle curves) and 600 GeV/c^2 (lower curves).

nuclear losses of R–baryons in 10 cm iron, 36 cm carbon and 11 m liquid hydrogen are shown in Fig. 5.9. It turns out that approximately the same amount of total energy is lost. The average number of nuclear interactions is however not the same. As can be easily derived from the cross section on free nucleons, the interaction lengths in iron, carbon and liquid hydrogen of an R–baryon are 14 cm, 32 cm and 610 cm, respectively. In 10 cm iron, 36 cm carbon, and 11 m liquid

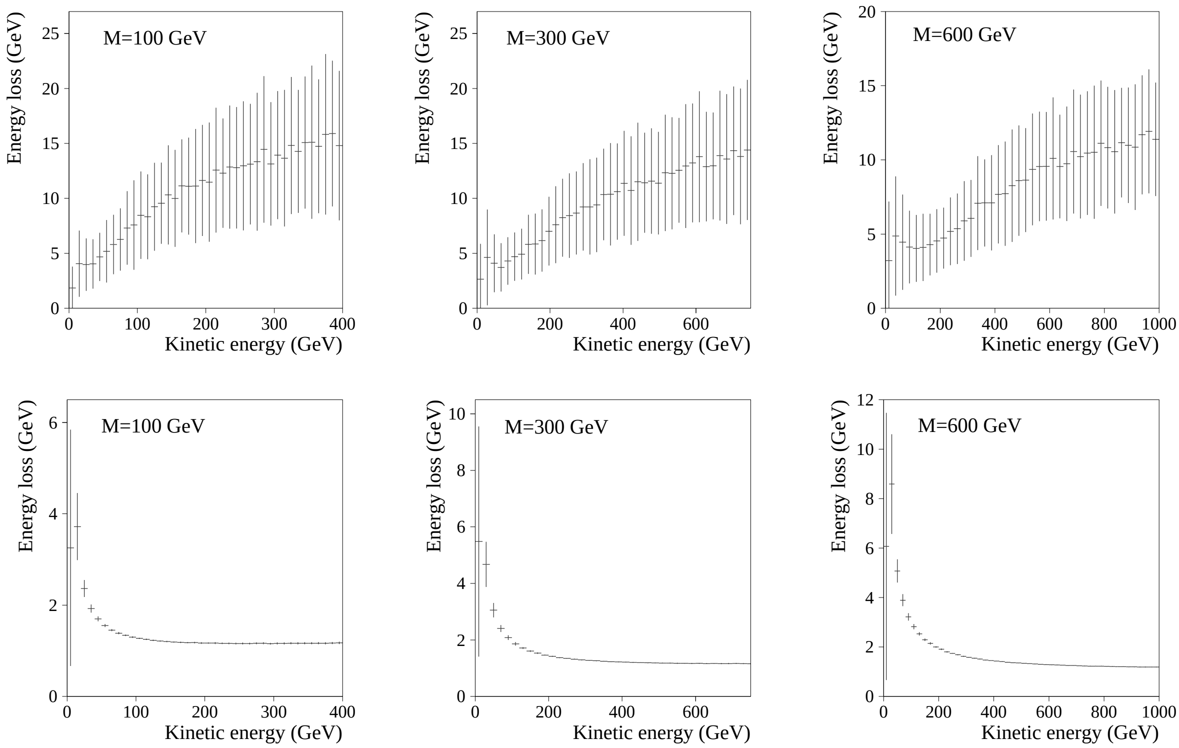

Figure 5.10: Profile histograms representing the average R–hadron energy loss in 1 m iron and the spread on this average as a function of kinetic energy for the total energy loss (upper figures) and pure ionization losses for a singly charged R–hadron without nuclear interactions (lower figures).

hydrogen roughly 0.7, 1.1 and 1.8 collisions take place. However, the amount of energy lost in a collision increases with increasing atomic number (see Fig. 5.8), and the overall result is that approximately the same amounts of energy are lost.

5.5.5 Total energy losses

The total energy loss in 1 m iron, i.e. the sum of nuclear energy losses and ionization losses, is determined for R–hadron with various masses. Results are displayed in Fig. 5.10. The ionization losses for a singly charged R–hadron traversing 1 m iron without suffering any nuclear interactions are shown as well. Nuclear losses completely dominate at high energies.

5.5.6 Nuclear energy losses versus ionization losses

A direct comparison between the energy losses of an R–hadron suffering only nuclear collisions, and those of an R–hadron suffering ionization losses as well as nuclear collisions, is shown in Fig. 5.11. At a kinetic energy of 300 GeV, ionization losses are responsible for a shift of the mean value of the energy loss of 0.9 GeV, slightly less than the value displayed in the ionization figure for $M = 100$ GeV in Fig. 5.10. This is obviously due to the fact that the R–hadron may change charge and hence may be neutral during part of the trajectory. At a kinetic energy of 20 GeV, the shift is larger, 1.9 GeV for this R–hadron mass. Thus, for low–energetic heavy hadrons, ionization losses are comparable to nuclear losses, while at high kinetic energies, nuclear losses completely dominate, as expected.

5.5.7 Dependence of energy losses on the phase space function

To evaluate the dependence on the parameter Q_0, appearing in the phase space function $F(Q)$, it is varied from 0.6 GeV/c^2 to 1.7 GeV/c^2. From Fig. 4.3, we note that the available phase space for $2 \rightarrow 3$ scattering decreases slightly for increasing Q_0, and therefore the energy loss is expected

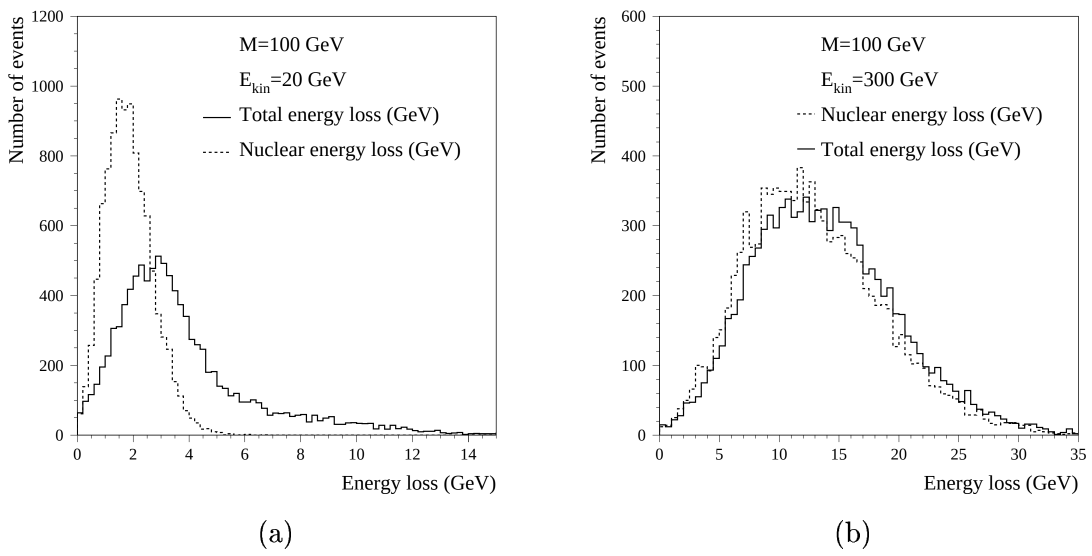

Figure 5.11: A comparison of total energy loss and the nuclear energy loss alone in 1 m iron for an R–hadron with mass 100 GeV for a kinetic energy of 20 GeV (a) and of 300 GeV (b). The mean values of the distributions shown in Fig. (a) are 3.8 GeV and 1.9 GeV respectively, while those in Fig. (b) are 13.8 GeV and 12.9 GeV respectively.

Mass (GeV/c^2)	Kinetic energy (GeV)	Q_0 (GeV/c^2)	$< E_{loss} >$ in 1 m iron (GeV)
100	20	0.6	3.8
		1.1	3.8
		1.7	3.8
100	300	0.6	14.3
		1.1	13.8
		1.7	13.3
100	500	0.6	20.5
		1.1	20.2
		1.7	19.9
600	20	0.6	6.5
		1.1	6.5
		1.7	6.5
600	300	0.6	6.8
		1.1	6.0
		1.7	5.6
600	500	0.6	12.1
		1.1	10.6
		1.7	9.6

Table 5.1: The mean value of the energy loss in 1 m iron for different values of Q_0. The default value is $Q_0 = 1.1$ GeV/c^2.

to decrease for increasing Q_0. For two values of the R–hadron mass, the total energy loss in 1 meter iron is studied for different values of Q_0, and the results are shown in Table 5.1. The dependence on Q_0 of the total energy loss is small, and indeed losses are smaller for increasing Q_0-values.

5.5.8 Penetration depth

In order to estimate the penetration depth of R–hadrons, the traversed path of an R–baryon in 1 m iron is studied. The typical energy of R–hadrons which are not stopped in the calorimeters is relevant, since those hadrons reach the outer parts of a typical detector; often the muon chambers. In Fig. 5.12, the traversed length in iron is shown for different R–hadron masses, with a maximum length of 1 m. A rapid saturation takes place, i.e. above a rather moderate value R–hadrons will punch through a typical calorimeter.

5.6 Comparison of ALEPH and ATLAS simulations

Summarizing, the differences between the ALEPH model and the new model are the following:

- The cross section for nuclear scattering in the two models differ. While in ALEPH, the cross section at low momentum vanishes, it is constant in ATLAS. At high momentum, the cross section for R-meson nucleon scattering is the same in the ALEPH and the new model. However, the ALEPH model does not take into account baryons, which have a cross section 3/2 times larger than R-mesons.

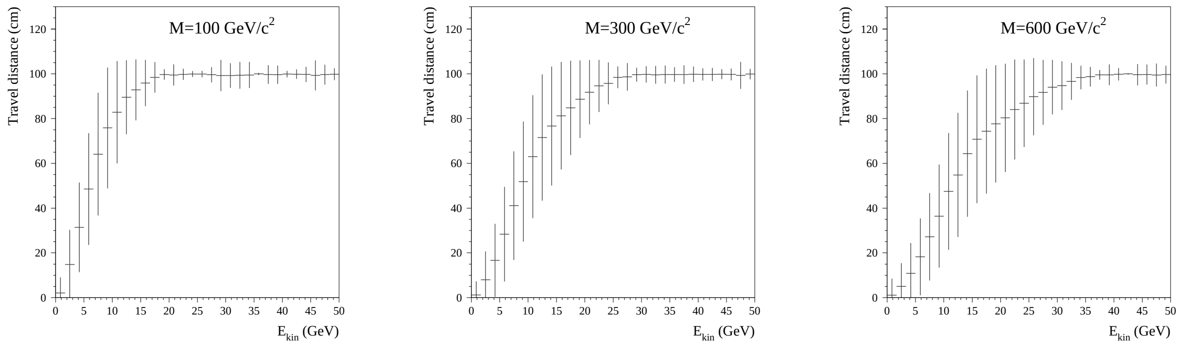

Figure 5.12: Comparison of traversed path of a singly charged R–baryon for different values of the R–hadron mass. The vertical lines represent the spread on the mean value.

- Baryon number exchange is not taken into account in the ALEPH model. R-mesons convert quickly to R-baryons, having a larger nuclear scattering cross section. Thus, more interactions occur. Besides, the possible formation of a doubly charged baryon can cause additional ionization losses.

- The way in which the final state multiplicity is determined differ. In ALEPH, KNO multiplicities are used, while in the new model, the available phase space is used as starting point. The difference occurs at high momenta, where the ALEPH model would result in a slightly smaller multiplicity.

In order to compare the ALEPH model and the new model, energy losses in 1 m iron are evaluated. In Fig. 5.13, energy losses are displayed as a function of the kinetic energy for three R-hadron masses. We observe that energy losses are comparable.

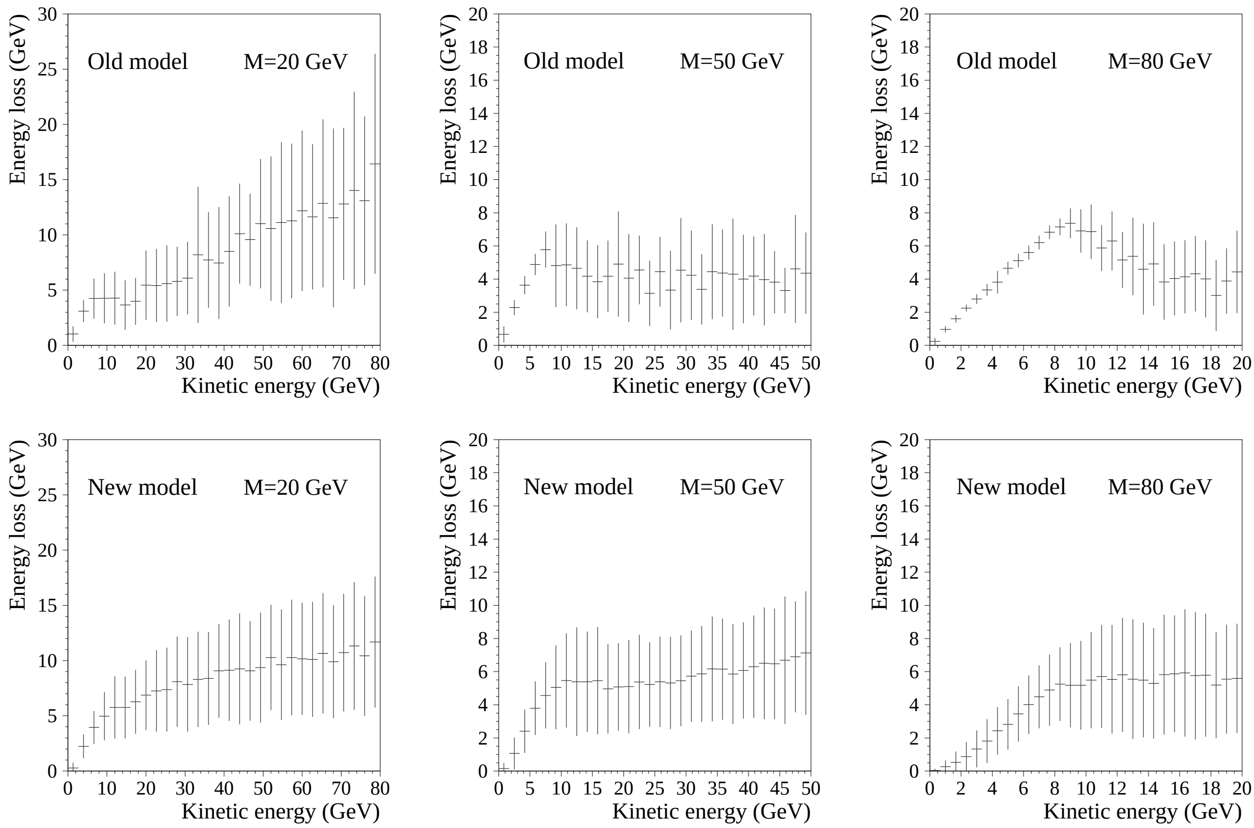

Figure 5.13: Profile histograms representing the average R-hadron energy loss in one meter iron and the spread on this average as a function of its kinetic energy, for the ALEPH (figures above) and the new (figures below) model.

Part II

ALEPH analysis

Chapter 6

LEP and the ALEPH detector

In this chapter, the ALEPH detector will shortly be described. In Section 6.1, some basic concepts are explained which are relevant for the understanding of colliding-beam experiments such as ALEPH and ATLAS. For en extensive overview of techniques in experimental particle physics, see e.g. Ref. [54]. Readers who already posses the basic knowledge of collider physics are advised to skip the first section. The remaining part of this chapter is devoted to a description of the ALEPH detector. This includes a short description of LEP in Section 6.2, and a summary of the most relevant parts of the ALEPH detector in Section 6.3.

6.1 Introduction

6.1.1 Accelerators

Two main types of accelerators are in use today. In a *linear* accelerator, a beam of particles passes through a straight vacuum tube via a chain of radio-frequency cavities to accelerate the particles. In a *cyclic* accelerator, or *synchrotron*, the beam is constrained in a circular path of fixed radius by a ring of magnets, and acceleration is accomplished as the particles traverse the cavities in the ring repeatedly. During the acceleration-process the magnetic field and the radio frequency of the cavities must be increased coherently in order to keep the beam in the same radius. At present, the largest and most famous synchrotron examples are LEP, described below, the Tevatron, just outside Chicago, and the LHC, discussed in Chapter 11. The energy eventually reached by a particle accelerated inside a synchrotron is determined by several factors. In the case of electrons, the most important limitation is synchrotron radiation. A particle of charge e, traveling with velocity β and energy $E = m\gamma c^2$, loses per revolution an energy given by [4]

$$\delta E = \frac{4\pi}{3}\frac{e^2\beta^3\gamma^4}{R}, \tag{6.1}$$

where R is the radius of curvature of the orbit. For an electron or positron accelerator, synchrotron radiation forms the main obstacle for reaching high energies. For protons of the same energy, the amount of energy lost to synchrotron radiation is a factor of $(m_p/m_e)^4 \approx 2000^4$ less, making proton beams more attractive for operating at high energies. However, the disadvantage of a hadron collider is that protons are composite particles, made of partons like quarks or gluons. Each parton carries only a fraction of the proton energy, and thus, while in electron-positron collisions the full beam energy is transformed into the production of new particles, in proton-proton collision only a small (unknown) fraction is used. Also, the parton-parton center-of-mass frame is not in the laboratory frame, so that the hard scattered system generally will carry a large momentum-component in the beam direction.

6.1.2 Terminology

The reaction rate R for a given process is given by

$$R = \sigma L, \tag{6.2}$$

where σ is the cross section (in units of cm^2) for the process and L is the luminosity (in units of $\mathrm{cm}^{-2}\ \mathrm{s}^{-1}$) of the machine, or the amount of particles crossing each other per second per surface unit. The *integrated luminosity* $\mathcal{L} = \int \mathrm{d}tL$ gives the number of collisions in a certain time interval:

$$N = \sigma \mathcal{L}. \tag{6.3}$$

For instance, the process $e^+e^- \to q\bar{q}$ has a cross section of approximately 10^2 pb= 10^{-34} cm^2. An *event* is an occasion where two elementary particles collide.

6.1.3 Colliding-beam detectors

When the two beams intersect, a collision may take place, resulting in the production of a large number of charged and neutral particles, which must be detected simultaneously. Because of the different character of the produced particles, typical experiments incorporate several types of detector techniques, often built up cylindrically with the axis in the direction of the beams. The main tasks of a particle detector are:

- Tracking of particles.
- Momentum measurement of particles.
- Particle identification.
- Triggering.
- Data acquisition.

At present, very large multicomponent detectors are built, which integrate many different subdetectors. The main components of a colliding beam detector are the following. First, the particle usually traverses a *tracking* detector. These are either finely segmented solid state devices, or gas-filled chambers with high voltage electrodes (often thin anode wires), providing gas amplification of ionization electrons. The resulting free charges drift to detection wires with the help of a electric and magnetic fields. This allows the spacial coordinates where the ionization occurred to be reconstructed and measured, and the trajectory of the particle to be reconstructed. The momentum of the particle can be inferred from the curvature of the trajectory in the magnetic field. The tracking system must be as transparent as possible in order to avoid effects like showering. After the tracking system, typically an *electromagnetic calorimeter* is traversed, where particles produce electromagnetic showers, which enable us to measure their energies and to identify them. A *hadronic calorimeter* usually surrounds the electromagnetic calorimeter to record the energies of neutral and charged hadrons that are not stopped in the electromagnetic calorimeter. Since the hadronic calorimeter is intended to stop most charged and neutral particles, the size is large and the structure is compact. Typical calorimeters are made of a dense, inactive, material to stop the particles, interleaved with active layers to record the interactions. Behind the hadron calorimeters, *muon chambers* may be located, which identify muons, the only particles passing the hadronic calorimeter. The size of a high energy experiment depends on the energies of the particles produced: the higher the energy of the particles, the deeper they penetrate. Also, the momentum resolution $\sigma(p)/p$ is proportional to p, but inversely proportional to r^2, where r is the radius of the tracking system. Thus, high energetic particles require large tracking systems.

Since the particle density decreases with $1/r^2$, highest accuracy of recording (granularity) is necessary at the inner radii of a detector, while it may decrease at outer radii.

Often only a fraction of the collisions is interesting. In order to determine whether the information of all subdetectors must be kept and written to tape, a *trigger* system is needed. Such a system uses typically information of the fastest detector components, so that a decision is taken fast. A trigger system consists often of different levels. If the trigger classifies an event as interesting, it is written to tape by the data-acquisition system. In ALEPH, the typically a few events per second was recorded to tape, while at LHC, the rate will be roughly 100 Hz.

6.2 The Large Electron Positron collider

The LEP (Large Electron Positron) machine was a synchrotron in which electrons and positrons circulated in opposite directions. Figs. 6.1 and 6.2 show an overview. The circumference of

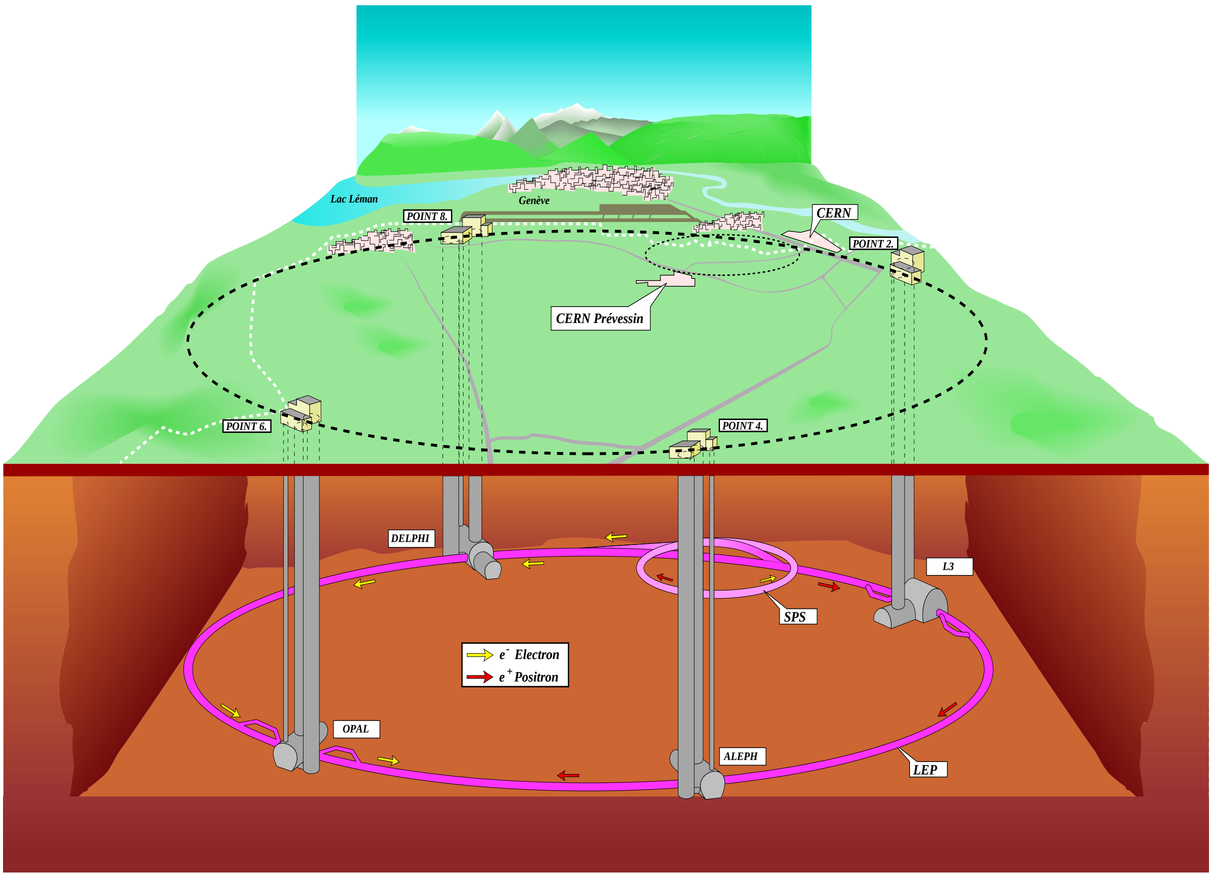

Figure 6.1: The location of the LEP ring in Geneva, Switzerland. This figure is obtained from Ref. [77].

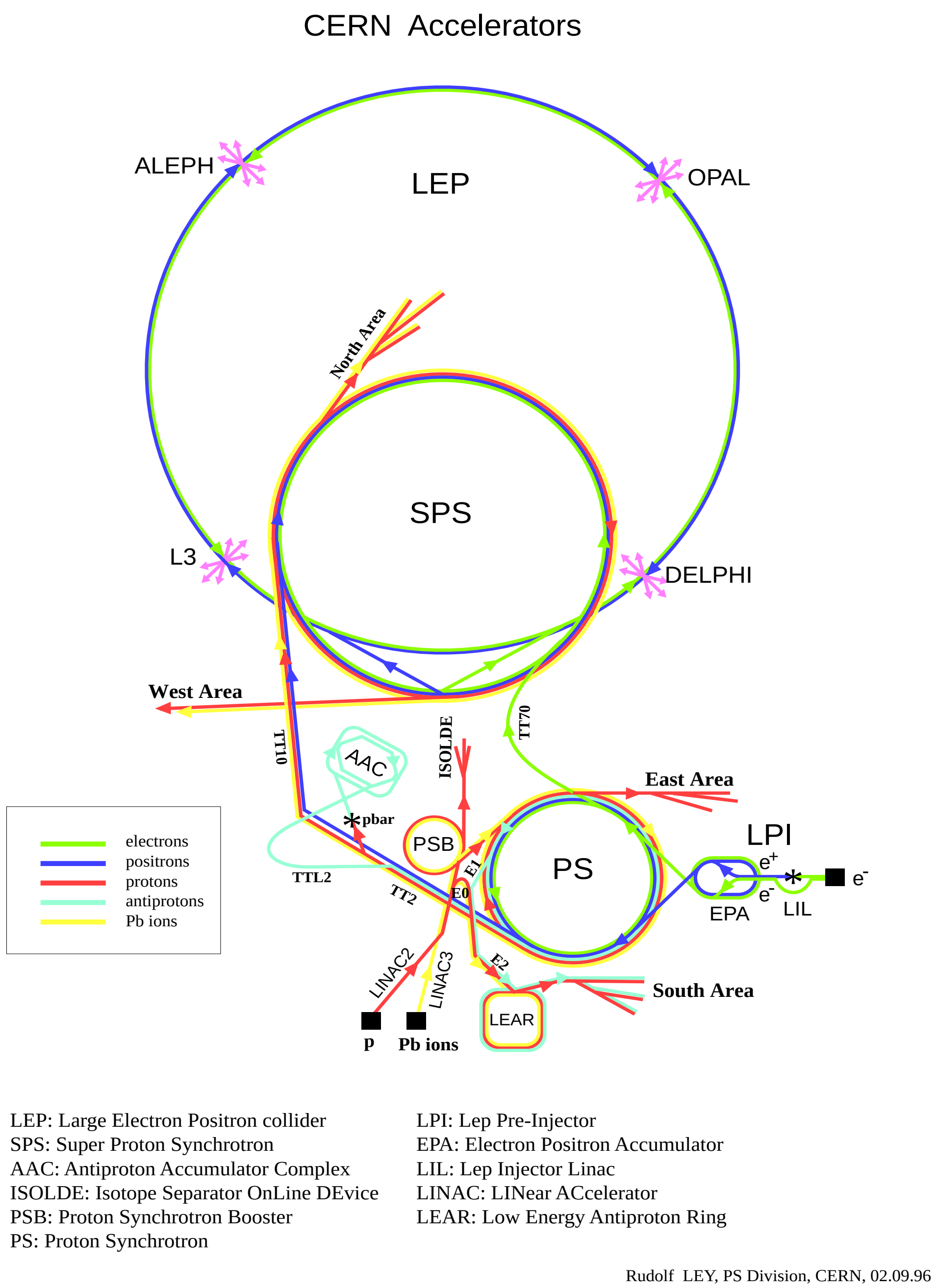

Figure 6.2: The LEP ring, with the chain of pre-accelerators, and the location of the four experiments. This figure is obtained from Ref. [77].

the LEP ring was 26.7 km and it was located in between the Jura mountains and lake Geneva. Colliding two beams of opposite charge allowed to use the same magnets and vacuum pipe for both beams, kept separated by electrostatic separators. Dipole magnets were used to bend the beam. The LEP project had two stages. At the first stage (LEP1), standard Radio Frequency (RF) cavities were used for acceleration, providing a center of mass energy of 91.2 GeV, the Z-boson mass. During the second stage (LEP2), a center-of-mass energy from 163 GeV, the threshold to produce two W-bosons, up to 209 GeV was reached. This was possible due to the replacement of the RF cavities by super-conducting cavities. The injection of positrons and electrons in the LEP ring started in a Lepton Pre-Injector (LPI) complex. This consisted of a linear electron accelerator (Lep Injector Linacs, LIL) producing 200 MeV electrons, and an electron-positron accumulator (EPA), accelerating them to 600 MeV. Positrons were produced by colliding 600 MeV electrons on a tungsten target, after which they were accelerated up to 600 MeV by the EPA. Electrons and positrons were accelerated further in the Proton Synchrotron (PS) to 3.5 GeV. Then the Super Proton Synchrotron (SPS) accelerated them up to 20 GeV, and finally they were accelerated further up to the final center-of-mass energy in the LEP ring. At four locations in the ring, the electron and positron beams intersected. At these locations large experimental halls were located, accommodating four experiments: ALEPH, DELPHI, L3 and OPAL, all being general purpose experiments. An overview of the LEP ring and the four experiments is given in Fig. 6.2.

6.2.1 Coordinate system

At LEP, the z-axis is defined to be in the direction of the electron beam, the x-axis points toward the center of LEP, and the y-axis points upward. The radius $r = \sqrt{x^2 + y^2}$. The polar angle to the z-axis is called θ, and the azimuthal angle is called ϕ.

6.3 The ALEPH experiment

6.3.1 Overview

A detailed description of the ALEPH (Apparatus for LEP PHysics) detector and of its performance can be found in Refs. [78, 79], and only a summary is given here. The design of the ALEPH detector followed the typical layout for a typical multi-purpose detector.The ALEPH detector could be divided into a tracking system at the inner radii, calorimeters in the middle and the muon chambers at the outside, adding up to a total dimension of $12\times12\times12$ m^3. The ALEPH detectors and the different subsystems are displayed in Fig. 6.3.

6.3.2 Tracking system

The vertex detector The vertex detector (VDET) was used for tracking closest to the interaction point, where the particle density and radiation level was highest. The detector consisted of two concentric layers of silicon wafers with double sided read-out. The vertex detector measured 24 cm in diameter and 1 m in length. Its spatial resolution was 12 μm, enabling identification of long-lived hadrons with lifetimes around 1 ps.

Inner tracking chamber The Inner Tracking Chamber was a conventional, cylindrical shaped, multi-wire drift chamber, which surrounded the vertex detector. It has a length of 2 meter, and an inner and outer radius of 13 and 29 cm respectively. It consisted of eight concentric layers of chambers, thereby providing eight $r\phi$ tracking points. The gas in the multi-wire drift chamber was a mixture of Argon (50%) and C_2H_6 (50%) at atmospheric pressure. The resolution in the $r\phi$-direction was ca 150 μm, while it was a few cm in the z-direction. Besides providing track measurements, the ITC provided information to the first level trigger.

Time projection chamber The time projection chamber (TPC) was the main tracking device in the radial region between 31 and 180 cm, surrounding the inner tracking chamber. Its total

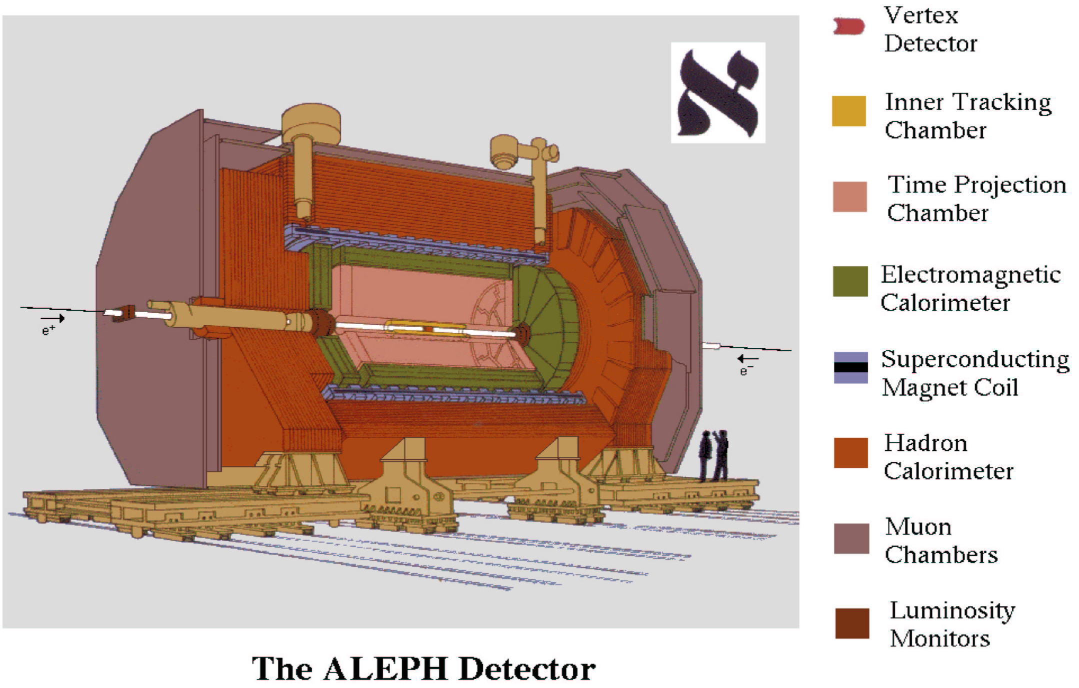

Figure 6.3: Subsystems in the ALEPH detector. This figure is obtained from Ref.[77].

length was 4.4 m, which was divided into two half-detectors, separated by a membrane at negative voltage, making the drift-length 2.2 m. The TPC was filled with a mixture of Argon (91%) and CH_4 (9%), slightly above atmospheric pressure. When a charged particles passed the TPC, it caused ionization of the gas mixture. An electric field of 115 Vcm^{-1} caused the ionization electrons to drift to the endplates, where the signal was recorded with a system of multi-wire proportional chambers. Up to 21 $r\phi$ coordinates were determined by the position of the electron avalanches on the endplates. The corresponding z coordinates were determined by the drift time. The TPC reconstructed charged tracks with a transverse momentum resolution of

$$\sigma\left(\frac{1}{p_T}\right) = 6 \times 10^{-4} \oplus 5 \times 10^{-3}/p_T \quad (\mathrm{GeV/c})^{-1}. \tag{6.4}$$

The accuracy of the determination of the $r\phi$ coordinates depended strongly on the inhomogeneities in the magnetic and electric fields. Laser tracks were used to precisely determine the inhomogeneities. Besides tracking, the task of the TPC was to identify particles, by measuring the ionization loss $\mathrm{d}E/\mathrm{d}x$ of a charged particle using the amplitude of the signal recorded at the end plates.

6.3.3 Calorimeters

The electromagnetic calorimeter The electromagnetic calorimeter (ECAL) consisted of layers of lead as absorbing material and proportional tubes as active material, operated in a gas mixture of Xe (80%) and CO_2 (20%). It had a length of 4.77 m, and inner and outer radii of 185 and 225 cm, respectively. The ECAL consisted of a barrel and two endcaps. Traversing electrons, positrons and photons produced electromagnetic showers in the lead, which resulted in ionization in the gas mixture in the active layer. An avalanche towards the anode wires resulted, which was measurable. The cathode layer of the proportional tubes were segmented in 3×3 cm pads, read out in towers pointing to the vertex. This gave the calorimeter an excellent spacial resolution. The energy resolution for electrons was at LEP2

$$\frac{\sigma(E)}{E} = \frac{0.18}{\sqrt{E/\mathrm{GeV}}} + 0.009. \tag{6.5}$$

This form is generic for most calorimeters and follows from the fact that energy deposition is the result of a stochastic process (left term) and overall detector noise (right term). At small polar angles and in the overlap region the resolution was slightly smaller.

The hadronic calorimeter The HCAL measured the energy deposited by hadrons and provides tracking of muons. It had an inner and outer radius of 3 m and 4.68 m respectively. It was made of 23 layers of 1 cm thick plastic streamer tubes, separated by 5 cm iron. The latter also provided the main mechanical support for the ALEPH detector. The thickness corresponded to 7.2 interaction lengths, enough to contain most hadronic showers at LEP energies. The structure was similar to that of the ECAL, build up from barrels and end-caps. The streamer tubes were operated in a mixture of argon (22.5 %), CO_2 (47.5%) and isobutane (30%). The energy resolution of the HCAL was for pions in the central region

$$\frac{\sigma(E)}{E} = \frac{0.85}{\sqrt{E/GeV}}. \tag{6.6}$$

6.3.4 The muon chambers

To identify muons, muon chambers were constructed around the HCAL. They consisted of two layers of streamer tubes, the outer layer positioned at a radius of 4.80 m.

6.3.5 The magnet system

The magnet was a superconducting solenoid coil which generated a magnetic field of 1.5 T in the z-direction. It was made of NbTi/Cu conductor and operated at a temperature of 4.4 K, achieved with liquid helium cooling. The current running through the coil was 5000 A. The HCAL acted as return yoke for the magnetic field.

6.3.6 Luminosity monitors

The integrated luminosity was the central value needed for the calculation of cross sections of observed processes. The luminosity was determined by measuring small-angle elastic (Bhabha) electron scattering, for which the cross section is precisely known. To measure this value, two small calorimeters, the LCAL (built at the Niels Bohr Institute) and the SiCAL, were installed, covering polar angles up to 2.6^o. At LEP2, in total ca 700 pb^{-1} was collected.

6.3.7 Trigger and readout

The purpose of ALEPH is to record all interactions from an e^+e^- annihilation and Bhabha scattering. The trigger was organized in three levels: a Level 1 hardware based trigger, using the ECAL and the ITC, a Level 2 hardware based trigger, using additionally the TPC, and a software based Level 3 trigger, making final checks. Approximately 30 different physics triggers were used, of which the most important ones were the following:

- *Total energy trigger:* the energy measured in the ECAL had to be above 9 GeV in the barrel, or 3 GeV in the end-caps together.
- *Single muon trigger:* a particle leaving tracks in the ITC and drift chambers must penetrate at least four HCAL planes.
- *Random trigger:* random events were selected independent of any trigger output, to study the detector noise.
- *Back-to-back trigger:* two back-to-back track segments in ITC and TPC.
- *Single charged electromagnetic trigger:* the energy measured in the ECAL must be above 1 GeV in the barrel, or 1.2 GeV in the end-caps together.

After the Level 1 trigger, the event rate was 2-10 Hz, while the Level 2 and 3 triggers reduced this further to 1-5 Hz. The efficiency for recording interesting physics events was close to 100%. If an event took place, all subdetectors were read out, and the information was stored on tape. These data, called raw data, were passed to an offline reconstruction program JULIA, taking care of pattern recognition, reconstruction of tracks and calorimeter energy deposits.

6.3.8 Track reconstruction

The track of a charged particles in a magnetic field has the form of a helix, and can be described by five parameters [79]. In ALEPH, a charged track is classified as a good track if it has $\cos\theta > 0$, at least 4 hits in the TPC, $|d_0| < 2$ cm and $|z_0| < 10$ cm, where θ is the angle of the track with the beam axis, d_0 the signed impact parameter [79], and z_0 the distance of closest approach.

6.3.9 Lepton identification and energy flow

One of the relevant issues for our analysis is lepton identification in JULIA. For electron identification, information from the ECAL and the TPC is used. Electrons and hadrons have significantly different shower characteristics. The transverse and longitudinal shower shapes are used as estimators, together with the ratio between the reconstructed measured momentum and the associated energy in the ECAL. Concerning muon identification, the requirements are a reconstructed charged particle together with characteristic hits in the HCAL and in the muon chambers. For more details about lepton identification the reader is referred to Refs. [78, 79].

A useful package of algorithms combining tracking information with calorimeter measurements is the *energy flow* package [79], which classifies tracks and calorimeter deposits as electrons, muons, charged tracks (if not identified as electron or muon), photons and neutral hadrons. For this purpose, the energy flow package combines calorimeter information with tracking information, so that any double counting is avoided. For the calculation of energies of all charged tracks (if not classified as electron or muon), the pion mass is assumed. For a charged R-hadron with momentum $\mathbf{p}$ measured in the tracking system, the particle energy is thus calculated as $\sqrt{m_\pi^2 + \mathbf{p}^2}$. The real mass is unknown for the detector, and is not counted. As an example, consider a charged R-hadron, with mass 75 GeV, and momentum 40 GeV/c. While the deposited energy cannot be larger than $E_{kin} = 10$ GeV/c^2, it will result in a measured energy $E \approx 40$ GeV/c! For a neutral R-hadron, no such effect occurs. A neutral R-hadron is identified as neutral hadron, and only the energy deposited in the calorimeter is measured. The energy and momentum of the neutral hadron are equal (massless assumption) and are given by the deposited energy.

At this stage it is useful to explain how the missing energy, missing mass, visible energy, visible mass, missing momentum and visible momentum are calculated with the energy flow package in ALEPH [80]. The visible energy E_{vis} in an event is calculated by taking the scalar sum of the energies of all energy flow objects. The missing energy is then simply defined as $\sqrt{s} - E_{vis}$. The visible momentum vector $\mathbf{p}_{vis}$ is calculated by taking a vector sum of the momenta of all energy flow objects, and the missing momentum vector points in opposite direction: $\mathbf{p}_{miss} = -\mathbf{p}_{vis}$. The visible mass is defined as the scalar sum of the masses of all energy flow objects, whereby for all charged tracks, if not identified as electron or muon, the pion mass is assumed. The missing mass in an event is defined as $\sqrt{|(\sqrt{s} - E_{vis})^2 - \mathbf{p}_{vis}^2|}$.

6.4 Achievements of LEP and ALEPH

The LEP accelerator operated from September 1988 until November 2000, with an eventual center-of-mass energy far above the value it was designed for! During LEP1 (1988-1995), the main goal was the precise determination of the Z-mass, the Z-width, and the Z-couplings. During LEP2 (1997-2000), the properties of the W-boson have been explored in great detail. The comparison of measurements and theoretical predictions of these quantities have been the most detailed tests for the Standard model ever made, and has qualified the Standard Model as the most successful description for the interactions of elementary particles.

Chapter 7

ALEPH: Monte Carlo simulation

An ALEPH search analysis is based on comparing real data, taken by ALEPH, with Monte Carlo simulated standard model events and signal events. This chapter focuses on the Monte Carlo generation. Before discussing the generation of signal and background events, we briefly discus in Section 7.2 the topology of the events. This discussion will be continued in more detail in the next Chapter. The Monte Carlo generation of signal events will be discussed in Section 7.3, including gluino hadronization. Then, in Section 7.4, a short resume of the Monte Carlo generation of the standard model background processes is given, followed by a few remarks about the data samples used in the analysis.

7.1 Overview

In Fig. 7.1, the different stages in an ALEPH analysis are displayed. The layout of the scheme is not unique for the ALEPH experiment, but is similar for every high energy physics experiment. Below, we pay attention to each of the four stages in the generation of the R-hadron signal, the standard model background, and the raw data.

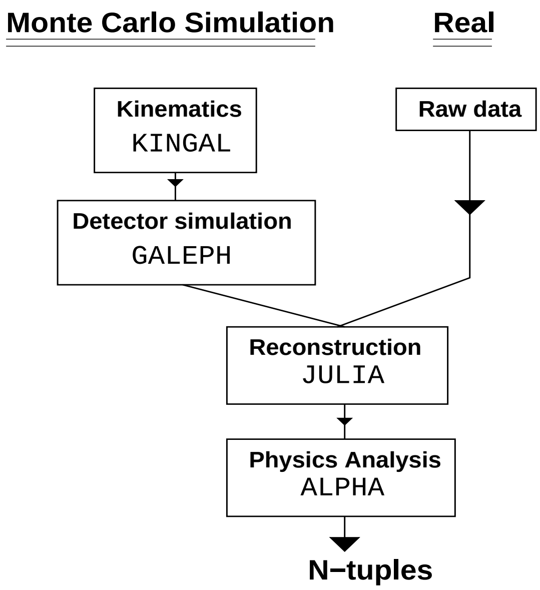

Figure 7.1: Overview of the different stages in an analysis, together with the corresponding ALEPH programs.

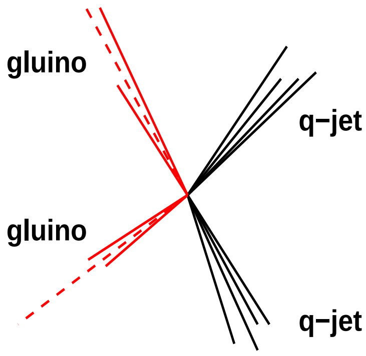

Figure 7.2: The final state topology of $e^+e^- \to \tilde{t}\bar{\tilde{t}} \to c\tilde{g}\bar{c}\tilde{g}$ events is two acoplanar jets and missing energy.

7.2 Search channel and topology

The focus of the ALEPH analysis is to search for LSP gluinos produced via $e^+e^- \to \tilde{t}\bar{\tilde{t}} \to c\tilde{g}\bar{c}\tilde{g}$, because of the relative lightness of the scalar top quark, as was mentioned in Section 2.5.2.

The final state topology of the process $e^+e^- \to \tilde{t}\bar{\tilde{t}} \to c\tilde{g}\bar{c}\tilde{g}$ is a pair of acoplanar[1] jets from the hadronization of the c and the $\bar{c}$, accompanied by 'missing energy' carried away by the mass of the two gluinos, as is displayed in a simplified way in Fig. 7.2. The presence of the gluino introduces a missing energy signal, though a less significant one than for non-strongly interacting stable supersymmetric particles. The reason for this missing energy signal is that the mass of the gluino cannot be measured, and all charged particles are assumed to have the pion mass and all neutral particles to be massless.

The R-hadron signatures in ALEPH are strongly dependent on the charge of the R-hadrons. The reason was already briefly mentioned in Section 6.3.9: for a neutral R-hadron, only the energy as measured in the calorimeter is recorded, while for a charged R-hadron, the momentum is measured. Thus, two neutral R-hadrons always result in a large missing energy, because the momentum is missing. Two charged R-hadrons have smallest amount of missing energy. We come back to this issue during the discussion of the selections in Chapter 8. Besides missing energy and jets, an R-hadron could leave tracks in the muon chambers, if it penetrates the calorimeters and is charged. Thus, some leptonic activity is expected.

The event topology depends strongly on the mass difference ΔM between stop and gluino. For events with small ΔM, only a small amount of energy is available for the recoiling c-quark system, which results in a small particle multiplicity and small visible energy. In addition, the R-hadrons tend to be emitted back to back. In contrast, events with large ΔM are characterized by large particle multiplicity and visible energy. Chapter 8 presents a more extensive discussion.

In conclusion, R-hadrons events are characterized by acoplanar jets and missing energy, but the amount depends (i) on the charge of the two R-hadrons and (ii) on the mass difference between the stop and the gluino. In addition, a signal in the muon chambers can be found.

[1]For clarification, two jets (or particles in general) are called *acoplanar* if they are not back-to-back with each other in the plane perpendicular to the beam axis, while they are called *coplanar* if they are. These terms should not be confused with *collinear* and *acollinear* jets, which are jets that are aligned (i.e. back-to-back in space) and not aligned, respectively, along a certain common axis. The terms *planar* and *aplanar* refer to *event* shapes rather than to two jets or particles. Planar events are events which consist of particles that lay in a plane, while *aplanar* events contain particles distributed everywhere in space, i.e. spherical events.

7.3 R-hadron signal simulation

7.3.1 Generation of the hard event

As explained in Section 2.5.2, gluinos may be produced at LEP via $e^+e^- \to \tilde{t}\bar{\tilde{t}} \to c\tilde{g}\bar{c}\tilde{g}$, and hadronize subsequently into R-hadrons. To generate events, the PYTHIA event generator version 6.156 is used [81], rather than version 5.7, which is common in ALEPH. Version 6.156 contains an improved treatment of the parton shower phase by matching it on to matrix elements for the relevant radiation processes, thereby allowing interferences between the radiating partons to be handled correctly. For example, in the decay $\tilde{t} \to c\tilde{g}$, the gluon radiation angles in radiation off stop, gluino and charm are correlated. Including matrix elements allows treating these correlations correctly. Besides, the matrix elements account for the spin of the radiating particle, a feature which was not present in PYTHIA 5.7. Since the generation of R-hadron events is not available in the default version of PYTHIA, it had to be extended with a few routines [82]. An example of the formation of two R-hadrons in the simulation is displayed in Fig. 7.3. In order to understand the topology of the R-hadron signal events at event generator level, some distributions for R-hadron events in the channel $e^+e^- \to \tilde{t}\bar{\tilde{t}} \to c\tilde{g}\bar{c}\tilde{g}$ are given in Fig. C.1 and C.2.

Radiation off squark and gluinos Stable gluinos and squarks are allowed to radiate gluons [83] as any other coloured particle. Due to their large mass, only very few gluons will be radiated.

Squark and gluino hadronization As discussed in Section 2.5.2, the stop has a longer lifetime/decay length than the typical hadronization scale (roughly 1 fm), and has time to hadronize

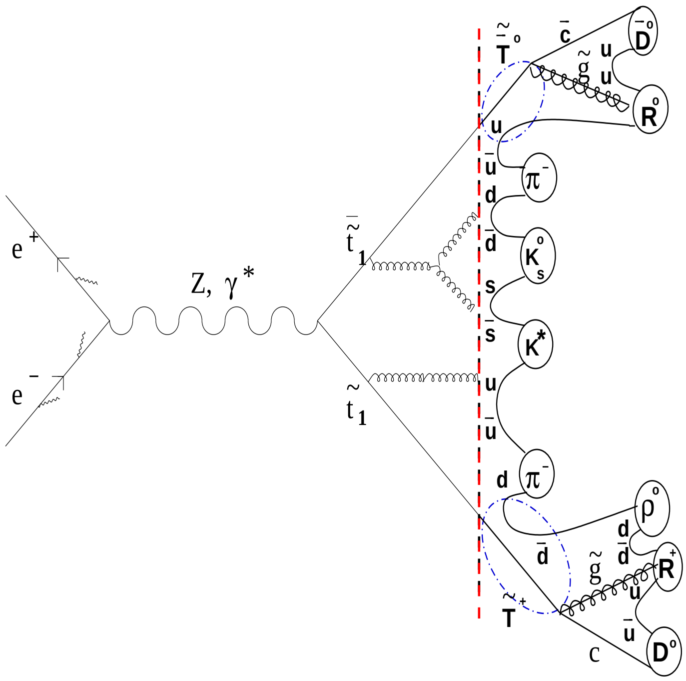

Figure 7.3: An example of the formation of two R-hadrons. At the right side of the vertical dashed line, hadronization takes place.

R-hadron	Amount (%)
$\tilde{g}u\bar{u}, \tilde{g}d\bar{d}$	38
$\tilde{g}u\bar{d}$	18
$\tilde{g}d\bar{u}$	20
$\tilde{g}d\bar{s}, \tilde{g}s\bar{d}$	10
$\tilde{g}u\bar{s}$	5
$\tilde{g}s\bar{u}$	6
$\tilde{g}s\bar{s}$	1
$\tilde{g}qqq$	1
$\tilde{g}\bar{q}\bar{q}\bar{q}$	1

Table 7.1: Fractions of the different R-hadrons produced in the hadronization process. These numbers are obtained by generating 2000000 events with R-hadrons.

before it decays. Dedicated routines have been developed for stop and for gluino hadronization. Fragmentation is handled with a Peterson fragmentation function [84]. This fragmentation parameter ϵ is extrapolated from that measured for b quarks [85] according to

$$\frac{\epsilon_{\tilde{q},\tilde{g}}}{\epsilon_b} = \frac{m_b^2}{m_{\tilde{q},\tilde{g}}^2}. \tag{7.1}$$

For the gluino, which is attached to two, rather than one, string pieces, the fragmentation is applied to each of the two pieces, thereby giving a larger energy loss than for a (s)quark.

R-mesons, R-baryons and R-gluino balls production are possible. All R-hadrons made of a given squark or gluino are assumed to have equal masses, with an electric charge of -1, 0 or 1, determined by the quark and squark content. The relative fractions of charged and neutral R-hadrons depend on the probability $P_{\tilde{g}g}$ to form a gluon-gluino bound state, which is essentially unknown and can vary between 0 and 1. The default value for this probability is 0.1, based on the fact that the gluino is a color octet. The fractions of charged and neutral hadrons are then obtained by simple isospin statistics, and are typically half and half, except for gluino R-hadrons, for which the additional possibility to form a gluino-gluon bound state enhances the fraction of neutral R-hadrons by an unknown amount. The fractions of different R-hadron types are displayed in Table 7.1. The amount of baryons is roughly 2%. The amount of R-mesons containing s-quarks is 23%, and the remaining R-mesons contain u and d quarks, half of them is charged and half of them is neutral.

In the processes studied here, R-hadrons are produced in pairs, so that double neutral (R^0R^0), mixed ($R^0R^\pm$) or double charged ($R^\pm R^\pm, R^\pm R^\mp$) final states are possible. There is no significant correlation between the electric charges of the two gluino R-hadrons, as is illustrated in Fig. 7.4. Charge conservation is ensured by the presence of additional fragmentation particles in the final state.

Stop-hadron decay We assume the branching ratio of the subsequent stop decay into charm and gluino to be 100%. This decay is isotropic and trivial due to the fact that the stop and anti-stop are scalars. As described above, the stop quark has time to hadronize in a stop R-hadron before decaying, thus the decay in $c\tilde{g}$ occurs inside the stop R-hadron. It is described in the framework of the spectator model [86], in which the bound state quarks act as spectators, i.e. they do not influence the stop decay.

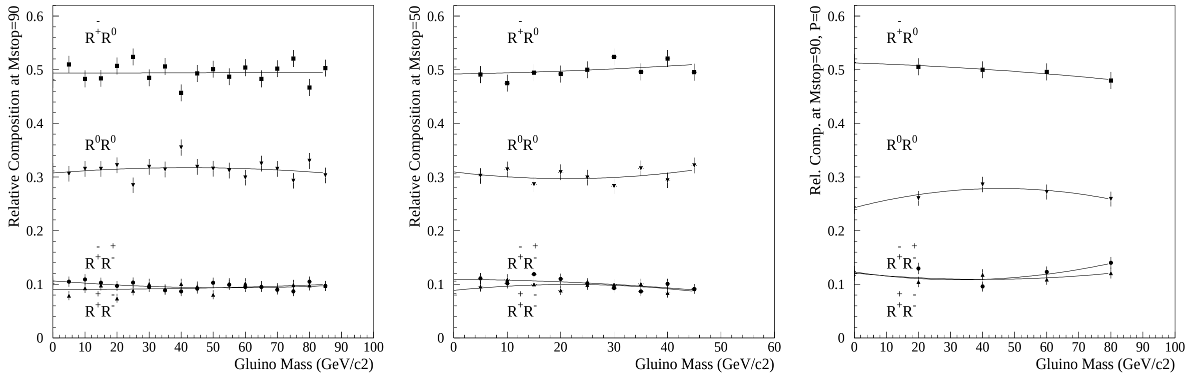

Figure 7.4: Charge composition as function of $M_{\tilde{g}}$ if $M_{\tilde{t}} = 90$ GeV/c^2 (left) and if $M_{\tilde{t}} = 50$ GeV/c^2 (middle), and if $P(\text{gg}) = 0$ (right). No significant correlation is seen.

7.3.2 R-hadronic interaction in the detector

The ALEPH detector simulation program is a GEANT3 based program called GALEPH. This program fully simulates all materials and responses of all sub-detectors of ALEPH. The exact simulation of R-hadrons in ALEPH is extensively discussed in Section 5.3.

7.3.3 Free parameters in event simulation

Several unknown parameters, listed below, are needed to fully specify the R-hadron phenomenology, and may be the source of sizable systematic errors:

- The probability $P_{\tilde{g}g}$ to form a gluon-gluino bound state. This quantity is essentially unknown and can vary between 0 and 1. For $P_{\tilde{g}g} = 0$, the fractions of double neutral, mixed and double charged final states are approximately 25%, 50%, and 25%, respectively. In the configuration in which $P_{\tilde{g}g} = 1$ (unlikely for gluino masses in excess of 25 GeV/c^2 [19, 36]), only purely neutral final states are produced.

- The effective spectator mass $M_{\text{spec}}^{\text{eff}}$ of squark and gluino R-hadrons. It roughly corresponds to the difference between the constituent mass and the current algebra mass. The value obtained from hadron mass spectroscopy is $M_{\text{spec}}^{\text{eff}} = 0.5^{+0.5}_{-0.2}$ GeV/c^2. The spectator mass influences the center-of-mass energy of the string spanned between the charm-quark and the spectator quark, and therefore the energy available for the production of extra hadrons. A higher value for m_{spec} results in principle in a slightly smaller multiplicity, but the effect is expected to be very tiny.

- The gluon constituent mass M_{g}^{c}. Its value is estimated from glueball searches [64] to be $M_{\text{g}}^{\text{c}} = 0.7^{+0.3}_{-0.4}$ GeV/c^2, typically twice smaller than the quark constituent mass. A change in the gluon constituent mass influences only events with gluino-gluon bound states. In those events, a higher gluon constituent mass means that less energy is available for the surrounding string systems and consequently for hadronization. This may result in a slightly smaller multiplicity. Again, the effect is tiny and may totally be washed out by other factors.

- The total cross section σ_{RN} of R-hadron-nucleon scattering. In the detector simulation, it is assumed to be equal to the cross section $\sigma_{\pi\text{N}}$ of pion-nucleon scattering, and to have the same $\sqrt{s}$ dependence. Thus, the R-hadronic interaction length is calculated using the cross section in the high momentum region, where the additive quark rule applies for cross section calculations [56, 60], see also Section 3.3.2. For a $\tilde{\rm g}$g bound state, the cross section is different from that for pion-nucleon scattering: when such a state scatters on a proton there are only 3 possibilities rather than 6 to attach a Pomeron, but each counts for a factor 9/4. Thus, the cross section is $(3/6) * 9/4 = 9/8$ larger. Similarly, the R-baryon ($\tilde{\rm g}$qqq) cross section can be seen to be 3/2 larger. For squark-R-mesons ($\tilde{\rm q}\bar{\rm q}$), the same argument yields a ratio of 1/2 while, for squark-R-baryons ($\tilde{\rm q}$qq), the ratio is equal to unity. From the above it follows that it is reasonable to use an average R-hadronic interaction cross section identical to that of pions, with an uncertainty of ±50%. As was explained in Section 5.3.2, there were a few objections to this approach, but these will be covered by the systematic error analysis.

- The stop mixing angle may be a source of uncertainty. As explained in Section 2.5.1, the size of the mixing angle influences the size of the stop coupling to the Z boson, which influences the amount of ISR and FSR in stop pair production. This, in turn, influences slightly the topology of the event. The default value for the mixing angle is 56^o, corresponding to maximal mixing.

7.3.4 Simulated signal samples

In order to design the selection criteria, hundreds of simulated signal samples of 1000 events each were generated for the channel $\rm e^+e^- \to \tilde{t}\bar{\tilde{t}} \to c\tilde{g}\bar{c}\tilde{g}$. For squark pair production, samples with squark and gluino masses ranging from 0 to 90 GeV/c^2 with a typical 5 GeV/c^2 step were generated, with two values of the squark mixing angle: *(i)* 0° and *(ii)* the value for which the squark coupling to the Z vanishes, *i.e.*, 56° for stops and 68° for sbottoms. An interface from PYTHIA 6.156 was not available and was written for this purpose. All samples were reconstructed with JULIA and processed through the detector simulation program GALEPH. The analysis program used here was CHAMINOU [87], a general program for supersymmetry searches in ALEPH. An examples of an R-hadron event is displayed in Fig. 3 (for $m_{\tilde{\rm t}}$= 80 GeV/c^2, $m_{\tilde{\rm g}}$= 75 GeV/c^2) and in Fig. 7.5 (for $m_{\tilde{\rm t}}$= 80 GeV/c^2, $m_{\tilde{\rm g}}$= 30 GeV/c^2).

7.4 Background simulation

Before reviewing the Monte Carlo generators used for the generation of Standard Model background events, we discuss first which Standard Model background processes could mimic R-hadron events.

7.4.1 Standard Model background processes

The Standard Model background consists of several processes. Their Feynman diagrams and cross sections are displayed in Fig. 7.6 and Fig. 7.7 respectively:

- Two-fermion processes: $e^+e^- \to f\bar{f}(\gamma)$. These processes are displayed in Fig. 7.6(b) and 7.6(f). The fermion f can be a quark, in which case it usually is referred to as $q\bar{q}$ background. The topology of two fermion events depends on whether a high energetic photon is emitted or not. If no photon is emitted, the collinearity, the angle between the two outcoming fermions or jets, is close to 180^o; in other words the fermions are 'back to back'. Furthermore, the visible energy is close to the center-of-mass energy and the total

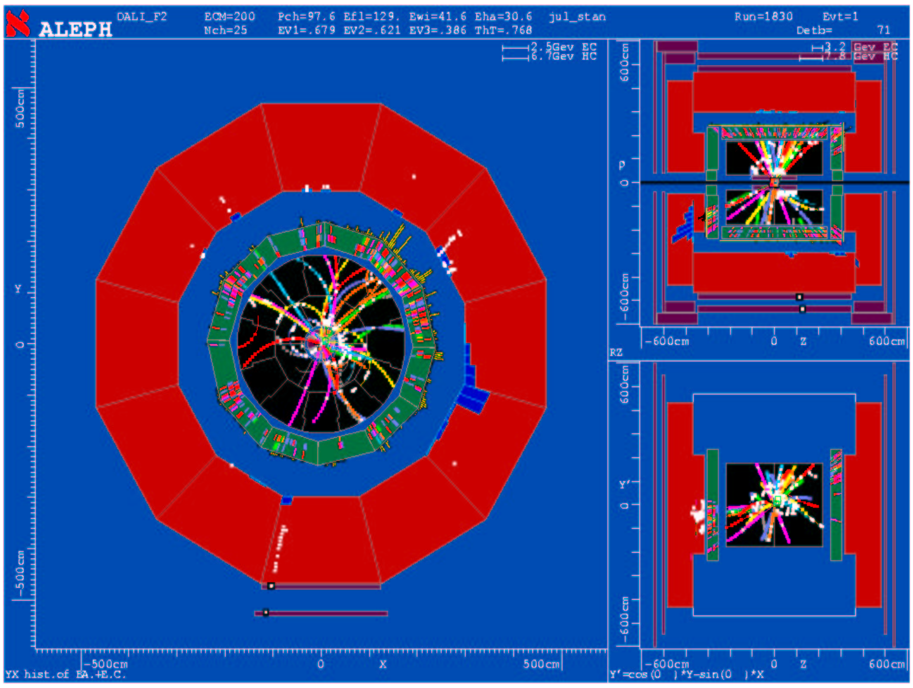

Figure 7.5: A simulated R-hadron event in the ALEPH detector. A neutral R-hadron is produced, which changes charge somewhere in the calorimeters, and reaches the muon chambers while being charged, leaving hits (in the negative y-direction). Also, a charged R-hadron is produced at $\phi = 135^0$, reaching the hadronic calorimeter but not the muon chambers.

(vector sum) momentum is close to zero, since it cancels in all directions. Such events could mimic R-hadron events with very high R-hadron mass, since such R-hadrons would also be emitted back to back. In case one or more high energy photons are emitted, the configuration differs. The photon is preferably emitted with an energy such that the mass of the $f\bar{f}$ system is close to the Z-boson mass. The energy of the photon is

$$E_\gamma = \frac{s - m_{f\bar{f}}^2}{2\sqrt{s}} \approx \frac{s - m_Z^2}{2\sqrt{s}} \tag{7.2}$$

This feature is referred to as radiative return to the Z-resonance. Most photons are emitted collinear with the incoming electron or positron, and would escape in the beam-pipe. Only photons with large transverse momenta can be detected. If the photon is detected, no missing energy signal is present. If the photon escapes into the beam-pipe, the total visible energy is close to the Z-mass, and the missing momentum in the direction of the beam-axis is large. All the above properties make it possible to distinguish this background from R-hadron events. The special case in which the outgoing fermions are an electron and a positron, which is referred to as Bhabha scattering. Bhabha events are characterized by a large amount of electromagnetic energy in the forward region, a small total transverse momentum, and a visible energy close to twice the beam energy, deposited in the forward region. The electron pairs are produced in a back to back configuration.

- Two-photon processes, $e^+e^- \rightarrow e^+e^-f\bar{f}$. This process is displayed in Fig. 7.6(a). In the majority of these events, the final electron or positron escapes undetected into the beam pipe, resulting in a large amount of missing energy in the transverse direction. The final

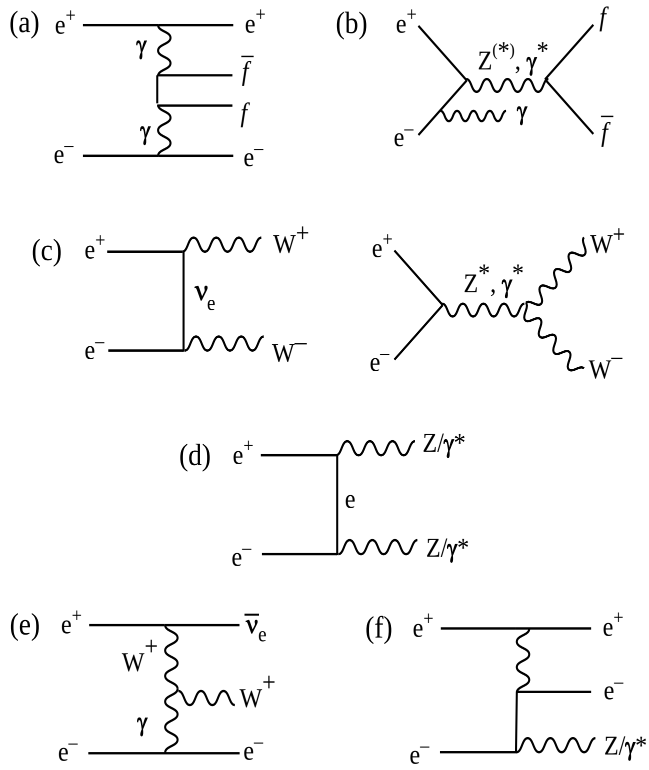

Figure 7.6: Feynman diagrams of Standard Model background processes at LEP2. This figure is obtained from Ref. [71].

state fermions can be quarks or leptons. The events are characterized by large amount of missing energy, low multiplicity, small total transverse momentum and a lot of visible energy near the beam-axis. All these features make it easy to distinguish these events as background.

- Four-fermion processes. We distinguish several different kinds of four-fermion processes:
  - WW-pair production. The pair production of a $W^{\pm}$ occurs via a t- or an s-channel exchange, as can be seen in Fig. 7.6(c). Each W has the possibility to decay leptonically ($W^{\pm} \to \ell^{\pm}\nu$) or hadronically ($W^{\pm} \to q\bar{q}$). The final state topology depends on the decay of the W-bosons. In case both W's decay leptonically, the missing energy can be large due to escaping neutrinos. Since no jets are present, such events can easily be distinguished from R-hadron events. On the contrary, if both W's decay hadronically, the event contains jets, the missing energy is small, the event multiplicity is large, and the event is rather spherical. Such events are much like R-hadron events with a small R-hadron mass, and are difficult to reject. Also, events with one W decaying leptonically, form a problem, since such events are characterized by missing energy due to the escaping neutrino, by one charged lepton, and by two acoplanar jets. These features are approximately the same as one expects for a signal event containing a singly charged R-hadron, which can fake a muon.

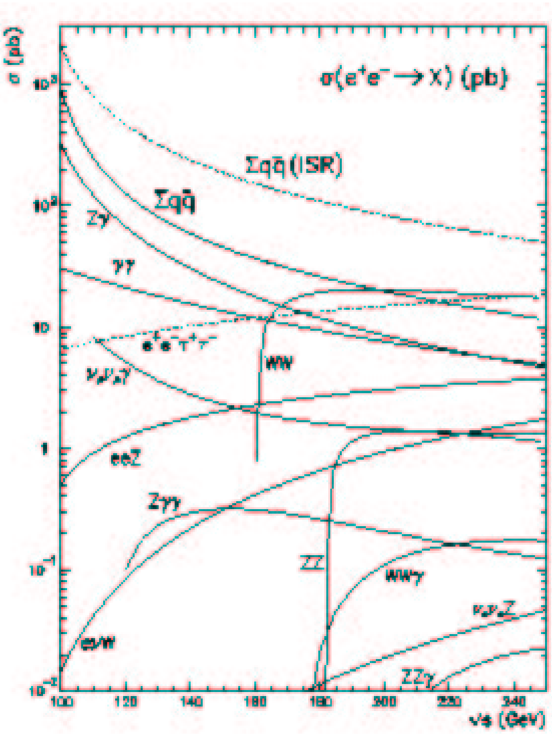

Figure 7.7: Cross sections of the Standard Model background processes. This figure is obtained from Ref. [71].

- ZZ or $\gamma\gamma$ - pair production, displayed in Fig. 7.6(d). The decay modes of the Z-boson are $Z \to q\bar{q}$ (70%),$Z \to l^+l^-$ (10%), $Z \to \nu\bar{\nu}$ (20%). As for WW-pair production, the topology depends on the decay mode, and these events mimic in some cases R-hadron events. However the production cross section is relatively small.
- Weν-production. This process, displayed in Fig. 7.6(e), occurs via the production of a single W. Typically the initial electron or positron escapes in the beam-pipe, resulting in events with a large longitudinal missing momentum, and a small transverse momentum. In case the W decays leptonically, the event has small multiplicity and visible mass. If it decays hadronically, the multiplicity is larger and the visible mass is close to the W-mass. For the same reason as for WW-background events, which decay leptonically, these events mimic R-hadron events.
- Zee-production, see Fig. 7.6f. As in the Weν-background, it often happens that one (or both) of the initial electron or positron escapes in the beam-pipe, resulting a large longitudinal missing momentum and small transverse momentum. The topology of such events depends on the decay channel of the Z-boson. The main problem for our analysis are events in which the Z-boson decays hadronically, in which case the event is characterized by two acoplanar jets, a high multiplicity, and a visible mass close to that of the Z-boson. These events mimic R-hadron events with small R-hadron mass.

7.4.2 Simulated background samples

For the simulation of the standard model background processes, Monte Carlo samples have been used with corresponding luminosities much larger than the luminosity of the data. In Table 7.2,

Standard model process	Generator	reference
Bhabha scattering	BHWI01	[88]
Other two-fermion processes	KORALZ	[89]
Two-photon processes	PHOTO02	[90]
W^+W^--pair production	KORALW	[91]
$We\nu$	GRC4F	[92]
Zee, ZZ, $Z\nu\bar{\nu}$	PYTHIA	[93]

Table 7.2: Standard Model background samples together with the generators used and their reference.

the physics event generators are listed, together with their references. For this analysis, background samples were available which were already processed through the whole chain of event generation, detector response with GALEPH, reconstruction with JULIA, and physics analysis with CHAMINOU.

7.5 Data samples

As for the background samples, data samples were available which had already been processed through the whole chain, including the analysis program CHAMINOU. The integrated luminosities and center-of-mass energies of the data which will be analyzed are indicated in Table 7.3.

Year	Luminosity [pb^{-1}]	Energy range [GeV]	$\langle\sqrt{s}\rangle$ [GeV]
2000	9.4	207-209	208.0
	122.6	206-207	206.6
	75.3	204-206	205.2
1999	42.0	-	201.6
	86.2	-	199.5
	79.8	-	195.5
	28.9	-	191.6
1998	173.6	-	188.6
1997	56.8	-	182.7

Table 7.3: Integrated luminosities, center-of-mass energy ranges and mean center-of-mass energy values for the data collected during the years 1997-2000. In total, 674 pb^{-1} was collected.

Chapter 8

ALEPH: Selections

In order to distinguish signal from background, a set of selection criteria must be developed, which is sensitive to the signal. An excess of events in the ALEPH data in comparison with Standard Model predictions, will allow us to claim a discovery, while an agreement may allow us to exclude the signal. The selection therefore forms the most central issue of the whole analysis. The following aspects are covered in this chapter. In Section 8.1 some definitions related to the development of a selection will be given. In Section 8.2, the statistical method will be presented which will be used to exclude (or discover maybe?) an R-hadron signal. Also, the optimization of the selection is presented there. In Section 8.3, possible event variables will be discussed which are used in the selection. Section 8.4 consists of a presentation of the different selections, and discusses how to switch between them. Finally, in Sections 8.5 and 8.6, the total selection efficiency and the background expectations are given. This Chapter ends with a few remarks about searching for gluinos from sbottom decay.

8.1 Definitions

Whether the selection applied on data and generated events, is appropriate, depends on two quantities:

- the signal *efficiency* ϵ describes the efficiency of a certain selection on a signal sample and is defined as

$$\epsilon = \frac{\text{Number of selected events}}{\text{Number of generated signal events}}. \tag{8.1}$$

- the number of *background* events n_b that survives after the selection.

By comparing real data of a certain luminosity, with background samples with the same luminosity, it is possible to exclude or discover a signal. An event from the data-sample, surviving all cuts of a certain selection, is called a *candidate*.

The amount of candidates N in a sample depends on the total amount of events in the data sample, represented by the luminosity $\mathcal{L}$, on the efficiency ϵ of the selection, and on the cross section σ of a process, as follows

$$N = \epsilon\sigma\mathcal{L}. \tag{8.2}$$

Before we start going into detail of how to make an appropriate selection, it is useful to first discuss the statistical method, on which the analysis is based.

8.2 Extraction of search results

8.2.1 The significance of a signal

In an experiment, based on event counting, in which the average number of events ν after applying a selection, is small, the probability of observing n events is given by the Poisson distribution function:

$$P(n,\nu) = \frac{\nu^n}{n!}e^{-\nu}. \tag{8.3}$$

The mean value and the variance of the Poisson distribution are both equal to ν. For large values of ν, the Poisson distribution function approaches a Gaussian distribution function.

If the expected number of background events is n_b, then the probability that, due to a statistical fluctuation, a number of n_o events or more is observed, is

$$\alpha = \sum_{i=n_o}^{\infty} \frac{n_b^i e^{-n_b}}{i!}. \tag{8.4}$$

The quantity α is a measure for the significance of a signal. To claim a discovery of a signal for physics beyond the standard model, the value of α must be very close to zero. The most commonly used discovery criterion is $\alpha < 5.7\times10^{-7}$, which would correspond to a Gaussian standard deviations from the standard model value of 5σ. In other words, the *confidence* in the hypothesis, that the signal is present, and that the observed number is not due to a statistical fluctuation, is then 99.999943%.

In the absence of any significant deviation from the standard model hypothesis, exclusion limits on the signal can be set. The way, in which exclusion limits are set, depends on whether we take into account the expected background, or not. The former method is called the *method with background subtraction*, while the latter case is referred to by *method without background subtraction.* Since in this case it is not a-priori clear which method is best, we discuss both.

8.2.2 Confidence level without background subtraction.

In case the reliability of the background is small, and the expected amount of background passing the selection is small, upper limits on the signal cross section can be set assuming that all observed events are signal events. Since we actually set limits on the number of signal plus background events, this method results in conservative limits on the signal. Let n_o be the observed number of candidates, ν_s the unknown average number of signal events, ν_b the expected average number of background events. If $\nu_c = \nu_s + \nu_b$ is the unknown mean number of candidates, we define the quantity ν_o as the ν_c value, such that the probability of finding in the search experiment a number of events i less than or equal to n_o is 1-α. Thus,

$$1-\alpha = \sum_{i=0}^{n_o} e^{-\nu_c}\frac{\nu_c^i}{i!}. \tag{8.5}$$

In other words, the probability, that we would observe, due to fluctuations, more events than n_o, is less than α. The usual criterion for exclusion is α =0.05, and in that case we have excluded the hypothesis, that both signal and background were present, with 95% confidence level (CL). In table 8.2.2 we list the 95% CL upper limit on the average expectation value of the signal, ν_{95}^n when n events are observed. The advantage of this method is that no assumptions are made on the character of the background and consequently no systematic errors arise from this source.

n_o	ν_n^{95}
0	3.00
1	4.74
2	6.30
3	7.75
4	9.15
5	10.51
6	11.84
7	13.15
8	14.43
9	15.70

Table 8.1: The 95% CL upper limit on the average expectation value of the signal, ν_n^{95}, when n events are observed and no background is subtracted.

8.2.3 Confidence level with background subtraction.

In some cases there is not enough information available to distinguish between signal and background, e.g. when the expected signal is very small. A consequence would be that a downward fluctuation of the observed background would result in a much too optimistic exclusion of the signal. However, the confidence level observed for the signal plus background hypothesis can be normalized to the confidence level observed for the background-only hypothesis [94]. If the unknown average mean number of events is a sum of signal and background events $\nu_c = \nu_s + \nu_b$, the average expected number of background events is ν_b, and n_o is the observed number of candidates, we define

$$1 - \alpha = \frac{\sum_{i=0}^{n_o} \frac{(\nu_b+\nu_s)^i e^{-(\nu_b+\nu_s)}}{i!}}{\sum_{i=0}^{n_o} \frac{\nu_b^i e^{-\nu_b}}{i!}}. \tag{8.6}$$

Thus, $1-\alpha$ is the likelihood ratio between the signal+background hypothesis and the background-only hypothesis for observing a number of candidates i which is less than or equal to n_o. The usual exclusion criterion is $\alpha \leq 0.05$. Then, the probability is at least 0.95 that the average number of signal events is below ν_s, or the confidence level is 95%. Note that 'subtracting' background should thus not be taken too literally, a *normalization* with the expected background is applied rather than a *subtraction* of all expected background from the signal.

8.2.4 Selection optimization

To determine the positions of the most important cuts, the N_{95}-method [95] is used. The purpose of this method is to exclude a process, assumed not to take place, as strongly as possible, at a given confidence level, here 95%. The selection is considered to be optimal if the 95 % CL average upper limit on the signal cross section, $\bar{\sigma}_{95}$, is minimal, thereby excluding R-hadrons with masses as large as possible. Let's first discuss how to optimize a selection if no background subtraction is applied. Let k_n be the 95% CL upper limit set on the expectation value of a signal when n events are observed. The number of observed events, n, is selected from a Poisson distribution with average value ν, see Eq. (8.3), which, if the process is assumed not to take place, is the average expected number of background events ν_b. The k_n values are given in Table 8.2.2. Now, in a fraction $P(0, \nu_b)$ of a series of gedanken experiments, no candidate events will be found, and the 95 % CL upper limit on the number of signal events is k_0. In a fraction of $P(1, \nu_b)$ of the experiments, one candidate events will be found, and the 95 % CL upper limit on the number of signal events is k_1, etc. The average value of k is then

$$< k >= \sum_{n=0}^{\infty} k_n P(n, \nu_b) \simeq 3(1 + 0.581\nu_b - 0.032b^2 + 0.005\nu_b^2 - ...). \tag{8.7}$$

where the latter expansion is only good for $\nu_b < 1$. The selection is optimal, when $< k >$ is as small as possible.

The case in which background is subtracted is equally simple, the only difference is in the calculation of the average: instead of using a Poisson distribution function, we use the likelihood ratio:

$$< k >= \sum_{n=0}^{\infty} k_n \frac{P(n, \nu_b + \nu_s)}{P(n, \nu_b)}. \tag{8.8}$$

Again, the selection is optimal, when $< k >$ is as small as possible. Whether a similar expansion as the one in Eq. (8.7) is possible or not, depends on the amount of expected background. From now on, the smallest value for k will be called $\bar{n}_{95}$. Translating this into an upper limit at 95% on the average signal cross section is done with the help of Eq. (3.2):

$$\bar{\sigma}_{95} = \frac{1}{\epsilon\mathcal{L}} \bar{n}_{95}. \tag{8.9}$$

In conclusion, selection optimization following the N_{95} procedure is based on the minimization of the expected upper limit at 95% on the average signal cross section, $\bar{\sigma}_{95}$.

8.3 Event variables

In Section 7.2 was already mentioned that the final state topology of the process $\mathrm{e^+e^-} \to \tilde{\mathrm{t}}\bar{\tilde{\mathrm{t}}} \to \mathrm{c}\tilde{\mathrm{g}}\bar{\mathrm{c}}\tilde{\mathrm{g}}$ is a pair of acoplanar jets from the hadronization of the c and the $\bar{\mathrm{c}}$, accompanied by missing energy carried away by the mass of the two stable gluinos. As was also mentioned, the event topology depends strongly on charge of the R-hadrons, and on the mass difference ΔM between stop and gluino. Although the missing energy signature is less prominent than for events with squarks decaying into jets plus a weakly interacting LSP, the presence of some missing energy signal, in combination with acoplanar jets allows to apply a selection based on two acoplanar jets. The discriminant variables listed below were designed for generic acoplanar jet searches in ALEPH [87]:

- the visible mass M_{vis} and energy E_{vis}, computed with all energy-flow particles, see Section 6.3.9;
- the energy E_{12} detected within 12° from the beam axis;
- the total energy carried by neutral hadrons, E_{NH};
- the energy of the most energetic lepton, E_ℓ;
- the energy in a 30° half-angle cone around the most energetic lepton, E_ℓ^{30};
- the energy computed without the identified leptons, E_{had};
- the energy measured in a 30° azimuthal wedge around the direction of the missing transverse momentum, E_{Wedge};

- the energy measured beyond 30° from the beam axis, E_{30};

- the momentum transverse to the beam axis, computed with all energy flow particles, p_T, without neutral hadrons, p_T^{exNH} and with good tracks only, p_T^{ch};

- the number of good tracks, N_{ch};

- the acoplanarity angle Φ_{acop}, between the directions of the momenta in the two event hemispheres, projected onto a plane perpendicular to the beam axis. Here, the hemispheres are defined with respect to a plane perpendicular to the thrust axis (see below). An event with two back to back jets has an acoplanarity angle close to 180^0;

- the transverse acoplanarity angle, Φ_{acopT}, defined as above, but the hemispheres are now defined with respect to the transverse thrust axis, *i.e.*, the thrust axis of the event projected onto a plane perpendicular to the beam axis. This variable useful for events which are very unbalanced along the z-axis. The transverse acoplanarity angle is close to 180^0 for events which are nicely balanced when projected onto a plane perpendicular to the beam axis;

- the cosine of the polar angle of the missing momentum vector, $\cos\theta_{\mathrm{miss}}$;

- the cosine of the polar angle of the thrust axis, $\cos\theta_{\mathrm{T}}$;

- the event thrust T, a measure for the degree of collimation of the event. $T = max_{\hat{n}} \frac{\sum_i |\vec{p}_i \cdot \hat{n}|}{\sum_i |\vec{p}_i|}$ where the sum is over reconstructed particles i, and the thrust axis $\hat{n}$ is the direction which maximizes T. The thrust ranges between 0.5 (for events with jets homogeneously distributed in space, open events) and 1 (perfectly collimated jets);

- the polar angle of the scattered electron, θ_{scat}, computed from the missing energy and momentum under the hypothesis that the event originates from a $\gamma\gamma$ interaction, in which one of the electrons is scattered but undetected due to detector inefficiencies. The other electron is undeflected, going into the beam-pipe. The scattering angle in 2-photon events is in general close to zero, while it is much larger in case of Weν-events.

In order to account for the dependence of the selection on the center-of-mass energy, relevant cuts will be performed in terms of variables normalized to the beam-energy.

8.4 Selections

Selection criteria follow to some extent those developed for the ALEPH squark searches described in Ref. [96, 71], where the topology was also acoplanar jets, but where the LSP was neutral and did not interact. However, new cuts are introduced, and all existing cut values were re-optimized with the $\bar{N}_{95}$ method. This was to account for the reduced missing energy, the larger integrated luminosity and the center-of-mass energy increase, and to include the subtraction of the four-fermion and $\mathrm{q\bar{q}}$ backgrounds, which will be explained later. Also, three rather than two different selections were developed for small, intermediate and large ΔM values. Below, the preselection and the three selections will be discussed. All cut values are summarized given in Table 8.2.

8.4.1 Preselection

A common preselection for the three selections was developed against two-photon events, characterized by their small visible energy and their boost along the beam direction. To reject these events, M_{vis} was required to exceed $15\,\mathrm{GeV}/c^2$, p_T to be larger than $2.5\%\sqrt{s}$ and N_{ch} to be in excess of 7. Moreover, the angles Φ_{acop} and Φ_{acopT} were both required to be smaller than $178.5°$, $\cos\theta_{\mathrm{miss}}$ and $\cos\theta_{\mathrm{T}}$ smaller than 0.85 and E_{12} smaller than $0.5\%\sqrt{s}$. The distributions of the visible energy, the number of charged tracks, the acoplanarity and the thrust after this preselection are shown in Figs. 8.1, 8.2, 8.3, 8.4 and 8.5 for the data, and for the background expected from different sources. In the same figure, the signal is displayed for two different values of ΔM. Let us look in more detail at the visible energy distribution. Two things must be noted. First of all, for small ΔM, the R-hadron composition is clearly visible: double-charged-R-hadrons events have largest visible energy, and double-neutral-R-hadrons events have smallest visible energy, while mixed events are in between. This pattern is explained by remembering that registered energy is $\sqrt{\mathbf{p}^2 + m_\pi^2}$ for charged R-hadrons, and counted in the visible energy sum (see Section 6.3.9), while for neutral hadrons only the calorimeter deposit is taken into account. For large ΔM, the three peaks are merged because of the much broader visible energy distributions. Secondly, note that the visible energy recorded in the ALEPH detector is anomalously large: the production of two R-hadrons of 75 GeV cannot result a the visible energy above 50 GeV. This is of course again directly related to the same issue with the calculation of the visible energy by the energy flow algorithm. It assumes the R-hadron to be a pion, which has an energy equal to its momentum which is entirely measured. However, for an R-hadron, the energy registered in the detector is not equal to its momentum, since the mass is not negligible!

8.4.2 Low ΔM selection

The low ΔM selection is mainly designed to remove two-photon background. Characteristics of these events are already mentioned in section 7.4.1. All cuts are summarized in table 8.2 and are clarified below. Many two-photon events are characterized by low momentum tracks with small track radius. In that case, the energy deposit in the calorimeters and the associated track are not necessarily in line anymore. As a result, the energy flow algorithm sometimes fails to associate these calorimeter objects to the right charged tracks, but instead associates them to neutral objects. Consequently, the total p_T of the event is overestimated. To reject these neutral objects, cuts on the p_T are made, and an upper cut on the total energy resulting from neutral hadronic objects is imposed:

- $p_T^{exNH} > 0.02\sqrt{s}$
- $p_T^{ch} > 0.015\sqrt{s}$
- $E_{NH} < 10\%\sqrt{s}$

The $\gamma\gamma$ events that pass these cuts are mainly $\gamma\gamma \to q\bar{q}$ events with low visible mass, aligned around the beam axis due to the scattered electron(s). Thus, the missing momentum vector of these events, as well as the thrust-axis, points in a direction close to the beam-axis. These features are also characteristic for $q\bar{q}\gamma$-events with the photon escaping into the beam-axis. In order to reject these events, we impose the following cuts:

- $E_{12}/\sqrt{s} < 0.001$
- $\cos\theta_{\mathrm{miss}} > 0.8$

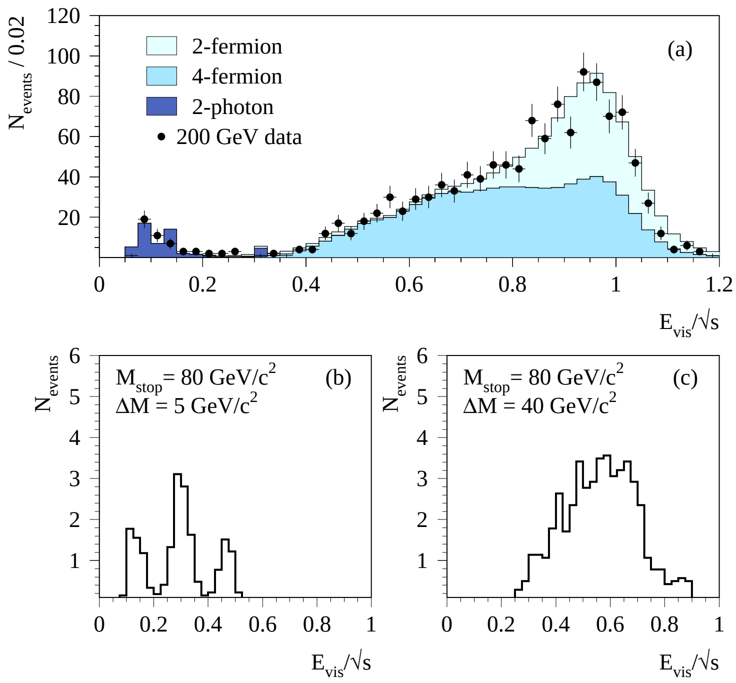

Figure 8.1: Distributions of the visible energy E_{vis} observed in the data at $\sqrt{s} = 200\,\mathrm{GeV}$ (dots with error bars) and expected from various background sources (shaded histograms), after the preselection cuts (a). The lower two plots show the expected distributions for the signal, with $\Delta M = 5\,\mathrm{GeV}/c^2$ (b) and $40\,\mathrm{GeV}/c^2$ (c).

- $\cos\theta_{\mathrm{T}} > 0.8$

When a scattered electron from $\gamma\gamma \to q\bar{q}$ goes undetected into the beam-pipe or other insensitive part of the detector, not all the electron energy is recorded. To ensure that only events are selected in which the electron is detected properly, we impose:

- $\theta_{\mathrm{scat}} > 5^\circ$

At this stage, most two-photons events are rejected and the remaining cuts are designed to reject other background processes. In some $q\bar{q}$ events high energetic neutrinos are produced from a semi-leptonic decay of the quark. That means the neutrino is produced within a jet, and the missing momentum vector is not isolated. To reject these events, we impose the following cut:

- $E_{\mathrm{Wedge}}/\sqrt{s} < 12.5\%$

To remove other $q\bar{q}$ events, we require:

- Thrust < 0.96

The WW and the Weν_{e} backgrounds are effectively reduced by cuts on the visible energy:

- $E_{vis} < 50\%\sqrt{s}$
- $E_{\mathrm{had}} > 10$ GeV and $< 40\%\sqrt{s}$

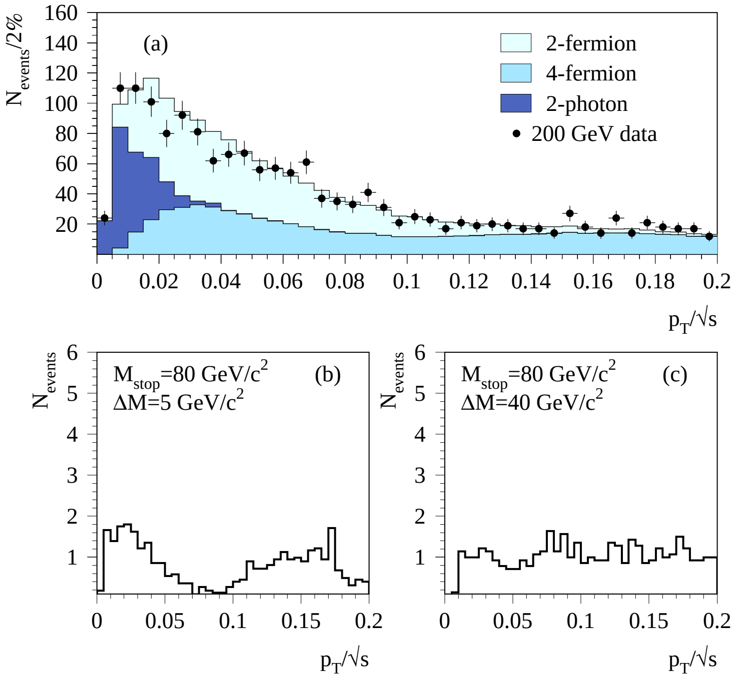

Figure 8.2: Distributions of the ratio of the transverse momentum p_T and the center-of-mass energy $\sqrt{s}$ observed in the data at $\sqrt{s} = 200\,\mathrm{GeV}$ (dots with error bars) and expected from various background sources (shaded histograms), after the preselection cuts (a). The lower two plots show the expected distributions for the signal, with $\Delta M = 5\,\mathrm{GeV}/c^2$ (b) and $40\,\mathrm{GeV}/c^2$ (c). For small ΔM, the R-hadron composition is again visible: double-charged and doubly neutral R-hadrons events have small p_T (since the p_T is only measured for charged particles), since the transverse momentum of the event is balanced. On the contrary, mixed R-hadrons events have large transverse momentum. For large ΔM, the three peaks are merged because of the broader p_T distributions.

Finally, to eliminate the remaining semi-leptonic events, the observation is used that R-hadrons are sometimes identified as high energetic muons. Thus, we require:

- $E_\ell/\sqrt{s} > 20\%$

8.4.3 Intermediate ΔM selection

The intermediate ΔM selection is developed to cover the efficiency gap which would arise if only one low and one high ΔM selection was used. Below, the cuts are explained which have changed in comparison with the low ΔM selection. The cut values are summarized in Table 8.2. As is shown in Figs. 8.1, 8.2, 8.3 and 8.4, the events have a higher multiplicity, transverse momentum and visible energy than the low ΔM signal events. This allows to set harder cuts against two-photon events:

- $p_T/\sqrt{s} > 4\%$
- $N_{\rm ch} > 11$
- $p_T/E_{\rm vis} > 12.5\%$

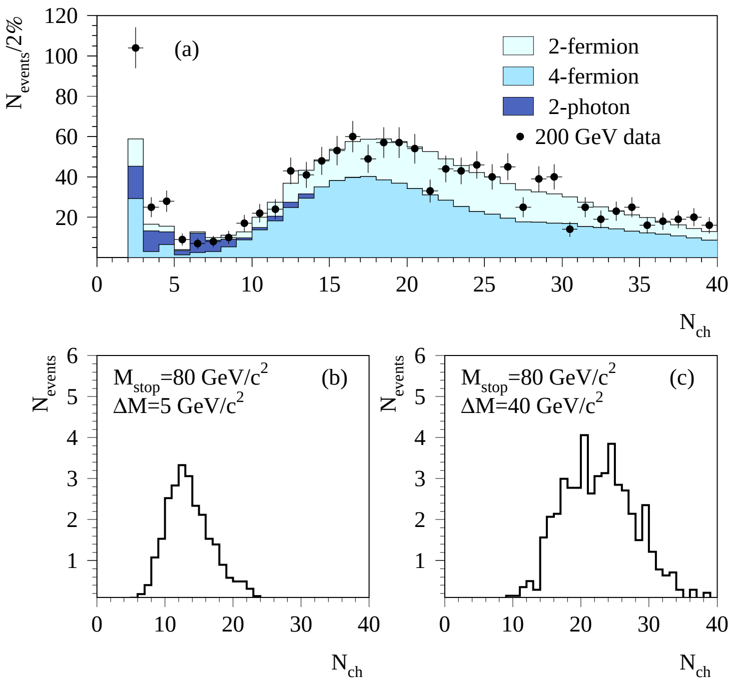

Figure 8.3: Distributions of the number of charged tracks observed in the data at $\sqrt{s}$ = 200 GeV (dots with error bars) and expected from various background sources (shaded histograms), after the preselection cuts (a). The lower two plots show the expected distributions for the signal, with ΔM = 5 GeV/c^2 (b) and 40 GeV/c^2 (c). Events with a large ΔM value, corresponding to a light gluino, clearly have a larger amount of charged tracks, since there is more energy available for the visible system.

Also, the events tend to be less back to back or more acoplanar, and stronger cuts can be imposed on the acoplanarity and transverse acoplanarity angle. The following cuts are effective against two-photon and $q\bar{q}(\gamma)$-background:

- $\Phi_{\text{acop}} < 176°$
- $\Phi_{\text{acopT}} < 177°$

A stronger cut can also be imposed on the scattering angle of the electron. The upper cut is useful against WW-events, which have a θ_{scat} value close to 90^o:

- θ_{scat} $[6°, 80°]$

The higher sphericity of the intermediate ΔM events allows to impose a harder cut on the thrust:

- T <0.94

As displayed in Fig 8.1, the events have a higher visible energy than the low ΔM events. That forces us to loosen the cuts against four-fermion background slightly:

- $E_{\text{had}} < 55\%\sqrt{s}$
- $E_{\text{vis}}/\sqrt{s} < 70\%$

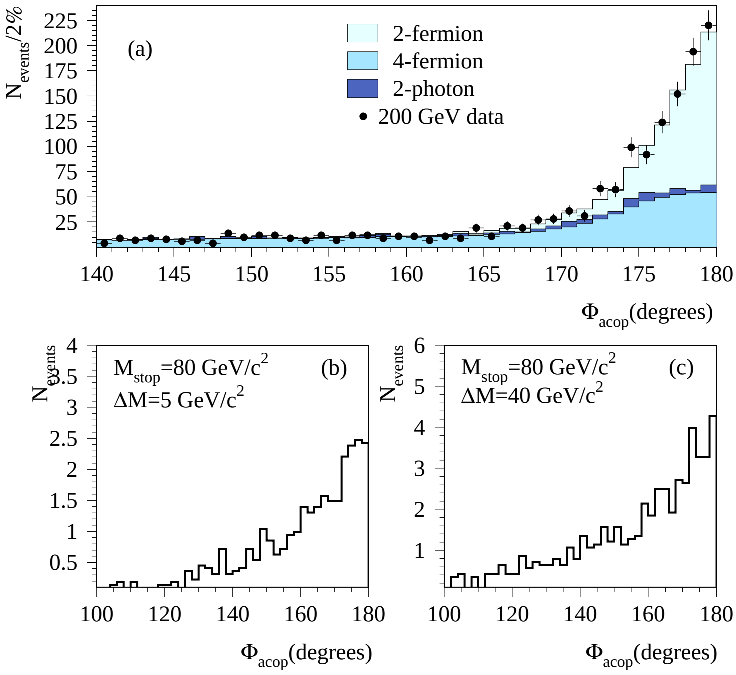

Figure 8.4: Distributions of the acoplanarity angle observed in the data at $\sqrt{s} = 200\,\mathrm{GeV}$ (dots with error bars) and expected from various background sources (shaded histograms), after the preselection cuts (a). The lower two plots show the expected distributions for the signal, with $\Delta M = 5\,\mathrm{GeV}/c^2$ (b) and $40\,\mathrm{GeV}/c^2$ (c). For small ΔM, the acoplanarity angle is larger than for large ΔM, since the R-hadrons are more back-to-back.

Finally, an R-hadronic 'muon' will not be isolated due to the fact that it is produced in a jet. Therefore, the following cut is useful against all background events with isolated leptons:

- $E_\ell^{30}/\sqrt{s} > 1\%$

8.4.4 The high ΔM selection

Signal events with high ΔM are similar to four-fermion and two-fermion background, but are in general quite different from two-photon events. This allows very efficient cuts against two-photon background:

- $p_T/\sqrt{s} > 7.5\%$
- $N_{\mathrm{ch}} > 18$
- $\cos\theta_{\mathrm{T}} > 0.85$
- $\theta_{\mathrm{scat}}[15°, 80°]$

Concerning $q\bar{q}$-background, several cuts stay the same as in the intermediate ΔM case, but other cut on the thrust can be tightened:

- T <0.92

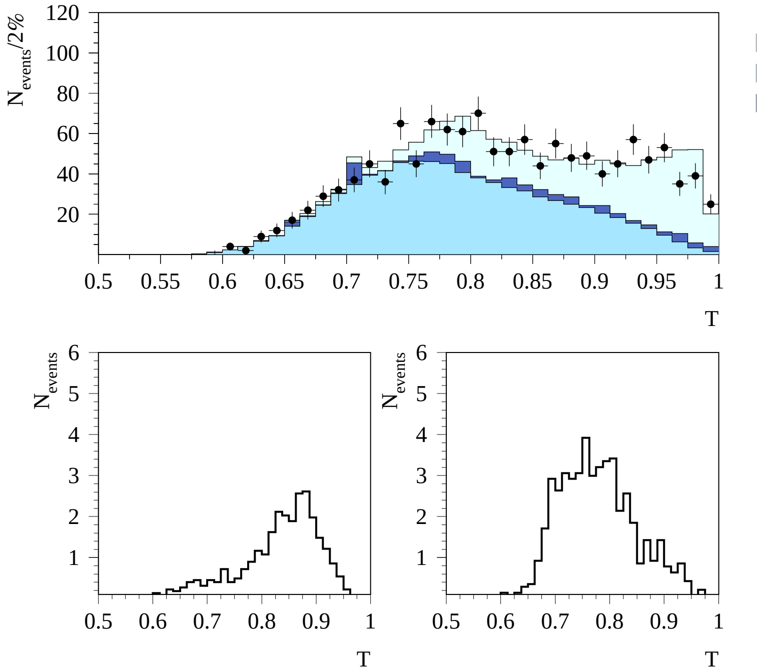

Figure 8.5: Distributions of the thrust T observed in the data at $\sqrt{s} = 200\,\text{GeV}$ (dots with error bars) and expected from various background sources (shaded histograms), after the preselection cuts (a). The lower two plots show the expected distributions for the signal, with $\Delta M = 5\,\text{GeV}/c^2$ (b) and $40\,\text{GeV}/c^2$ (c). R-hadron events with large ΔM have a smaller value for the thrust, since those events are more spherical. Events with large stop and gluino masses are more back-to-back, resulting in larger values for the thrust.

The high visible energy of the high ΔM signal events forces us to loosen the cuts on visible energy-related event variables:

- $E_{\text{vis}}/\sqrt{s} < 80\%$
- $E_{\text{had}} < 75\%\sqrt{s}$

The energy far from the beam-axis is large and an extra cut can be imposed against all events with visible energy close to the beam axis:

- $E_{30}/E_{\text{vis}} > 80\%$

All remaining cuts stay the same and are already explained in the previous section.

8.5 Selection efficiency

8.5.1 Low, intermediate and high ΔM selection efficiencies

The selection efficiencies were obtained from simulated samples (Section 3.1.5) for over 150 different values of $(m_{\tilde{t}}, m_{\tilde{g}})$, and were then parametrized as a function of $m_{\tilde{t}}$ and $m_{\tilde{g}}$ with a polynomial function. For example, the efficiency of the three selections is shown in Fig. 8.6 for $m_{\tilde{t}} = 80\,\text{GeV}/c^2$ and $m_{\tilde{t}} = 50\,\text{GeV}/c^2$ as a function of the gluino mass.

Variable	Small ΔM	Intermediate ΔM	Large ΔM
$M_{\rm vis}$	$> 15\,{\rm GeV}/c^2$	$> 15\,{\rm GeV}/c^2$	$> 15\,{\rm GeV}/c^2$
$p_T/\sqrt{s}$	$> 2.5\%$	$> 4\%$	$> 7.5\%$
$N_{\rm ch}$	> 7	> 11	> 18
$E_{\rm vis}/\sqrt{s}$	$< 50\%$	$< 70\%$	$< 80\%$
$E_{12}/\sqrt{s}$	$< 0.5\%$	$< 0.5\%$	$< 0.5\%$
$\cos\theta_{\rm miss}$	> 0.8	> 0.8	> 0.8
$\cos\theta_{\rm T}$	> 0.8	> 0.8	> 0.85
$\Phi_{\rm acop}$	$< 178.5°$	$< 176°$	$< 176°$
$\Phi_{\rm acopT}$	$> 178.5°$	$< 177°$	$< 177°$
$E_{\rm Wedge}/\sqrt{s}$	$< 12.5\%$	$< 12.5\%$	$< 12.5\%$
T	<0.96	<0.94	<0.92
$\theta_{\rm scat}$	$> 5°$	$[6°, 80°]$	$[15°, 80°]$
$p_T/E_{\rm vis}$	–	$> 12.5\%$	$> 12.5\%$
$p_T^{\rm ch}/\sqrt{s}$	$> 1.5\%$	–	–
$p_T^{\rm exNH}/\sqrt{s}$	$> 2\%$	–	–
$E_{\rm had}$	$[10\,{\rm GeV}, 40\%\sqrt{s}]$	$< 55\%\sqrt{s}$	$< 75\%\sqrt{s}$
$E_{\rm NH}/\sqrt{s}$	$< 10\%$	–	–
$E_{\rm NH}/E_{\rm vis}$	–	$< 30\%$	–
$E_\ell/\sqrt{s}$	$> 20\%$	–	–
$E_\ell^{30}/\sqrt{s}$	–	$> 1\%$	$> 1\%$
$E_{30}/E_{\rm vis}$	–	–	$> 80\%$

Table 8.2: Selection criteria for the search for R-hadrons from stop pair production in the acoplanar jet topology, in the three ΔM regions.

8.5.2 Switching points

The three selections may never be used at the same time, and hence it is necessary to switch between the selections at a certain ΔM value. The position of the switching point is determined with the $\bar{N}_{95}$ prescription, taking into account the expected background, to be summarized in Section 8.6. Since the switching-point values vary for different stop masses, a parameterization of the switching points values as a function of the stop mass is made. These switching ΔM values tend to decrease with the stop mass. For example, for $m_{\tilde{t}} = 80\,{\rm GeV}/c^2$, the switching ΔM values are 16 and $33\,{\rm GeV}/c^2$, while for $m_{\tilde{t}} = 40\,{\rm GeV}/c^2$, these values are 4 and 20, respectively. In Fig. 8.7, we display the switch points of the selections as a function of the stop mass.

8.5.3 Total efficiency

To obtain the efficiency at every stop mass value, a linear interpolation between the different stop mass values is made. The resulting efficiency in the stop mass-gluino mass plane is shown in Fig. 8.8(a). Efficiencies in between 0% and 30% are achieved.

8.6 Expected background

In Table 8.3, the composition of the background is given for small, intermediate and large ΔM selections. Contrary to the squark searches presented in Ref. [96], the number of background

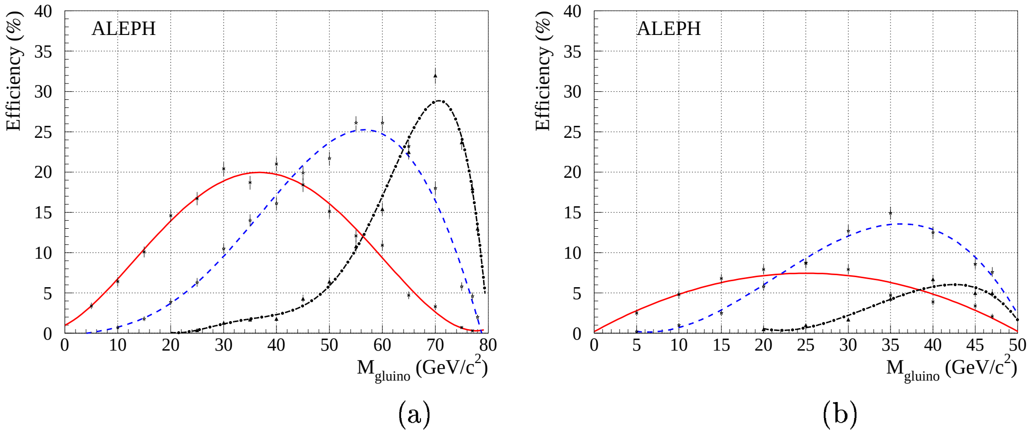

Figure 8.6: The three parametrized selection efficiencies for $m_{\tilde{t}} = 80\,\mathrm{GeV}/c^2$ (a) and $m_{\tilde{t}} = 50\,\mathrm{GeV}/c^2$ (b) as a function of $m_{\tilde{g}}$ (full curve, large ΔM selection; dashed curve, intermediate ΔM selection; and dot-dashed curve, small ΔM selection). The dots with error bars show the actual efficiencies obtained from the individual simulated samples.

events is not negligible. As will be shown in Table 9.1 in Chapter 9, the background is well understood, allowing background subtraction. Due to the relatively poorly understood physics of two-photon events, only two- and four-fermion background are subtracted.

8.7 Sbottom quarks

The same selection is applied to search for gluinos produced via $e^+e^- \rightarrow \tilde{b}\bar{\tilde{b}} \rightarrow b\tilde{g}\bar{b}\tilde{g}$. Monte Carlo signal events are produced as explained in Section 7.3, with one exception. While stop quarks would hadronize before decaying into gluinos, sbottom quarks decay promptly into gluinos, because the decay is a tree level process rather than a loop process. The switching-points of the three selections were determined, and the resulting efficiency is displayed in Fig. 8.8. The efficiency of the low ΔM selection is approximately the same as for $e^+e^- \rightarrow \tilde{t}\bar{\tilde{t}} \rightarrow c\tilde{g}\bar{c}\tilde{g}$, while those

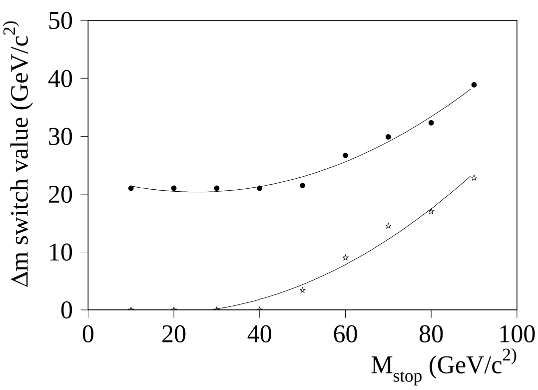

Figure 8.7: The switching points of the selections as function of $m_{\tilde{t}}$. The upper line represents the ΔM values where to switch between intermediate and high ΔM, while the lower line represents the values where to switch between low and intermediate ΔM.

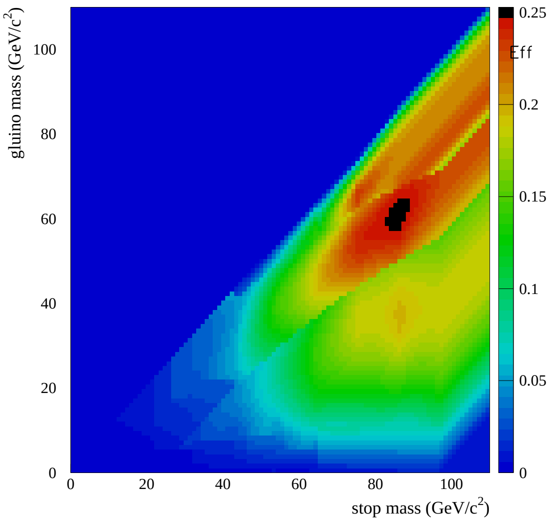

(a)

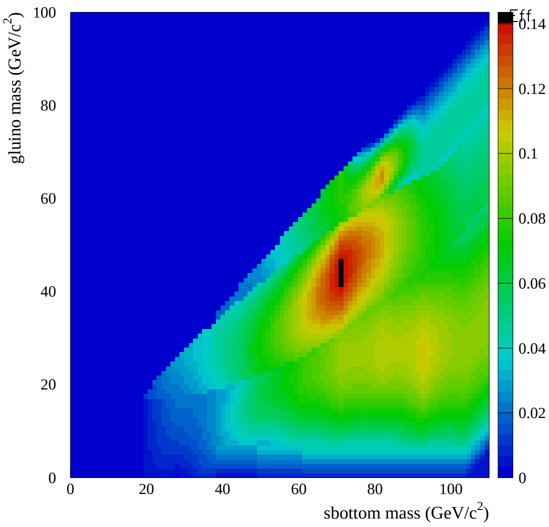

(b)

Figure 8.8: The selection efficiency for $e^+e^- \to \tilde{t}\bar{\tilde{t}} \to c\tilde{g}\bar{c}\tilde{g}$in the $m_{\tilde{t}}$- $m_{\tilde{g}}$ plane (left), and for $e^+e^- \to \tilde{b}\bar{\tilde{b}} \to b\tilde{g}\bar{b}\tilde{g}$in the $m_{\tilde{b}}$- $m_{\tilde{g}}$ plane (right).

of the intermediate and high ΔM selection were approximately 80% and 60% of the efficiency in $e^+e^- \to \tilde{t}\bar{\tilde{t}} \to c\tilde{g}\bar{c}\tilde{g}$. Additional rejection is achieved by using a b-tag variable P_{uds}, quantifying the probability of the event with respect to the presence of light quarks, based on the average distance between the track crossing points with the thrust axis and the primary vertex. A high P_{uds} means that most particles origine from the primary vertex, as expected for light quark fragmentation. Applying a cut $P_{uds} > 0.5$ on the candidate events gives no extra rejection. The selection turned out not to be efficient enough to exclude any sbottom quark masses due to decrease of the efficiency in combination with a much smaller production cross section for sbottom quarks.

Year	Luminosity	Background type	Small ΔM	Intermediate ΔM	Large ΔM
		2-photon	1.8	0.6	0.1
		$q\bar{q}$	0.7	0.4	0.1
2000	207.1	WW	0.9	7.5	12.0
		ZZ	0.8	3.0	2.9
		Weν	3.9	3.2	1.9
		Total	8.1	14.7	17.0
		2-photon	2.1	0.7	0.3
		$q\bar{q}$	0.7	0.4	0.1
1999	236.1	WW	0.9	8.5	13.6
		ZZ	0.9	3.4	3.3
		Weν	4.1	3.7	2.2
		Total	8.7	16.7	19.5
		2-photon	1.6	0.5	0.2
		$q\bar{q}$	0.6	1.4	1.0
1998	173.1	WW	0.7	6.3	10.0
		ZZ	0.7	2.5	2.4
		Weν	3.3	2.7	1.6
		Total	6.9	13.4	15.2
		2-photon	0.5	0.2	0.1
		$q\bar{q}$	0.2	0.5	0.3
1997	56.3	WW	0.2	2.0	3.3
		ZZ	0.2	0.8	0.8
		ZZ	1.1	0.9	0.5
		Total	2.2	4.4	5.0

Table 8.3: The composition of the background for small, intermediate and large ΔM selections for each year

Chapter 9

ALEPH: Systematic uncertainties

The signal efficiencies may be affected by uncertainties in the simulation of the stop and gluino R-hadronization physics, by statistical uncertainties due to the limited size of the simulated samples, and by uncertainties related to the detector response for R-hadrons.

9.1 Physics uncertainties

Systematic effects from the physics assumptions were estimated by varying the free parameters of the simulation, as described in Section 7.3.3:

- The gluino-gluon bound state probability was assumed to be 10%. The effects of a probability variation from 0% to 100% depend on the stop and gluino masses. For light gluinos (around $30\,\mathrm{GeV}/c^2$), the efficiency increases with $P_{\tilde{\mathrm{g}}\mathrm{g}}$, i.e. with the fraction of $\mathrm{R}^0\mathrm{R}^0$ final states. Indeed, such light R-hadrons substantially interact in the calorimeters, and a search based on missing energy becomes more and more ineffective. It is only when two neutral R-hadrons are present in the final state that the missing energy becomes large enough to make the present selection still somewhat efficient. In contrast, for larger gluino masses and small mass differences, the two gluinos are produced approximately back to back with similar energies, and have almost no interaction in the calorimeters. This configuration leads to a cancellation in the measured missing transverse momentum in the $\mathrm{R}^0\mathrm{R}^0$ final state, so small values for the total transverse momentum result. At high masses and small mass differences, the selection efficiency therefore decreases when $P_{\tilde{\mathrm{g}}\mathrm{g}}$ increases. This effect is washed out with smaller gluino mass, until it turns on at gluino masses below around 30 GeV/c^2 and the selection efficiency becomes larger with increasing $P_{\tilde{\mathrm{g}}\mathrm{g}}$. A map of the corresponding uncertainty (up to ±20% in extreme cases) was built in the ($m_{\tilde{\mathrm{t}}}$, $m_{\tilde{\mathrm{g}}}$) plane.
- The R-hadronic interaction cross section in matter has an uncertainty of ±50%. This changes the selection efficiency by ±5% in the small ΔM region, and by a negligible amount otherwise.
- The effective spectator mass uncertainty yields relative efficiency variations of ±5%, ±3% and ±3% in the small, intermediate and large ΔM regions, respectively.
- The gluon constituent mass uncertainty has no visible effect.
- The uncertainty on the Peterson fragmentation parameter ϵ_{b} (varied here between 0.003 and 0.010) gives rise to an efficiency change of ±8%, irrespective of the ΔM value.

- The stop mixing angle is varied from the default value 56^o, corresponding to maximal mixing, to a value of 0^o, corresponding to minimal mixing. The efficiency change was about $\pm 5\%$ for all ΔM regions.

9.2 The statistical uncertainty on the efficiency

The statistical error on the signal efficiency, $\Delta\epsilon$, can be derived from the variance of the binomial distribution, and is given by

$$\Delta\epsilon = \sqrt{\frac{\epsilon(1-\epsilon)}{N}}. \tag{9.1}$$

The limited statistics of the 150 signal samples (1000 events each) turns out to lead to an uncertainty of ca 3-4%. Besides, the parametrization of the efficiencies with a polynomial have an uncertainty of ca 1-2%.

9.3 The statistical uncertainty on the systematic error of the signal

If we denote the efficiency of the selection, but with one parameter varied, by ϵ_i, and the efficiency of the default selection by ϵ_0, we can calculate the error of this variation, $\Delta(\frac{\epsilon_i}{\epsilon_0})$:

$$\Delta(\frac{\epsilon_i}{\epsilon_0}) = \frac{1}{\epsilon_0}\Delta\epsilon_i \oplus -\frac{\epsilon_i}{\epsilon_0^2}\Delta\epsilon_0, \tag{9.2}$$

where $\oplus$ denotes quadratic addition. The errors $\Delta\epsilon_0$ and $\Delta\epsilon_i$ are known from Eq. (9.1). With $N_i \approx N_0$=1000, and $\epsilon_i \approx \epsilon_0$, we find for the statistical uncertainty of the systematic error on the signal:

$$\Delta(\frac{\epsilon_i}{\epsilon_0}) \approx \sqrt{2}\sqrt{\frac{(1-\epsilon_0)}{\epsilon_0 N_0}}. \tag{9.3}$$

For the highest obtained values of the efficiency, this error is around 5%, and increases for decreasing efficiency. This value plays an important role for the interpretation of the selection efficiency, discussed in the previous section. How to incorporate this uncertainty in the analysis will be discussed in Section 9.6.

9.4 The uncertainties of the background simulation

Uncertainties arise from the simulation of the standard model background. These uncertainties were assessed by comparing the effect of each cut separately on the data and on the simulated background events after the preselection. We denote the efficiency of the preselection cuts plus one separate cut by ϵ_b, when applied on the background samples, and by ϵ_d, when applied on the data sample. The statistical uncertainty of the relative deviation is given by

$$\Delta(\frac{\epsilon_b}{\epsilon_d}) = \frac{1}{\epsilon_d}\Delta\epsilon_b \oplus -\frac{\epsilon_b}{\epsilon_d^2}\Delta\epsilon_d, \tag{9.4}$$

where $\oplus$ denotes quadratic addition. The first term can be neglected thanks to the fact that real luminosity of the Monte Carlo background samples is very high and many times higher than the luminosity of the data. Data samples and normalized background samples corresponding to

Single Cut	$\epsilon_d(\%)$	$\epsilon_b(\%)$	$\frac{\epsilon_b-\epsilon_d}{\epsilon_d} \times 100\%$
$p_T/\sqrt{s} > 7.5\%$	59.5	56.3	-3.2%
$N_{ch} > 18$	64.1	63.4	-0.7%
$E_{vis}/\sqrt{s} < 50\%$	5.8	5.7	-0.1%
$\cos\theta_{miss} < 0.8$	94.0	93.3	-0.7%
$\cos\theta_{thrust} < 08$	86.9	83.2	-3.7%
$\theta_{acop} < 176^o$	66.1	66.2	+0.1%
$\theta_{acop/} < 177^o$	71.7	73.4	+2.3%
$E_{Wedge}/\sqrt{s} < 12.5\%$	46.2	50.0	+3.8 %
$T < 0.92$	78.4	80.3	+1.9%
$\theta_{scat} > 15^o$	90.1	91.3	+1.2
$\theta_{scat} < 80^o$	33.4	35.4	-2.0%
$P_T/E_{vis} > 12.5\%$	53.7	52.0	-1.7%
$P_T^{ch}/\sqrt{s} > 1.5\%$	97.4	96.5	-0.9 %
$P_T^{exNH}/\sqrt{s} > 2\%$	93.7	93.6	-0.1 %
$E_{had}/\sqrt{s} < 40\%$	20.9	21.5	+0.6%
$E_{NH}/\sqrt{s} < 10\%$	66.0	63.2	-2.8%
$E_{NH}/E_{vis} < 30\%$	95.8	94.8	-1.0%
$E_l/\sqrt{s} > 20\%$	22.9	24.9	+2.0%
$E_l^{30}/\sqrt{s} > 1\%$	69.1	69.9	+0.8%
$E_{30}/E_{vis} > 80\%$	82.2	83.9	+1.7%

Table 9.1: Efficiencies of some of the strongest cuts, applied separately after the preselection. The uncertainty due to all cut variations turn out to be within the statistical uncertainty due to a limited amount of background and data samples, corresponding to 207 pb^{-1}.

an integrated luminosity of 207.1 pb^{-1} are used, which is after preselection roughly 1800 events. Neglecting the second term in Eq. (9.4), and using Eq. (9.1), the statistical uncertainty of the relative deviation is seen to be

$$\Delta(\frac{\epsilon_b}{\epsilon_d}) = \frac{\epsilon_b}{\epsilon_d^2}\sqrt{\frac{\epsilon_d(1-\epsilon_d)}{N_0}}. \tag{9.5}$$

In Table 9.1, the efficiencies of the preselection plus the separate cut on background samples, ϵ_b, and on data samples, ϵ_d, are given. Of the three selections, the strongest cuts are tested. All deviations between background and data efficiencies are found to be within the statistical uncertainty. The relative differences, although compatible with the uncertainty due to limited statistics, were conservatively added in quadrature, for a total possible deviation of 9%.

9.5 Other uncertainties

Beam-related backgrounds, which affect the determination of the event variable E_{12}, were not simulated. The effect on the selection efficiency, determined from events collected at random beam crossings, is a relative decrease of 5%.

9.6 Incorporation of uncertainties in the analysis

Taking into account beam related background implies simply subtracting 5% of the efficiency for all values of the gluino and the stop mass. Background related uncertainties were taken into account by subtracting the total error of the background, 9%, from the subtractable background in the three selections (details in next chapter). Physics uncertainties and the statistical uncertainty were quadratically added and taken into account following the method of Ref. [97]. The method is based on Taylor expanding the expression of the confidence level as given in Eq. (8.6) around the value ν_0, which is the upper limit point ν in case there were no uncertainties at all. If the difference between ν and ν_o is $\Delta\nu$, it can be proved that

$$\Delta\nu = \frac{\nu_0 + b - n_{obs}}{\nu_o + b} \frac{\nu_o^2 (\Delta\epsilon)^2}{2}, \tag{9.6}$$

where $\Delta\epsilon$ is the error from physics uncertainties and the statistical uncertainty. Uncertainties are then incorporated by making a shift

$$\nu \rightarrow \nu + \Delta\nu, \tag{9.7}$$

and calculating the eventual limits on the cross section with this new value.

Chapter 10

ALEPH: Results and interpretations

This chapter summarizes the results of the search for $e^+e^- \to \tilde{t}\bar{\tilde{t}} \to c\tilde{g}\bar{c}\tilde{g}$. Final results are published in [98], and intermediate results have been published in [99, 100, 101].

10.1 Combination of different energies

Data samples of different $\sqrt{s}$ are used. Two complications arise in the combination of the different data samples. Firstly, we must account for the fact that for instance a candidate in the sample with $\sqrt{s} = 183$ GeV is only a good candidate in the stop mass region $m_{\tilde{t}} < 91$ GeV. To exclude higher stop masses, this data sample is used for exclusion. Secondly, different data samples are used in the analysis, each with their own center of mass energy, their own number of candidates, and their own resulting 95% C.L. exclusion on the number of signal events. Having a 95% C.L. limit on the average number of signal events ν_s^i for energy sampling i, and using Equation (8.2), it is not hard to see that

$$\sum_{\sqrt{s_i}>2m_{\tilde{t}}} \nu_s^i > \sum_i \epsilon_i \sigma(\sqrt{s_i}, m_{\tilde{q}})\mathcal{L}_i, \tag{10.1}$$

from which is follows that

$$\sigma(\sqrt{s_1}, m_{\tilde{q}}) < \frac{\sum_{\sqrt{s_i}>m_{\tilde{q}}} \nu_s^i}{\sum_{\sqrt{s_i}>m_{\tilde{q}}} \epsilon_i \frac{\sigma(\sqrt{s_i}, m_{\tilde{q}})}{\sigma(\sqrt{s_1}, m_{\tilde{q}})}\mathcal{L}_i}. \tag{10.2}$$

For more details the reader is referred to Ref. [71]. This method for combining different collision energies is used here, just like in Ref. [96].

10.2 Results and interpretation

The observed number of candidates in the data samples taken during 1997, 1998, 1999 and 2000 are summarized in Table 10.1. These numbers are compatible with the expected number of standard model background events.

In the framework of the MSSM with R-parity conservation, the outcome of this search can be translated into constraints in the ($m_{\tilde{t}}$,$m_{\tilde{g}}$) plane when the stop quark decays with a 100% branching fraction into a stable gluino and a c quark. Regions excluded by this search at 95% C.L. are shown in Fig. 10.1, for $\theta_{\text{mix}} = 56°$ and 0°, corresponding to vanishing and maximal stop coupling to the Z, respectively. Assuming that the stop decays into stable gluino with a 100% branching fraction, if the gluino mass is larger than 30 GeV/c^2, and if the mass difference between

Year	Luminosity [pb^{-1}]	Small ΔM		Int. ΔM		Large ΔM	
		Obs.	Exp.	Obs.	Exp.	Obs	Exp.
2000	207.3	6	8.1	11	14.7	17	17.0
1999	236.9	9	8.7	15	16.7	19	19.5
1998	173.6	7	6.9	11	13.4	17	15.2
1997	56.8	1	2.2	5	4.4	4	5.0
Total	674.6	23	25.9	42	49.2	57	56.7

Table 10.1: The numbers of candidate events observed in the data between 1997 and 2000, and the numbers of events expected from standard model background sources, for the small, intermediate and large ΔM selections.

the stop and the gluino is larger than 3 GeV/c^2, the 95% C.L. smaller mass bound on the stop decaying into stable gluinos is found to be 85 GeV/c^2, and 80 GeV/c^2 for stop mixing angle of 0^o respectively 56^o. All stop masses below these values are excluded. These limits are independent of the R-hadron's charge.

10.3 Combination of different analyses

As can be seen from Fig. 10.1, no absolute stop mass limit can be extracted from the results of the acoplanar jet plus missing energy search alone. An absolute mass limit is obtained by combining the searches which have been performed in parallel to the present search. These analyses include the following:

- A new theoretical analysis based on the hadronic Z-width [34], excluding all gluino masses below 6.3 GeV/c^2 at the 95% confidence level, see Section 2.3.1.
- A search for the process $e^+e^- \to q\bar{q}\tilde{g}\tilde{g}$ with a gluon splitting into a pair of stable gluinos, using LEP 1 data, so that lower gluino masses could be covered. The selections were partly based on already existing selections [98]. Combined with the analysis described in Ref. [34], this search resulted in a 95% C.L. absolute lower limit of 26.9 GeV/c^2 on the mass of a gluino LSP.
- A search for the process $e^+e^- \to q\bar{q}\tilde{q}\bar{\tilde{q}}$ with a gluon splitting into a pair of stable squarks, using LEP 1 data and existing selections. Combined with the analysis of Ref. [34], this search resulted in a 95% CL lower limit of 15.7 GeV/c^2 on the mass of a stable squark [98]. As above, existing LEP1 selections were applied [98].
- A search for the pair production of stable squarks, $e^+e^- \to \tilde{t}\bar{\tilde{t}}$ and $\tilde{b}\bar{\tilde{b}}$, relevant in case the squarks are stable. This analysis also covers small mass differences between the stop and the gluino, where the stop would have a measurable lifetime. Stable stop masses between 5 and 95 GeV/c^2 and stable sbottom masses between 7 and 92 GeV/c^2 were excluded at 95% CL [98], obtained by using results of [38].

The result of the combination is displayed in Fig. 10.2. All stop masses below 80 GeV/c^2 are excluded at 95% C.L. when either the stop or the gluino is the lightest supersymmetric

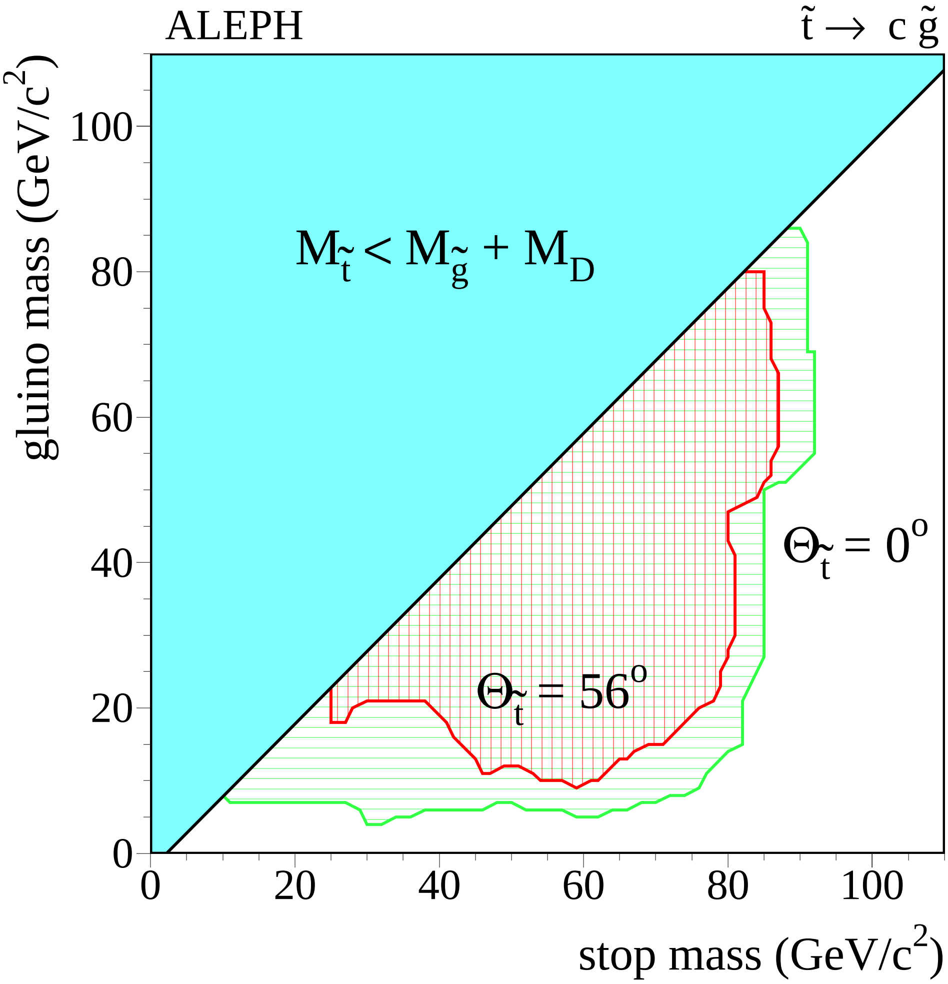

Figure 10.1: The 95% CL excluded regions in the plane ($m_{\tilde{t}}$, $m_{\tilde{g}}$) from the acoplanar jet search at LEP 2, for maximal (horizontal hatching) and minimal (cross hatching) stop coupling to the Z. The shaded area corresponds to a stable stop and is not accessible to this search. The macros for the production of this file are those applied in Ref. [37].

particle. When combined with the result of Ref. [37], all stop masses below 63 GeV/c^2 are excluded irrespective of the nature of the LSP.

10.4 Conclusion

A search has been performed for scalar tops decaying into stable gluino at center-of-mass energies from 183 to 209 GeV. The number of candidates observed are consistent with the background expected from standard model processes, and excluded regions in the (stop mass-gluino mass) plane are derived. For a gluino mass larger than 30 GeV/c^2 and a mass difference between stop and gluino larger than 3 GeV/c^2, the process $e^+e^- \rightarrow \tilde{t}\bar{\tilde{t}} \rightarrow c\tilde{g}\bar{c}\tilde{g}$ is excluded at 95% C.L. for stop masses below 80 GeV/c^2.

Together with LEP1 analyses and a stable squark analysis, a stop quark NSLP is excluded up to masses of 80 GeV/c^2 if the LSP is a gluino. For the first time limits on the masses of squarks decaying into stable gluinos, have been derived independent of the R-hadrons charge.

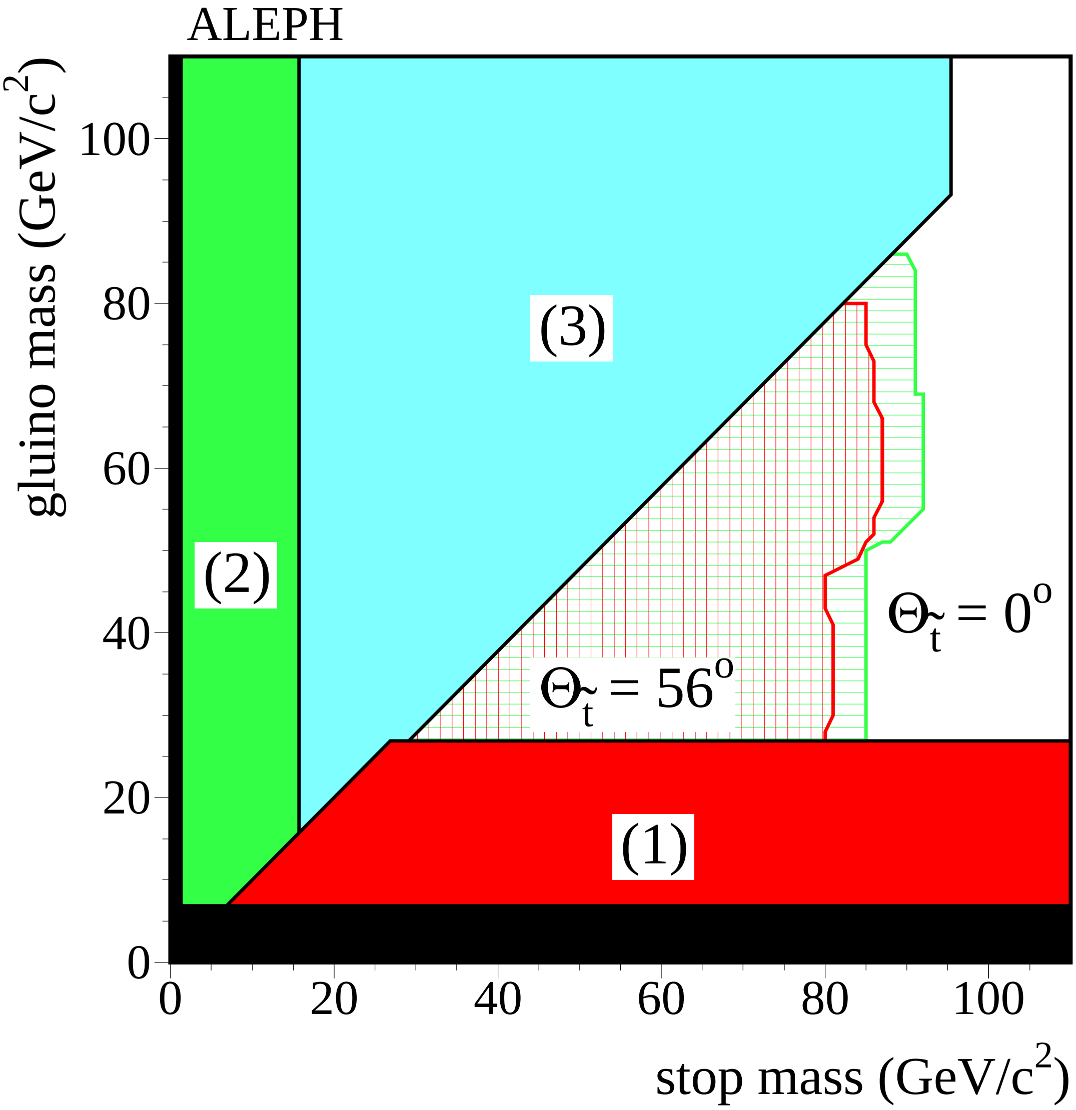

Figure 10.2: The 95% C.L. excluded regions in the plane $(m_{\tilde{t}}, m_{\tilde{g}})$ from the combination of all searches presented in this paper. The black area at very small gluino and squark masses is excluded by the precise measurement of the Z line-shape [34]; Regions (1), (2) and (3) are excluded by the search for $e^+e^- \to q\bar{q}\tilde{g}\tilde{g}$ at LEP 1, for $e^+e^- \to q\bar{q}\tilde{q}\bar{\tilde{q}}$ at LEP 1, and for heavy stable charged particles from $\tilde{q}\bar{\tilde{q}}$ production at LEP 2, respectively. The hatched areas are excluded by the acoplanar jet with missing energy search at LEP 2. The macros for the production of this file are those applied in Ref. [37]

Part III

ATLAS analysis

Chapter 11

LHC and the ATLAS detector

This section starts with a brief overview of the LHC accelerator at CERN. It describes the main components and discusses some technological challenges in building the LHC. Next, the layout and detector subsystems in the ATLAS detector will briefly be reviewed, with emphasis on those aspects which are important for R-hadrons. Finally, a short explanation about trigger strategies in ATLAS is given, since there are some interesting complications associated with heavy hadrons.

11.1 The Large Hadron Collider

11.1.1 Goals

The Large Hadron Collider (LHC) is a synchrotron storage ring which will provide proton-proton collisions with a center of mass energy of 14 TeV, the highest energy ever reached in an accelerator. In addition to proton-proton collisions, the LHC will be able to provide collisions between heavy nuclei such as lead. The main intention for building the LHC is to find the Higgs boson and to find signals for new physics. The design luminosity is $10^{34}\text{cm}^{-2}\text{s}^{-1}$. With beam crossings in the detectors, which are 25 ns apart, this means that each beam crossing will involve approximately 23 interactions. This is an experimental challenge but necessary for reaching possible new phenomena at energies 1-2 TeV.

11.1.2 Design

The Large Hadron Collider is being installed in the old LEP tunnel. Since the energy losses in the form of synchrotron radiation are small, and since the radius of the LHC ring is defined by that of the LEP tunnel, the limiting parameter in the center of mass energy of the proton proton collisions is the strength of the magnets. The magnet system is complicated by the fact that two beams of equally charged particles must collide, requiring separate magnet channels for each beam. The magnet system is therefore technologically the most challenging component of the LHC. Twin-bore magnets will be used so that the magnet channels use the same mechanical structure and cryostats, but have different coil assemblies and beam tubes. The superconducting magnets are using niobium-titanium superconducting coils and are cooled by super-fluid Helium. The maximum magnetic field strength is 8.65 T, a limit imposed by economics. Particles are injected into the LHC with the help of the already existing particle injector system at CERN. This system includes the 50 MeV Linac, the 1 GeV booster, the 26 GeV Proton Synchrotron (PS) and the 450 GeV Super Proton Synchrotron (SPS), see Fig. 6.2 for their location. The 450 GeV protons will then be injected in the LHC ring and will be accelerated to 7 TeV. The whole sequence takes approximately 400 seconds. At four locations in the LHC ring interaction points are located, where the two proton beams cross, and experiments are built. The ALICE experiment is devoted to study the quark-gluon plasma which arises in collisions of heavy nuclei. The other three experiments are devoted to study proton proton collisions. The LHCb experiment will study CP-violation in the b-quark system. The ATLAS and CMS experiments are general purpose detectors designed to do measurements for Standard Model physics as well as to discover signals for new physics. Some of these detectors will be built in the existing experimental halls from LEP, while for others, like ATLAS, a new cavity has been made.

11.1.3 Coordinate system

The x, y, and z-axis, r, and the angles θ and ϕ are defined in the same way as at LEP. Rather than using the polar angle θ, positions are usually given in terms of the pseudorapidity $\eta = -\ln\tan|\theta/2|$, a quantity having nice properties under Lorentz boosts along the z-axis.

11.2 ATLAS

The ATLAS (A large Toroidal LHC ApparatuS) detector consists of several subsystems, forming a layered structure with inner detectors, calorimeters and a muon spectrometer, analogue to ALEPH. In Fig. 11.1, the main components of the ATLAS detector are shown. An overview of the ATLAS detector can be found in Ref. [102]. The dimensions of the detector will be 22 meter high and 44 meter long.

11.2.1 Inner Detector

The high luminosity and corresponding high track density expected at LHC requires the tracking parts of the detector to have excellent performance in pattern recognition and momentum and vertex measurements. In ATLAS, tracking will be done with the Inner Detector (ID), which has an outer radius of 1.15 m and a length of 5 meter. It consists of three subsystems: the Pixel Detectors (PD) at the innermost radii, the Semi-Conductor Tracker (SCT) in the middle, and the Transition Radiation Tracker (TRT) at the outer radii. It can be divided into a barrel region, with layers arranged in concentric cylinders, and two endcap regions, with layers perpendicular to the beam axis. It has a pseudorapidity coverage of $|\eta|$ <2.5, and full coverage in the azimuthal ϕ direction. Details about the inner detector can be found in Ref. [103], and only some relevant facts will be summarized below.

Pixel detector Pixel detectors are used to provide measurements closest to the interaction point, where the track density is highest. High granularity is achieved with pixels of semi-conducting material using silicon. There are three precision layers, so every track has typically three tracking points in the pixel region. Although the radiation resistance is high, the pixels will have to be replaced after a few years of running. The resolution is 50 μm in $r\phi$-direction and 300 μm in the beam direction. The sampling time (the time of data taking) is the same as the bunch crossing time: 25 ns.

Semiconductor tracker Semiconducting strip detectors (SCT) are used further away from the vertex region. Each detector unit is a p-on-n silicon wafer of 6.4×6.4 cm^2, with 768 strips of 80μm pitch. In total, typically eight silicon micro strip layers are crossed by every track. The

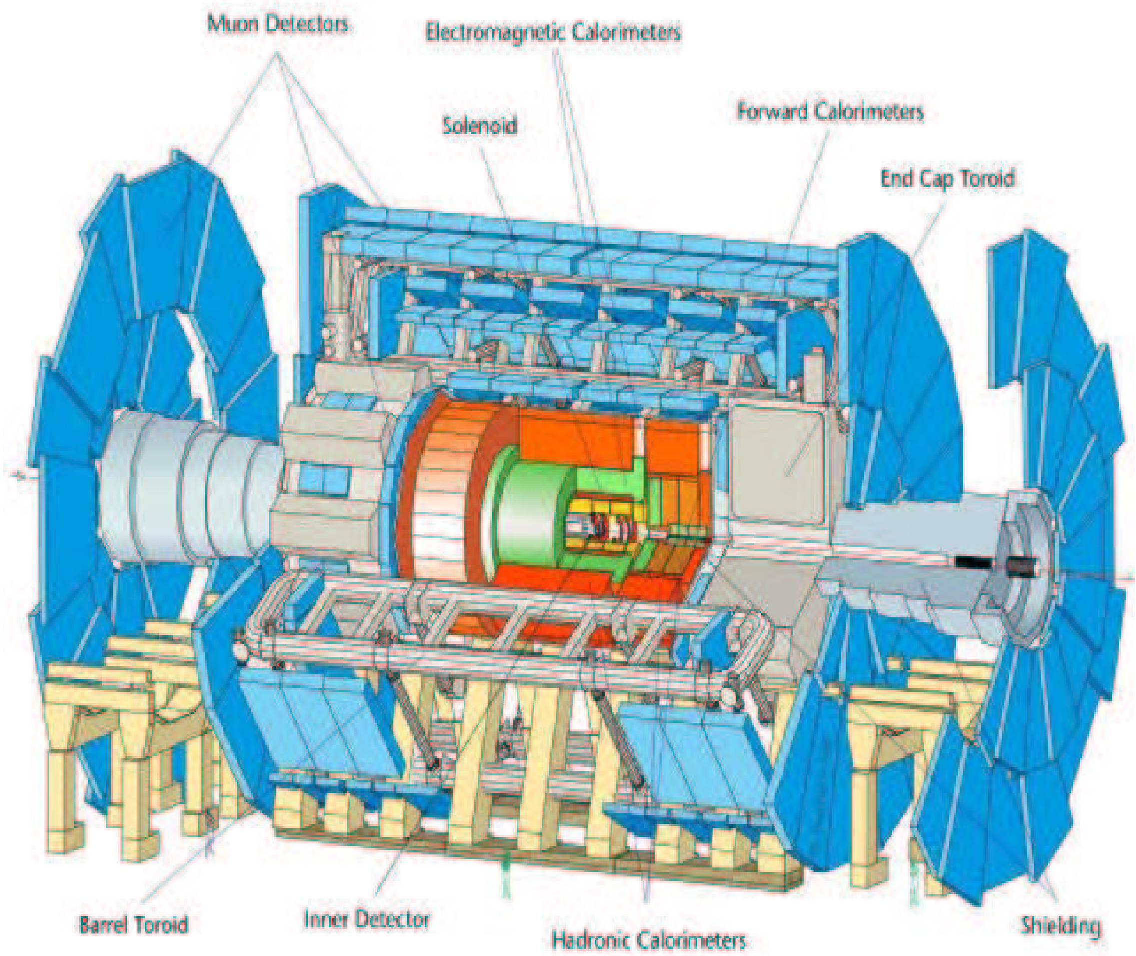

Figure 11.1: The layout of the ATLAS detector, with the different subsystems. This figure is obtained from Ref. [102].

resolution is approximately 16 μm in $r\phi$-direction and 580 μm in the beam direction. Again the sampling time is 25 ns. Both pixel and SCT detector require cold operation.

Transition Radiation Tracker At the larger radii, where the track density is lower, straw tubes are used for continuous tracking. These provide precise tracking at high rate with a relatively small amount of material, reducing the costs considerably. The straws are 4 mm diameter and have a 30 μm wire of tungsten in the middle. They are filled with a mixture of 70% Xe, 30% CO_2 and a small amount of O_2. A large number (36 in the barrel region) of tracking points is provided by the TRT, and the accuracy of position measurement is roughly 170μm. Particles traversing a straw cause ionization electrons to drift to the wire. The maximum drift-time is approximately 40 ns. The straw layers are interleaved with radiator material, where transition radiation (TR) photons are produced. Transition radiation is a threshold effect, arising when an ultra-relativistic particle crosses the boundary between two media of different dielectric and magnetic properties. In a few words, the solution to the inhomogeneous Maxwell equations in both media gives rise to a continuous energy loss. Because the solutions in the media do not match, a solution to the homogeneous Maxwell equations must be added, in order to match the continuity equations. This additional solution is transition radiation. The emittance of transition radiation depends, apart from the media and the distance between the boundaries, on the Lorentz boost factor γ of the traversing charged particle and is therefore suited for particle identification at high energies. Hits in the TRT are registered with respect to two discriminator levels: a low threshold level, corresponding to a normal hit, or a high threshold level, corresponding to a transition radiation hit.

With these thresholds, particle identification can be achieved in two (highly correlated) ways:

- By counting the number of straw hits exceeding the high threshold discriminator level [102].
- By using the Time-over-Threshold method (ToT) [102, 104], i.e. measuring the time which a signal is above the low threshold discriminator level. The more energy a particle deposits, the longer the signal will remain above the threshold [102], and thus, by measuring the time elapsed between a signal exceeding and falling below the threshold, it is possible to extract information about the $\mathrm{d}E/\mathrm{d}x$.

11.2.2 Calorimeters

One of the signals for SUSY is large missing transverse energy. Therefore it is important that the calorimeter system has a coverage as close to 4π as possible. In the ATLAS detector, a coverage up $|\eta|$ =4.9 will be achieved. The ATLAS calorimeter consists of an electromagnetic calorimeter and a hadronic calorimeter. An extensive overview can be found in Ref. [102].

The electromagnetic calorimeter The electromagnetic calorimeter consists of a barrel and two endcap calorimeters. It will conform everywhere to an 'accordion' geometry of liquid Argon as active material and lead as absorber. The total thickness of the barrel and endcap calorimeter is 24 and 26 radiation lengths respectively. It is contained inside a cryostat with a length of 6.8 m, an inner radius of 1.15 meter and an outer radius of 2.25 m. Right after the cryostat wall in the barrel region ($|\eta|$ <1.5) the solenoid magnet is located just in front of the calorimeter. After the solenoid, in the region $|\eta|$ <1.8 the electromagnetic calorimeter begins with a presampler detector. Its function is to correct for energy losses in the preceding inner detector, cryostats, and magnet coil. The barrel EM calorimeter has a coverage $|\eta|$ <1.5 and is composed of two identical half barrels. The endcap calorimeters are each divided in two coaxial wheels: an outer wheel (coverage 1.4< $|\eta|$ <2.5) and an inner wheel (coverage 2.5< $|\eta|$ <3.2). In the region devoted to precision physics ($|\eta|$ <2.5) the EM calorimeter is segmented into three longitudinal sections. The first section closest to the beam axis acts as preshower detector, the middle section is designed to contain the largest fraction of the electromagnetic showers, and a back section is to record the remaining part of the shower. At $|\eta|$ >2.5, the calorimeter is only divided in two longitudinal sections. All EM calorimeter cells point toward the interaction point. The granularity of the electromagnetic calorimeter is highest near the interaction point and decreases with increasing radii. The drift-time of the electrons resulting from a particle traversing the liquid Argon is about 300-600 ns, and thus a typical pulse can last about 20 bunch crossings [105]. The length of data-taking when a positive trigger signal is given, is approximately 125 ns [105], which is enough to reconstruct the signal's shape accurately.

The hadronic calorimeter The hadronic calorimeter surrounds the electromagnetic calorimeter. It consists also of a barrel calorimeter, which coverage the region up to $|\eta|$ <1.7 and two endcap calorimeters, which cover up to $|\eta|$ =4.9. In the barrel region, the hadronic calorimeter consists of plastic scintillator tiles with a thickness of 3 mm as active material, interleaved with iron absorber tiles of 14 mm. These tiles are placed in the radial direction and staggered with depth. The tile calorimeter has an inner radius of 2.3 meter and an outer radius of 4.3 meter. It consists of a central barrel ($|\eta| <1$) and two extended barrels ($0.8< |\eta| <1.7$). The central barrel is longitudinally segmented in three tile layers, which are 1.4, 3.9 and 1.8 interaction lengths thick, and azimuthally into 64 modules. The extended barrels are longitudinally segmented in two tile layers, and azimuthally segmented as the central barrel. The total thickness from the interaction point to the outer edge of the tile region is 9.2 interaction lengths at $\eta =0$. If the outer support is included, the thickness is 11 interaction lengths. The sampling time is about 175 ns. Rather than using scintillation light, the endcap region uses a different sampling technique, which has better radiation resistance. At each side, the endcap region is divided into a hadronic endcap calorimeter, covering the region $1.5< |\eta| <3.2$, and a high density forward calorimeter, covering the region $3.1< |\eta| <4.9$). The hadronic endcap calorimeters consist of two independent wheels, both with outer radius 2 m, which are placed one behind the other in the z-direction. The endcap hadronic calorimeter uses liquid Argon as active material, interleaved with copper as absorber. The forward calorimeter consists of three sections, and uses tungsten instead of copper, which has an even higher radiation resistance. The time of data-taking in case a positive trigger signal is received is about 125 ns.

11.2.3 Muon spectrometer

The muon spectrometer is the largest subsystem in the ATLAS detector, used for the identification and high precision measurements of muons [106]. The measurements of muon momenta makes use of the magnetic deflection of muon tracks in a 0.5-2 T magnetic field. Four different chamber technologies are used in the muon spectrometer, each covering a different geometrical region and physics purpose. The overall layout of the muon chambers is shown in Fig. 11.2. The system

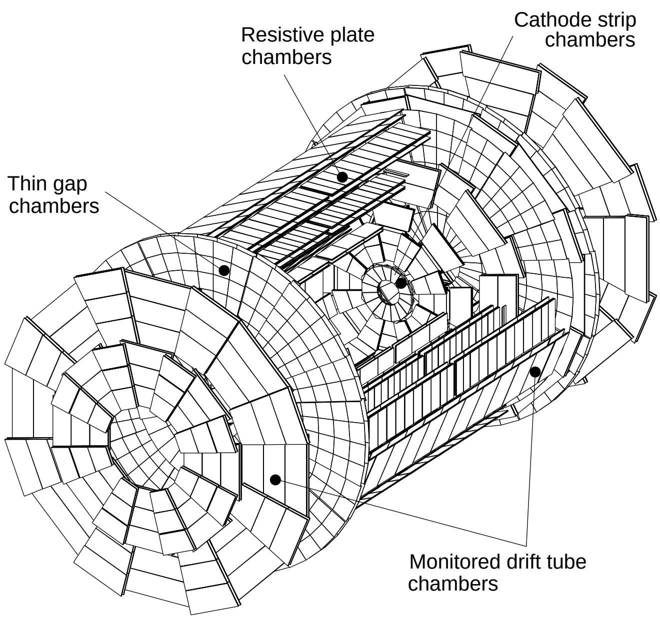

Figure 11.2: The layout of the muon spectrometer, with the four different chamber technologies. This figure is obtained from Ref. [102].

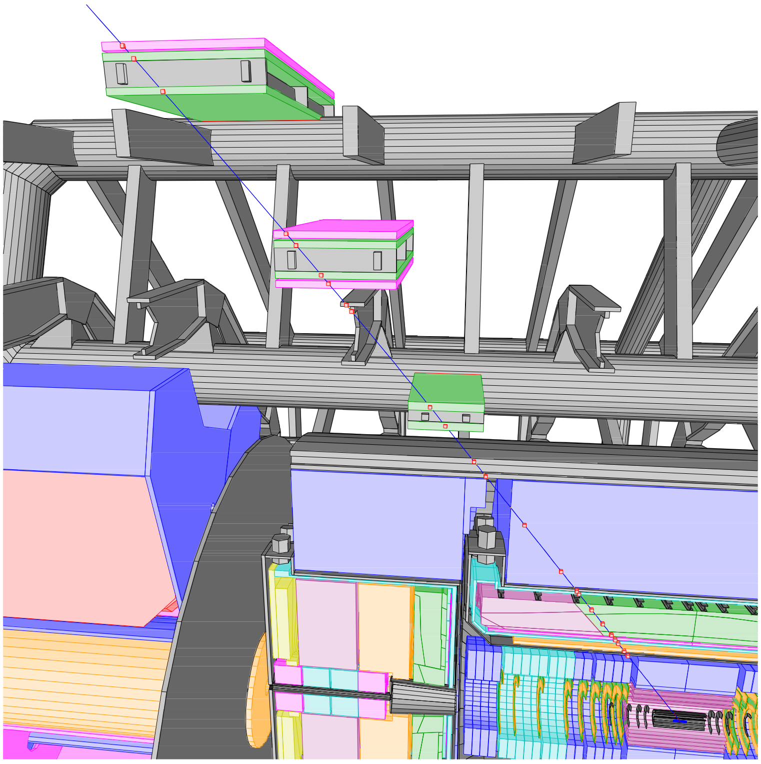

Figure 11.3: The layout of the muon spectrometer, with the four different chamber technologies. This figure is obtained from Ref. [102].

consists of three subsystems: a barrel part and two endcap parts. In the barrel region ($|\eta| < 1.0$), the magnetic field is provided by eight superconducting air-toroid magnets, in the endcap regions ($2.7 < |\eta| < 1.4$), it is provided by superconducting endcap magnets, while in the transition region, a superposition is used. In the barrel region, three layers of muon chambers are arranged in three cylindrical layers parallel with the beam axis. In the endcap, the chambers are arranged in four layers orthogonal to the beam axis. In Fig. 11.3, we show a trajectory of a muon through the different subdetectors. The muon system serves a threefold purpose:

- It provides precision measurement of momenta of charged particle.
- It serves as trigger.
- It serves as bunch crossing time identification.

The first purpose, providing precision measurements, is performed in both endcap and barrel region by Monitoring Drift Tubes (MDT's) in the region $0 < \eta < 2.0$. Three layers of MDT's are located at 4.93 m, 7.12 m and 9.48 m. These are aluminum tubes with a diameter of 3 cm, and a central W-Re wire of 50 μm, filled with a gas mixture of 93% Ar and 7% CO_2. The drift times in such tubes are on average approximately 300 ns, with a maximum of 700 ns. The tube-lengths range from 70 to 630 cm. A particle which crosses the drift chamber ionises the chamber gas along its path, and the electrons drift to the anode-wire under influence of an electric field. The position of the particle is calculated by measuring the drift time of the electrons to the anode-wire. The space resolution is roughly 80 μm. This measurement requires a starting time t_0, which corresponds to the time-of-flight for a particle from the interaction vertex to the fired station. At values of $2 < |\eta| < 2.7$, Cathode Strip Chambers (CSC's) are used for precision measurements, being more radiation proof. These are multiwire proportional chambers, with a much smaller drift-time of approximately 30 ns, and a resolution is about 60 μm. The gas mixture is 30% Ar, 50%CO_2 and 20%CF_4. The way in which the time-of-flight is measured is the same as for MDT's.

The second purpose, triggering, is performed by tree layers Resistive Plate Chambers (RPC's) in the barrel region ($\eta < 1$), while in the endcap three layers of Thin Gap Chambers (TGC) are used. The RPC's consist of gas gaps of 2 mm thickness. The signal produced by the ionization electrons is read out by metal strips on each side of a gas gap. Fast measurements are provided, typically within 10 ns. The space-time resolution is about 1 cm $\times$ 1 ns. In the region $1 < |\eta| < 2.4$, Thin Gap Chambers (TGC's) are used. These are very similar to multiwire proportional chambers, with drift times less then 10 ns. Unlike the TGC's, these are based on collecting ionization electrons on a wire, resulting in a slightly slower response than that of RPC's. The position of the trigger stations is displayed in Fig. 11.4.

The third purpose, bunch crossing time identification, is performed with the same techniques as providing trigger measurements. The probability that a muon is assigned to the wrong bunch crossing is less than $\mathcal{O}(10^{-5})$ [107]. Although the identification of the bunch crossing time is relevant for this work, as will be outlined in Section 13.3.1, a detailed description about the way in which bunch crossing identification takes place is beyond the scope of this work. For more details the reader is referred to Ref. [107].

11.2.4 Magnet system

ATLAS has a superconducting magnet system, consisting of two magnets: a central solenoid and three large air-core toroids. In Fig. 11.1 the magnet system can be seen. The overall dimensions of the magnet system is 26 m in length and 20 meter in diameter. The Central Solenoid (CS) provides the Inner Detector with a magnetic field of approximately 2 T. It uses as superconductor a mixture of NbTi, Cu and Al. The inner and outer diameter are 2.44 meter and 2.63 meter respectively. The CS is built in front of the calorimeters. This has the advantage that the size is smaller, reducing the costs considerably. The disadvantage is the possibility that particles start showering already in the the CS instead of in the calorimeters. This effect is minimized by using a shared cooling system for the CS and the liquid Argon Calorimeters, eliminating two vacuum walls. The CS is cooled with liquid Helium of 4.5 K. The current which must be supplied to the CS is 8kA.

The air-core toroids (a barrel and two endcap toroids) provide a magnetic field of approximately 4 T to the muon spectrometer. The two endcap toroids have a length of 5 meter, an outer diameter of 10.7 meter and an inner diameter of 1.65 meter. The barrel toroid has an inner and outer diameter of 9.4 and 20.1 meter, respectively. Both endcap and barrel toroids consist of eight coils with rectangular shape, which are assembled radially and symmetrically around the beam axis, see Fig. 11.1. All coils are made of the same material as the CS. The barrel coils have individual cryostats around them to avoid forces between them, and to provide mechanical stability. The coils in the endcap toroids are instead housed in one cryostat. Radial overlap between the barrel toroid and the endcap toroids is assured. As the CS, the magnets are cooled by a constant flow of Helium at 4.5 K. The magnets require a current of 21 kA.

11.2.5 Trigger system

At high luminosity, approximately 23 fundamental collisions per bunch crossing take place. Bunch crossings take place with a frequency of 40 Hz, resulting in an interaction (i.e. parton-parton) rate of approximately 10^9 per second. Due to a limited storage capacity, the event storage rate will be approximately 100 Hz at high luminosity. Thus, selection of interesting physics processes constitutes one of most important issues in ATLAS. To achieve such a large reduction of the initial input rate, the ATLAS trigger is organized in three sequential levels: the Level 1 trigger (LVL1), the Level 2 trigger (LVL2), and the Event Filter (EF). The LVL1 trigger reduces the event rate from 40 MHz to 75 kHz. While waiting for the decision of the LVL1 trigger, the data from all detector parts are stored locally in pipe-line memories. All detector parts are synchronized with the LHC bunch crossing time each 25 ns by taking into account the delay of particles traveling with the speed of light. Synchronization is achieved by suitable delay lines, so that the digits from the inner parts arrive simultaneously at the pipe-lines as those from the outermost muon station. If the LVL1 trigger classifies an event as interesting, all detector information which possibly belongs to the event is stored. It depends on the particular subdetector how long the time of data taking is. Although it is rare that a certain tube or cell is hit again in the next bunch crossing, it may happen that information of the next events is stored. E.g. during the 700 ns of measurements of the muon-precision chambers, 28 other bunch crossing have taken place and some overlap is thus expected! If the events is identified as passing the trigger selection in the LVL1 trigger, the event is ‘transported‘ to the LVL2 trigger, otherwise it is lost. If the LVL2 trigger gives valid identification, the event is analyzed by the EF. In case the event is interesting, it is written to disk. The LVL2 and the EF together reduce the event rate by a further factor of 1000. Details about the LVL1 and higher level trigger systems can be found in Ref. [108] and Ref. [109], respectively. Since the muon trigger is one of the important triggers for this study, its main properties will shortly be reviewed.

The muon trigger Several muon trigger schemes can be distinguished [106, 109]. Currently, the following trigger schemes are proposed for muons:

- A low luminosity trigger for low p_T muons, denoted by $\mu 6$. It will select muons with $p_T > 6$ GeV. The way in which muons are selected is displayed in Fig. 11.4. Muons are qualified

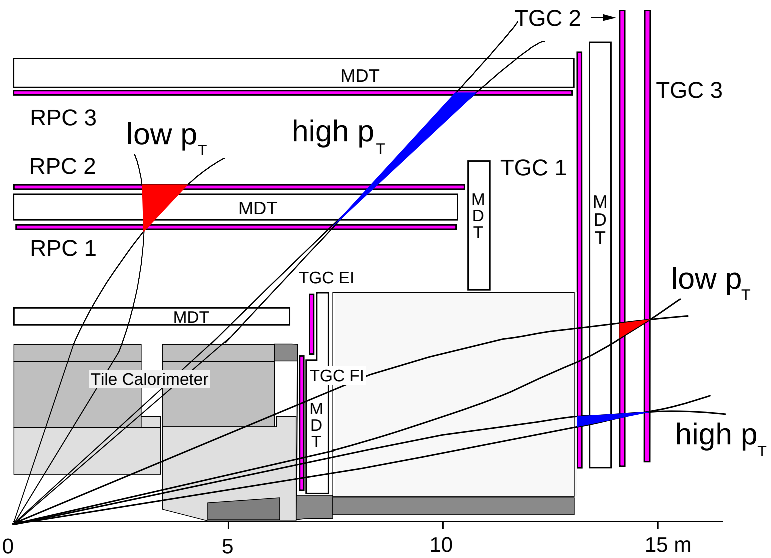

Figure 11.4: The position of the trigger stations and the identification of muons in the two muon trigger schemes. This figure is obtained from Ref. [102].

Region	Trigger station	Distance (cm)	Used in $\mu 6$?	Used in $2\mu 10$?
Barrel	RPC1	r=673	yes	yes
	RPC2	r=750	yes	no
	RPC3	r=986	no	yes
Endcap	TGC1	z=1291	no	yes
	TGC2	z=1407	yes	no
	TGC3	z=1454	yes	yes

Table 11.1: Trigger stations and their position. The names of the trigger stations correspond to those displayed in Fig. 11.4. The distance means the distance to the beam axis for barrel trigger stations, and the distance to a plane orthogonal to the beam axis for the endcap trigger stations. Trigger stations for $\mu 20i$ and $2\mu 10$ schemes are the same.

as passing the selection or not by measuring their deflection angle (the smaller the velocity of the muon, the larger the deflection angle) and by requiring a coincidence in the trigger stations RPC1 and RPC2. In the endcap region, a low p_T muon candidate is found if there are three out of four possible hits in the outer two TGC planes (TGC2 and TGC3).

- A high luminosity trigger for two high p_T muons with $p_T > 10$ GeV/c, denoted by $2\mu 10$. A high p_T muon in the barrel region is defined if the low p_T criteria are satisfied, and if in addition a third hit is found in the outermost station RPC3. A high p_T muon candidate in the endcap region must satisfy the low p_T criteria, and in addition it must have at least two hits in the inner TGC1 station.

- A high luminosity trigger for an isolated high p_T muon with $p_T > 20$ GeV/c, denoted by $\mu 20i$. Selection criteria are similar to the previous scheme.

A summary of which trigger stations are used in which triggers is given in Table 11.1. The way in which the trigger functions is as follows. The muon trigger can basically be fired at any time, i.e. it is not directly integrated with the LHC clock. The association of the trigger to the right bunch crossing is a non-trivial task, and an ongoing point of discussion [110, 107] even for ordinary muons. An important quantity in the muon trigger is the so-called temporal gate of the muon stations, which is the time window within which the coincidence must take place. There are many complicated issues which must be taken into account when deciding the minimal temporal gate time [109, 110, 107], of which some of the most relevant issues are the following:

- The time-of-flight of a muon between the layers. For the endcap layers (RPC's), this is 0.8 m/c $\approx$3 ns for the low p_T trigger, and 2.4 m/c $\approx$8 ns for the high p_T trigger. For the endcap (TGC's), this is 0.5 m/c $\approx$ 1.6 ns for the low p_T trigger, and 1.6m/c $\approx$5 ns for the high p_T trigger.

- The propagation of the signal to the read out electronics, which depends on the distance between the hit position and the electronics, roughly a few ns. As was mentioned in the previous section, the response of the RPC's is slightly faster than that of the TGC's, and thus for the TGC's a larger temporal gate time may therefore be preferred.

- The propagation of the signals along the strips, also a few ns.

- The clock of the electronics is counting in steps of 3.125 ns, thereby inducing an uncertainty on the exact time of arrival of the signal.

For a 100% muon trigger efficiency, the temporal gate time should be as large as possible, i.e. 25 ns, however such a large value would induce an unacceptable amount of background [110]. This background is mainly the result of pions and protons produced in the forward directions, which interact hadronizally with the beam pipe, the detector, and the detector walls and produce thereby thermal neutrons, with fluxes of at least 1000 Hz/cm^2! Such neutrons are captured and result in low energy photons, which in turn react via the Compton effect, whereby electrons are produced. The latter cause tracks in the muon system. A second source of background is cosmic muons. In conclusion, the accidental coincidence rate is enormous, and thus the windows must be as tight as possible. A reasonable (but not fixed!) temporal gate time, allowing a high efficiency to record signal muons, and rejecting as much background as possible, is for the muon triggers based on RPC stations currently taken to be approximately 18 ns [109, 110, 111]. For the TGC's, no detailed studies have been done, however no drastic differences from 18 ns are expected [110]. For slow particles, having a larger time-of-flight, it is therefore obvious that the temporal gate time results in an inefficiency for recording such events. Although a preliminary study was presented in Ref. [111], detailed studies on the exact time necessary for the RPC's and TGC's to be fired are necessary in the future.

Calorimeter triggers An extensive description about the performance of the calorimeter triggers can be found in Ref. [105, 108, 109], and only very few relevant aspects are mentioned here. The calorimeter trigger uses as input so-called trigger towers of granularity of $\Delta\eta \times \Delta\Phi = 0.1 \times 0.1$ from the electromagnetic and the hadronic calorimeters, which can then form a region-of-interest (ROI). These towers are formed by analogue summation of the energies of corresponding cells. To calculate the missing transverse energy E_T^{miss}, vector summation is performed over the transverse energies of all cells. To calculate the scalar transverse visible energy, E_T, scalar summation is performed over the transverse energies of all cells. At first-level triggering, only the calorimeter cells are used. When the event is built, additional information of other subdetectors can be used, and it is more a sum of all reconstructed particles.

While the pulse-shapes in the calorimeters extend over several bunch crossing, the sampling rate of the calorimeter trigger is 40 MHz (every 25 ns). The shaping-time necessary for the trigger to make a decision whether a cell was hit or not is roughly 15 ns, and thus only a small fraction of the whole signal shape is used by the trigger to make a decision.

Missing and visible energy As was just mentioned, at first level trigger the E_T^{miss} and E_T are calculated by taking the vector respectively scalar sum of the transverse energies of all cells. When the event is build, the p_T values as measured in the inner detector and in the muon chambers are used in the calculation of the sum, like the energy-flow package in ALEPH. Thus, it is strictly speaking more correct to speak of missing and visible transverse momentum of an event, rather than the energy.

For R-hadron events, the definition of missing and visible transverse energy should be as follows. For charged R-hadrons detected in the inner detector, their p_T is counted in the sum, while for neutral R-hadrons the transverse energy as measured in the calorimeter is counted. If the R-hadron is detected in the muon chambers, but not in the inner detector, the p_T as measured in the muon chambers is counted, while if it is detected in both, only the inner detector is counted.

Chapter 12

Detection of heavy hadrons

In Chapter 5, typical manifestations of R-hadrons have already been discussed, such as baryon conversion, total energy losses, and energy losses per interactions in different materials. In this Chapter, the typical signatures are studied of single R-hadrons in the different ATLAS subdetector. After giving introductory remarks in Section 12.1, signatures in the inner detector, in the calorimeters, and in the muon chambers will be investigated in Sections 12.3, 12.4 and 12.5, respectively. In view of the analysis presented in the next Chapter, relevant responses will be parameterized. Finally, the combination of all subdetectors is discussed. Although the results in this Chapter are constantly presented in terms of R-hadrons, it must be emphasized that the *results presented below are valid for heavy hadrons arising from any kind of color octet.* Thus, all signatures discussed here are independent of the event topology!

12.1 Which signatures?

In ATLAS, the signatures which can be used for the detection of single heavy stable hadrons are the following:

- High transverse momentum for charged hadrons.
- Heavy ionization in the tracking system, in case the R-hadrons are charged and slowly moving.
- A characteristic pattern of energy deposition in the calorimeters.
- A large time-of-flight, measurable with the muon chambers.

The results below are based on generating single R-hadrons and propagating them through the ATLAS detector with the full simulation framework ATLSIM version 8.0.3. Reconstruction is performed with the Athena reconstruction framework version 8.0.3., unless explicitly mentioned that reconstruction is done within ATLSIM. Based on that fact that 98% of the R-hadrons are mesons, as was shown in Chapter 2, all generated R-hadrons are mesons.

12.2 Transverse momenta in the inner detector

As has been explained in Chapter 2, heavy particles are often produced with high p_T values. Ideally, the measured momentum should be very sharply peaked around the generated momentum of the R-hadron. However, multiple scattering, nuclear interactions and overlapping tracks cause

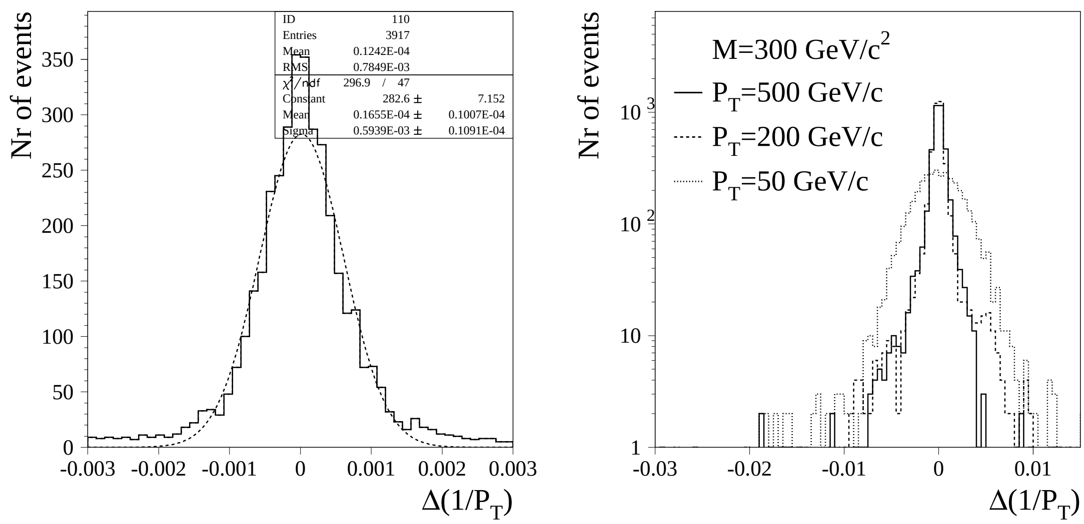

Figure 12.1: Left: $\Delta(1/p_T)$, the difference between the reconstructed and generated $1/p_T$ for an R-hadron of 300 GeV and p_T = 500 GeV/c, fitted with a gaussian. Right: distribution for $\Delta(1/p_T)$ for an R-hadron of 300 GeV and different p_T values, averaged over η.

tracks to be lost or produce tails in the reconstructed parameters. The momentum resolution of a real detector, based on particle deflection in a magnetic field, receives two main contributions:

- An uncertainty arising from measuring the curvature of the particle in the magnetic field. For a homogeneous magnetic field, the contribution to the momentum resolution from this measurement error is for N equidistant measurements over a traversed length L is [112, 113]

$$\frac{\sigma(p_T)}{p_T} = \frac{\sigma(r\phi)p_T}{0.3BL^2}\sqrt{\frac{720}{N+4}}, \tag{12.1}$$

  where $\sigma(r\phi)$ is the measurement error in one dimension.

- An uncertainty arising as a consequence of multiple scattering. The contribution to the momentum resolution is [113]

$$\frac{\sigma(p_T)}{p_T} = \frac{0.05}{BL}\sqrt{\frac{1.43L}{X_0}}, \tag{12.2}$$

with X_0 the radiation length. In both expressions B is in Tesla, L and x_0 in meter and p_T in GeV/c. The momentum resolution for R-hadrons as measured by the inner detector is investigated. For this purpose, single positively charged R-hadrons are generated with various masses (100 GeV/c^2, 300 GeV/c^2, 600 GeV/c^2), transverse momenta, and η values, and reconstructed. The momentum resolution $\Delta(1/p_T) = 1/p_t(\text{true}) - 1/p_t(\text{reconstructed})$ is given by a Gaussian distribution, as can be seen in Fig. 12.1 (left). In Fig. 12.1 (right), the distribution for $\Delta(1/p_T)$ is displayed for an R-hadron of different momentum. In Fig. 12.2, the widths of these Gaussian distributions, $\sigma(1/p_T)$, are displayed for fully simulated and reconstructed R-hadrons of different momenta, as function of η. In view of the ATLAS analysis presented in the next Chapter, the transverse momentum resolution is parameterized as follows. ATLFAST contains parameterizations for the momentum resolution of muons in the inner detector, following closely the general

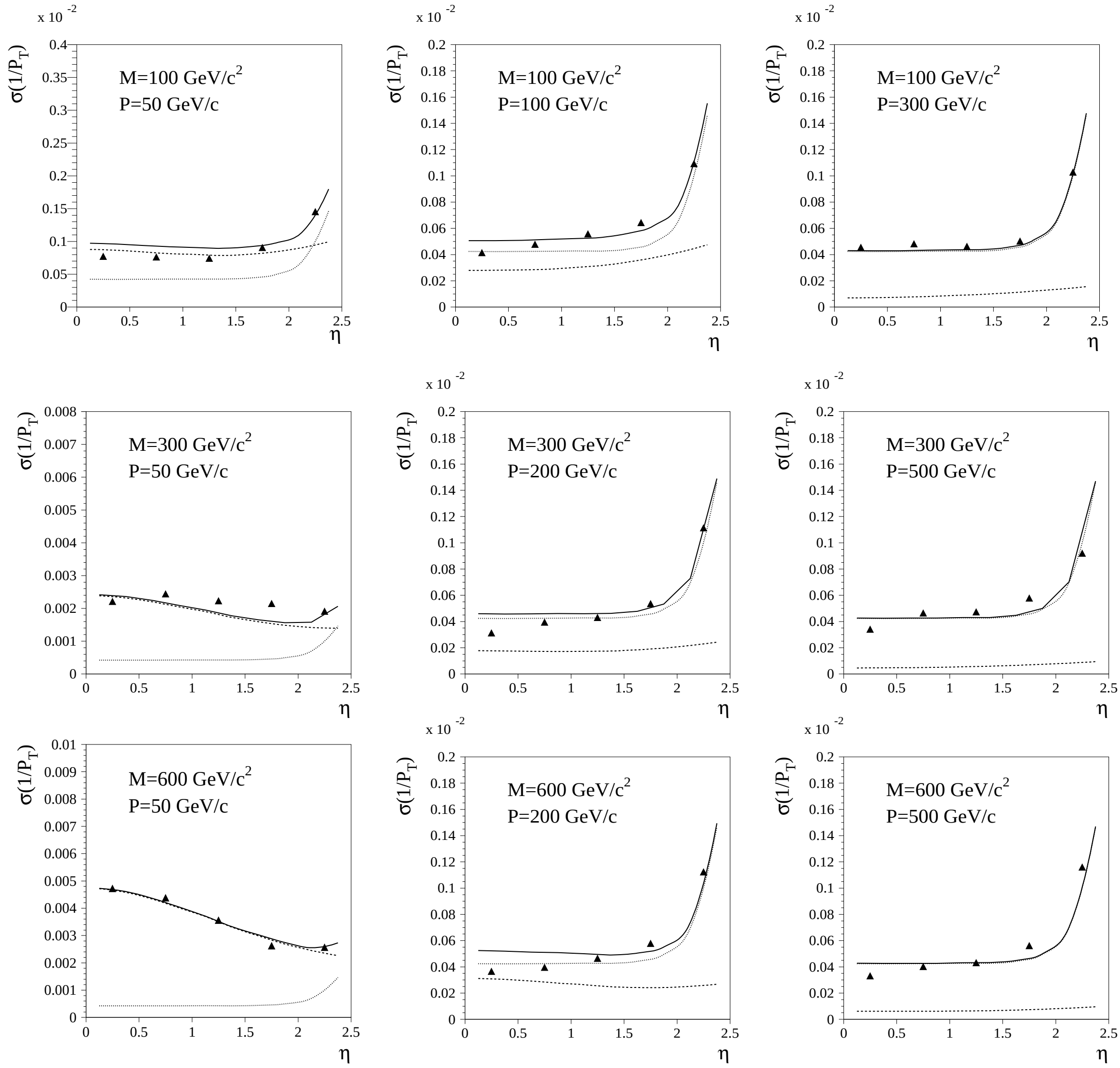

Figure 12.2: A comparison of the momentum resolution $\sigma(1/P_T) = \frac{1}{p_T^{true}} - \frac{1}{p_T^{rec}}$ in the full simulation and reconstruction framework (solid triangles) and the parameterizations in ATLFAST (solid lines). For ATLFAST, also displayed are the separate contributions due to multiple scattering (dashed line) and the measurement error (dotted line).

expressions for the momentum resolution in Equations (12.1) and (12.1). A simple correction of the multiple scattering term for $\beta \neq 1$ turned out to be enough for a reasonable description of the momentum resolution of R-hadrons. Thus, for fast R-hadrons, the momentum resolution is the same as that for muons. The parameterizations, as well as a comparison with full simulation, are shown in Fig. 12.2.

12.3 Signatures in the TRT detector

A heavy slow charged ionizing particle results in a significant amount of δ electrons and ionization energy deposit in the TRT. R-hadrons can identified by counting the number of high threshold hits, and by using the Time-over-Threshold method.

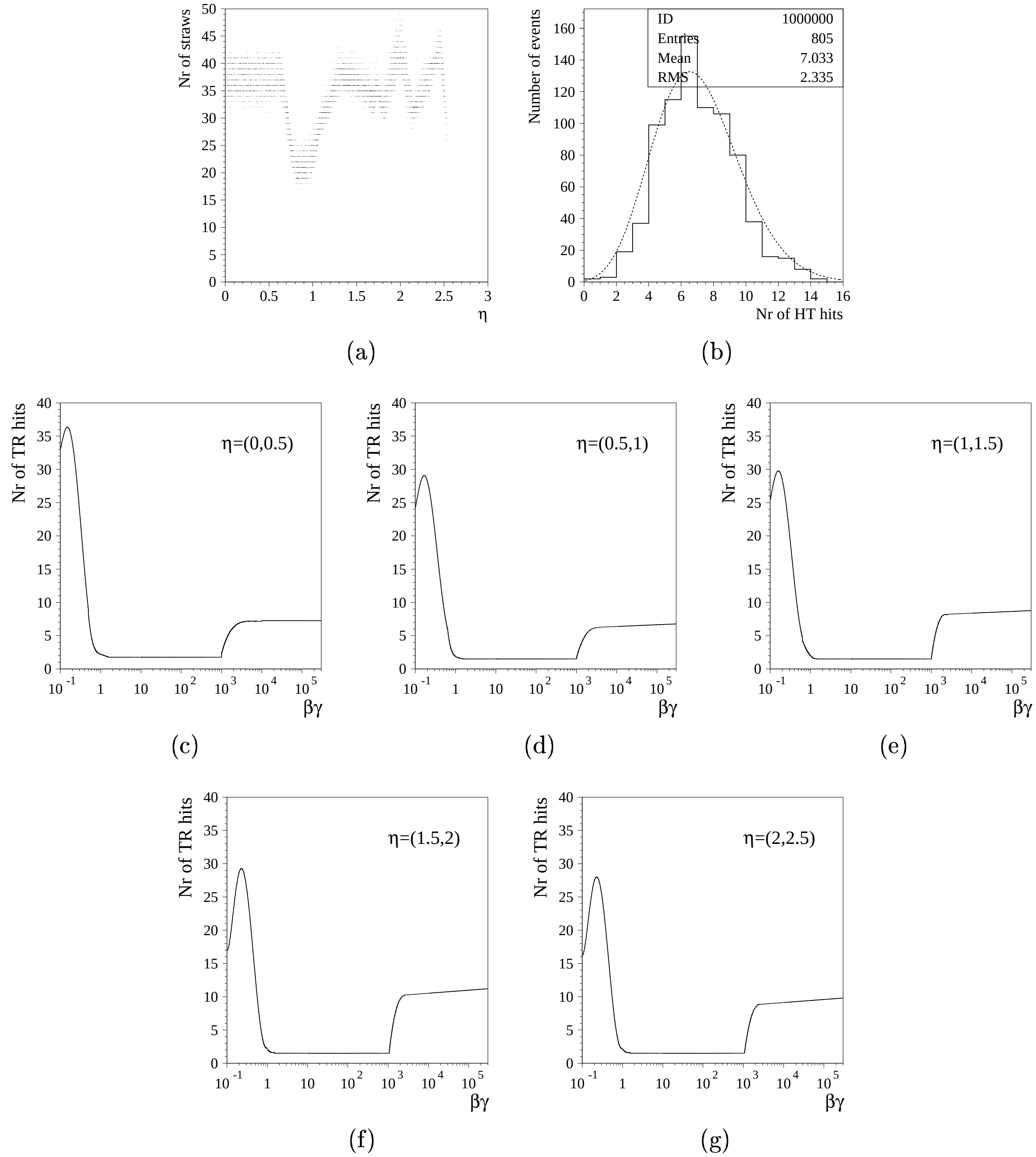

Figure 12.3: (a) The number of straws hit as function of η. (b) Distribution of the number of high threshold hits, for high energy muons with a fixed value of $\gamma\beta$ in the region $\eta < 0.5$, fitted with a Poisson distribution. (c)-(g) Average number of HT hits as function of $\gamma\beta$ of a particle for different regions of η.

12.3.1 Method 1: Counting HT hits

To study the number of high threshold hits of R-hadrons, and to compare them with those of electrons and muons, R-hadrons of different mass (100 GeV/c^2, 300 GeV/c^2, 600 GeV/c^2), transverse momenta and η-values have been generated, as well as muons and electrons with various

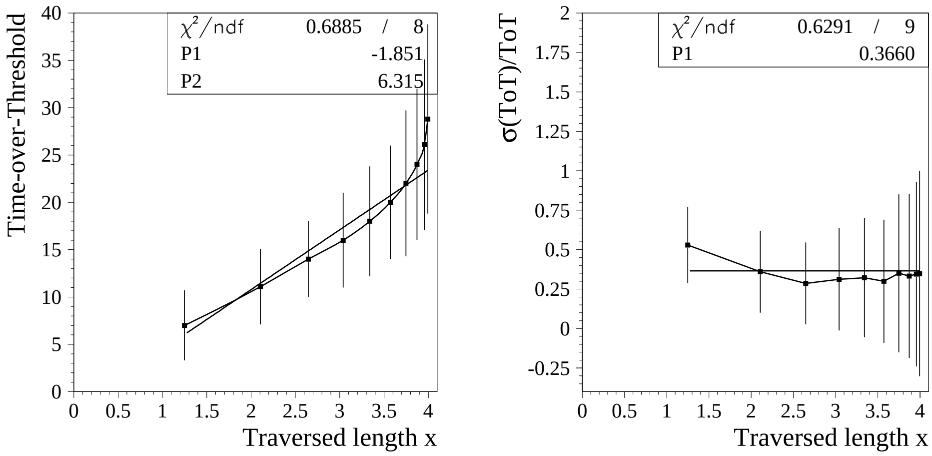

Figure 12.4: Left: the ToT as function of the traversed length in the straw for a 5 GeV pion, fitted with a first degree polynomial. Data points are obtained from Ref. [104]. Right: error as obtained from the top left figure divided by their central value, fitted with a constant.

transverse momenta and η-value, and reconstructed. In Fig. 12.3(a) the number of straws hit by a particle is displayed as function of η. The number of straws varies with η, and so does the the average amount of high threshold hits. The TRT detector is therefore divided into five η regions, and the average amount of high threshold hits is studied as function of $\beta\gamma$ of the particle. Note that real velocities are relevant for the production of TRT hits, rather than transverse quantities! A simple parameterization of this average is made, shown in Fig. 12.3(c)-(g). As is shown in Fig 12.3(b), the amount of high threshold hits for a certain η and $\beta\gamma$ value are given by a Poisson distribution. Thus, given the particle's η and $\beta\gamma$ value, the number of high threshold hits is given by a Poisson distribution around the mean value as given by the parameterized functions. It is seen that the transition radiation hits can play a role for R-hadron identification only for $\beta\gamma \lesssim 1$, or $\beta \lesssim 0.7$. On the other hand, the number of HT hits can be used to separate R-hadrons with $\beta \gtrsim 0.7$, which are minimum ionizing, from very high p_T muons, being in the relativistic rise region.

12.3.2 Method 2: Time-over-Threshold

It is possible to identify particles by making use of the fact that every particle deposits a certain energy per unit distance $\mathrm{d}E/\mathrm{d}x$ in a straw. Rather than recording the exact size of the signal, proportional to $\mathrm{d}E/\mathrm{d}x$, the TRT electronics can measure the time of a signal being above a certain threshold (the low threshold). This time depends on the deposited energy [104]; a heavily ionizing particle manifests itself by a large time-over-threshold (ToT). Note that the ToT never exceeds the maximal drift time of roughly 40 ns. Ref. [104] has shown that the recent changes in TRT electronics affect the discrimination power of the ToT-method. In Ref. [104], the pion-electron separation is determined using the testbeam results for beam energies of 1, 2, 3, 5 and 9 GeV. These results can used in two ways to study the identification of R-hadrons:

- To use the *proportionality* between the *traversed length* in the straw, which is proportional to the $\mathrm{d}E/\mathrm{d}x$, and the ToT in the straw. Ref. [104] has shown the dependence of the ToT on the hit distance to the anode in the straw: the closer to the anode wire the track hits are located, the larger the ToT. Translating the hit distance to the anode into the

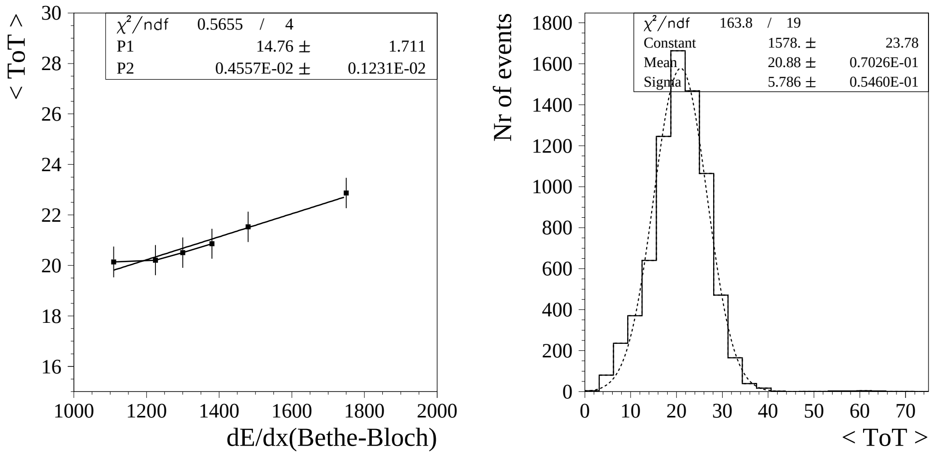

Figure 12.5: Left: the relation between the dE/dx of a pion, and its average ToT. Right: a 1-dimensional projection of the ToT for central values (between 0.8 and 1.2 mm) of the distance of closest approach, fitted with a gaussian.

traversed length in the straw, and remembering that dE $\sim x$, we expect the ToT to be linear dependent on the traversed length x. However, Fig. 12.4 shows a different behaviour: the signal increases significantly if the straw is hit very close to the anode wire. Fig. 12.4 also shows the error on the ToT; the error divided by the ToT is roughly constant. Although a fit with a straight line is possible, the unexpected increase of the ToT at small hit distances from the wire makes this method inappropriate to establish the dependence of the ToT on the dE/dx. [1]

- To use the relation between the ToT averaged over all hit distances in a straw, <ToT>, on the dE/dx following from the Bethe-Bloch description. This can be obtained from testbeam data of pions of different energies. Pion testbeam data are available with dE/dx

[1] An explanation is that a particle crossing a straw close to the anode produces electrons, having a large spread in the drift distances to the anode. A particle hitting the straw far away produces electrons which drift distance to the anode wire is approximately equal.

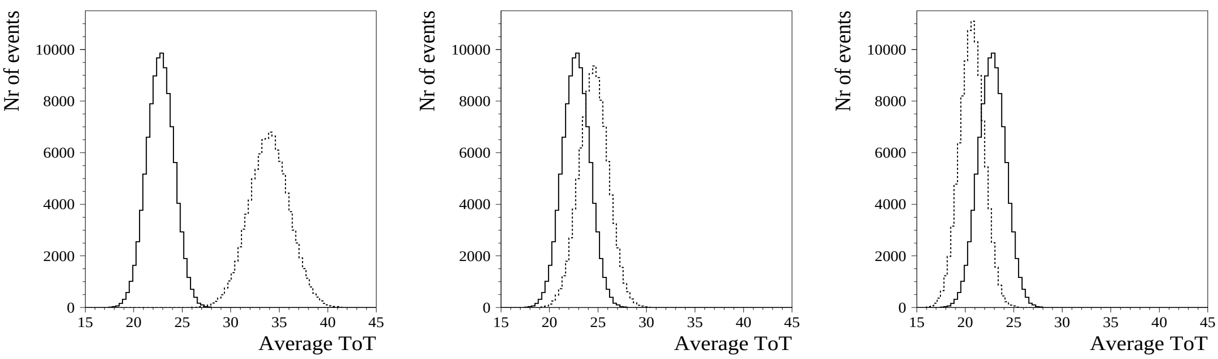

Figure 12.6: The average ToT if a particle hits 33 straws, the average over all eta values, for ultra-relativistic pions with dE/dx=1700 mip (black curve) and for R-hadrons of $\beta = 0.5$ (left), $\beta = 0.7$ (center) and $\beta = 0.9$ (right)

values from almost minimum ionizing particles (mip's) to far into the relativistic rise, and thus we have an accurate description of the <ToT> as function of the theoretical $\mathrm{d}E/\mathrm{d}x$. In Fig. 12.5 the <ToT> is displayed as function of the theoretical $\mathrm{d}E/\mathrm{d}x$. The linear dependence between the $\mathrm{d}E/\mathrm{d}x$ of the particle and its <ToT> in a straw enables us to extrapolate the $\mathrm{d}E/\mathrm{d}x$ for R-hadrons in the region of the Bethe-Bloch function where $\mathrm{d}E/\mathrm{d}x$ is proportional to $1/\beta^2 \times \mathrm{d}E/\mathrm{d}x(\mathrm{mip})$ and to obtain the expected <ToT>. The <ToT> is Gaussian distributed, as is shown in Fig. 12.5. The actual <ToT> measured in the detector is then given by a Gaussian distribution around the average, with a σ as obtained from Fig. 12.4. Although the latter method will not be used in the analysis in the next Chapter, it is possible to estimate the separation power of the ToT method between heavy hadrons and ultra-relativistic electrons and pions (realistic situation if a strong cut on the transverse momentum is implied). Thus, a gedanken experiment is done with 100000 measurements, for different β values, and an average ToT is generated and compared to that of ultra-relativistic pions. Results are displayed in Fig. 12.6. It is seen that for R-hadrons with velocities $\beta = 0.5$, $\beta = 0.7$ and $\beta = 0.9$ a separation of 5.3σ, 1.3σ and 1.5σ can be obtained. Note that for high β values the R-hadron becomes less ionizing than the ultra-relativistic pion, i.e. it becomes a mip.

The number of high threshold hits and the <ToT> in the TRT are the only estimators of $\mathrm{d}E/\mathrm{d}x$ that we have. These estimators are very highly correlated, so that the separation power of the two together is only slightly larger than the separation power of the best single estimator.

12.4 Signatures in the calorimeters

12.4.1 Energy deposit

To study signatures in the calorimeters, singly charged R-mesons have been generated and reconstructed. It must be noted that the results presented below do not depend on the initial charge of the R-hadron due to repeated charge flipping! In Fig 12.7, the number of interactions, which an R-hadron undergoes when traversing the ATLAS calorimeters (left), and when entering the muon system (middle) is displayed as a function of η for an R-hadron which punches through. In

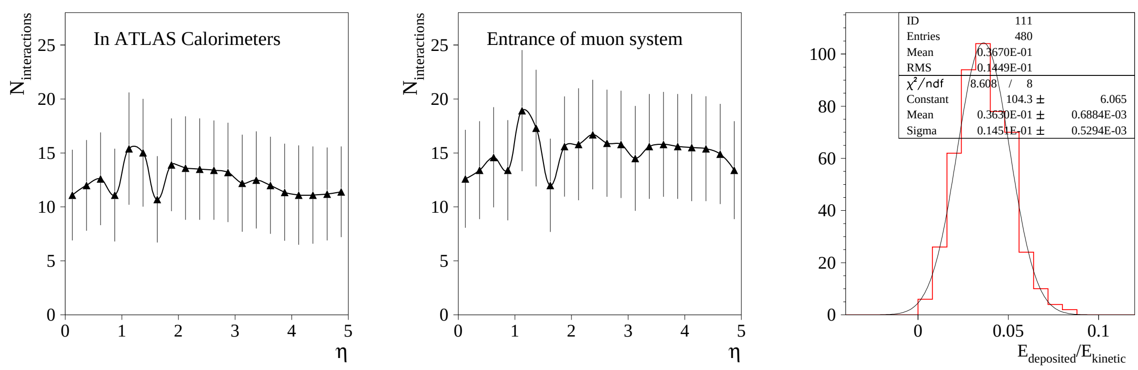

Figure 12.7: The average number of interactions and its spread in ATLAS as function of η, for a punching through R-hadron at the end of the ATLAS calorimeters (left) and at the entrance of the muon system (middle). Right: typical distribution of the energy deposit divided by the kinetic energy, for an R-hadron with M=300 GeV/c^2 and a kinetic energy of 600 GeV in the central region of the detector ($\eta < 0.8$).

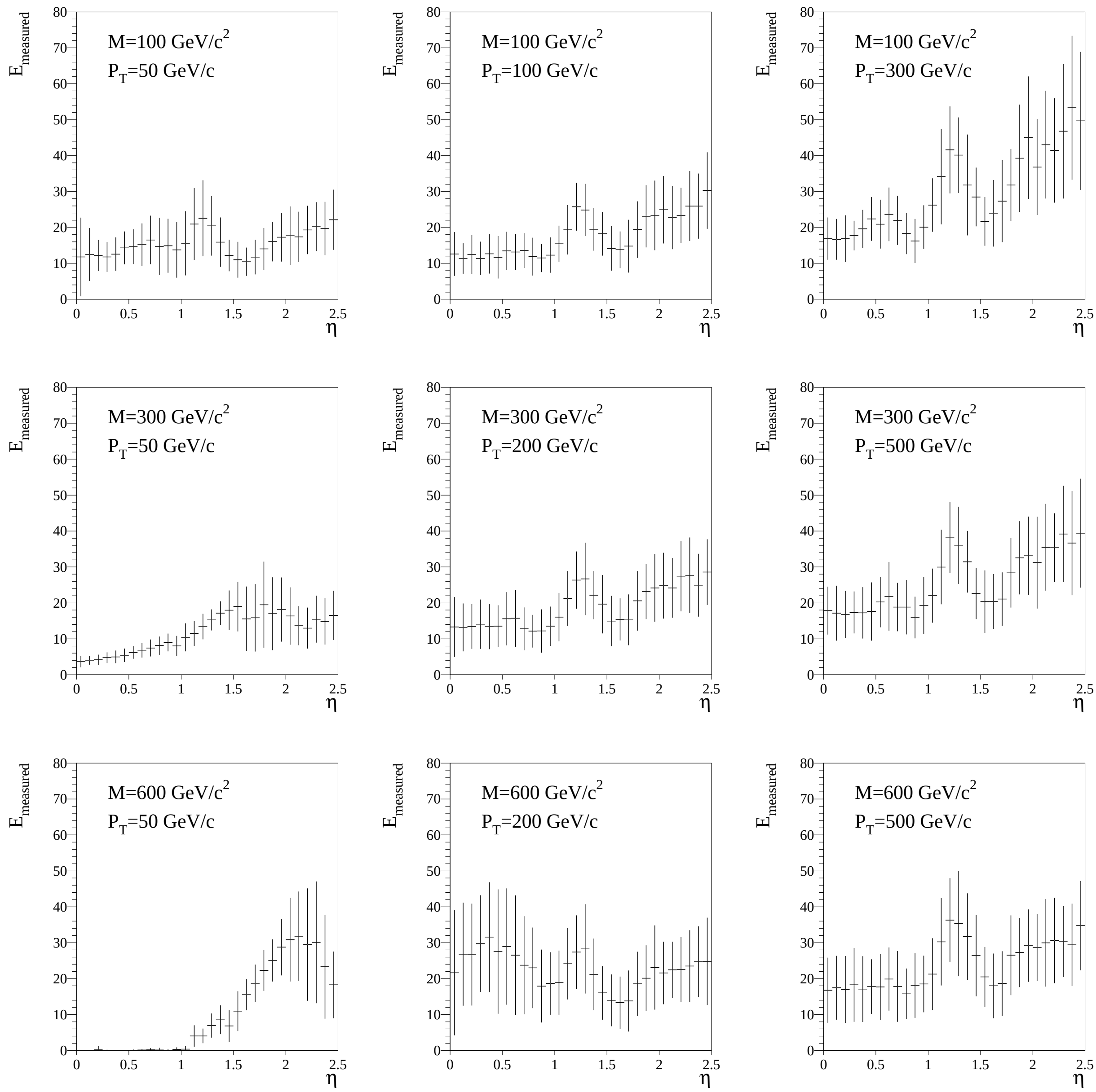

Figure 12.8: Profile plots, representing the energy deposit and its spread for as function of η for different mass values and different p_T values. The ingoing R-hadron is a positively charged meson. Results are obtained by full simulation with ATLSIM and reconstruction with Athena.

Fig. 12.8, the total energy measured in the ATLAS calorimeters is displayed as function of η for various R-hadrons. When plotting the ratio of the total energy deposit in the ATLAS calorimeters and the kinetic energy of the R-hadron as function of the kinetic energy on a double logarithmic scale, this ratio is found to follow a power law. Double logarithmic fits for the energy deposit divided by the kinetic energy as function of the initial kinetic energy are given in Fig. 12.9. The slope is approximately -0.9, translating into $E_{depos} = constant \times E_{kinetic}^{0.1}$. For electrons, it would be $E_{depos} = E_{kinetic}$, while for muons, which have a constant energy deposit over a long range of kinetic energies, the slope would be -1. To parameterize the energy resolution of the calorimeter,

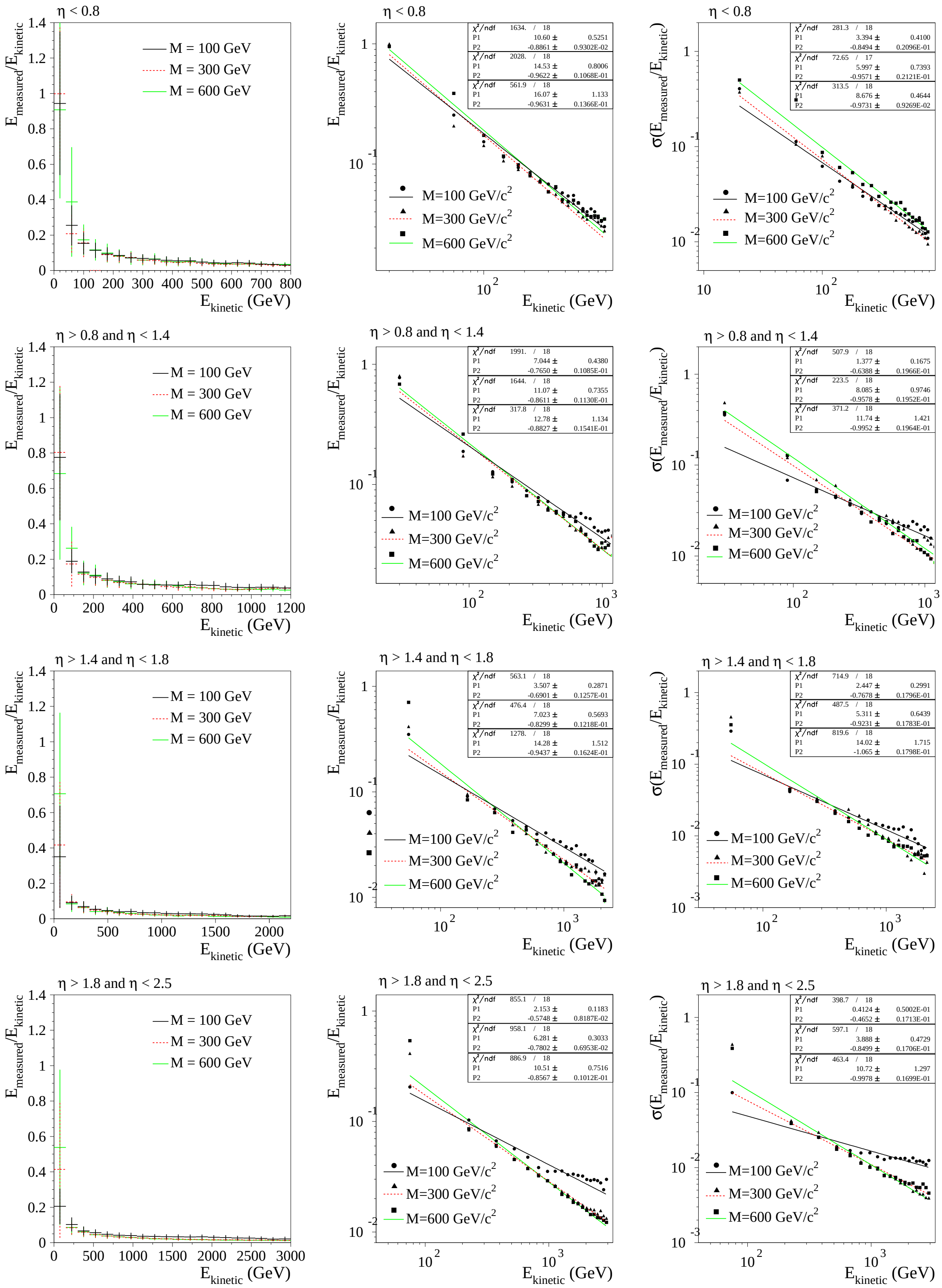

Figure 12.9: The energy deposit in the ATLAS calorimeters (electromagnetic plus hadronic) divided by the kinetic energy for different η regions in the ATLAS calorimeters, fitted with straight lines. The fit results are displayed in each plot for M=100 (top statistics), 300 (middle statistics) and 600 GeV (bottom statistics). These results are obtained by full simulation with ATLSIM and reconstruction with Athena.

i.e. the accuracy to record the energy deposit, the same guess is made, and results are shown in Fig. 12.9. Again approximately straight lines are obtained on double logarithmic scales.

Taking a close look at Fig. 12.8 and 12.9 and comparing these figures with the R-hadron energy loss in 1 m iron, displayed in Fig. 5.10, a few points are noteworthy. First of all, the energy as measured in ATLAS is sometimes larger than the real energy lost by the R-hadron in the material. This can be explained by remembering that the *measured* energy is directly related to the calibration of the calorimeter and that this does not necessarily represent the real energy which the R-hadron has *deposited*. In particular, for slow R-hadrons the unphysical situation is encountered that more energy is measured in the calorimeters than the total kinetic energy of the hadron. However, the same feature is present for slow charged particles not suffering hadronic interactions, and thus this has nothing to do with the simulation of hadronic interactions. The reason is that the calorimeters are calibrated so that they correctly measure the energy of electrons. Slow particles are heavily ionizing and produce thereby δ electrons. Their presence may result in incorrect energy deposit measurements.

12.4.2 Longitudinal calorimeter profile

The energy deposit is studied for an R-hadron in the different calorimeter compartments of the ALTAS detector, for an ingoing charged R-meson. Results are displayed in Fig. 12.10. The charge of the ingoing hadron flipping repeatedly in the calorimeters, the energy deposits do not depend on the initial charge. It must be noted that the profiles of penetrating R-hadrons and muons are similar, apart from the absolute energy deposits. Note however that the *average* profiles for muons and R-hadrons are the same, but probably not the deposits event-by-event. For R-hadrons, flipping charge, fluctuations in the energy loss are considerably larger than for muons! In contrast, the shape of the profiles for electrons and pions differ considerably. Second, for penetrating R-hadrons and for muons, the deposited energy is linearly proportional to the thickness of the calorimeter compartment: the energy deposits in the tile calorimeter are 2.7, 8.6 and 3.9 GeV for the three different compartments, which are 1.4, 3.9 and 1.8 interaction lengths thick. Thus, energy deposits are relatively constant along the trajectory of the particle, if it does not stop.

12.4.3 Lateral calorimeter profile

Besides the longitudinal profile, R-hadrons have a characteristic lateral energy profile. The lateral energy profile is investigated and compared to that of pions, muons and electrons. Due to the fact that it is considerably easier and faster to access information in ATLSIM directly, this study is entirely done within the ATLSIM framework, i.e. first generating single particles (positively charged R-mesons), processing them through the detector, and reconstructing with the XKALMAN-package. The latter provides the particle momentum when entering the calorimeter system. New routines have been developed for this purpose, where linear extrapolation is performed of the track from the point where entering the calorimeter system, into the different calorimeter compartments. In order to estimate the width of an R-hadron shower, the energy is investigated as measured inside a wedge of x degrees in the ϕ direction and y degrees in the η direction. The total energy in the ATLAS calorimeters is then calculated by summing the calibrated energy as measured in a cell, which satisfies:

- $\Delta\eta < \max(x,\, \Delta\eta_{cell}/2)$
- $\Delta\phi < \max(x,\, \Delta\phi_{cell}/2)$,

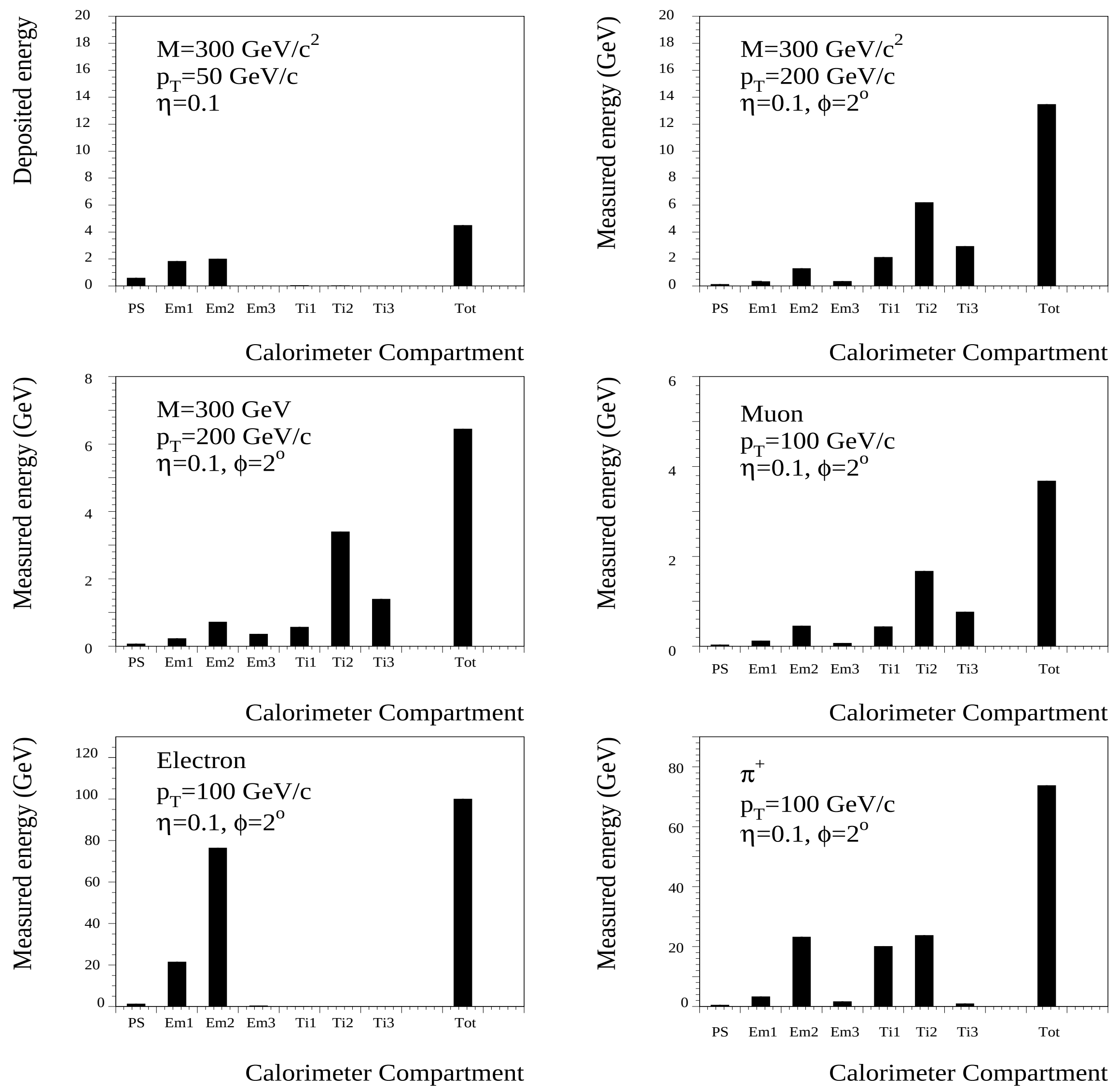

Figure 12.10: Energy deposit in the different compartments of the ATLAS calorimeter in the central barrel region. Top: R-hadrons of mass 300 GeV/c^2 and p_T = 50 GeV/c(left), getting stopped in the calorimeters, and p_T = 200 GeV/c (right), punching through. Middle: deposit for a charged particle with M = 300 GeV/c^2 not suffering hadronic interactions (left), and deposit for ordinary muons (right). Bottom: deposits for electrons (left) and pions (right). The abbreviations on the x-axis for the different compartments are the Presampler (PS), the first (EM1), second (EM2) and third (EM3) compartment of the electromagnetic calorimeter, and the first (Ti1), second (Ti2) and third (Ti3) compartment of the tile calorimeter. Singly charged R-mesons have been fully simulated in ATLSIM, and reconstructed in Athena, allowing easy access to energy deposits in the calorimeter compartments.

where $\Delta\eta$ is the difference between the η value of the cell-center and the η value of the extrapolated track, and ditto for $\Delta\phi$. The granularity of a calorimeter compartment is denoted by $\Delta\eta_{cell} \times \Delta\phi_{cell}$. For clarity the procedure is illustrated in Fig. 12.11. For this study, particles are generated in the central detector region, with an η value in between 0 and 0.1 rad, and an arbitrary ϕ direction. Results are shown in Fig 12.12. It can be seen that for R-hadrons with large kinetic energy, the shower is even wider than that of a pion, while slow R-hadrons exhibit showers which are as narrow as muon showers. However, the eventual shower shape depends

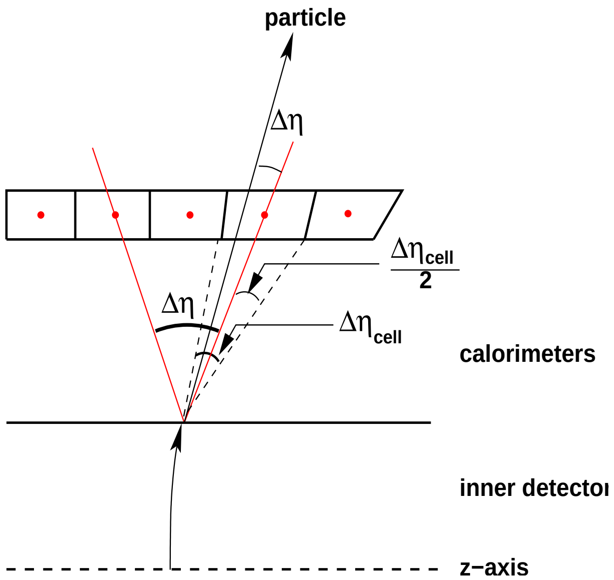

Figure 12.11: Illustration of the selection of a calorimeter cell in the η direction. The energy of the cell which is crossed will always be taken into account. Depending on the wedge size, the cells at the left and right cell of the crossed cell will also be taken into account in the energy measurement.

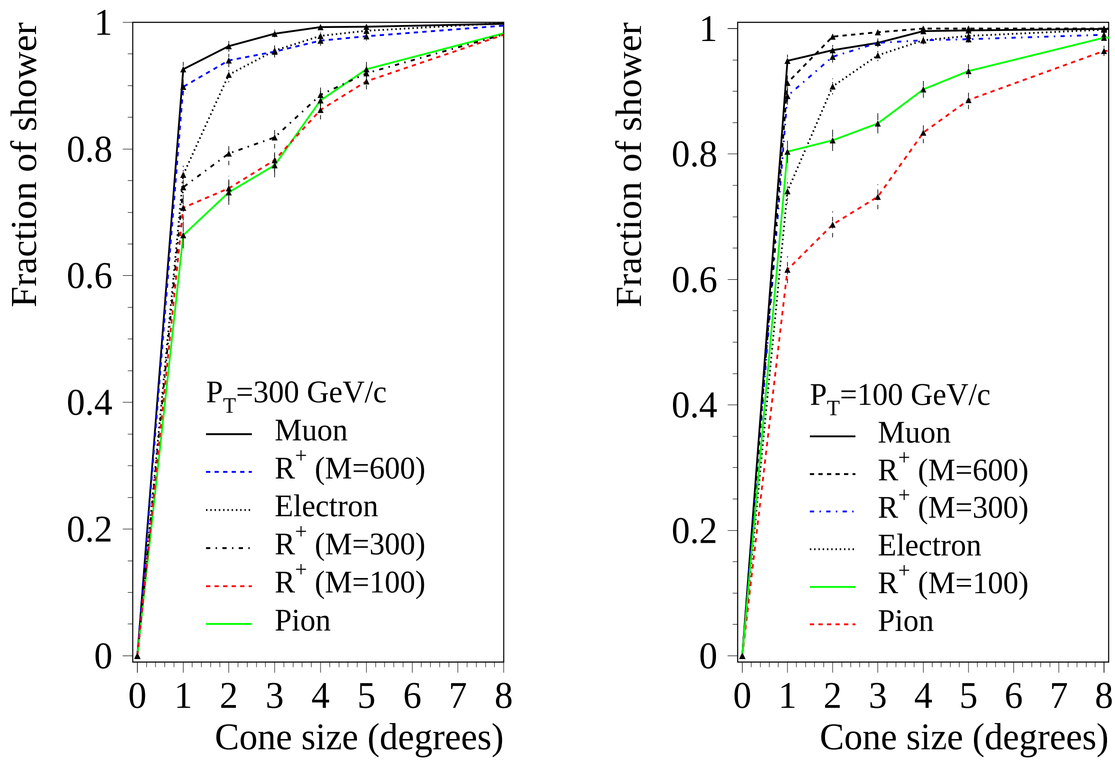

Figure 12.12: Lateral energy profile for muons, electrons, pions and R-hadrons of different masses with $p_T = 100$ GeV/c(left) and $p_T = 300$ GeV/c(right).

highly on the amount of other particles produced in the hadronization process. Although the broadness of the shower profile could possibly be used in discriminating R-hadrons from other particles, in particular from high p_T muons, a detailed parametrization of the shower width is therefore left for a future study.

12.5 Signatures in the muon chambers

12.5.1 Time-of-flight

Time-of-flight measurements in ATLAS are possible thanks to the large size of the muon chambers and the excellent timing precision ($\simeq$ 1 ns). Precision measurements in the barrel and endcap regions are done with the MDT's. As already explained in Section 11.2.3, the position of a particle crossing the MDT's is derived from the drift-time of the electrons in the tube, requiring a starting time t_0 to measure the time. This time is a function of (i) the detector geometry and the response of the front-end electronics, and (ii) of the velocity β of the particle, influencing the arrival time at the MDT stations (the *time-of-flight*). The hits in the three layers of MDT's are reconstructed to a track, the goodness of which is characterized by a χ^2. For a heavy particle with $\beta \ll 1$, the χ^2 of a track reconstructed with a time t_0 assuming $\beta = 1$ will in general be bad (high), since the drift time t_D and thus drift distance are overestimated, as is clarified in Fig. 12.13. Instead, the χ^2 of a track, reconstructed with the right β-value, should be much better. The dependence of the χ^2 value on the assumed β value can be used to measure the β value of the particle. This idea was originally posed in Ref. [114] and applied in Ref. [115], however their results are not valid for strongly interacting particles. The fact that R-hadrons interact non-negligibly in the detector results in a significantly smaller velocity at the muon chambers than that at generation. In Fig. 12.14 the velocity at the second (middle) layer of MDT's (r = 7.11 m) is shown, β_{end}, as function of the β_{start}, the velocity at the vertex, for R-hadrons, and for particles which only interact electromagnetically. Naturally, only R-hadrons punching all the way through the calorimeters are considered. For example, a 300 GeV R-hadron

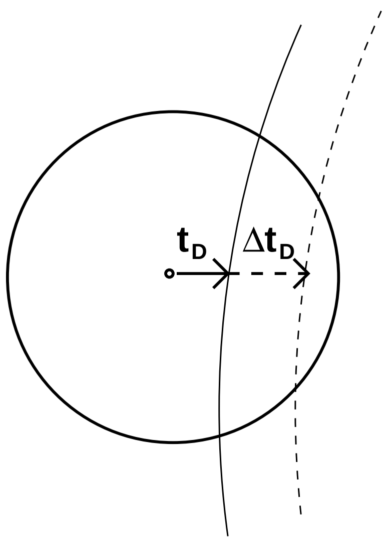

Figure 12.13: Because it takes a slow particle longer to reach the MDT's, the drift time t_D in the tube is overestimated by a time Δt_D, so that the particle seems to come from further than it actually comes.

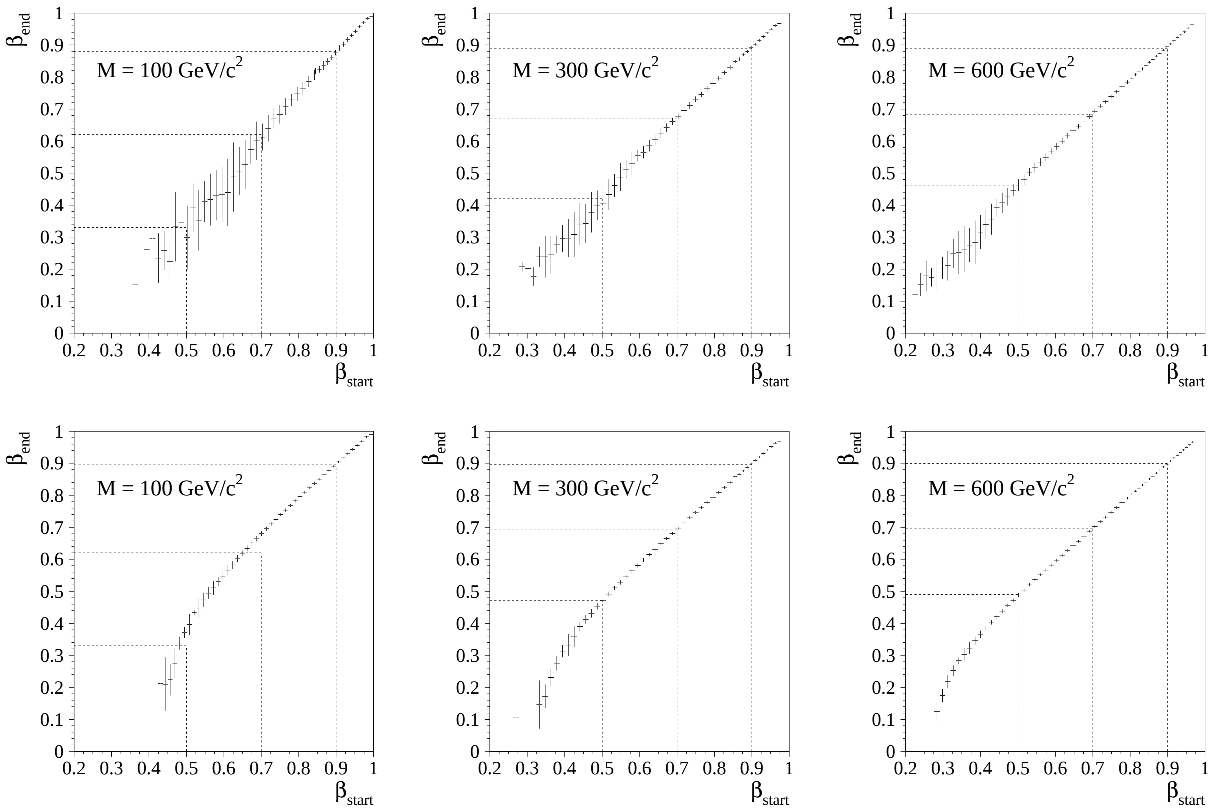

Figure 12.14: Figures above: The velocity β_{end} as measured at the second layer of MDT's (7.11 m) in the central barrel region ($\eta = 0.1$) as function of the velocity β_{start} at the vertex. The horizontal lines correspond to the spread on the mean value. We generate singly charged R-mesons, since mesons are most probably arising in the hadronization process, and the change in velocity is maximal when starting with a charged particle. Note that heavy particles punch through even if they have very small β_{start} values, thanks to their large kinetic energy. Figures below: the same, but for particles only interacting electromagnetically.

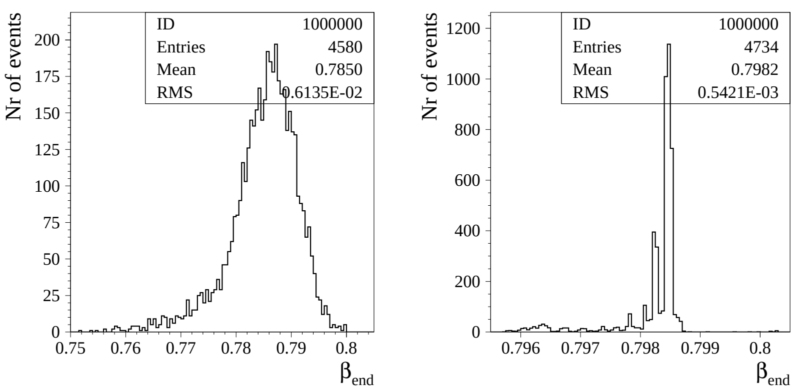

Figure 12.15: The distribution of β_{end} as measured at the first layer of MDT's (6.92 m) when $\beta_{start} = 0.9$ for a particle suffering nuclear and electromagnetic interactions (left) and one only suffering electromagnetic interactions (right). The spread in β_{end} is much larger in the former case, as expected. The mass of the generated R-hadron was 300 GeV/c^2.

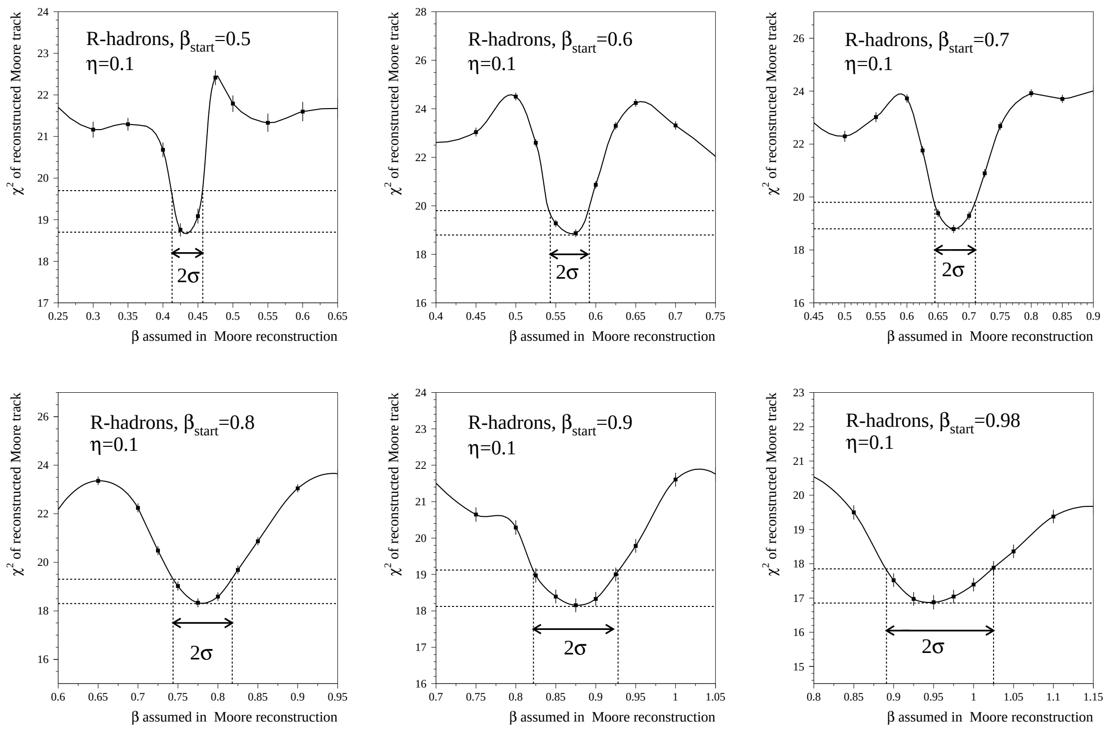

Figure 12.16: For different values of the generated velocity β_{start}, the χ^2 of the track is shown as function of the β value used in the reconstruction of the track. Singly charged mesons have been generated, fully simulated in ATLSIM, and reconstructed using the Moore package in Athena. To determine the accuracy of the measured β value, a Gaussian behaviour of the χ^2 function is assumed for reasonable β-values. The error is determined by investigating where the χ^2 value is one unit above the minimum, corresponding to one standard deviation. These figures are obtained for R-hadrons with a mass of 300 GeV/c^2.

with velocity $\beta_{start} = 0.5$ and 0.9 reaches the muon chambers with velocity $\beta_{end} = 0.42$ and 0.88, respectively, if it indeed punches through the calorimeters. On the other hand, a particle only interacting electromagnetically reaches them with $\beta_{end} = 0.48$ and 0.89, respectively, a much smaller difference! The difference between these two in the shapes of the β_{end} distributions is shown in Fig. 12.15, for β_{start} is 0.8. Naturally, the spread of the velocity of a strongly interacting particle is much larger. Despite the change in velocity, it is still possible to use the method of Reference [114]. However, the way in which we derive our results differ. Reference [114] applies an iteration method in order to find the β value for which the χ^2 of the reconstructed track was lowest. However, this is too time-consuming to realize at present within Athena. Instead, single R-hadrons (positively charged mesons) with a fixed β_{start} value were generated, fully simulated in the ATLAS detector, and subsequently reconstructed, hereby varying the time t_o with a certain β_{start} value. This procedure is performed within the Moore-package in Athena. Thus, we simply assume an iteration procedure to be available in the future, and state results *if* such a procedure would exist.

In Fig. 12.16, our method to estimate β is demonstrated for R-hadrons with different generated β_{start} values in the central part of the detector ($\eta = 0.1, \phi = 2^o$). Just like Ref.[114], a rather constant value of $\sigma(\beta)/\beta^2$ is obtained, as displayed in Fig 12.17. This result can be explained if we assume the uncertainty in the beta measurement to be generated by an uncertainty in the

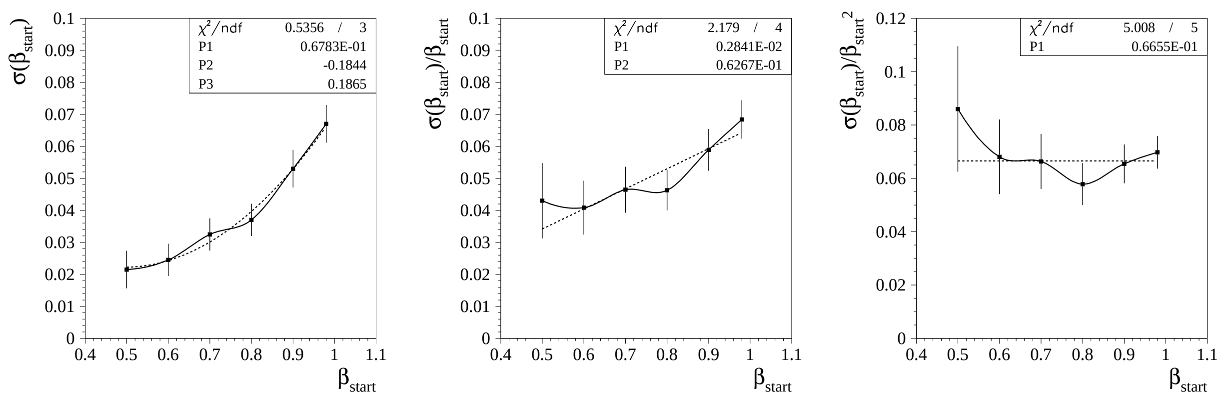

Figure 12.17: The accuracy of the β measurement, $\sigma(\beta)$, as function of β.

drift time measurement:

$$\sigma(\beta) = \sigma\Big(\frac{1}{c}\frac{\Delta x}{\Delta t}\Big) = \frac{\Delta x}{c}\sigma\Big(\frac{1}{\Delta t}\Big) = -\frac{\Delta x}{c}\frac{1}{\Delta t^2}\sigma(\Delta t) \tag{12.3}$$

$$= -\frac{\Delta x}{c}\frac{1}{\Delta t^2}\sigma(t_{measure} - t_{drift}) = \beta^2\frac{c}{\Delta x} \times k, \tag{12.4}$$

where Δx and Δt are the distance and travelling time between the interaction vertex and the muon chambers, and where we have assumed that $\sigma(t_{measure} - t_{drift}) = \sigma(-t_{drift}) = -k$. Thus, $\sigma(\beta)/\beta^2$ is to first approximation expected to be constant. From Fig 12.17, the accuracy of the MDT's to measure β for a strongly interacting particle is estimated to be:

$$\sigma(\beta)/\beta^2 = 0.067 \pm 0.029 \tag{12.5}$$

The result in Eq. 12.5 is conservative for two reasons. First of all, just like Ref. [114], we have studied only particles in the central region of the detector ($\eta = 0.1$). Assuming the uncertainty in β to be the same in all η regions is a conservative approach, because the distance between the measuring stations increases with increasing η, thereby improving the resolution. Secondly, the fact that the β-value of the R-hadron at the muon chambers is has a certain spread results in a broader χ^2. All in all, the value quoted above must not be interpreted as final, but as first estimate.

An investigation of the number of nuclear interactions in the muon system (see Table 13.2) showed that a significant amount of R-hadrons undergo a nuclear interaction, thereby changing charge. The above results are obtained in a region of the detector, where the ATLAS muon system is fairly transparent for R-hadrons. However, the presence of cryostates and support structures results in a large uncertainty in the reconstruction of R-hadron events, as will be discussed in Section 13.3.1. Thus, the velocity measurements would be subject to a large uncertainty to measure the velocity. For this reason, it has not been used in the selection of events in Chapter 13.

12.6 Combination of signatures

The above studies have shown the typical behaviour of single R-hadrons in the ATLAS detector. The most useful separation variables to distinguish single R-hadrons from other charged and

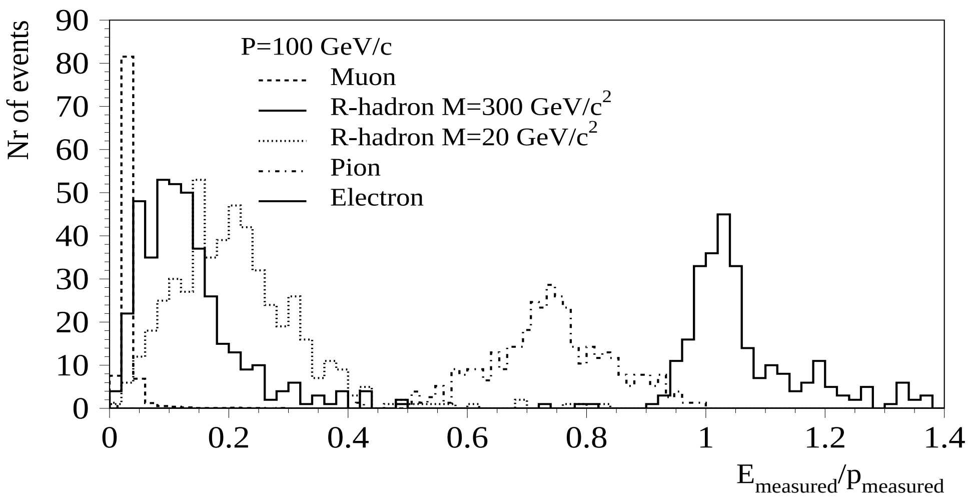

Figure 12.18: The ratio E/p for R-hadrons, muons, pions and electrons in the barrel region ($\eta = 0.1$). Singly charged R-mesons, muons, pions and electrons are generated and reconstructed. The solid line at the left is for R-hadrons, while that at the right is for electrons.

neutral particles are possibly a large momentum measured in the inner detectors, the number of HT hits in the TRT, the energy deposit in the calorimeters, and the velocity as measured in the muon system. Combining momentum measurements with energy deposits, a useful separation variable is the quantity E/p, the ratio of the total measured energy and the momentum. In Fig. 12.18, E/p is displayed for R-hadrons, muons and pions in the barrel region. Clearly, this ratio is small for R-hadrons, but not as small as for muons. As such, it may be an excellent separation variable. In Fig. 12.19 the overall behaviour of R-hadrons in the ATLAS detector is displayed.

In conclusion, this chapter has shown that R-hadrons in many respects would behave quite different from Standard Model particles, but also from other particles associated with new physics such as neutralino, or stable sleptons. With the exception of the E/p signature, the proposed signatures typically provide separation powers of the order of one sigma, and some of the estimators are correlated in any event. Ideally, all relevant signatures should be combined in one optimal discriminating variable, with e.g. a neural network trained on typical signal and background events. This, however, does not make sense with the present level of detailed understanding of the apparatus response. Large samples of real data will be needed to tune the simulation in order to make a reliable optimized discriminating variable. In the following, an analysis of the discovery potential is performed on the basis of event topology alone, which does not require a very fine level of simulation of the response of the ATLAS detector.

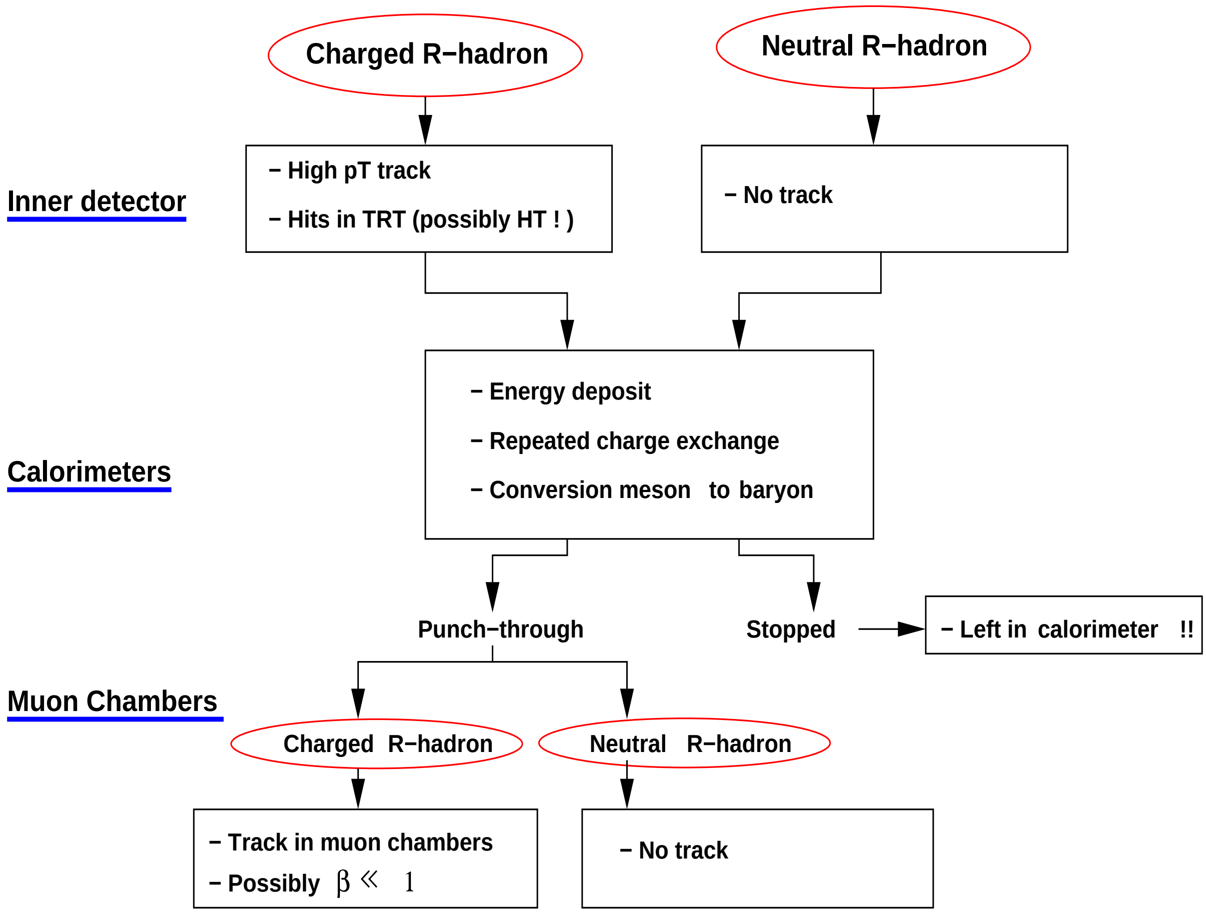

Figure 12.19: Possible manifestations of a typical R-hadron in ATLAS.

Chapter 13

ATLAS analysis

In this chapter, a preliminary analysis of the ATLAS discovery potential of R-hadrons in the channel $pp \to \tilde{g}\tilde{g}$ is presented. First in Section 13.1, relevant topics related to the generation of signal events are discussed, including the parameter space points, the event topology, and the incorporation of R-hadrons into the fast simulation framework ATLFAST++. Section 13.2 focuses on the generation of background processes. Section 13.3 is devoted to trigger issues relevant for R-hadron events. In Section 13.4, a selection is presented, and in Section 13.5 the discovery potential of the ATLAS detector for R-hadrons is investigated.

13.1 R-hadron signal simulation

13.1.1 Overview

The simulation of signal and background events is done within the framework of Athena, the object oriented ATLAS software. In Fig. 13.1, the analysis steps are displayed, starting with event generation, and finishing with physics analysis ntuples.

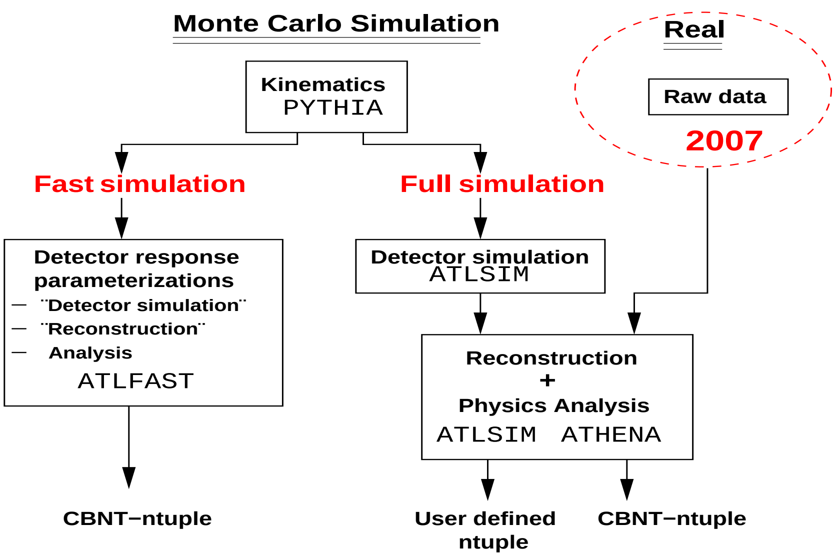

Figure 13.1: Event simulation in ATLAS. Real data are expected in 2007.

13.1.2 Search channel and parameter space

In Section 2.6.2, gluino production channels were divided into class I, II, and III, which was based on the fact whether a gluino was produced via a squark, decaying into a gluino and a quark, or not, influencing the event topology. The analysis presented in this chapter is based on class I events (pp $\rightarrow$ $\tilde{g}\tilde{g}$), where we do not have to worry about the branching ratio of squarks into gluinos. In some of the discussions below, comparisons are made with class II events.

There are no gluino LSP sample points available in the literature. In view of the results presented previously in this thesis, together with the existing searches for gluinos summarized in Section 2.2, the focus of the current analysis will be on gluinos with masses higher than the order of 100 GeV/c^2. In lack of any official parameter space points, the simplest possibility is to simply impose the masses of all supersymmetric particles at the electroweak scale, rather than imposing a condition at the GUT scale and renormalizing down to the electroweak scale to get the correct mass values. The parameter space points chosen in this analysis are [53]:

$$\begin{aligned} m_{\tilde{q}} &= 800\,\mathrm{GeV}/c^2 \qquad & m_{\tilde{g}} &= 100\,\mathrm{GeV}/c^2, \\ m_{\tilde{q}} &= 800\,\mathrm{GeV}/c^2 \qquad & m_{\tilde{g}} &= 300\,\mathrm{GeV}/c^2, \\ m_{\tilde{q}} &= 800\,\mathrm{GeV}/c^2 \qquad & m_{\tilde{g}} &= 600\,\mathrm{GeV}/c^2. \end{aligned} \tag{13.1}$$

The masses of the other supersymmetric particles are also chosen to be 800 GeV/c^2 [53]. As long as they are not lighter than the squarks, they do not play a role.

The above gluino and squark masses are not favorable for split supersymmetry models. However, because all parameterizations of the R-hadron response have been made for masses of 100-600 GeV/c^2, we stick to the original proposal [53], with masses given by the above parameter space point. An extrapolation to higher gluino masses relevant for split supersymmetry models is expected to be discussed in a future study [119].

13.1.3 Event topology

In Appendix C, some relevant distributions at generator level are given for class I, II and III events. The event topology depends on the mass and charge of the R-hadrons.

Class I events are characterized by two R-hadrons being produced in a back-to-back configuration, with high momenta, which are balanced in the transverse plane. The transverse missing energy signal would only be significant for events in which one neutral and one charged R-hadron are detected, so that the p_T is unbalanced. Otherwise, no significant missing energy signal is present. The missing energy signal also depends on the R-hadron mass: larger masses result in a larger imbalance, and thus in a larger missing energy. Furthermore, a high p_T track in the inner detector is expected in case a charged R-hadron is produced. Heavier R-hadrons are generally produced with higher momenta then lighter R-hadrons. Finally, in a large fraction of R-hadron events the kinetic energy is larger than the energy lost in the detector, and thus a significant amount of activity is expected in the muon system.

For completeness, a few words about the topology of class II and III events. In such events, the R-hadrons are not produced back-to-back. The R-hadron momenta not being balanced, the missing energy signal is significantly larger. The event multiplicity is slightly larger than that in class I events. Also, the average velocity and momentum are in general higher than for class I. Again charged R-hadrons can be detected with the muon chambers.

13.1.4 Generation of hard event

The gluino hadronization routines as developed for the ALEPH simulation [82] are used. R-mesons and R-baryons are produced in pairs, with a quark composition as displayed in Table 7.1. Again there is no correlation between the charge of the two R-hadrons, and again double neutral, mixed, and double charged final states are possible. Contrary to the ALEPH simulation, we have also taken into account baryons. The free parameters and their default values used in the hadronization process are the same as those presented in Section 7.3.3.

Isolation

The muon trigger will play a crucial role in selecting R-hadron events, and muons will thus be the dominant background source. The jet structure around the gluino is investigated at event generator level and compared to that of isolated muons and non-isolated muons produced via b-quark decay. For this study, 50000 pp $\rightarrow$ Z/γ $\rightarrow$ $\mu^+\mu^-$ events and 50000 pp $\rightarrow$ Z/γ $\rightarrow$ b$\bar{\text{b}}$ events, with b decaying weakly into muons, have been generated, and compared to R-hadron class I and class II events. In all cases the $\hat{p}_T$ of the hard $2 \rightarrow 2$ process was required to be more than 50 GeV/c. Fig. 13.2 shows the distribution of the number of particles, the particles density, and the total p_T of the particles in a cone of size R $= \sqrt{\Delta\eta^2 + \Delta\phi^2}$ around the muon or R-hadron, excluding the muon or R-hadron itself (and not counting neutrinos).

13.1.5 R-hadron detector simulation: ATLFAST

While the GEANT3 routines would allow a full simulation based analysis, the fast simulation framework ATLFAST++ [117] is used to perform physics analysis of entire events. ATLFAST++ is based on simple parameterizations, rather than complete tracking through the detector, saving a considerable amount of CPU time, as well as storage capacity. ATLFAST++ contains simple routines to simulate electrons, pions, photons, muons and jets. However, R-hadrons must be introduced by hand. For this purpose, the information of fully simulated single R-hadrons has been used to make parameterizations of:

- The momentum resolution of inner detector, in the way as explained in Section 12.2.

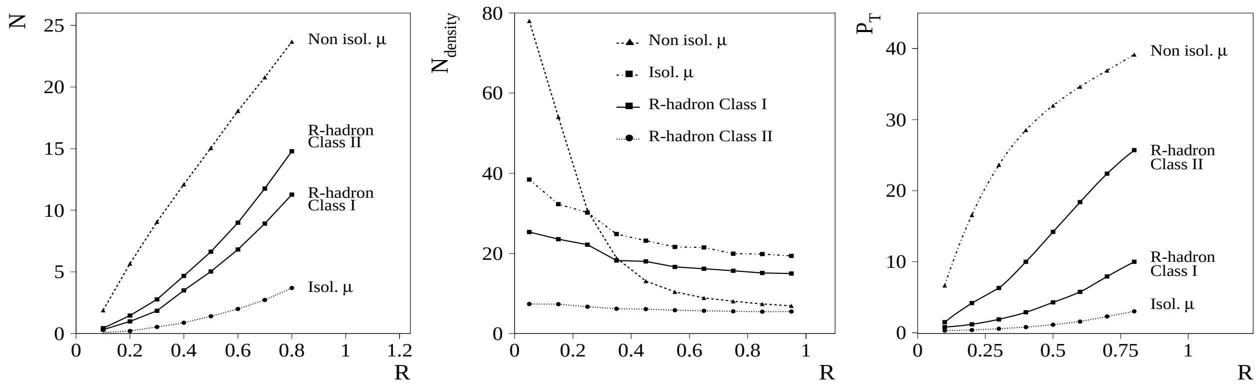

Figure 13.2: Left: mean value of the average number of particles N in a cone around the muon direction as function of the cone radius R. Middle: mean value of the particle density $N_{density}$ around the muon direction as function of the cone radius R, defined as $N_{density} = (N(R_1) - N(R_2))/(R_1^2 - R_2^2)$. Right: mean value of the transverse momentum, p_T, in a cone around the muon or R-hadron direction as function of the cone radius R.

- The response in the calorimeter. This includes the number of interactions and the total energy loss in the detector, in a manner shown in Section 12.4. Also, the energy loss per interaction, obtained from Section 5.5.3, and continuous losses are parameterized. The latter enables us to predict whether an R-hadron penetrates through the calorimeters into the muon chambers, or not.

- The momentum resolution of the muon spectrometer, obtained from the velocity, as explained in Section 12.5. If the R-hadron reaches the muon system, the default probability to measure its momentum is 75%, based on (i) the fact that R-hadrons always convert to baryons, and (ii) the fact that the probabilities that the R-hadron ends up as R^+, R^0, R^- and R^{++} are approximately equal, and that there is only one neutral baryon.

In order to simulate R-hadrons, ATLFAST++ has been extended with R-hadron routines [118], a non-trivial task, because ATLFAST is either suited for particles depositing no energy in the calorimeters, like muons, or particles depositing all their energy. R-hadrons are divided into non-isolated R-hadrons and isolated R-hadrons, the latter being defined to have no activity in a cone of ΔR=0.4, just like isolated muons. R-hadrons can be added to jets, and they can be recorded in the muon chambers. A short write-up will be available in Ref. [119].

The parameterizations of the deposited energy and the transverse momentum resolution as presented in Chapter 12 would allow access to the variable E/p for R-hadrons. However, no such information is accessible for ordinary particles: ATLFAST does not include extrapolation from track to calorimeter deposit. Furthermore, no transition radiation information is included in ATLFAST, and adding this information for all particles is beyond the scope of this work. The lack of this information for normal particles is the reason that the analysis below will be based on kinematic and topological variables only.

13.1.6 Simulated signal samples

Signal samples were generated for $M_{\tilde{g}}$ = 100, 300 and 600 GeV/c^2, while $M_{\tilde{q}}$ = 800 GeV/c^2, in bins of $\hat{p}_T$, the transverse momentum exchanged in the hard process. The width of the bin is chosen so that the number of generated events in each $\hat{p}_T$ bin is assured to be larger than the number corresponding to 1 fb^{-1}. The differential cross sections for three mass values are shown in Fig. 13.3 as a function of $\hat{p}_T$.

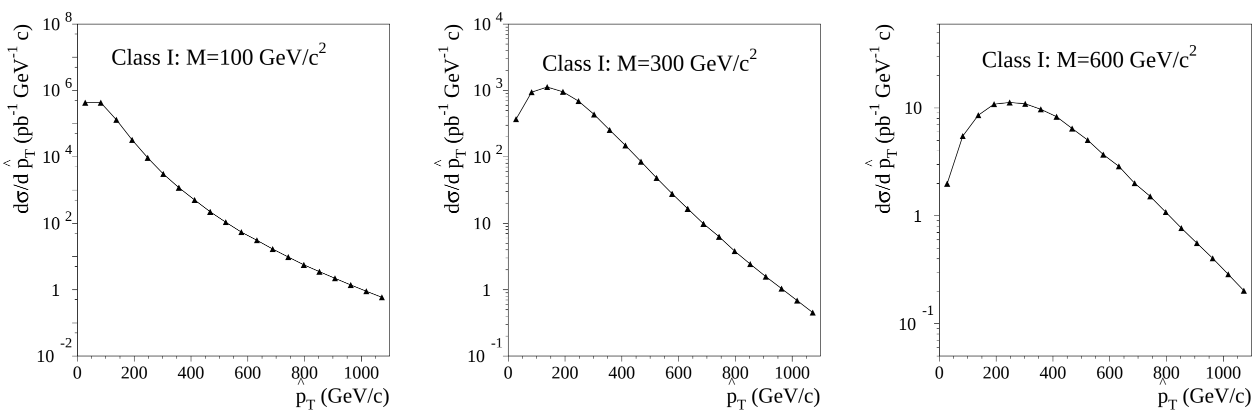

Figure 13.3: Differential cross section dσ/d$\hat{p}_T$ as function of $\hat{p}_T$ for class I events with R-hadrons of mass 100, 300 and 600 GeV/c^2.

The simulation assumes LHC to be running at low luminosity, because (i) the cross sections for gluino production are anyway high, and (ii) the low luminosity muon trigger has a larger efficiency than the high luminosity trigger, as will be shown later. Pile-up is included.

13.2 Background simulation

13.2.1 Standard Model background processes

Let us now consider the most important Standard Model background events. No supersymmetry background sources will be considered.

First of all, QCD background have a very high cross section and thus present a potential background problem. The cross section for QCD events drops rapidly with increasing $\hat{p}_T$, as is shown in Fig.13.4. The p_T of the fragmentation particles is further suppressed by the soft fragmentation function of light partons. Furthermore, the long lifetime of pions and kaons effectively prevents them from decaying into muons before they get absorbed in the calorimeter. However, the fast weak decays of high p_T b-quarks and t-quarks will produce high p_T muons, and thus present a serious background, because of the presence of high p_T muons.

Second, events with single Z and W production form a potential background source. Such events may result in muons, and these events are likely to pass the trigger criteria. The p_T value for most muons produced from Z and W is of the order of $M_Z/2$, and thus on average smaller than those of R-hadrons, as was shown in Appendix C. Thus, we expect much of this background to be effectively removed by a p_T cut on muons.

Third, events where two gauge bosons are produced may be a background source. Two heavy particles are produced in the hard process, which can decay into high p_T muons.

The differential cross sections for the main background processes is shown in Fig. 13.4.

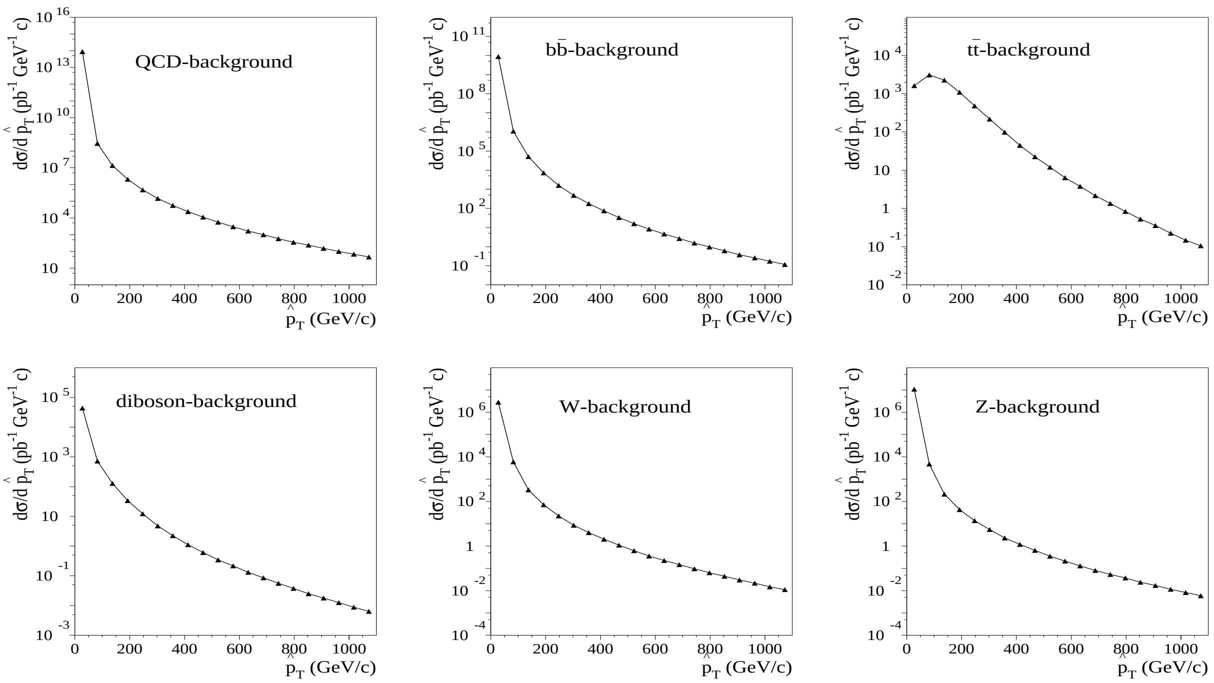

Figure 13.4: Differential cross section $d\sigma/d\hat{p}_T$ as function of the $\hat{p}_T$ for the primary $2 \to 2$ background processes.

13.2.2 Generated background samples

For the generation of QCD background, the events have been divided into events only containing b-quarks in the hard process, events only containing t-quarks in the hard process, and events which do not contain b- and t-quarks in the hard process. In the following, QCD events refer to all QCD processes but without the production of $b\bar{b}$ and $t\bar{t}$ in the hard process, while we will refer to $b\bar{b}$ and $t\bar{t}$ events for QCD events only containing $b\bar{b}$ and $t\bar{t}$ in the hard process, respectively. Both QCD and $b\bar{b}$ events have been generated in logarithmic $\hat{p}_T$ bins. The number of generated events in each $\hat{p}_T$ bin is assured to be larger than that corresponding to 1 fb^{-1}. The only exception to this rule is in the region of very small $\hat{p}_T$, which have very large cross sections, but which do not pass the trigger cut. Generating a number of events corresponding to 1 fb^{-1} is beyond the scope of this work, and would only be relevant for a full trigger rate study.

The generation of events with single Z, W, diboson and $t\bar{t}$ events is also done in bins. The width of the bins is chosen according to the cross section, and the number of generated events in each $\hat{p}_T$ bin is assured to be larger than that corresponding to 1 fb^{-1}.

13.3 R-hadron triggers

Before discussing the selection criteria for R-hadron events, it is necessary to discuss some aspects related to triggering. There are currently different trigger menus available in ATLAS [108, 109]. Although these are still subject to changes, the most relevant ones will be discussed below.

13.3.1 The muon trigger

In Ref. [111], the possibility has already been investigated to use the muon trigger for the detection of slow charged particles, not interacting hadronically, in the central region of the ATLAS detector. Estimates for the efficiencies were given by requiring a coincidence between the two involved trigger stations within a time window of 18 ns. For example, the efficiency of the low luminosity trigger was found to be 90% for particles with $\beta = 0.2$. However, the fact that such slow particles would arrive at the muon stations 125 ns after the bunch crossing, or 100 ns after an ordinary muon would arrive, was not taken into account. Thus, when the trigger is fired, and data-taking starts, the information of an event which came four bunch crossings later is recorded. The relevant information of the slow particle from the inner detector and calorimeters is probably already lost. To which extent the relevant information extracted, depends on different factors, like the velocity of the R-hadron, and the manner in which the data are recorded in the different subsystems, and we come back to this issue in Section 13.5.

Muon trigger efficiency

Here, a preliminary study is made of the efficiency of the muon trigger by requiring the R-hadron to be recorded in the correct event. The conditions of an R-hadron firing the muon trigger and being assigned to the right event are then the following:

- The R-hadron arriving at the muon stations must be charged and must have $\eta < 2.5$.
- As required in Ref [111], the R-hadron has a coincidence in the two trigger stations within the temporal gate of the trigger stations, which is taken to be 18 ns both for RPC's and TGC's [110], and see Section 11.2.5. For example, for the RPC's at $\theta = 0^0$, this would correspond to $\beta > 0.5$ for the high luminosity trigger stations and $\beta = 0.14$ for the low luminosity trigger stations.

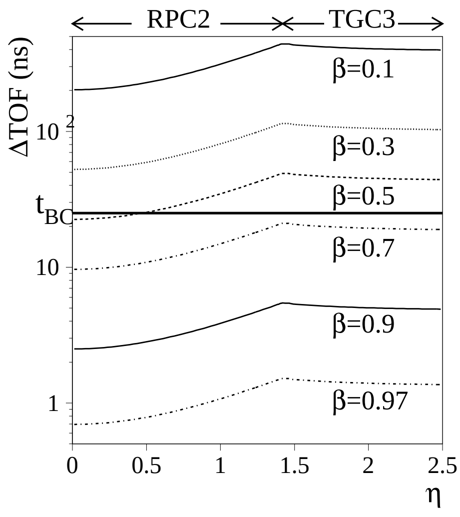

Figure 13.5: The difference in time-of-flight Δ TOF at RPC2 and TGC3 between an non-interacting particle traveling with velocity β in a certain η-region, and a particle traveling with the speed of light, as function of η. The bunch crossing time t_{BC} is the maximum difference allowed by the trigger.

- The delay of a heavy particle compared to that of a muon must be less than 25 ns, so that the trigger is fired within the right event. This puts an upper limit on the maximum time-of-flight (TOF) of a particle at the trigger stations . The TOF information in GEANT is not available by default and has been introduced in ATLSIM version 7.5.0 [120] for this purpose. In Fig. 13.5, the difference in time-of-flight ΔTOF between a non-interacting particle with $\beta < 1$ and a particle $\beta = 1$ at RPC2 (7.5 m) and TGC3 (14.5 m) is shown. The latter stations are the last involved stations for a low luminosity muon trigger. Looking at the central detector region ($\eta = 0$), we see that the particle must have $\beta \gtrsim 0.5$ in order to reach the last trigger station in time. For a high luminosity trigger making use of the last trigger station in the barrel region (10 m), this limit would be $\beta > 0.6$. In Fig. 13.6, the delay at the last trigger stations for low luminosity is shown for fully simulated R-hadrons of masses 100, 300 and 600 GeV of different p_T values as function of η. As was already shown in Fig. 12.14, a light R-hadron is more delayed than a heavy one with the same starting velocity. Since particles are generated with a fixed p_T value rather than a fixed β value, particles in the large η region have naturally a larger probability of reaching the station, simply because their absolute velocity is larger, as can be seen from Figure 13.7.
- The deflection angle of the R-hadron in the magnetic field must be smaller than that of the relevant muon (6 or 10 GeV). The deflection angle only depends on p_T, and since R-hadrons are produced with high momenta, this condition is always satisfied.

In order to obtain an estimate for the muon trigger efficiencies, R-hadron events in class I and II have been generated within the Athena framework, followed by detector simulation and analysis in ATLSIM. The $1\mu6$ and the $2\mu10$ trigger menus have been simulated in a highly simplified way by requiring R-hadrons to satisfy the above criteria. Results are shown in Table 13.1.

Two things must be noted in this table. Firstly, the efficiencies for the class II events are higher than those for class I events, since in the former the average velocity if larger. Secondly, the efficiency is maximally a bit below 90%. This number can be explained by remembering that the R-hadrons reaching the muon chambers are most probably R-baryons, and there is only

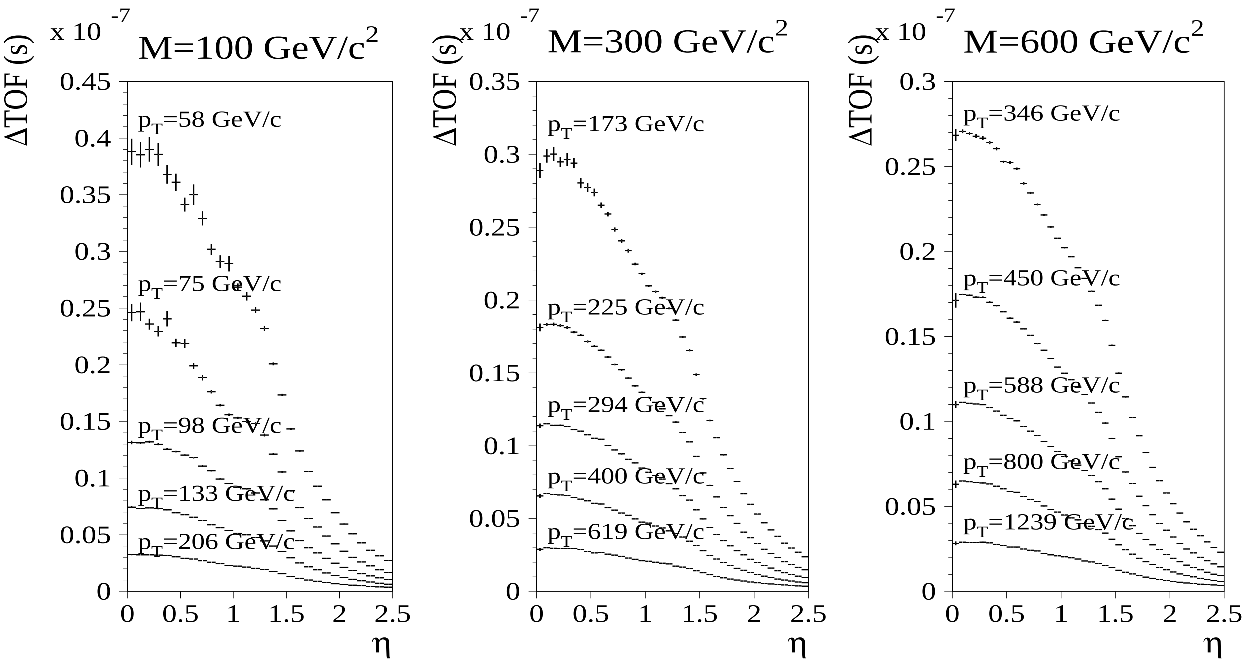

Figure 13.6: The difference in time of flight ΔTOF as function of η at RPC2 and TGC3 between an R-hadron of mass 300 GeV/c^2 and a particle traveling with $\beta = 1$. The displayed momenta correspond to β-values at $\eta = 0$ of 0.5, 0.6, 0.7, 0.8, 0.9 and 0.98.

roughly 10% probability that both R-baryons are neutral, following from simple combinatorics. Appearantly in this case the velocity of the two R-hadrons is so high, that a large fraction of them reach the muon chambers.

In the calculations of the efficiencies of the muon trigger, all charged R-hadrons reaching the muon chambers are assumed to produce hits in the trigger planes. Due to support structures and the presence of the magnet, it is possible that a nuclear reaction takes place. For high p_T muons, the probability to undergo a nuclear interaction is very small, and the efficiency of a

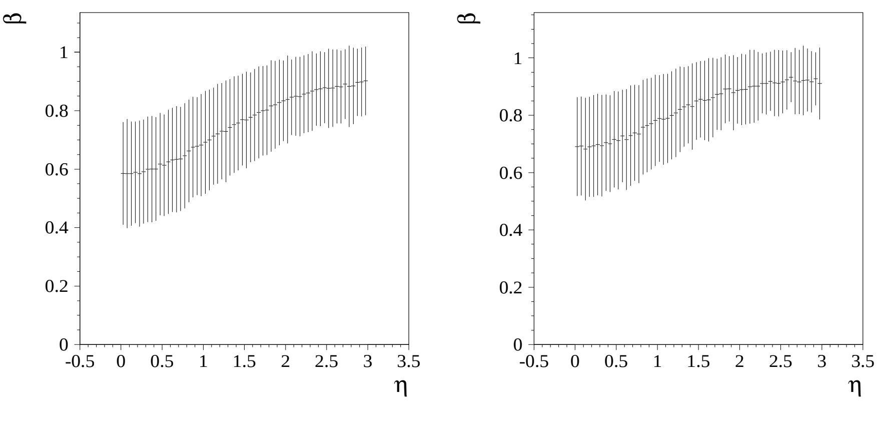

Figure 13.7: The value of the generated velocity β as function of η of one of the R-hadrons in an event, for class I events (left) and class II events (right) where M = 300 GeV/c^2.

Trigger	Mass	Luminosity	Efficiency Class I (%)	Efficiency Class IIa (%)
$1\mu6$	100	Low	61	87
		High	58	86
	300	Low	67	83
		High	63	81
	600	Low	60	66
		High	59	61
$2\mu10$	100	Low	28	52
		High	24	49
	300	Low	33	46
		High	29	41
	600	Low	34	33
		High	27	29

Table 13.1: An estimate of the trigger efficiency for class I and II events (defined in Section 11.2.5). These results are based on fully simulated R-hadrons in the ATLAS detector, requiring the conditions given in Section 13.3.1.

muon to fire the trigger is very close to 100% [102]. For an R-hadron, however, the probability for nuclear interactions is much larger. The fraction has been evaluated with full simulation in the barrel and the endcap region. Since the support structures depend on η, R-hadrons have been generated in five different η regions. Results are shown in Table 13.2. This table shows that there is indeed a non-zero probability that an R-baryon converts into another baryon. A charged R-hadron can remain charged, or it can become neutral, in which case the track would stop. On the other hand, a neutral R-baryon could convert into a charged one. This aspect introduces an important extra uncertainty in using the muon triggers and tracking in the muon chambers, and has to be accounted for when deriving final results.

A complication: delay

Even if the R-hadron fires the muon trigger in time to be recorded within the right event, it is not a priori certain whether the detector information of all the separate subsystems can still be used when building the event. The further away the subdetector, the larger is the delay. As an example, let us consider a particle in the central barrel region, which would just reach the RPC2 muon trigger station in time, i.e. with a velocity $\beta = 0.5$.

region	η	5-10 m (total)	6.7-7.2 m (LL)	6.7-9.9 m (HL)
barrel:	$\eta(0, 0.5)$	30%	7%	17%
	$\eta(0.5, 1.0)$	40%	10%	30%
	$\eta(1.0, 1.5)$	45%	7%	15%
region	η	7-15 m (total)	14.1-14.5 m (LL)	12.9-14.5 m (HL)
endcap	$\eta(1.5, 2.0)$	60%	2%	3%
	$\eta(2.0, 2.5)$	75%	2%	3%

Table 13.2: Fraction of R-hadrons undergoing one or more nuclear interactions in the muon system. The probabilities are displayed for the entire system, and for the region in between the two trigger stations at low (LL) and high (HL) luminosity.

For the pixels and silicon detectors, the following can be remarked. First of all, the delay in the central region is very small (maximum 1 and 2 ns for pixels and silicon, respectively), since their location is very close to the vertex. Second, for these detectors a hit is based on detecting a certain amount of charge [103]. Slow R-hadrons are late, but would be heavily ionizing and certainly result in a hit. Third, we only make use of these detectors for momentum measurements, requiring only the hit positions, rather than the whole signal shape. Thus, the information of these subdetectors is reliable, if indeed we require the R-hadron to arrive at the muon chambers with a delay smaller than 25 ns.

For the TRT, the delay is slightly larger, roughly 4 ns at the outer layers at 1.1 m. However, this delay is only a small fraction of the maximum drift time is of 40 ns, and it would correspond to a drift distance of only 200 μm. A good reconstruction of the signal is probably possible.

For the calorimeters, the situation is similar. The time-interval over which data taking stretches in case of a positive trigger signal is roughly 125 and 175 ns for LiAr and Tile calorimeters, respectively, and thus the signal can probably be fully reconstructed. For the muon chambers the same arguments apply. Whether the calorimeter *trigger* stations, which need to respond quickly, can be used for detecting strongly delayed particles is not a priori clear, as will be explained below.

13.3.2 Calorimeter triggers

As has been explained in Section 11.2.5, the first level trigger is based on a quick analysis of the regions of interest (ROI's) in the calorimeters and the muon system, while at higher level the information is combined with tracking information [109].

For R-hadrons, it crucial to distinguish between the first and higher level calorimeter trigger: for example, it could happen that one charged and one neutral R-hadron are produced, resulting in an enormous p_T imbalance in the inner detector and thus E_T^{miss}. However, no such imbalance is present in the calorimeters, and it is therefore possible that it does not pass the first level calorimeter trigger. The same arguments hold for the triggers based on jet energy: an R-hadron energy deposit will never give rise to a very high energetic jet. However, if the event would pass the trigger requirements for other reasons, and the event is built, the R-hadron momentum is added to that of the jet (if indeed it would point in the same direction), resulting in a high p_T jet.

A complication for using calorimeter triggers arises if the R-hadrons would be heavily delayed, because the R-hadron signal would probably not be suitable for the trigger electronics to reconstruct the real pulse-shape of the signal. This is expected to have small effect for several

Menu	Requirement
$1\mu6$	One muons, which has $p_T > 6$ GeV/c.
$2\mu10$	Two muons, each of which has $p_T > 10$ GeV/c.
$1\mu20i$	One isolated muons with $p_T > 20$ GeV/c.
$Ex70E70$	$E_T^{miss} > 70$ GeV and a jet with $E_T > 70$ GeV.
$j400$	Jet $E_T > 400$ GeV.
$2j350$	Two jets, each of which has $E_T > 350$ GeV.
$Ex200$	$E_T^{miss} > 200$ GeV

Table 13.3: Trigger menus, as defined in Ref. [109]. These trigger menus are still highly subject to changes.

Background	$\frac{N_{trig}}{N_{gen}}$ (%)	σ (mb)	$N_{trig}(1\text{fb}^{-1})$	$N_{sel}(1\text{fb}^{-1})$
QCD $\hat{p}_T < 17\,\text{GeV}/c^2$	-	$4.8{\times}10^3$	-	-
QCD $17\,\text{GeV}/c^2 < \hat{p}_T < 35\,\text{GeV}/c^2$	0.04	1.4	$6.0{\times}10^8$	-
QCD $35\,\text{GeV}/c^2 < \hat{p}_T < 140\,\text{GeV}/c^2$	0.05	9.9×10^{-2}	5.2×10^7	-
QCD $140\,\text{GeV}/c^2 < \hat{p}_T < 560\,\text{GeV}/c^2$	0.8	3.2×10^{-4}	2.7×10^6	24
QCD $\hat{p}_T > 560\,\text{GeV}/c^2$	97.7	6.6×10^{-7}	5.5×10^5	168
$b\bar{b}$ $\hat{p}_T < 35\,\text{GeV}/c^2$	0.1	4.8×10^{-1}	4.9×10^8	-
$b\bar{b}$ $35\,\text{GeV}/c^2 < \hat{p}_T < 140\,\text{GeV}/c^2$	0.6	3.8×10^{-4}	2.3×10^6	-
$b\bar{b}$ $140\,\text{GeV}/c^2 < \hat{p}_T < 560\,\text{GeV}/c^2$	4.4	1.1×10^{-6}	5.1×10^4	4
$b\bar{b}$ $\hat{p}_T > 560\,\text{GeV}/c^2$	98.9	9.8×10^{-10}	9.7×10^2	10
$t\bar{t}$	29.8	4.9×10^{-7}	1.5×10^5	187
W	7.2	1.6×10^{-4}	1.1×10^7	47
Z	0.88	6.0×10^{-4}	5.3×10^6	4
diboson	6.2	2.5×10^{-6}	1.6×10^5	14
R-hadrons M=100 GeV/c^2	45.0	5.6×10^{-5}	2.5×10^7	393k
R-hadrons M=300 GeV/c^2	70.0	2.8×10^{-7}	1.97×10^5	54k
R-hadrons M=600 GeV/c^2	60.0	5.2×10^{-9}	3.1×10^3	1.2k

Table 13.4: Trigger efficiencies, cross sections, number of triggered events, and number of events after selection, in 1 fb^{-1}.

reasons. Firstly, the delay in the calorimeters is much smaller than that in the muon chambers and a large fraction of R-hadrons would fire the trigger. Secondly, for triggers based on E_T^{miss} it must be noted that if an R-hadron energy deposit would not result in a ROI, this would result in an even higher missing energy signal.

13.3.3 Simulation of the trigger menus

The trigger menus which will be used in this analysis are displayed in Table 13.3. First of all, ATLFAST allows particles and jets to satisfy certain requirements such as (i) muons and all other particles leaving a track in the inner detector must have a $\eta < 2.5$ and $p_T > 6$ GeV/c, (ii) particles recorded in the calorimeter must have $\eta < 5$, and (iii) jets are defined to have a transverse energy of at least 5 GeV in a cone of $\Delta R = 0.4$.

After events have been generated with ATLFAST, they are required to pass a set of trigger requirements. For this purpose, a pseudo-trigger is made, which includes the trigger menus as defined in Table 13.3. The muon trigger has been simulated as was mentioned in Section 13.3.1, i.e. including the time-of-flight requirement. The TOF is calculated by assuming the R-hadron to propagate in a straight line, a reasonable approximation given the high p_t values. The pseudo-trigger distinguishes between a 'first level trigger', where only calorimeter information and the muon triggers are used, and a 'high trigger', using all possible information. Table 13.4 shows cross sections, efficiencies of the pseudo-trigger, and number of events expected in 1 fb^{-1} for the different background and signal samples.

13.4 Selection

13.4.1 Variables

The global event variables used in the analysis related to the event topology are the following:

- The missing transverse energy E^T_{miss}, defined as explained in the end of Section 11.2.5.
- The transverse momentum of the most energetic muon or R-hadron in the muon chambers, denoted by $P_T^{\mu,R}$.
- The total visible energy of the event E^T_{sum}, defined as explained in the end of Section 11.2.5.
- The thrust of the event. The ATLFAST version including R-hadrons also calculates values for the thrust of an event [118], both calculated in the transverse plane (denoted by T_{xy}) and as well as in three dimensions, in the latter with a cut for all particles of $\eta < 2.5$. The definition of the (three-dimensional) thrust has been given in Section 8.3 and the transverse thrust follows directly. Class I events are expected to have a large thrust value, since most hadronic activity is expected around the two gluinos, produced back-to-back in the transverse plane.

Some relevant distributions for signal and background after second level trigger cuts are shown in Fig. 13.8 and Fig. 13.9. Fig. 13.10 shows the E^T_{miss} distribution for events where only calorimeter information is used, events where only the transverse momentum of one the two R-hadrons is measured, and events where two charged R-hadrons are measured. Note the significant difference in the average E^T_{miss}.

13.4.2 Cuts

The definition for the signal significance P applied here is the one as recommended by Ref. [102]:

$$P = \frac{S}{\sqrt{B}}, \tag{13.2}$$

where S and B are the number of background and signal events, respectively. The following cuts are chosen such as to optimize the quantity $S/\sqrt{B}$ for the sample with M=300 GeV/c^2:

- $E^T_{miss} > 150\,\mathrm{GeV}$;
- $E^T_{sum} > 180\,\mathrm{GeV}$;
- $p_T^{\mu,R} > 125\,\mathrm{GeV}$;
- $T_{xy} > 0.75$.

The value of the cut on the thrust represents the simple, elongated event structure, with two back-to-back gluinos in the transverse plane. Alternatively, one could have used the sphericity or circularity of the events to investigate the global event structure, but this would be complementary.

The above cuts are all related to the shape and kinematics of the events. The signal to noise ratio could be improved by using specific information of the muon system, such as velocity measurements or the intrinsic time resolution of the muon chambers, which is 0.7 ns [114] for non-interacting particles traveling with the speed of light. Requiring the arrival time to be larger than 2.1 ns (3σ) after that of a muon would already result in an enormous suppression factor, without losing much signal efficiency. However, detailed timing studies would be necessary for muon and R-hadrons in order to assess a good cut value. In addition, signatures such as the conversion from neutral to charged R-hadrons and the other way around, and the fact that two 'muons' of equal charge could be detected, would give additional rejection power. Finally, as was already shown in Fig. 12.18, the E/p ratio, if accessible, would improve the $S/\sqrt{B}$ ratio significantly.

13.5 Results and discussion

The number of signal and background events after applying the selection is given in Table 13.4. Although the selection is optimized for R-hadron masses of 300 GeV/c^2, the same selection can be applied for the other mass values. The total number of background events for 1 fb^{-1} is 457, and the total number of signal events in 1 fb^{-1} for M=100, 300 and 600 GeV/$c^2$is 393k, 54k, and 1.2k, respectively. For one year of running at low luminosity (10 fb^{-1}), this corresponds to a signal significance for M=100, 300 and 600 of $P = 5.8 \times 10^4$, $P = 8.0 \times 10^3$, and $P = 1.8 \times 10^2$. A higher signal significance can be achieved if the selection would be optimized for these other mass values. A signal significance of 5, the usual criterion for discovery, would be reached after only a few days of running. Even if the squark mass is large, so that the production channel via a squark propagator would be suppressed, the cross section is large enough to obtain high signal significances, because the production channel gg $\to \tilde{g}\tilde{g}$ is highly dominating: for example, for

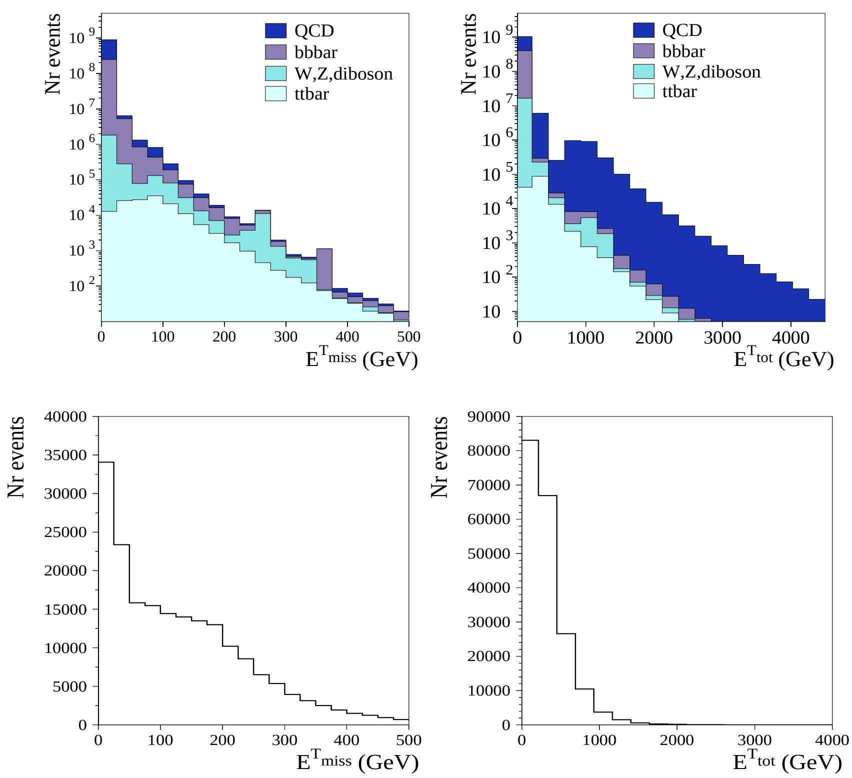

Figure 13.8: The missing transverse energy and the total visible energy, after high level trigger requirements. The number of events in these plots corresponds to that in 1 fb^{-1}.

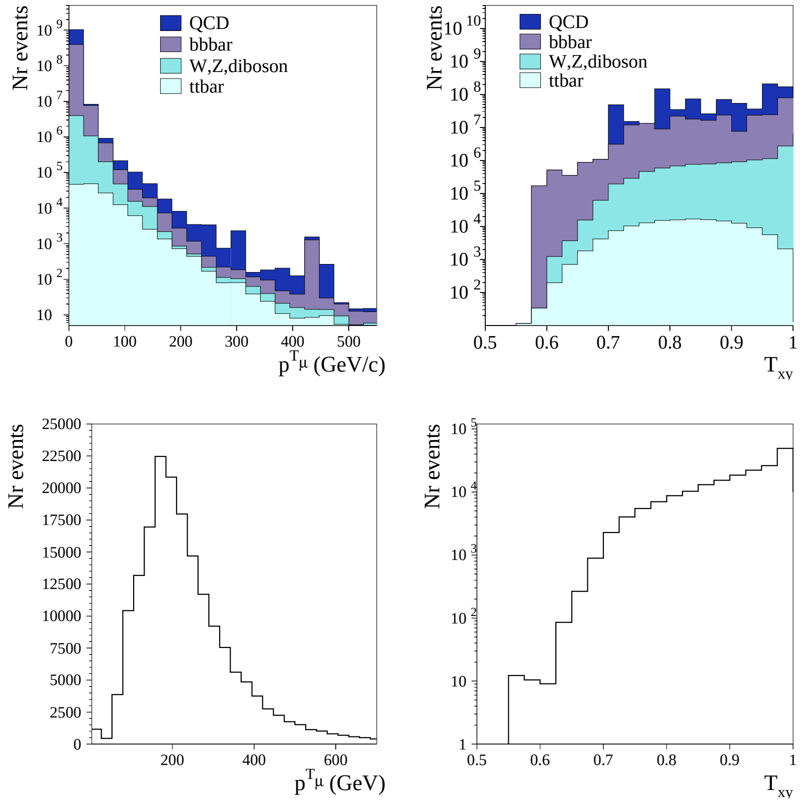

Figure 13.9: The p_T of the highest energetic muon or R-hadron, and the transverse thrust value, after high level trigger requirements. The number of events in these plots corresponds to that in 1 fb^{-1}.

M=300 GeV/c^2, only 4% of the events is generated via $q\bar{q} \rightarrow \tilde{g}\tilde{g}$.

The significances derived above may be affected by uncertainties, of which the following are dominant:

- The uncertainty on the parameter $P_{\tilde{g}g}$ (the probability to obtain a gluino-gluon state in the hadronization process, see Section 7.3.3), 0.1 by default. This uncertainty is investigated by generating events for which $P_{\tilde{g}g} = 1$ and $P_{\tilde{g}g} = 0$. The above selection criteria result in a signal significance of $P = 2.2 \times 10^3$ and $P = 5.4 \times 10^3$, respectively, for R-hadrons of 300 GeV/c^2. It must be noted that the selection is still effective: although no track in the inner detector is measured, the R-hadron can still be detected in the muon system, since it changes charge in the calorimeters. Thus, the missing energy signal can still be significant!

- The uncertainty coming from the nonzero probability for R-hadrons flipping charge in the muon system, as given in Table 13.2. Using the η distribution for R-hadrons as given Appendix C, the probability for an R-hadron to undergo a nuclear interaction in the entire muon system is roughly 50% due to the presence of support structures and cryostats. In these cases, R-hadrons can flip charge, or they can keep their charge. As can be seen from Table 13.2, a large fraction of R-hadron events would actually fire the muon trigger, and the uncertainty arises thus mainly from the reconstruction of such events. In a worse-case scenario, 50% of the R-hadrons would be reconstructed badly, and simply be completely lost. In that case, the number of signal events would be reduced with a factor 2, and so

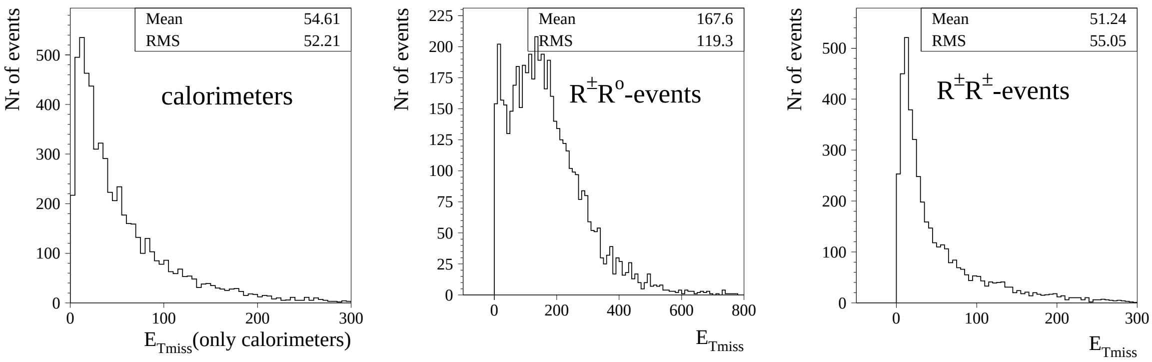

Figure 13.10: The missing transverse energy for class I events where M = 300 GeV/c^2 in case only calorimeter information is used (left), in case a neutral and a charged R-hadron are detected (center), and in case two charged R-hadrons are detected. Note that the production of two neutral R-hadrons can still result in a missing energy signal, because they can still be detected in the muon chambers. The normalization is arbitrary.

does the discovery potential. However, this would still result in a positive signal after only few days of running at low luminoscity.

- The presence of neutral R-hadrons in the inner detector and charged R-hadrons in the muon system. It is not certain what will happen to such events in the reconstruction software. This uncertainty has not been quantified, because a detailed knowledge about the response of the apparatus and of the final reconstruction software is needed. It is not expected to be a limiting factor for discovering R-hadrons.

- Uncertainties related to the generation of Monte Carlo events. For example, uncertainties on background and signal cross sections arise due to uncertainties in parton distribution functions, higher order corrections, etc. Also, uncertainties arise from limited Monte Carlo statistics in the regions of phase space where the cross section is very large. Also effects like calorimeter calibration may influence the above result. No attempt has been made to quantify these kind of uncertainties, but they are expected to be far below the order of magnitude such that they would form a potential danger for discovering R-hadrons.

In conclusion, although detailed studies are necessary on many aspects related to the detection of R-hadrons, this chapter has shown that R-hadrons produced via $pp \to \tilde{g}\tilde{g}$ with masses below the order of 600 GeV/c^2, the values traditionally studied for supersymmetry scenarios, can be quickly discovered at LHC running at low luminosity. Even without having a very detailed understanding of the ATLAS detector, which would for example be necessary for the discovery of the Higgs boson, a discovery of R-hadrons could be made at very early stages of the running of the LHC accelerator.

Chapter 14

Conclusion

In this thesis the interactions and detection of heavy stable hadrons have been studied. The focus has been on gluino R-hadrons, which are stable hadronized gluinos, arising in certain supersymmetry models.

The theoretical aspects of R-hadrons have been described in the first five Chapters. In Chapter 1 we have reviewed the theory of supersymmetry, which was meant to provide a general basis. In Chapter 2 some scenarios predicting R-hadrons have been reviewed, such as the so-called split supersymmetry models, which have recently become popular. Also, a summary was given on existing limits, and R-hadron production mechanisms were reviewed. Chapter 3 and 4 focused on hadronic interactions of light and heavy hadrons. A simple model, originally intended for R-hadrons, has been developed in Chapter 4 to describe the nuclear interactions of hadrons containing any new colour triplet or octet stable parton. We went through hadron mass spectra, nuclear scattering cross sections and interaction processes. Although the model should not be seen as the final description, it does form a good platform on which to build in the future. Chapter 5 outlined the implementation of the model into the GEANT 3 detector simulation framework, and some detector signatures were shown there, such as the conversion of R-mesons to R-baryons, energy losses in different materials, and losses per interaction. Also, the initial model used in ALEPH was discussed, and a simple comparison with the new model developed in Chapter 4 was made. No significant differences were found.

Chapters 5 to 10 were devoted to the search for R-hadrons using ALEPH data taken at LEP2 in the search channel $e^+e^- \to \tilde{t}\bar{\tilde{t}} \to c\tilde{g}\bar{c}\tilde{g}$. The selection developed for this purpose was based on acoplanar jets and missing energy. Using this selection, scalar top quarks have been excluded below 80 GeV GeV/c^2, given that the gluino mass is higher then 30 GeV/$c^2$and the mass difference between stop and gluino is smaller than 3 GeV/c^2. Together with searches performed in parallel, also based on LEP1 data, all scalar top masses have been excluded below 80 GeV, if the gluino is the lightest supersymmetric particle, and below 63 GeV/c^2 irrespectively of the nature of the lightest supersymmetric particle. The same selection was applied to search for gluinos in the channel $e^+e^- \to \tilde{b}\bar{\tilde{b}} \to b\tilde{g}\bar{b}\tilde{g}$, but no limits could be set.

Chapters 11 to 13 were devoted to the question what we will be able to see with the ATLAS detector. The signatures of single R-hadrons in the different subdetectors have been studied in Chapter 12. The response of all subdetectors was parameterized, and the resulting parameterizations were valid for any new colour octet stable parton. Due to the large number of uncertainties associated to e.g. the studies done for the TRT and the muon system, the analysis of the discovery potential of the ATLAS detector for R-hadrons in Chapter 13 is based on kinematic and topological variables only. The analysis focuses on R-hadron events in the channel $pp \to \tilde{g}\tilde{g}$ for LHC running at low luminosity, and makes use of fast simulation framework ATLFAST++.

ATLFAST++ has been extended to incorporate R-hadrons. Also, we addressed some important issues relevant for triggering of R-hadrons, and to some respect of any slowly moving charged particle, such as the possibility that slow R-hadrons could be associated with the wrong bunch crossing. A few relevant trigger menus have been studied for background and signal events. A selection is presented, and the signal significance reached after running one year at low luminosity is found to be enormous. Whether R-hadrons will really show up in the data at LHC or not, will unfortunately remain an unanswered question for the next few years. However, Chapter 13 has shown that R-hadrons, if they exist and have masses below the order of 600 GeV/c^2 will be discovered with absolute certainty within a short time of LHC running.

Appendices

Appendix A

Hadron mass spectra

Below, information about the quark model is given, which is relevant to understand the discussion about heavy hadron mass spectra in Section 4.3.2. For a detailed discussion about the quark model, I refer to Ref. [61]. The information presented below includes a short discussion about $SU(2)$ and $SU(3)$, as well as a very brief discussion about wavefunction symmetries associated with a hadron. As an example the π-ρ mass splitting will be discussed.

A.1 SU(2)

The symmetry group associated with the spin-state of a quark is $SU(2)$. A quark is contained in the fundamental spin doublet configuration of $SU(2)$. Denoting spin-doublets by **2**, the following combinations can easily be derived with Young-tableaux.

$$\begin{aligned} \text{q:}\quad & \mathbf{2} \\ \text{q}\bar{\text{q}}\text{:}\quad & \mathbf{2} \otimes \bar{\mathbf{2}} = \mathbf{1} \oplus \mathbf{3} \\ \text{qq:}\quad & \mathbf{2} \otimes \mathbf{2} = \mathbf{1} \oplus \mathbf{3} \\ \text{qqq:}\quad & \mathbf{2} \otimes \mathbf{2} \otimes \mathbf{2} = \mathbf{4} \oplus \mathbf{2} \oplus \mathbf{2} \end{aligned}$$

Thus, a quark anti-quark pair can form a spin-singlet, implying $s = 0$ ($s_z = 0$) or spin-triplet, implying $s = 1$ ($s_z = 1, 0, -1$). To calculate the mass splittings in Equation (4.1), we must evaluate $(\mathbf{S}_1 \cdot \mathbf{S}_2)$ for two partons 1 and 2, with associated SU(2) color matrices $\mathbf{S}_1$ and $\mathbf{S}_2$. We can find an expression for $(\mathbf{F}_1 \cdot \mathbf{F}_2)$ by writing

$$\begin{aligned} (\mathbf{S}_1 + \mathbf{S}_2)^2 &= \mathbf{S}_1^2 + \mathbf{S}_2^2 + 2(\mathbf{S}_1 \cdot \mathbf{S}_2) && \text{(A.1)} \\ 2(\mathbf{S}_1 \cdot \mathbf{S}_2) &= (\mathbf{S}_1 + \mathbf{S}_2)^2 - \mathbf{S}_1^2 - \mathbf{S}_2^2 && \text{(A.2)} \\ &= s_{1+2}(s_{1+2} + 1) - s_1(s_1 + 1) - s_2(s_2 + 1), && \text{(A.3)} \end{aligned}$$

where the magnitudes of the Casimir operators for the SU(2) representation are $\mathbf{S}^2 = s(s + 1)$, with s the total spin of the state. Again we have assumed left and right hand sides to operate on an SU(2) state $|i>$. If $|i>$ would be a single quark, contained in a **2** of SU(2), then $s = 1/2$, and the eigenvalue of $\mathbf{S}^2$ is $3/4$. For a quark pair, we saw above that there are two possibilities: a symmetric spin configuration, $s = 1$ ($s_z = 1, 0, -1$, the triplet state **3**) or an antisymmetric spin configuration $s = 0$ ($s_z = 0$, the singlet state **1**). It is this difference which is responsible for the mass splitting.

Dimension	λ^2
$\mathbf{1}$	0
$\mathbf{3}$	$\frac{4}{3}$
$\bar{\mathbf{3}}$	$\frac{4}{3}$
$\mathbf{8}$	3
$\mathbf{6}$	$\frac{10}{3}$
$\mathbf{10}$	6

Table A.1: Magnitudes of Casimir operators for some SU(3) representations

A.2 SU(3)

Following the quark model, $SU(3)$ is the symmetry associated with the colour and flavour of a quark. In order to understand which hadrons are formed from hadronization of a heavy coloured parton, let us look closer at the group $SU(3)_c$ of colour. Assuming that the quark forms the fundamental triplet configuration of $SU(3)_c$, it is possible to use Young-tableax to determine the colour representations resulting from combining quarks and anti-quarks. Denoting colour-triplets by $\mathbf{3}$, colour anti-triplets by $\bar{\mathbf{3}}$, etc, the following combinations can be derived.

$$\begin{aligned}
\text{q:}&\quad \mathbf{3}\\
\text{q}\bar{\text{q}}\text{:}&\quad \mathbf{3}\otimes\bar{\mathbf{3}} = \mathbf{1}\oplus\mathbf{8}\\
\text{qq:}&\quad \mathbf{3}\otimes\mathbf{3} = \mathbf{6}\oplus\bar{\mathbf{3}}\\
\text{qqq:}&\quad \mathbf{3}\otimes\mathbf{3}\otimes\mathbf{3} = \mathbf{1}\oplus\mathbf{8}\oplus\mathbf{8}\oplus\mathbf{10}
\end{aligned}$$

For example, a quark and an anti-quark can either form a $\mathbf{1}$ or an $\mathbf{8}$ of $SU(3)$. Thus, it can form a colour singlet by itself, or by combining with a colour octet. Two quarks can form an anti-triplet, and thus, together with a third quark, form a colour singlet, as for ordinary baryons, or they can form a sextet, etc.

To calculate the mass splitting between different heavy hadrons, given in equation (4.1), we must evaluate the product $(\mathbf{F}_1\cdot\mathbf{F}_2)$ for two partons 1 and 2, with associated SU(3) color matrices $\mathbf{F}_1$ and $\mathbf{F}_2$. We can find an expression for $(\mathbf{F}_1\cdot\mathbf{F}_2)$ by writing

$$\begin{aligned}
(\mathbf{F}_1+\mathbf{F}_2)^2 &= \mathbf{F}_1^2+\mathbf{F}_2^2+2(\mathbf{F}_1\cdot\mathbf{F}_2) &\text{(A.4)}\\
2(\mathbf{F}_1\cdot\mathbf{F}_2) &= (\mathbf{F}_1+\mathbf{F}_2)^2-\mathbf{F}_1^2-\mathbf{F}_2^2 &\text{(A.5)}\\
&= \lambda_{1+2}^2-\lambda_1^2-\lambda_2^2, &\text{(A.6)}
\end{aligned}$$

where we have implicitly assumed left and right hand sides to operate on a color state $|i>$, e.g. a colour anti-triplet for two quarks in qqq. Here λ_i^2 is the eigenvalue of the Casimir operator working on an $SU(3)$ color state i. The value for λ_i^2 depends on the representation in which state i is contained. In table A.1, magnitudes of Casimir operators, λ^2 are given for some common $SU(3)$ representations. Thus, a colour triplet state has for example $\lambda^2=\frac{4}{3}$. Note that the left side of equation (A.4) represents the colour state of partons 1 and 2 together.

A.3 Wavefunctions

The wavefunction of a hadron as a whole can in short notation be written as a product:

$$\text{total} = (\text{space})\times(\text{colour})\times(\text{spin})\times(\text{flavour}) \tag{A.7}$$

Totally symmetric	$\phi_S\psi_S \equiv (\mathbf{10},\mathbf{4})$
	$\frac{1}{\sqrt{2}}(\phi_{M,S}\psi_{M,S} + \phi_{M,A}\psi_{M,A}) \equiv (\mathbf{8},\mathbf{2})$
Mixed symmetric	$\phi_S\psi_{M,S} \equiv (\mathbf{10},\mathbf{2})$
	$\phi_{M,S}\psi_S \equiv (\mathbf{8},\mathbf{4})$
	$\frac{1}{\sqrt{2}}(-\phi_{M,S}\psi_{M,S} + \phi_{M,A}\psi_{M,A}) \equiv (\mathbf{8},\mathbf{2})$
	$\phi_A\psi_{M,A} \equiv (\mathbf{1},\mathbf{2})$
Mixed anti symmetric	$\phi_A\psi_{M,A} \equiv (\mathbf{10},\mathbf{2})$
	$\phi_{M,A}\psi_S \equiv (\mathbf{8},\mathbf{4})$
	$\frac{1}{\sqrt{2}}(-\phi_{M,S}\psi_{M,A} + \phi_{M,A}\psi_{M,S}) \equiv (\mathbf{8},\mathbf{2})$
	$\phi_A\psi_{M,S} \equiv (\mathbf{1},\mathbf{2})$
Totally anti symmetric	$\phi_A\psi_S \equiv (\mathbf{1},\mathbf{4})$
	$\frac{1}{\sqrt{2}}(\phi_{M,S}\psi_{M,A} + \phi_{M,A}\psi_{M,S}) \equiv (\mathbf{8},\mathbf{2})$

Table A.2: The symmetries resulting from combination of SU(3) wavefunctions ϕ and SU(2) wavefunctions ψ. The subscripts S, A and M denote a totally symmetric wavefunction, a totally anti-symmetric wavefunction and a wavefunction with mixed symmetries. A combination like M, A means that a pair of quarks has a totally anti-symmetric wavefunction, while it has mixed symmetries with respect to the third quark. This table is obtained from Ref. [61].

If only ground-state particles are considered, the space part of the wavefunction is symmetric. This decomposition helps us to determine which configurations are allowed and which are forbidden for a given hadron. Denoting the $SU(3)$ wavefunctions by ϕ and the $SU(2)$ wavefunctions by ψ, all possible symmetry combination of combining $SU(3)$ and $SU(2)$ are given in Table A.2. Note that the $SU(3)$ part can refer both to colour and to flavour! As an example of how to use this table, consider the ordinary baryons consisting of three first generation quarks (p,n, Δ, etc). The three quarks are contained in colour singlet, implying an anti-symmetric colour wavefunction. In order to form a totally antisymmetric wavefunction (fermions), the flavour$\times$spin part must be symmetric. The first row in table A.2 gives us all possibilities corresponding to a symmetric flavour$\times$spin wavefunction. If the flavour-part is purely symmetric (corresponding to ϕ_S in the first row of Table A.2, i.e. uuu, ddd or symmetric configurations of uud and udd states), they must be part of a spin quartet, i.e. $s = 3/2$ ($s_z = 3/2, 1/2, -1/2, -3/2$), and only spin symmetric configurations (corresponding to ψ_S in the first row of table A.2) are allowed in this case. If on the other hand the flavour part is mixed, like mixed flavour symmetric combinations of uud- and udd-states, the partons must be part of a spin-doublet, i.e. $s = 1/2$ ($s_z = 1/2, -1/2$), and part of a flavour octet. The latter example was concerned with the wavefunctions associated with the three quarks in a bound state. Derivations for quark pairs contained in bound states can be obtained similarly.

Appendix B

Kinematics

Rather than to start immedeately with the derivation of two- and three-body phase space, let's consider first a simple 2-body scattering example. The metric $(1, -1, -1, -1)$ will be used.

B.1 2-body scattering

Consider two spinless particles with mass m_1 and m_2 and four-momenta of p_1 and p_2 respectively. In the laboratory frame, particle 2 is at rest and particle 1 approaches particle 2 with momentum $\mathbf{p_1}$, so that

$$p_1 = (E_1, \mathbf{p}_1), \qquad p_2 = (m_2, 0) \tag{B.1}$$

In the center of mass frame of the two particles, the four-momenta are given by

$$p_1^* = (E_1^*, \mathbf{p}_1^*), \qquad p_2^* = (E_2^*, \mathbf{p}_2^*). \tag{B.2}$$

These particles scatter. After scattering, we have particles 3 and 4, with four-momenta p_3 and p_4, respectively, and masses m_3 and m_4. The situation is illustrated in figure B.1. Per definition, the three-momenta in the center-of-mass frame are opposite and their magnitudes equal:

$$\mathbf{p}_1 = -\mathbf{p}_2, \qquad p^* = |\mathbf{p}_1| = |\mathbf{p}_2| \tag{B.3}$$

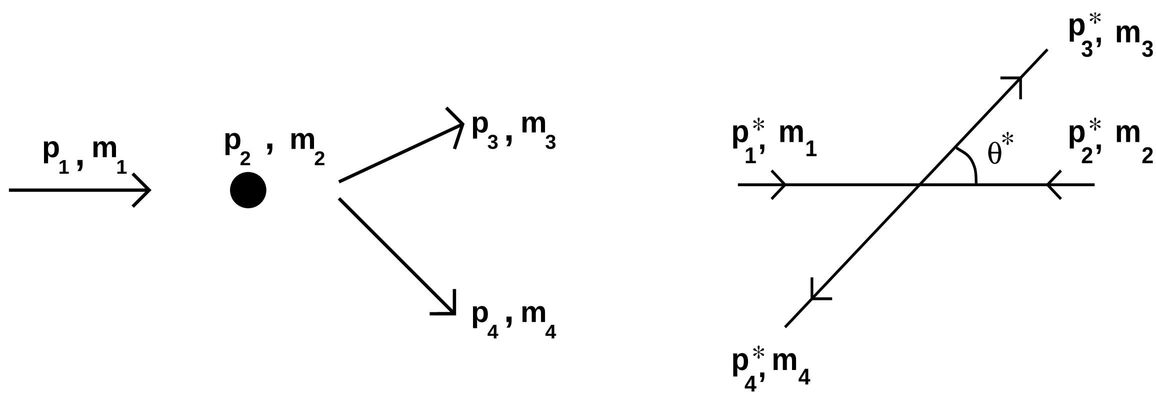

(a) (b)

Figure B.1: Two-body scattering in (a) the laboratory system and (b) the center-of-mass system.

The three Mandelstam variables are:

$$s = (p_1 + p_2)^2, \qquad t = (p_1 - p_3)^2, \qquad u = (p_1 - p_4)^2, \tag{B.4}$$

The first Mandelstam variable, s, is the center of mass energy of the interaction squared and can e.g. be calculated in the laboratory frame:

$$\begin{aligned} s &= (p_1 + p_2)^2 && \text{(B.5)} \\ &= (p_1^2 + p_2^2 + 2\mathbf{p_1} \cdot \mathbf{p_2}) && \text{(B.6)} \\ &= (m_1^2 + m_2^2 + 2E_1 m_2) && \text{(B.7)} \end{aligned}$$

Using this expression for s together with equation (B.3), it is easily derived that

$$p^* = \frac{\left[(s - m_1^2 - m_2^2)^2 - 4m_1^2 m_2^2\right]^{1/2}}{2\sqrt{s}} \tag{B.8}$$

The second Mandelstam variable, t, is the four-momentum transfer in the interaction. Independent of the system, t is given by

$$\begin{aligned} t &= (p_1 - p_3)^2 && \text{(B.9)} \\ &= m_1^2 + m_3^2 - 2E_1E_3 + 2|\mathbf{p}_1||\mathbf{p}_3|\cos\theta && \text{(B.10)} \end{aligned}$$

where $\mathbf{p}_1$, $\mathbf{p}_3$ and $\cos\theta$ are momentum of particle 1, particle 3 and the the scattering angle in the system. Defining t for a minimum scattering angle (θ=0) as

$$t_{min} = m_1^2 + m_3^2 - 2E_1E_3 + 2|\mathbf{p}_1||\mathbf{p}_3|, \tag{B.11}$$

the value for $\cos\theta^*$ is given by

$$\cos\theta^* = 1 + \frac{2(t - t_{min})}{4|\mathbf{p}_1||\mathbf{p}_3|} \tag{B.12}$$

Longitudinal and transversal momenta of the final state particle momenta are obviously related by

$$\cos\theta^* = \frac{p_z^*}{({p_T^*}^2 + {p_z^*}^2)^{1/2}}, \tag{B.13}$$

where p_T and p_z are the transverse and longitudinal momentum components. Relations (B.11), (B.12) and (B.13) are given merely as reference to the discussion in Section 5.5.2.

B.2 Phase-space

The partial decay rate of a particle with mass m_0 and 4-momentum p_0 into n particles with masses m_i and 4-momenta p_i ($i = 1, 2, ...$) in the rest-frame of the decaying particle is given by [4]

$$\mathrm{d}\Gamma = \frac{(2\pi)^4}{2m_0} |\mathcal{M}_0|^2 \mathrm{d}\Phi_n(p_0; p_1, p_2, ..., p_n) \tag{B.14}$$

Here $\mathcal{M}_0$ is the scattering amplitude, and $\mathrm{d}\Phi_n(p_0; p_1, p_2, ..., p_n)$ is an element of n-body phase-space, given by

$$\mathrm{d}\Phi_n(p_0; p_1, p_2, ..., p_n) = \delta^4(p_o - \sum_{i=1}^{n} p_i) \prod_{i=1}^{n} \frac{d^3 p_i}{(2\pi)^3 2E_i} \tag{B.15}$$

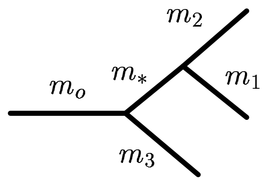

Figure B.2: A particle decaying into three final state particles via an intermediate state with mass m_*.

Thus, the decay is determined by two factors: couplings or matrixelements, and available phase-space. For two final state particles, the two-body phase space $d\Phi_2$ is for isotropic decay in the rest-frame of particle 0 given by

$$\begin{aligned} d\Phi_2 &= \frac{1}{64\pi^4}\frac{|\mathbf{p}_1|}{m_0} \\ &\propto \left(\frac{[m_0+m_1+m_2]}{m_0}\frac{[m_0-m_1-m_2]}{m_0}\frac{[m_0+m_1-m_2]}{m_0}\frac{[m_0-m_1+m_2]}{m_0}\right)^{\frac{1}{2}}, \end{aligned} \tag{B.16}$$

where we have used the expression in equation (B.8). For the calculation of the partial decay rate of three final state particles, it is appropiate to calculate the phase-space by introducing an intermediate state with mass m_*, see figure B.2. For $d\Phi_3(p_0;p_1,p_2,p_3)$, we have

$$\begin{aligned} &d\Phi_3(p_0;p_1,p_2,p_3) = \\ &\frac{d^3p_1}{(2\pi)^3 2E_1}\frac{d^3p_2}{(2\pi)^3 2E_2}\frac{d^3p_3}{(2\pi)^3 2E_3}(2\pi)^4\delta^4(p_0-p_1-p_2-p_3)\times 1 \\ &= \frac{d^3p_1}{(2\pi)^3 2E_1}\frac{d^3p_2}{(2\pi)^3 2E_2}\frac{d^3p_3}{(2\pi)^3 2E_3}(2\pi)^4\delta^4(p_0-p_1-p_2-p_3)\times\int d^4p_*\delta^4(p_*-p_1-p_2)\int dm_*^2\delta(p_*^2-m_*^2) \\ &= \int dm_*^2\frac{d^3p_1}{(2\pi)^3 2E_1}\frac{d^3p_2}{(2\pi)^3 2E_2}\delta^4(p_*-p_1-p_2)\frac{d^3p_3}{(2\pi)^3 2E_3}(2\pi)^4\delta^4(p_0-p_1-p_2-p_3)\delta(p_*^2-m_*^2)d^4p_* \\ &\propto \int dm_*^2\frac{d^3p_1}{(2\pi)^3 2E_1}\frac{d^3p_2}{(2\pi)^3 2E_2}(2\pi)^4\delta^4(p_0-p_1-p_2)\frac{d^3p_3}{(2\pi)^3 2E_3}\frac{d^3p_*}{(2\pi)^3 2E_*}(2\pi)^4\delta^4(p_0-p_*-p_3) \\ &= \int dm_*^2\int d\Phi_2(p_*;p_1,p_2)d\Phi_2(p_0;p_*,p_3) \end{aligned} \tag{B.17}$$

where we have used in the third line that $\int d^4p_*\delta(p_*^2-m_*^2) = \int d^3p_*\int dE_*\delta(E_*^2-\mathbf{p}_*^2-m_*^2) = \int d^3p_*/(2E_*)$. The exact calculation of the expression in equation (B.17) is however far from trivial. Let's try to evaluate 2- and 3-body phase space in terms of Q, the energy for the production of kinetic energy for final state particles. To warm up, we derive an expression for $d\Phi_2$ in terms of Q first. After that, a few examples of an evaluation for $d\Phi_3$ are given, starting with the simpliest case of three massless final state particles, and ending with an example relevant for the case of R-hadron nucleon scattering.

Case (0): $\mathbf{Q = m_0 - m_1 - m_2 \ll m_1 \ll m_2 \approx m_0}$

An expression for 2-body phase space in terms of Q can be derived with these assumptions, starting from equation (B.16):

$$d\Phi_2(p_0;p_1,p_2) \propto \frac{1}{m_0^2}\sqrt{2m_0Q2m_2m_1} \tag{B.18}$$

$$\propto \sqrt{\frac{m_1m_2}{m_0^3}}\sqrt{Q} \tag{B.19}$$

Case (i): $\mathbf{m_1 = m_2 = m_3 = 0;\ Q = m_0}$

From equations (B.16) and (B.17), we derive that in this case

$$\begin{aligned}
\mathrm{d}\Phi_3(p_0;p_1,p_2,p_3) &\propto \frac{1}{m_0^2}\int_0^{m_0}\frac{\mathrm{d}m_*}{m_*}m_*^2(m_0+m_*)(m_0-m_*) && \text{(B.20)}\\
&\propto m_0^2 && \text{(B.21)}
\end{aligned}$$

Case (ii): $\mathbf{m_1 = m_2 = 0;\ Q = m_0 - m_3 \approx 0;\ m_* < m_0 - m_3}$

In this case, we can derived that

$$\begin{aligned}
\mathrm{d}\Phi_3(p_0;p_1,p_2,p_3) &\propto \tfrac{1}{m_0^2}\int_0^Q \tfrac{\mathrm{d}m_*}{m_*}\sqrt{2m_0 2m_3(Q^2-m_*^2)}\sqrt{m_*^4}\\
&\propto \sqrt{\tfrac{m_3}{m_0^3}}\int_0^Q \mathrm{d}m_* m_*\sqrt{Q^2-m_*^2} && \text{(B.22)}\\
&\propto \sqrt{\tfrac{m_3}{m_0^3}}Q^3
\end{aligned}$$

Case (iii): $\mathbf{m_1 = 0; Q = m_0 - m_2 - m_3 \ll m_2 \ll m_3 \approx m_0}$

Here, the expression for 3-body phase space is seen to be

$$\begin{aligned}
\mathrm{d}\Phi_3(p_0;p_1,p_2,p_3) &\propto \frac{1}{m_0^2}\int_{m_2}^{m_2+Q}\frac{\mathrm{d}m_*}{m_*}\sqrt{m_0 Q m_3 m_2}\sqrt{m_2 Q m_2 Q} && \text{(B.23)}\\
&\propto \sqrt{\frac{m_2 m_3}{m_0^3}}Q^{5/2} && \text{(B.24)}
\end{aligned}$$

Case (iv): $\mathbf{Q = m_0 - m_1 - m_2 - m_3 \ll m_1, m_2;\ m_1, m_2 \ll m_3 \approx m_0}$

Under these assumptions, the expression for $\mathrm{d}\Phi_3(p_0;p_1,p_2,p_3)$ can be evaluated to be

$$\begin{aligned}
\mathrm{d}\Phi_3(p_0;p_1,p_2,p_3) &\propto \frac{1}{m_0^2}\int_{m_1+m_2}^{m_1+m_2+Q}\frac{\mathrm{d}m_*}{m_*}\sqrt{2m_0(Q+m_1+m_2-m_*)2m_3(m_1+m_2)} && \text{(B.25)}\\
&\qquad\times\sqrt{(m_1+m_2)(m_*-m_1-m_2)2m_1 2m_2} && \text{(B.26)}\\
&\propto \sqrt{\frac{m_1 m_2 m_3}{m_0^3}}(m_1+m_2)\int_{m_1+m_2}^{m_1+m_2+Q}\frac{\mathrm{d}m_*}{m_*}\sqrt{Q+m_1+m_2-m_*} && \text{(B.27)}\\
&\qquad\times\sqrt{m_*-m_1-m_2} && \text{(B.28)}\\
&\propto \sqrt{\frac{m_1 m_2 m_3}{m_0^3}}Q^2. && \text{(B.29)}
\end{aligned}$$

Phasespace for R-hadron nucleon scattering

If m_0 denotes the $\sqrt{s}$ available in the scattering process, and m_1, m_2 and m_3 denote the pion mass, proton mass, and R-hadron mass, respectively, the ratio between $\mathrm{d}\Phi_2$ and $\mathrm{d}\Phi_3$ can be derived from case (0) and case (iv):

$$\frac{\mathrm{d}\Phi_3(p_0;p_1,p_2,p_3)}{\mathrm{d}\Phi_2(p_0;p_2,p_3)} = \sqrt{m_1}Q^{3/2} \tag{B.30}$$

An interpolation between case (iii) and (iv) gives

$$\frac{\mathrm{d}\Phi_3(p_0;p_1,p_2,p_3)}{\mathrm{d}\Phi_2(p_0;p_2,p_3)} = \sqrt{1+\frac{Q}{2m_\pi}}Q^{3/2}. \tag{B.31}$$

Appendix C

Distributions

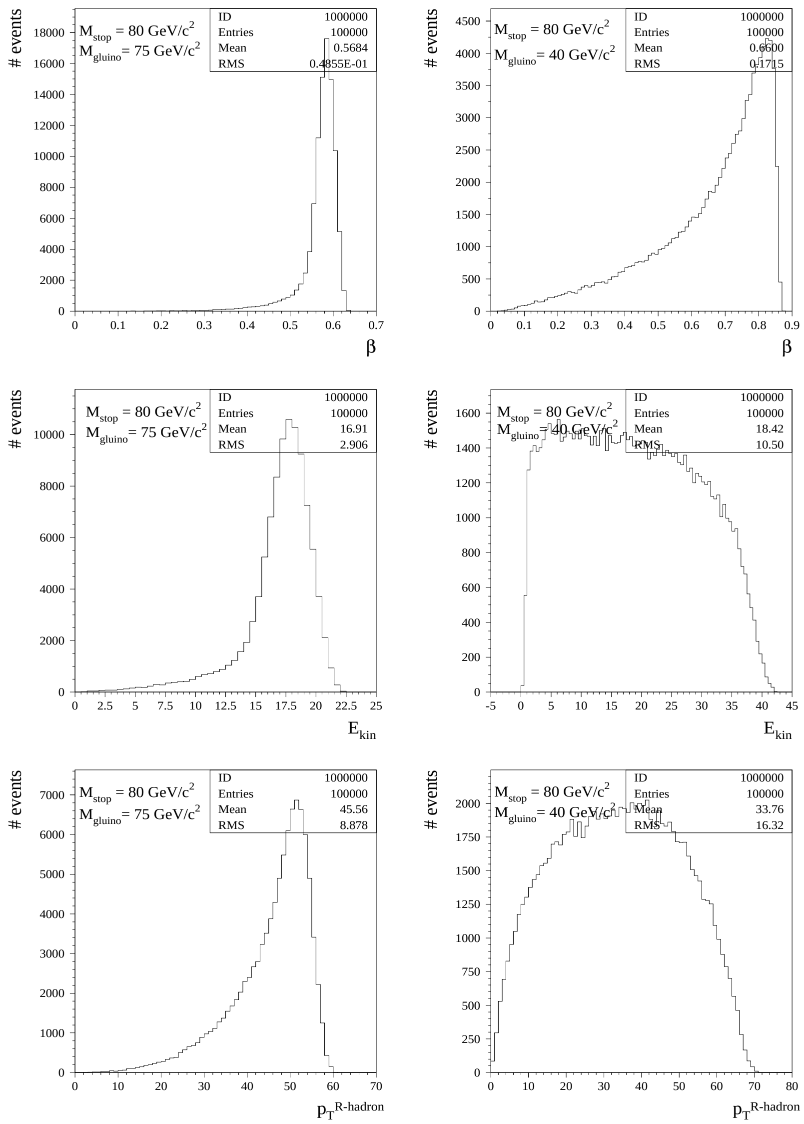

Figure C.1: Distributions for the velocity β, the kinetic energy E_{kin} (in GeV), and the transverse momentum p_T (in GeV/c) of an R-hadron in produced via $e^+e^- \to c\tilde{g}\bar{c}\tilde{g}$.

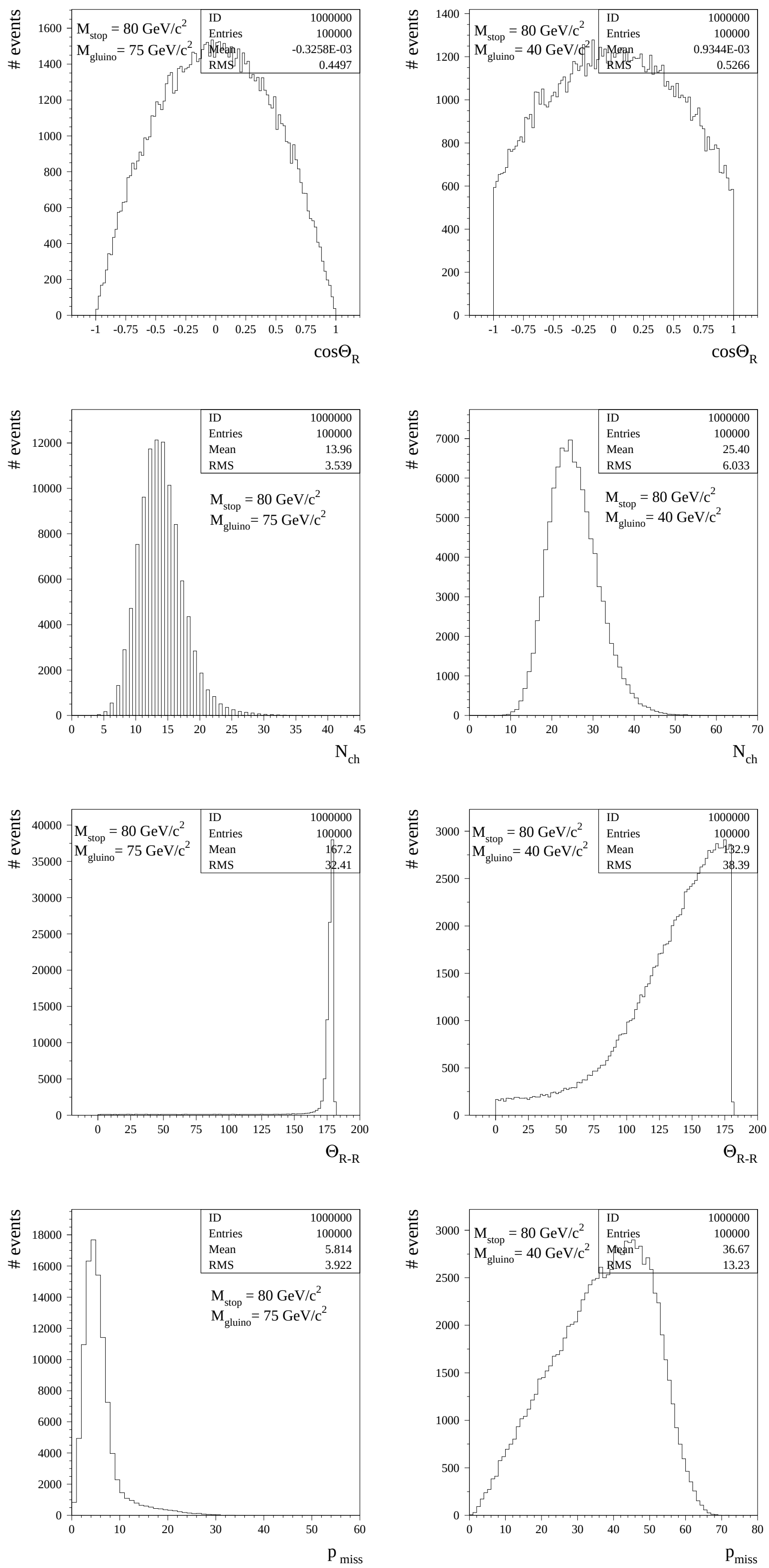

Figure C.2: Distributions for the production angle θ of the R-hadron, the event mupliplicity N_{ch}, the angle between the two produced R-hadrons θ_{R-R} (in degrees), and the missing momentum P_{miss} (in GeV/c) for the production of two R-hadrons in channel $e^+e^- \rightarrow \tilde{g}c\tilde{g}\bar{c}$. The latter is calculated by taking the vector sum of all stable particles except for the R-hadrons.

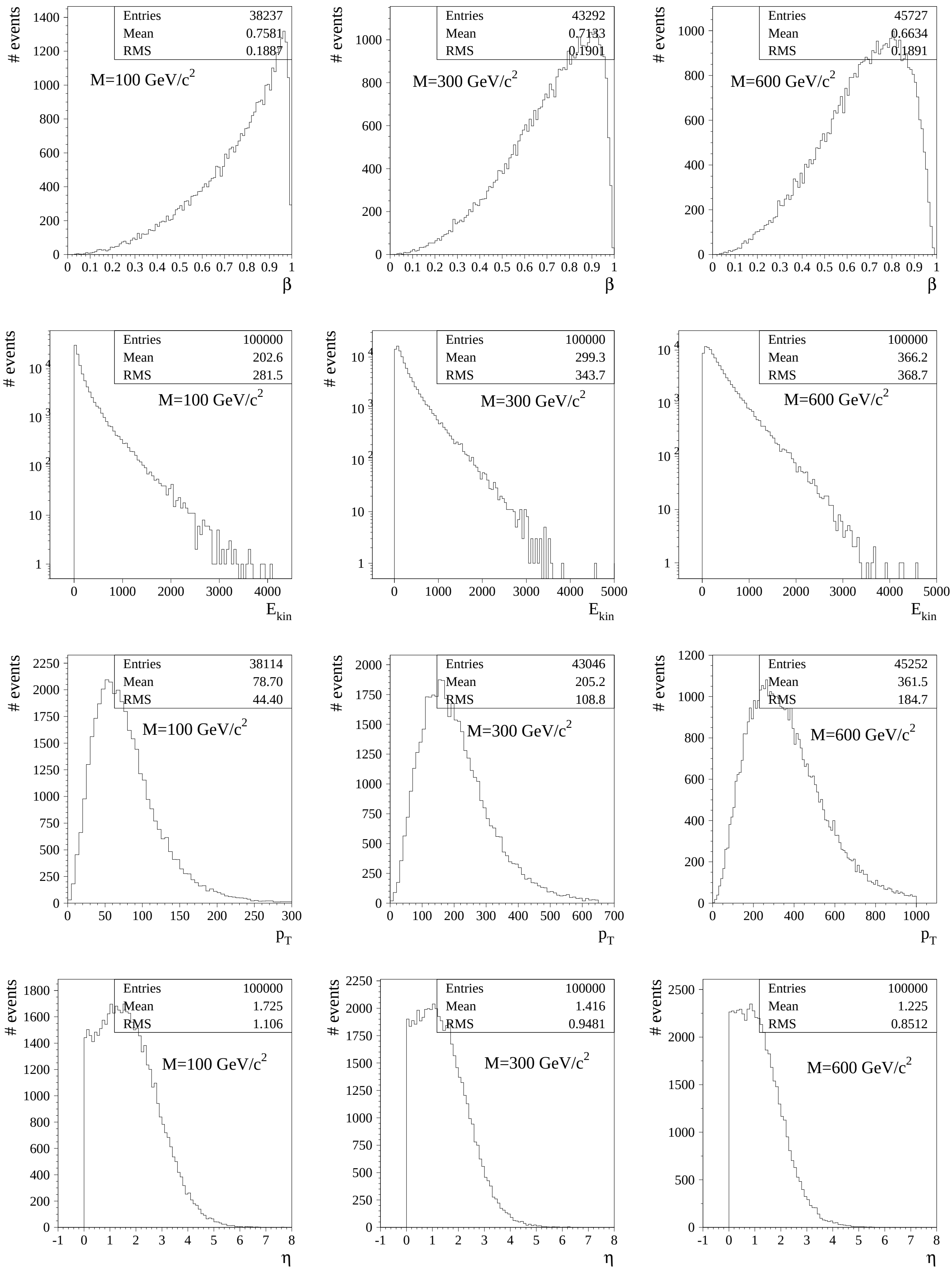

Figure C.3: Distributions for the velocity β, the kinetic energy E_{kin} (in GeV), the transverse momentum p_T (in GeV/c) and the η-value of an R-hadron in the class I channel ($pp \to \tilde{g}\tilde{g}$) for $M_R = 100$, 300 and 600 GeV/c^2. The distributions for β and p_T are made requiring $\eta < 2.5$.

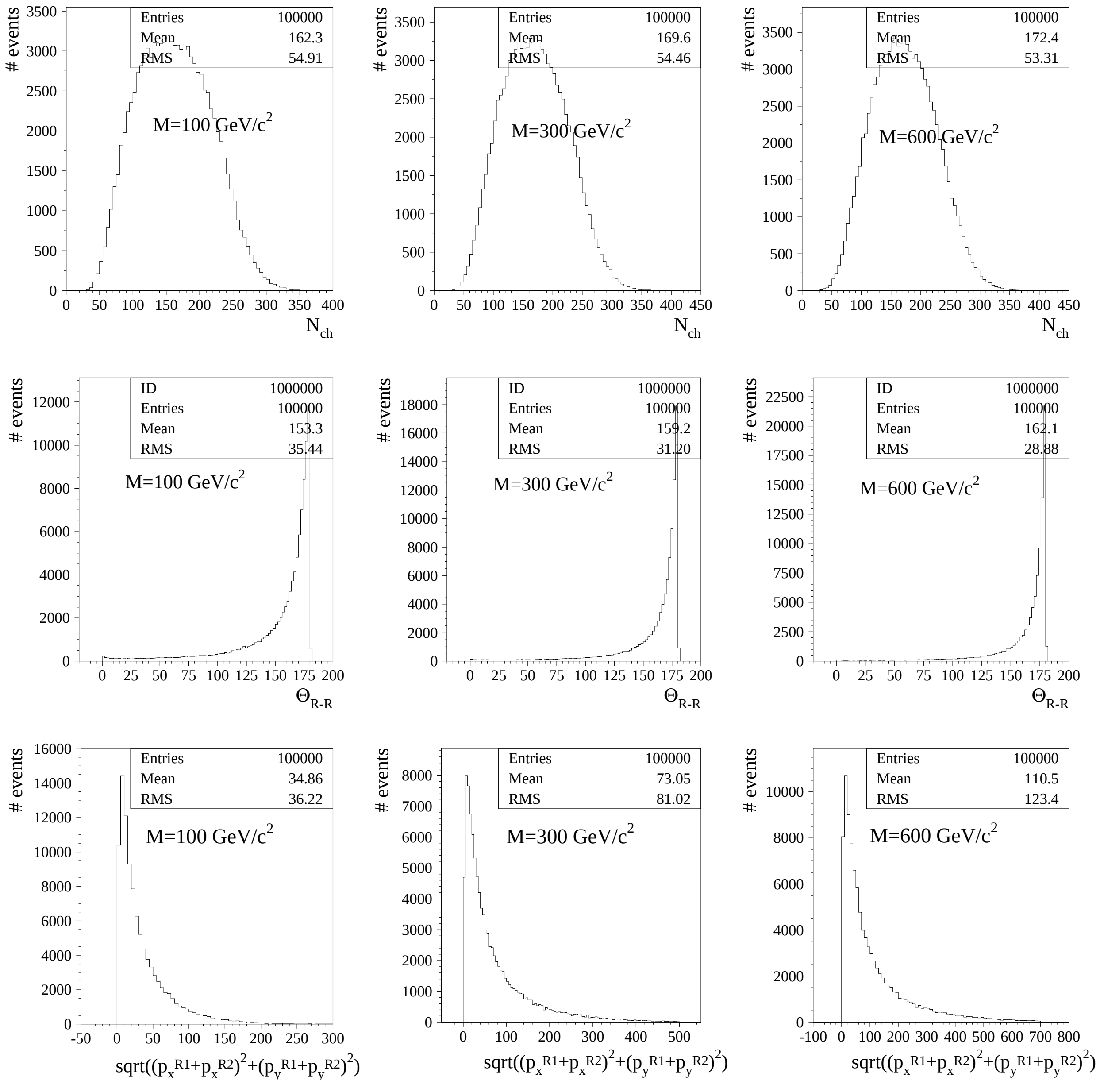

Figure C.4: Distributions for the event mupliplicity N_{ch}, the angle between the two produced R-hadrons θ_{R-R} (in degrees) and the vector sum of the momenta (in GeV/c) of the two R-hadrons in the transverse plane for R-hadrons events in the class I channel ($pp \to \tilde{g}\tilde{g}$) for $M_R = 100$, 300 and 600 GeV/c^2.

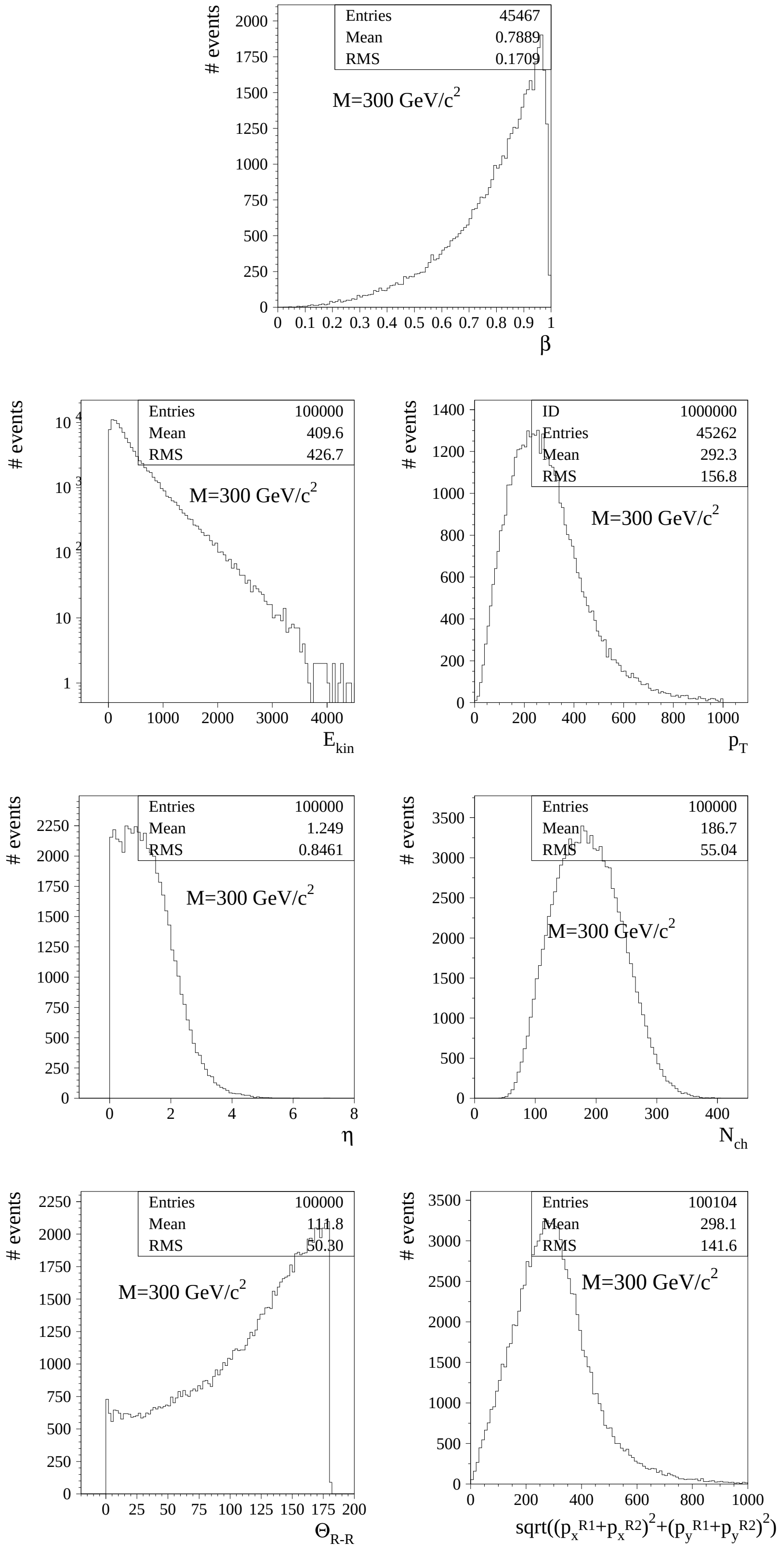

Figure C.5: Relevant distributions for the production of two R-hadrons in class II events (pp $\rightarrow$ $\tilde{q}\tilde{g} \rightarrow \tilde{g}\tilde{g}q$) for M_R=300 GeV. The units for E_{kin} and p_T are GeV and GeV/c, respectively. Again the β and p_T distributions are made only taking into account particles with $\eta < 2.5$.

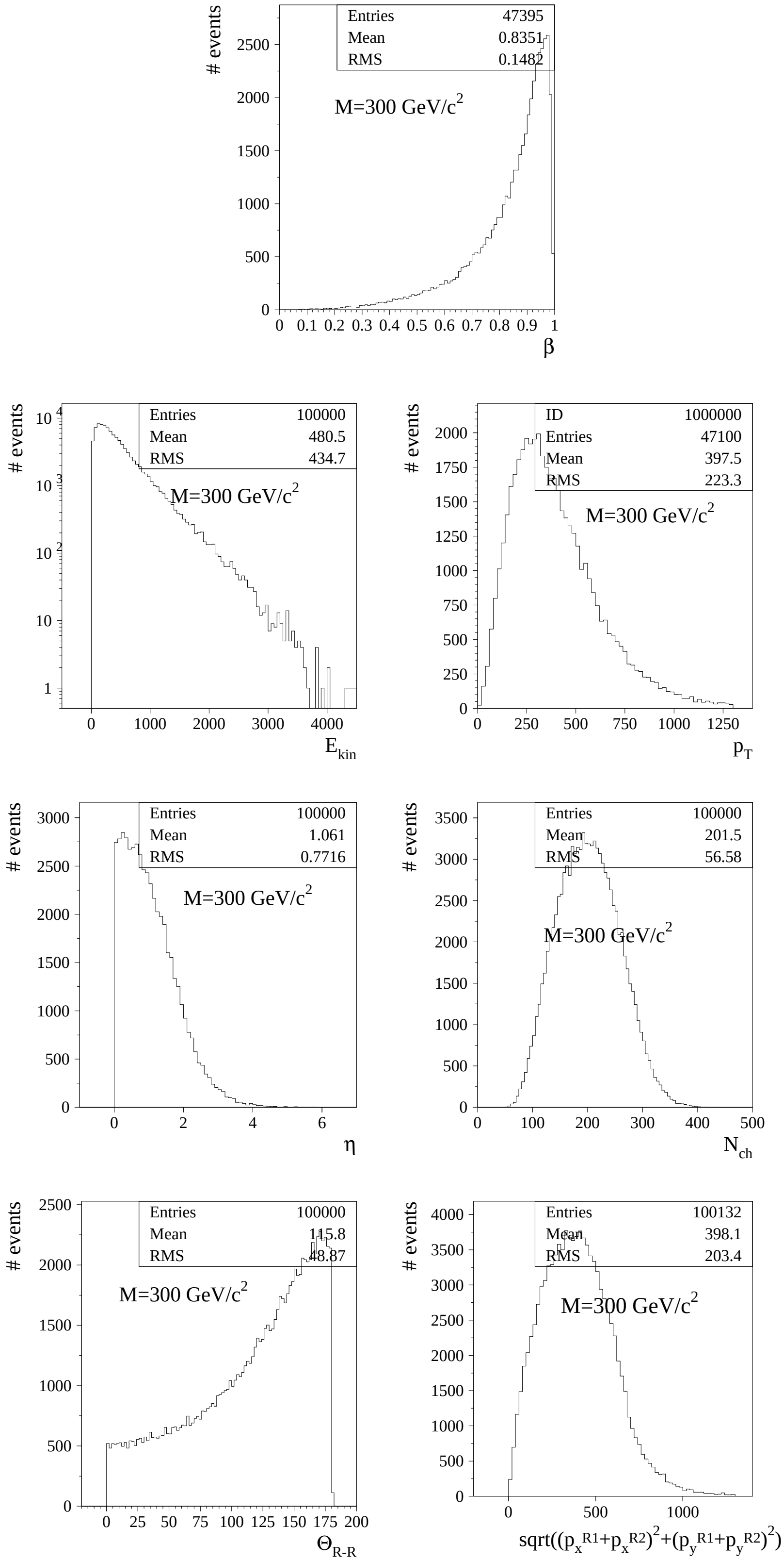

Figure C.6: Relevant distributions for the production of two R-hadrons in class III events (pp $\to$ $\tilde{q}\tilde{q} \to \tilde{g}\tilde{g}qq$) for M_R=300 GeV. The units for E_{kin} and p_T are GeV and GeV/c, respectively. Again the β and p_T distributions are made only taking into account particles with $\eta < 2.5$.

Bibliography

[1] H.P. Nilles, *Phys. Rept.* **110** (1984) 1;
H.E. Haber and G.L. Kane, *Phys. Rept.* **117** (1985) 75;
R. Barbieri, *Riv. Nuovo Cim.* **11N4** (1988) 1.

[2] C. Quigg, *Gauge Theories of the Strong, Weak and Electromagnetic Interactions*, Westview Press, 1997.

[3] K. Aoki, Z. Hioki, R. Kawabe, M. Konuma, T. Muta, *Electroweak theory*, Supplement of the Progress of Theoretical Physics, 73, 1982.

[4] The Review of Particle Physics 2002 Edition, K. Hagiwara et al., *Phys. Rev.* **D 66** (010001) 2002.

[5] S.P. Martin, *A supersymmetry primer*, appeared in: *Perspectives on supersymmetry*, edited by G. Kane, Advances Series on Directions in High Energy Physics, Vol. 18., World Scientific Publishing Company, Singapore, 1998.

[6] M.E. Peskin, D.V. Schroeder, *An introduction to Quantum Field Theory*, Perseus Books, Cambridge, 1995.

[7] A.C. Kraan, *Neutrinos: masses, mixing and decay*, August 2001, Thesis for the Degree 'Master of Science'. Available at `www.nbi.dk/~ackraan`

[8] J. Wess and B. Zumino, *Nucl. Phys.* **B 70** (1974) 39.

[9] X. Tata, *What is supersymmetry and how do we find it?*, Lectures presented at the IX Jorge A.S̃wieca Summer School, Campos de Jordao, Brazil, 1997.

[10] H. Dreiner, *An introduction to explicit R-parity violation* appeared in: *Perspectives on supersymmetry*, edited by G. Kane, Advances Series on Directions in High Energy Physics, Vol. 18., World Scientific Publishing Company, Singapore, 1998.

[11] M. Drees and K.I. Hikasa, *Phys. Lett.* **B 252** (1990) 127.

[12] N. Arkani-Hamed and S.Dimopoulos, hep-th/0405159.

[13] G.F. Giudice and A. Romanino, Split supersymmetry, hep-ph/0406088.

[14] I.F.M. Albuquerque, G. Farrar and E.W. Kolb,*Phys. Rev.* **D 59** (1999) 015021.

[15] V. Berezinsky, M. Kachelriess and S. Ostapchenko, *Phys. Rev.* **D 65** (2002) 083004.

[16] D.N. Spergel and P.J. Steinhardt, astro-ph/9909386.

[17] S. Mitra, astro-ph/0409121.

[18] S. Balberg, G.R. Farrar, T. Piran, Astrophys. J. **548** (2001) 179.

[19] H. Baer, K. Cheung and J.F. Gunion, *Phys. Rev.* **D 59** (1999) 075002, and references therein.

[20] S. Raby, *Phys. Lett.* **B 422** (1998) 158.

[21] A. Brignole, L.E.Ĩbanez and C.M̃unoz, *Nucl. Phys.* **B 422** (1994) 125.

[22] C.H. Chen, M .Drees, and J.F.G̃union, *Phys. Rev.* **D 55** (1997) 330.

[23] W. Kilian, T. Plehn, P. Richardson and E. Schmidt, hep-ph/0408088.

[24] J.L. Hewett, B. Lillie, M. Masip, T.G. Rizzo, hep-ph/0408248.

[25] J. Ellis et al., *Nucl. Phys.* **B 238** (1984) 453.

[26] G.R. Farrar and P. Fayet, *Phys. Lett.* **B 76** (1978) 575.

[27] C. Friberg, E. Norrbin and T. Sjöstrand, *Phys. Lett.* **B 403** (1997) 329.

[28] T. Appelquist, H. Cheng, B.A. Dobrescu, *Phys. Rev.* **D 64** (2001) 035002.

[29] P.H. Frampton and P.Q. Hung, Pham Quang, *Phys. Rev.* **D 58** (1998) 057704.

[30] H. Fritzsch, *Phys. Lett.* **B 78** (1978) 611.

[31] P. Fishbane, S. Meshkov, P. Ramond, *Phys. Lett.* **B 134** (1984) 81.

[32] G. Ingelman, C. Wetterich,*Phys. Lett.* **B 174** (1986) 109.

[33] M.L. Perl *etal*, *Int. J. Mod. Phys.* **A 16** (2001) 2137.

[34] P. Janot, *Phys. Lett.* **B 564** (2003) 183.

[35] The DELPHI Coll., *Eur. Phys. J.* **C 26** (2003) 505.

[36] A. Mafi and S. Raby, *Phys. Rev.* **D 62** (2000) 035003.

[37] The ALEPH Coll., *Phys. Lett.* **B 537** (2002) 5.

[38] The ALEPH Coll., *Phys. Lett.* **B 488** (2000) 234.

[39] See e.g.: ALEPH Coll., *Eur. Phys. J.* **C 25** (2002) 339;
DELPHI Coll., *Phys. Lett.* **B 478** (2000) 65;
L3 Coll., *Phys. Lett.* **B 517** (2001) 75;
OPAL Coll. ,*Phys. Lett.* **B 572** (2003) 8;
CDF Coll., *Phys. Rev. Lett.* **90** (2003) 131801.

[40] E.W. Kolb and M.S. Turner, *The Early Universe*, Addison-Wesley, 1990.

[41] S. Dimopoulos, D. Eichter, R. Esmailzadeh and G.D. Starkman, *Phys. Rev.* **D 41** (1990) 2388;
R. De Rujula, S.L. Glashow and U. Sarid, *Nucl. Phys.* **B 333** (1990) 173.

[42] T.K. Hemmick et al., *Phys. Rev.* **D 41** (1990) 2074.

[43] D. Javorsek et al., *Phys. Rev.* **D 65** (2002) 072003.

[44] R.N. Mohapatra and V.L. Teplitz, *Phys. Rev. Lett.* **81** (1998) 3079.

[45] R.N. Mohapatra and S. Nussinov, *Phys. Rev.* **D 57** (1998) 1940.

[46] S.W. Barwick, P.B. Price and D.P. Snowden-Ifft, *Phys. Rev. Lett.* **64** (1990) 2859.

[47] G.F. Giudice, E.W. Kolb and A. Riotto, PRD **64** (2001) 023508.

[48] D.H. Lyth and E.D. Stewart, *Phys. Rev. Lett.* **75** (1995) 201.

[49] H. Eberl, A. Bartl, W. Majerotto, *Phys. Lett.* **B 349** (1995) 127.

[50] K. Hikasa and M. Kobayashi, *Phys. Rev.* **D 36** (1987) 724.

[51] W. Beenakker, R. Höpker, M. Spira and P .Zerwas, *Nucl. Phys.* **B 492** (1997) 51.

[52] T. Sjöstrand, L. Lönnblad, S. Mrenna, P. Skands, PYTHIA-6.3 manual, hep-ph/0308153, T. Sjöstrand et al, *Comput. Phys. Commun.* **135** (2001) 238.

[53] Frank Paige, private communication

[54] R. Fernow, *Introduction to experimental particle physics*, Cambridge University Press, Cambridge, 1986.

[55] M.L. Perl, *High Energy Hadron Physics*, John Wiley & Sons, New York, 1974.

[56] A. Donnachie and P.V. Landshoff, *Phys. Lett.* **B 296** (1992) 227.

[57] H. Hesefeldt, GHEISHA user manual: *The Simultion of Hadronic Showers*, PITHA 85/02.

[58] W.S.C. Williams, *An introduction to Elementary Particle Physics*, Second edition, Academic Press, New York, 1971.

[59] G.E. Brown and A.D. Jackson, *The nucleon-nucleon interaction*, North-Holland Publishing Company, Amsterdam, 1976.

[60] J.F. Gunion and D.E. Soper, *Phys. Rev.* **D 15** (1977) 2617.

[61] F. Close, *An introduction to quarks and partons*, Academic Press, London, 1979.

[62] A.C. Kraan, *Interactions of heavy stable hadronizing particles*, *Eur. Phys. J.* **C 37** (2004) 91.

[63] A. De Rujula, H Georgi and S.L. Glashow, *Phys. Rev.* **D 12** (1975) 147

[64] M.R. Pennington, *"Glueballs: The naked truth"*, hep-ph/9811276, in *Proceedings of the Workshop On Photon Interactions And The Photon Structure, Lund, 1998*, edited by G. Jarlskog and T. Sjöstrand (CERN, 1998), p. 313.

[65] M. Chanowitz and S. Sharpe, *Phys. Lett.* **B 126** (1983) 225

[66] F. Buccella, G.R. Farrar, A. Pugliese,*Phys. Lett.* **B 153** (1985) 311

[67] M. Foster and C. Michael, *Phys. Rev.* **D 59** (1999) 094509

[68] T. DeGrand et al., *Phys. Rev.* **D 12** (1975) 2060

[69] GEANT detector Description and Simulation Tool (manual), CERN, Geneva, 1993.

[70] Z. Koba et al, *Nucl. Phys.* **B 40** (1972) 317

[71] G. Sguazzoni, *Scalar quark searches with the ALEPH experiment at LEP2*, PhD thesis, 2000.

[72] Code available on: http://www.nbi.dk/∼ackraan.

[73] A manual is available on http://atlas.web.cern.ch/Atlas/GROUPS/SOFTWARE/ DOCUMENTS/simulation.html#atlsim

[74] C. Arnault, AGE, Version v1, ATL-SOFT-95-020, and Version v2r1, 1997

[75] P. Nevski et al., DICE-95, ATL-SOFT-95-014, 1995.

[76] P. Nevski et al., Reconstruction interface for DICE-95, ATLAS-SOFT/95-draft, 1995.

[77] Web-reference: `www.google.com`.

[78] The ALEPH Coll., *Nucl. Instrum. and Methods* **A 294** (1990) 121.

[79] The ALEPH Coll., *Nucl. Instrum. and Methods* **A 360** (1995) 481.

[80] The Aleph physics analysis package V125 (Alpha) userguide, ALEPH 99-087 SOFTWR 99-001J.

[81] T. Sjöstrand et al., Comput. Phys. Commun. **135** (2001) 238.

[82] T. Sjöstrand, private communication;
See also `http://www.thep.lu.se/~torbjorn/Pythia.html`.

[83] E. Norrbin and T. Sjöstrand, *Nucl. Phys.* **B 603** (2001) 297.

[84] C. Peterson, D. Schlatter, I. Schmitt and P.M. Zerwas, *Phys. Rev.* **D 27** (1983) 105.

[85] I.G. Knowles and T. Sjöstrand, *"QCD event generators"*, in Workshop on Physics at LEP 2, CERN, Geneva, Switzerland, 2-3 Feb 1995.

[86] G. Altarelli, N. Cabibbo, G. Corbo, L. Maiani, G. Martinelli, *Nucl. Phys.* **B 208** (1982) 365.

[87] Chaminou global selection program, see http://duflot.home.cern.ch/duflot/chaminou.html.

[88] S. Jadach, W. Placzek and B.F.L. Ward, *Phys. Lett.* **B 390** (1997) 298.

[89] S. Jadach, B.F.L. Ward and Z. Was, *Comput. Phys. Commun.* **79** (1994) 503.

[90] J.A.M. Vermaseren, *"Two gamma physics versus one gamma physics and whatever lies in between"*, Presented at Gamma-Gamma Workshop, Amiens, France, Apr 8-12, 1980;
The ALEPH Coll., *Phys. Lett.* **B 313** (1993) 509.

[91] S. Jadach et al., *Comput. Phys. Commun.* **119** (1999) 272.

[92] J. Fujimoto, *Comput. Phys. Commun.* **100** (1997) 128.

[93] T. Sjöstrand, *Comput. Phys. Commun.* **82** (1994) 74.

[94] A.L. Read, *Modified Frequentist Analysis of Search Results (The CLs Method)*, Appeared in Yellow Report CERN 2000-005.

[95] The ALEPH Coll. *Phys. Lett.* **B 313** (1993) 299;
J.F. Grivaz and F. Le Diberder, LAL **92-37** (1992).

[96] The ALEPH Coll., *Phys. Lett.* **B 413** (1997) 431.

[97] R.D. Cousins and W.L. Highland, *Nucl. Instrum. and Methods* **A 320** (1992) 331.

[98] ALEPH Collaboration (written by A.C. Kraan and P. Janot), *Search for stable hadronizing squarks and gluinos in e+e- collisions up to $\sqrt{s}$ = 209 GeV*, *Eur. Phys. J.* **C 31** (2003) 327

[99] ALEPH collaboration (written by A.C. Kraan), *Search for stop decay into stable gluino with the ALEPH detector*, July 2002, Contributed paper to The 31st International Conference on High Energy Physics (ICHEP2002), Amsterdam, The Netherlands, 24-31 July.

[100] ALEPH collaboration (written by A.C. Kraan and P. Janot), *Search for stable hadronizing squarks and gluinos in e^+e^- collisio ns up to $\sqrt{s}$ = 209 GeV.*, March 2002, 23pp. Contributed paper to The XVII Rencontres de Physique de la Vallee d'Aoste, La Thuile, Italy, 9-15 March 2003.

[101] A.C. Kraan, *Stop and sbottom searches at LEP.*, May 2003, hep-ex/0305051, Published in Proceedings to The XXXVIIIth Rencontres de Moriond, devoted to Electroweak Interactions and Unified Theories, Les Arcs, France, 15-22 March 2003.

[102] The ATLAS Coll., *"ATLAS: Detector and physics performance technical design report. Volume 1",* "CERN-LHCC-99-14".

[103] ATLAS Inner Detector, Technical Design Report, CERN/LHCC/97-16, 1997.

[104] C. Driouichi, Doctoral Thesis, Lund, 2004.

[105] ATLAS Liquid Argon Calorimeter, Technical Design Report, CERN/LHCC 96-41, 1996.

[106] ATLAS Muon Spectrometer, Technical Design Report, CERN/LHCC/9722, 1997.

[107] A. Nisati, ATLAS note, ATL-DAQ-98-083.

[108] ATLAS Level-1 Trigger, Technical Design Report, CERN/LHCC/1998-14, 1998.

[109] ATLAS High-Level Trigger, Data Acquisition and Controls, Technical Design Report, CERN/LHCC/2003-022, 2003.

[110] Aleandro Nisati, private communications.

[111] A. Nisati, S. Petrarca and G. Salvini, *Mod. Phys. Lett.* **A 12** (1997) 2213.

[112] R.L. Glückstern, *Nucl. Instrum. and Methods* **24** (381) 1963.

[113] K. Kleinknecht, *Detectors for particle radiation*, Cambridge university press, Cambridge, 1987.

[114] G. Polesello and A. Rimoldi, ATLAS note, ATL-MUON-99-006.

[115] S. Ambrosiano, B. Mele, S. Petrarca, G. Polesello and A. Rimoldi, *Journal for High Energy Physics* **0101** (2001) 014 (ATL-PHYS-2002-006)

[116] Simulating Supersymmetry with ISAJET 7.0 / ISASUSY 1.0, Argonne Accel.Phys., 0703-720, 1993.

[117] ATLFAST usermanual, ATL-PHYS-98-131, see also `http://www.hep.ucl.ac.uk/atlas/atlfast/`

[118] Work performed in collaboration with J.B. Hansen.

[119] A.C. Kraan, J.B. Hansen and P. Nevski, ATLAS note, in preparation.

[120] Pavel Nevski, private communication.